

**INVESTIGATION OF TECHNIQUES FOR DETERMINING THE
RESIDUAL STRESSES IN WC-17Co THERMAL SPRAYED COATINGS
AND STUDYING THE EFFECT OF RESIDUAL STRESS ON ITS
ABRASION RESISTANCE**

OLUSEYI PHILIP OLADIJO

A thesis submitted to Faculty of Engineering and Built Environment, University of the Witwatersrand, in fulfillment of the requirements for the degree of Doctor of Philosophy

Johannesburg, 2013

DECLARATION

I declare that this thesis is my own unaided work. It is being submitted for the Degree of Doctor of Philosophy in the University of the Witwatersrand, Johannesburg. It has not been submitted before for any degree or examination in any other University.

Oluseyi Philip Oladijo

3rd May, 2013.

ABSTRACT

The aim of this project was to investigate the techniques for determining the residual stresses in WC-17Co thermal sprayed coatings and to study the effect of residual stress on abrasion resistance on different substrates. The choice of the substrate was due to their different coefficients of thermal expansion (aluminium, super-invar, 304L stainless steel, mild steel and brass). Coatings of about 200µm were successfully deposited on all the substrates.

Coatings were deposited by a high velocity oxy-fuel spraying system (HVOF), and characterized by evaluating the coating phases and wear resistance, and the residual stresses were determined via non-destructive methods. Investigations involved both as-sprayed and their annealed counterparts to ascertain the effect of heat treatment.

Non-destructive determination of residual stresses in the WC-Co coated systems was exceptionally challenging in that the coatings were only 200 microns thick. The best suited techniques for investigation of WC were diffraction-based strain scanning using penetrating radiation such as thermal neutrons (most penetrating), high energy synchrotron X-rays (100 keV enables 20 micron penetration) and laboratory X-rays (limited to 5 micron penetration). Laboratory X-rays (Necsa, using Co radiation), thermal neutrons (ANSTO, Australia) and X-ray synchrotron (ESRF, France) were successfully employed to resolve the stress conditions. The neutron investigations enabled two approaches for the determination of the in-surface stresses, direct measurements (good results for the low neutron attenuation substrates), and indirect determination using stress balance conditions inferred from the through thickness depth profiles measured in the substrates (applicable to all the higher neutron attenuating substrates). Investigations were expanded to the study of the influence of annealing at 40% of the respective substrate melting temperatures. For each substrate, the through thickness stress profile differences between the grit-blasted reference material (final before the HVOF coating) and the grit-blast coated samples were used to determine the elastic contributions purely ascribed to the coating process. This required exceptional positional resolution neutron diffraction investigations (positional accuracies better than 0.01 mm). There were both small compressive and low tensile stresses on the as-sprayed coated samples. After annealing, the stresses became substantially more compressive. The near-surface trends of the grit-blasted substrates were completely relaxed after annealing, with thermal stresses being the dominant

mechanism for residual stress induced due to the large difference in the coefficients of thermal expansion (CTE) between the WC coatings and the substrates.

The three-body abrasive tests were carried out on the parent materials (substrate), grit blasted substrates, as-sprayed coatings and heat treated coatings. The contributions of each coating process were established. There was about 45-50% reduction in the wear of grit-blasted samples compared to the substrates, whilst 80-95% reduction in the wear of the coatings compared to substrates was found. The wear resistance is due to many different contributions, but there was a strong correlation between the residual stress and wear resistance of the coating.

DEDICATIONS

To Almighty God for making this research a success, despite all odds.

To my parents Mr and Mrs Oladijo for their care and prayer.

To my beloved wife Mrs Elizabeth Oladijo and Oloyede family for their support and prayer.

ACKNOWLEDGEMENTS

First and foremost, my profound gratitude goes to God Almighty, who is the author and owner of my life.

I wish to express my gratitude and deep appreciation to my supervisors, Professor L.A. Cornish, Dr A.M. Venter and Dr N. Sacks for nurturing me till the end of this research work. I will remain grateful to you, for your effective supervision, constructive criticisms, dedication, and moral support. Indeed you are too much to be ignored and cheers! I am also grateful to Professor I. Sigalas, who is an architect of this great opportunity.

My appreciation also goes to Mr T. Ntsoane for putting in extra hours during the residual stress measurement at the X-ray Diffraction Unit, Necsa, Pretoria. Also, Patience Segonyane and Ryno Van der Merwe are thanked for their assistance during the SEM analysis at Necsa, Pretoria. Dr V. Luzin is highly appreciated for his assistance during the Neutron measurement at ANSTO, Australia.

I am indeed grateful to Department of Science and Technology (DST)/National Research Foundation (NRF) Centre of Excellence in Strong Materials (CoE-SM) for funding this research and providing other financial support. The Administrative Manager and staff of the CoE-SM are thanked for their love and support. I also wish to express my appreciation to the Financial Aid Office, University of the Witwatersrand, for financial support. Necsa is thanked for support, especially for allow me to carry out the research work.

My profound appreciation goes to all the postgraduate students of my supervisor, for their love and care. I also wish to thank the technical and support staff of the Necsa, and the School of Chemical and Metallurgical Engineering, University of the Witwatersrand, for their contributions to the success of this work.

Also, I wish to thank my parents and guardians for their care and love since my childhood. Thank you once more being part of my history.

To all my friends and family, especially Mr Leke Sufianu, Mr Kehinde Ogunyanda, Mr Edwin Adanisha, Miss T. Moipolai, Mr Oluseye Fadiran, Mr Paul Elaho, Dr Mrs Popoola, Mr Sunday Oladijo, Mr Augustine Oladijo, Damilola Oloyede, Ayomide Oloyede, Segun

Oladijo, Damilola Oladijo, Ayomide Oladijo, Mr E. Chinaka, Mr R. Brayshaw, Mr Rotimi Adeniyi, St Jude prayer warrior members, Yound Adult Family, Holy Trinity Catholic Church members (Bramfontein) and host of others. Thank you all for your support and good companionship.

Finally, my profound gratitude and appreciation go to my beloved wife, Elizabeth Oladijo, for understanding, support, endurance and above all, assist me during the collation of this thesis, I promise to continue to love you more. To my unborn children (Peter and Philomena), I can't wait for your arrival in the family soon.

TABLE OF CONTENTS

DECLARATION	ii
ABSTRACT.....	iii
DEDICATIONS.....	v
ACKNOWLEDGEMENTS	vi
TABLE OF CONTENTS.....	viii
LIST OF FIGURES	xi
LIST OF TABLES	xviii
CHAPTER ONE	1
1.0 INTRODUCTION.....	1
1.1 MOTIVATION	3
1.2 RESEARCH QUESTIONS.....	3
1.3 HYPOTHESIS	4
1.4 AIMS AND OBJECTIVES.....	4
CHAPTER TWO	5
2.0 LITERATURE REVIEW.....	5
2.1 INTRODUCTION.....	5
2.2 WC-Co	5
2.3 PHASE EQUILIBRA IN THE W-C-Co SYSTEM	6
2.4 WC-Co THERMAL SPRAY COATINGS	7
2.4.1 Introduction	7
2.4.2 Microstructure of HVOF WC-Co.....	10
2.4.3 Phase Compositions in WC-Co Coatings.....	11
2.5 COATING MICROHARDNESS.....	13
2.6 SURFACE PREPARATION AND MEASUREMENT	14
2.7 RESIDUAL STRESS	16
2.7.1 Residual Stress Development in Formed Components	17
2.7.2 Residual Stresses of WC-Co coatings	21
2.7.3 Measurement of Residual Stress.....	22
2.7.4 X-Ray Residual Stress Measurement	23
2.7.5 Principles of X-ray diffraction residual stress measurement.....	25
2.7.6 Sources of Error.....	27
2.7.7 Neutron Diffraction	28
2.7.8 Biaxial state condition for neutron diffraction	29
2.7.9 Synchrotron Radiation XRD	30
2.8 WEAR RESISTANCE.....	33
2.8.1 Types of Wear	33
2.8.2 Three-Body Abrasion	34
2.8.3 Abrasion Wear Mechanism of Sintered WC-Co Alloys	35
2.8.4 Hardness of Abrasive material	37
2.9 HEAT TREATMENT OF WC-Co	38
CHAPTER THREE	41
3.0 EXPERIMENTAL PROCEDURE	41
3.1 Introduction	41
3.2 Materials.....	41

3.3	Powder.....	43
3.4	Powder characterization	44
3.5	Coating procedure	44
3.6	Coating characterization.....	45
3.7	Test procedures	46
3.7.1	Residual stresses analyses	46
3.7.2	X-ray diffraction measurement.....	47
3.7.3	Fundamental equations for stress measurement with 2D XRD.....	50
3.7.4	The mean penetration depth	51
3.7.5	Neutron diffraction stress measurement	51
3.7.6	Synchrotron stress measurements at ESRF	53
3.8	Abrasion wear testing.....	55
3.9	Heat treatment procedure.....	56
CHAPTER FOUR RESULTS.....		58
4.1.	BATCH A (COMMERCIAL SAMPLES)	58
4.1.1.	Effect of Substrates on the Microstructure of Thermally Sprayed WC-17 wt%Co Coatings	58
4.1.1.1	Introduction.....	58
4.1.1.2	Results.....	58
4.1.1.3	X-ray diffraction	58
4.1.2.	X-ray diffraction measurements of residual stress in WC-Co thermally sprayed coatings onto metal substrates	69
4.1.2.1.	Introduction.....	69
4.1.2.2.	Results.....	69
4.1.3.	Effect of substrate on the 3 body abrasion wear of HVOF WC-17wt%Co coatings.....	74
4.1.3.1.	Introduction.....	74
4.2.	BATCH B RESULTS (SUBSTRATES PROCURED FROM GOODFELLOW, UK)	80
4.2.1.	Microstructural characteristics of HVOF sprayed WC-Co coatings on metal substrates.....	80
4.2.1.1.	Introduction.....	80
4.2.1.2.	Results.....	80
4.2.2.1.	Introduction.....	91
4.2.2.2.	Results.....	91
4.2.3.1	Introduction.....	104
4.2.3.2.	Results.....	104
4.2.4.	Effect of heat treatment on the abrasive wear of samples with thermally sprayed WC-Co coatings.....	109
4.2.4.1.	Introduction.....	109
4.2.4.2.	Results.....	109
CHAPTER 5: DISCUSSION.....		141
5.1.	Batch A (Commercial samples)	141
5.1.1.	Effect of substrates on the microstructure of thermally sprayed WC-17wt% Co coating.....	141
5.1.2.	X-ray diffraction measurement of residual stress in WC-Co thermally sprayed coatings onto metal substrates	143
5.1.3.	Effect of substrate on the 3-body abrasion wear of HVOF WC-17wt%Co coatings	147
5.2.	Batch B (Substrate procured from Goodfellow in UK)	152

5.2.1. Microstructural characteristics of HVOF sprayed WC-Co coatings on metal substrates	152
5.2.2. Systematic investigation of residual strains associated with WC-Co coatings thermal sprayed onto metal substrates	156
5.2.3. Residual stress in thin WC-Co coated systems studied by high-precision neutron diffraction.....	161
5.2.4. Effect of heat treatment on the microstructure and abrasive wear of thermal sprayed WC-Co coatings.....	166
CHAPTER 6	175
6.0. Conclusions and recommendation	175
6.1. Conclusions	175
REFERENCES	178
APPENDIX A.....	199
APPENDIX B	201

LIST OF FIGURES

Figure 2.1. Simplified equilibrium phase diagram for the binary W-C system [1988Sch].	6
Figure 2.2. Partial equilibrium phase diagram for W-C, showing three allotropic forms of W_2C , β , β' and β'' , with metastable γ , WC_{1-x} [1990Mas, 1992Bak].	6
Figure 2.3. Relationship between powder properties, spraying technique and coating properties [2005Mac].	9
Figure 2.4. Representation of abrasive grit blasting where: (1) nozzle; (2) suction chamber;	14
Figure 2.5. Origins of residual stress during coating processes [2011Azi].	17
Figure 2.6. Schematic representation of the thermal spray process, listing the primary variables that influence the quality of thermal spray coatings [2004Dav].	18
Figure 2.7. Schematic representation of the HVOF thermal spray process [2009Kam].	18
Figure 2.8. Schematic representation of the formation of a thermal spray coating, showing the coating is built up as droplets of semi-molten powder are flattened onto the substrate by the force of impact, with typical features: splat-like structure, pores, partially melted or unmelted powder particles and oxidised particles [1999Sto, 2004Dav].	19
Figure 2.9. Sample and laboratory coordinate systems [URLRes]: a) $\psi = 0$ and b) $\psi = \psi_i$ (sample is rotated through some known angle ψ_i), where D = X-ray detector, S = X-ray source, and N = Surface normal.	26
Figure 2.10. Schematic diagram of ASTM-G65 wear test machine [2010Mab].	34
Figure 3.1. Sample geometry and measurement positions for the strain analyses.	43
Figure 3.2. Side and top view of the D8 Discover for measuring residual stresses at Necsa.	48
Figure 3.3. Schematic diagram of the XRD strain measurement $\sin^2\psi$ technique for measurement of the residual stress [1996Cly]. The top diagrams show the experimental conditions at $\psi = 0^\circ$ with the bottom diagrams showing the conditions at inclined ψ values.	49
Figure 3.4. KOWARI neutron strain scanner at ANSTO, Australia.	52
Figure 3.5. Schematic diagram showing the locations where samples were extracted from the as-procured plates, designated as parent material (reference state throughout this study), grit-blasted substrate and coated sample.	54
Figure 3.6. Measurement geometries employed with (a) Synchrotron and (b) Neutron diffraction investigations [2004Kel].	55
Figure 3.7. General set-up of Dry Sand Rubber Wheel test rig showing vibratory feeder, testing chamber silo for the abrasive particles, flow rate meter and hook for loading.	56
Figure 4.1. SEM-SEI micrograph and EDX spectrum of starting WC-17wt%Co powder.	58
Figure 4.2. XRD patterns of the starting WC powder and as-sprayed coatings.	59
Figure 4.3. Optical micrograph of WC-17wt% Co coatings (bottom) on aluminium.	60
Figure 4.4. Optical micrograph of WC-17wt% Co coating (bottom) on 304L stainless steel showing coating and holes.	60
Figure 4.5. Optical micrograph of WC-17wt% Co coating (bottom) on brass.	61
Figure 4.6. SEM-BSE image of WC-17 wt% Co coating on the aluminum substrate, showing WC (light), cobalt binder (medium), and pores (black).	62
Figure 4.7. SEM-BSE image of WC-17 wt% Co coating on brass substrate, showing WC (light), cobalt binder (medium), and pores (black).	62
Figure 4.8. SEM-BSE image of WC-17 wt% Co coating on 304L stainless steel, showing WC (light), cobalt binder (medium), and pores (black).	63
Figure 4.9. SEM-BSE image of WC-17 wt% Co coating on super-invar substrate, showing WC (light), cobalt binder (medium), pores (black), and microcracks.	64
Figure 4.10. Grain size distribution of the coatings on different substrates: (a) aluminium, (b) 304L stainless steel, (c) super-invar, and (d) brass.	65
Figure 4.11. AFM surface profiles of WC-17wt% Co coatings on different substrates: (a) aluminium, (b) 304L stainless steel, (c) super-invar, and (d) brass.	66

Figure 4.12. Microhardness values of WC-Co coatings and the different substrates.	67
Figure 4.13. Correlation between the grain sizes and microhardnesses of the WC-17Co coatings on the different substrates.	67
Figure 4.14. Correlation between the porosity and microhardnesses of the WC-17Co coatings on the different substrates.	67
Figure 4.15. Correlation between the substrate coefficients of linear thermal expansion and microhardness of the WC-17Co coatings on the different substrates.	68
Figure 4.16. Correlation between the surface roughness and microhardness of the WC-17Co coatings on the different substrates.	68
Figure 4.17. Correlation between the melting point and surface roughness of the WC-17Co coatings on the different substrates.	68
Figure 4.18. Correlation between the coefficient of thermal expansion and surface roughness of the WC-17Co coatings on the different substrates.	68
Figure 4.19. Plot of d-spacing against $\sin^2\psi$ for as-sprayed coating on the brass substrate. ...	69
Figure 4.20. Residual stresses in as-coated WC-Co coatings deposited on the different substrates.	70
Figure 4.21. Correlation between the coating microhardness and residual stresses values of the WC-17Co coating on the different substrates.	71
Figure 4.22. Correlation between the coefficient of thermal expansion of the substrates and residual stresses values of the WC-17Co coating on the different substrates.	71
Figure 4.23. Correlation between the substrate specific heat capacity and residual stresses of the WC-17Co coatings on the different substrates.	71
Figure 4.24. Correlation between the substrate melting points and residual stresses of the WC-17Co coatings on the different substrates.	72
Figure 4.25. Correlation between the substrate coefficients of thermal expansion and residual stresses of the WC-17Co coatings on the different substrates.	73
Figure 4.26. Correlation between the substrate coefficients of thermal expansion and residual stresses of the WC-17Co coatings on the different substrates.	73
Figure 4.27. Morphology of silica abrasive procured from Rolfes Silica, South Africa.	74
Figure 4.28. Average cumulative mass loss for each coated sample on abrasive wear testing.	75
Figure 4.29. Wear rates of as-received coated substrates after 30 minutes of abrasive wear testing.	75
Figure 4.30. SEM-BSE micrographs of the worn WC-17Co coating surfaces on the aluminum substrate, showing extensive cracking and fragmentation of the carbides (WC (light) and Co (dark)).	76
Figure 4.31. SEM-BSE micrographs of the worn WC-17Co coating surface on brass, showing cracks, individual pull-out of carbides and binder removal around the harder carbides standing prone (WC (light) and Co (dark)).	77
Figure 4.32. SEM-BSE micrographs of the worn WC-17Co coating surface on super-invar, showing cracks and preferential binder removal around harder carbides standing prone (WC (light) and Co (dark)).	77
Figure 4.33. SEM-BSE micrographs of the worn WC-17Co coating surface on 304L stainless steel, showing few cracks, pull-out of carbides and preferential binder removal around free standing carbide grains (WC (light) and Co (dark)).	78
Figure 4.34. SEM-BSE images of cross-sections of WC-17%Co coating on aluminum, showing WC (light), cobalt binder (medium), and pores (black).	80
Figure 4.35. SEM-BSE images of cross-sections of WC-17%Co coating on brass, showing WC (light), cobalt binder (medium), pores (black) and microcracks on the right hand image.	81

Figure 4.36. SEM-BSE images of cross-sections of WC-17%Co coating on mild steel, showing WC (light), cobalt binder (grey), pores (black), with microcracks on the left hand image.....	82
Figure 4.37. SEM-BSE images of cross-sections of WC-17%Co coating on super-invar, showing WC (light), cobalt binder (grey), and pores (black).	82
Figure 4.38. SEM-BSE images of cross-sections of WC-17%Co coating on 304L stainless steel, showing WC (light), cobalt binder (medium), and pores.	83
Figure 4.39. SEM-BSE image of a Vickers hardness indentation on the cross-section of WC-17%Co coating on super-invar.....	83
Figure 4.40. XRD patterns of the starting powder and as-sprayed coatings.....	85
Figure 4.41. Macrohardness values of WC-17Co coatings on the different substrates.	86
Figure 4.42. Correlation between the grain sizes and microhardness of the WC-17Co coatings on the different substrates, showing slight decreases of hardness but scattered.	87
Figure 4.43. Correlation between the porosity and microhardness of the WC-17Co coatings on the different substrates, showing hardness decreased with increasing porosity.	87
Figure 4.44. Correlation between the substrate and coating microhardness of the WC-17Co coatings on the different substrates, showing increasing coating hardness with substrate hardness.....	87
Figure 4.45. Correlation between the substrate melting point and microhardness of the WC-17Co coatings on the different substrates, showing a slight increase.....	87
Figure 4.46. Correlation between the substrate coefficient of thermal expansion and microhardness of the WC-17Co coatings on the different substrates, showing a slight increase.	88
Figure 4.47. Plot of d -spacing versus $\sin^2\psi$ for the as-sprayed WC-17Co coating on aluminum substrate.	88
Figure 4.48. Plot of d -spacing versus $\sin^2\psi$ for the as-sprayed WC-17Co coating on brass substrate.	88
Figure 4.49. Plot of d -spacing versus $\sin^2\psi$ for the as-sprayed WC-17Co coating on mild steel substrate.	89
Figure 4.50. Plot of d -spacing versus $\sin^2\psi$ for the as-sprayed WC-17Co coating on 304L stainless steel substrate.	89
Figure 4.51. Plot of d -spacing versus $\sin^2\psi$ for the as-sprayed WC-17Co coating on super-invar substrate.	89
Figure 4.52. Summary of residual stresses determined in for the as-sprayed WC-Co coatings deposited on the different substrates of this study. The results for aluminum is given by the first bar plot that is not labelled.	90
Figure 4.53. Residual strain depth dependence determined from the lattice plane spacing of the $\{311\}_{\text{Cu}}$ and $\{101\}_{\text{WC}}$ Bragg peaks measured with synchrotron X-ray diffraction on the thinned wedge brass sample. The bottom figures show an enlarged view of the results at the near surface region. Legend: ● = substrate in-plane component; ▲ = substrate normal component; ○ = WC in-plane component; Δ = WC normal component.	92
Figure 4.54. Residual strain depth dependence determined from the lattice plane spacing of the $\{311\}_{\text{Cu}}$ Bragg peak measured with neutron diffraction on brass sample. The bottom figures show an enlarged view of the results at the near surface region. The lines through the symbols represent polynomial curve fits to enable stress calculations at corresponding depth values. Legend: ● = substrate in-plane component; ▲ = substrate normal component.....	93
Figure 4.55. Residual strain depth dependence determined from the lattice plane spacing of the $\{200\}_{\text{Ni}}$ and $\{101\}_{\text{WC}}$ Bragg peaks measured with synchrotron X-ray diffraction on the thinned wedge invar sample. The bottom figures show an enlarged view of the results at near	

surface region. Legend: ● = substrate in-plane component; ▲ = substrate normal component; ○ = WC in-plane component; Δ = WC normal component.	94
Figure 4.56. Residual strain depth dependence determined from the lattice plane spacing of the {200} _{Ni} Bragg peak measured with neutron diffraction on invar sample. The bottom figures show an enlarged view of the results at the near surface region. The lines through the symbols represent polynomial curve fits to enable stress calculations at corresponding depth values. Legend: ● = substrate in-plane component; ▲ = substrate normal component.	95
Figure 4.57. Residual strain depth dependence determined from the {311} _{Fe-γ} reflection in the 304L stainless steel substrate and {101} _{WC} Bragg peaks measured with synchrotron X-ray diffraction. The bottom set of figures show an enlarged view of the results at the near surface regions. Legend: ● = substrate in-plane component; ▲ = substrate normal component; ○ = WC in-plane component; Δ = WC normal component.	95
Figure 4.58. In-plane residual stress depth dependence determined from the lattice strain results of the {311} _{Cu} and {101} _{WC} Bragg peaks measured with synchrotron X-ray diffraction on the thinned wedge brass sample. The near surface residual stress of the WC determined with laboratory X-rays (Co radiation) is also indicated [2012Ola]. Legend: ● = substrate in-plane stress; ○ = WC in-plane stress; ▲ = WC near surface stress (laboratory X-rays).	97
Figure 4.59. In-plane residual stress depth dependence determined from the fitted lattice strain results of the {311} _{Cu} Bragg peak measured with neutron diffraction on the 25 x 25 mm ² brass sample.	98
Figure 4.60. In-plane residual stress depth dependence determined from the lattice strain results of the {200} _{Ni} and {101} _{WC} Bragg peaks measured with synchrotron X-ray diffraction on the thinned wedge invar sample. The near surface residual stress of the WC determined with laboratory X-rays (Co radiation) is also indicated [2012Ola]. Legend: ● = substrate in-plane stress; ○ = WC in-plane stress; ▲ = WC near surface stress (laboratory X-rays).	99
Figure 4.61. In-plane residual stress depth dependence determined from the fitted lattice strain results of the {200} _{Ni} Bragg peak measured with neutron diffraction on the 25 x 25 mm ² super invar sample.	100
Figure 4.62. In-plane residual stress depth dependence determined from the lattice strain results of the {311} _{Fe-γ} and {101} _{WC} Bragg peaks measured with synchrotron X-ray diffraction. The near surface residual stress of the WC determined with laboratory X-rays (Co radiation) is also indicated [2012Ola]. The substrate coating interface was set at 0 mm. Legend: ● = substrate in-plane stress; ○ = WC in-plane stress; ▲ = WC near surface stress (laboratory X-rays).	100
Figure 4.63. Plastic strain profiles (eigenstrains) for brass determined from strain results of X-ray synchrotron (left) and neutron diffraction (right). Legend: ● = grit blast in-plane component; ▲ = grit blast normal component; ○ = as-coated in-plane component; Δ = as-coated normal component.	101
Figure 4.64. Plastic strain profiles (eigenstrains) for super invar determined from strain results of X-ray synchrotron (left) and neutron diffraction (right). Legend: ● = grit blast in-plane component; ▲ = grit blast normal component; ○ = as-coated in-plane component; Δ = as-coated normal component.	102
Figure 4.65. Plastic strain profiles (eigenstrains) for 304L stainless steel determined from strain results of X-ray synchrotron investigations. Legend: ● = grit blast in-plane component; ▲ = grit blast normal component; ○ = as-coated in-plane component; Δ = as-coated normal component.	102
Figure 4.66. Experimentally measured through-thickness stress profiles for steel samples in: a) as-sprayed and b) annealed conditions at 700°C, also with the profiles measured on the substrates only.	105

Figure 4.67. Experimentally determined through-thickness stress profiles for mild steel samples in: a) as-sprayed and b) annealed conditions and model fit of the experimental data.	106
Figure 4.68. Measured in-plane residual stresses (MPa) in the aluminium substrates: (a) Grit-blast only sample preparation stage; (b) Grit-blast sample, annealed at 375°C.	106
Figure 4.69. Measured in-plane residual stresses (MPa) in WC-coated aluminium samples: (a) As-coated condition; (b) Annealed at 375°C.	107
Figure 4.70. Strains in coated samples of different substrate materials.	108
Figure 4.71. Optical micrograph of cross-section of annealed WC-17wt% Co coating (bottom) on brass, showing the good fit between the coating and irregular surface.	109
Figure 4.72. Optical micrograph of cross-section of annealed WC-17wt% Co coating (bottom) on mild steel substrate, showing holes, microcracks and the good fit between coating and irregular surface. The black area on the image is the alumina used for grit-blasted.	110
Figure 4.73. Optical micrograph of cross-section of annealed WC-17wt% Co coating (bottom) on super-invar, showing holes and good fit between coating and irregular surface. The black area in the coating-substrate interface is the alumina used for grit-blasted.	111
Figure 4.74. SEM-BSE images of cross-sections of annealed WC-17% Co coating on aluminum, showing WC (light), cobalt binder (medium), pores (black), microcracks and coating interface (right side).	111
Figure 4.75. SEM-BSE images of cross-sections of annealed WC-17% Co coating on brass, showing WC (light), cobalt binder (medium), pores (black), microcracks and coating interface (right side).	112
Figure 4.76. SEM-BSE images of cross-sections views of annealed WC-17% Co coating on mild steel, showing WC (light), cobalt binder (medium), pores (black), microcracks, carbide pull-out and coating interface (right side).	113
Figure 4.77. SEM-BSE images of cross-sections of annealed WC-17% Co coating on super-invar, showing WC (light), cobalt binder (medium), pores (black), microcracks, carbide pull-out (right side).	113
Figure 4.78. SEM-BSE images of cross-sections of annealed WC-17% Co coating on 304L stainless steel substrate, showing WC (light), cobalt binder (medium), pores (black), microcracks, carbide pull-out and coating interface (right side).	114
Figure 4.79. XRD patterns of the as-sprayed and annealed WC-17Co coatings on 304L stainless steel.	116
Figure 4.80. XRD patterns of the as-sprayed and annealed WC-17Co coatings on super-invar.	117
Figure 4.81. XRD patterns of the as-sprayed and annealed WC-17Co coatings on brass.	117
Figure 4.82. XRD patterns of the as-sprayed and annealed WC-17Co coatings on mild steel.	118
Figure 4.83. XRD patterns of the as-sprayed and annealed WC-17Co coatings on aluminum.	118
Figure 4.84. Macrohardness values of as-received substrate, as-sprayed and annealed WC-Co coating and the different substrates.	119
Figure 4.85. Residual stress of WC-17Co coating and substrate under different conditions.	121
Figure 4.86. Abrasive wear mass loss of the as-received substrates.	122
Figure 4.87. Abrasive wear mass loss of the grit-blasted substrates.	123
Figure 4.88. Abrasive wear mass loss of the WC-17Co as-coated deposits substrates.	123
Figure 4.89. Abrasive wear mass loss of the annealed WC-17Co coatings on the different substrates.	124

Figure 4.90. Summary of the wear rates of the different as-received substrates and WC-Co coatings under different conditions.....	125
Figure 4.91. SEM-SE micrographs of the worn super-invar as-received substrate, revealing plastic deformation (1), silica sand (shown by arrow) with appearance of small pit and deep grooves (2).	126
Figure 4.92. SEM-SE micrographs of the worn mild steel as-received substrate, revealing plastic deformation (1), silica sand (shown by arrow) with appearance of small pit (2) and grooves (3).	126
Figure 4.93. SEM-SE micrographs of the worn brass as-received substrate, revealing plastic deformation (1), silica sand (indicated by arrow), deep grooves (2) and appearance of small pits.....	127
Figure 4.94. SEM-SE micrographs of the worn 304L stainless steel as-received substrate, revealing plastic deformation (1), deep grooves and appearance of small pits (2).....	127
Figure 4.95. SEM-SE micrographs of the worn aluminium as-received substrate, revealing plastic deformation (1), silica sand (shown by arrow) with appearance of small pits (2).	128
Figure 4.96. SEM-SE micrograph of the worn grit-blasted mild steel substrate, revealing plastic deformation and silica sand (shown by arrow).....	128
Figure 4.97. SEM-SE micrograph of the worn grit-blasted 304L stainless steel substrate, revealing plastic deformation and silica sand (shown by arrow).....	129
Figure 4.98. SEM-SE micrograph of the worn grit-blasted brass substrate, revealing plastic deformation, deep grooves and silica sand (shown by arrow).....	129
Figure 4.99. SEM-SE micrograph of the worn grit-blasted aluminum substrate, revealing plastic deformation, deep grooves, silica sand (shown by arrow) with appearance of a small pits.....	130
Figure 4.100. SEM-SE micrograph of the worn grit-blasted super-invar substrate, revealing plastic deformation.....	130
Figure 4.101. SEM-SE micrographs of the worn WC-17Co coating surface on 304L stainless steel, showing fragmentation of carbides, and pull-out of carbides as a result of binder removal.	131
Figure 4.102. SEM-SE micrographs of the worn WC-17Co coating surface on aluminium substrate, showing fragmentation of carbides, microcracking and pull-out of carbides as a result of binder removal.	132
Figure 4.103. SEM-SE micrographs of the worn WC-17Co coating surface on mild steel, showing fragmentation of high relief carbides, cracking, pull-out of carbides due to binder removal.	132
Figure 4.104. SEM-SE micrographs of the worn WC-17Co coating surface on brass, showing fragmentation of carbides, microcracking, pull-out of carbides due to binder removal, high relief carbides and holes.	133
Figure 4.105. SEM-SE micrographs of the worn WC-17Co coating surface on super-invar, showing fragmentation of carbides, cracking and pull-out of carbides due to binder removal and groove formation.....	133
Figure 4.106. SEM-SE micrographs of the worn annealed WC-17Co coating surface on aluminum, showing fragmentation of carbides, cracked WC grains, and pull-out of carbides due to binder removal.	134
Figure 4.107. SEM-SE micrographs of the worn annealed WC-17Co coating surface on 304L stainless steel, showing fragmentation of carbides, cracked WC grains and pull-out of carbides due to binder removal.....	134
Figure 4.108. SEM-SE micrographs of the worn annealed WC-17Co coating surface on brass, showing fragmentation of carbides, cracking, smearing (shown by arrow), high relief carbides and pull-out of carbides due to binder removal.	135

Figure 4.109. SEM-SE micrographs of the worn annealed WC-17Co coating surface on mild steel, showing fragmentation of carbides, microcracking, smearing (shown by arrow), pull-out of carbides due to binder removal.....	135
Figure 4.110. SEM-SE micrographs of the worn annealed WC-17Co coating surface on super-invar, showing fragmentation of carbides, microcracking and pull-out of carbides (shown by arrow) due to binder removal.....	136
Figure 4.111. Correlation between the coefficients of thermal expansion and residual stresses of grit-blasted substrates	137
Figure 4.112. Correlation between the melting point and residual stresses of the grit-blasted substrate samples.	137
Figure 4.113. Correlation between the specific heat capacity and residual stresses of the grit-blasted substrate samples.	138
Figure 4.114. Correlation between the specific heat capacity and residual stresses of the annealed grit-blasted substrate samples.	138
Figure 4.115. Correlation between the coefficient of thermal expansion and residual stresses of the annealed grit-blasted substrate samples.....	138
Figure 4.116. Correlation between the substrate coefficients of thermal expansion and wear loss, showing no discernable relationship.....	138
Figure 4.117. Correlation between the melting temperature and wear mass loss, showing a possible maximum at $\sim 1100^{\circ}\text{C}$	139
Figure 4.118. Correlation between the substrate macrohardness and wear loss.....	139
Figure 4.119. Correlation between the substrate specific heat capacity and wear loss of the substrates.....	139
Figure 4.120. Correlation between residual stress (upper graph) and wear loss (bottom graph) of the as-sprayed and heat treated samples.....	140

LIST OF TABLES

Table 2. 1. Thermal spray process comparison [2004Dav].....	10
Table 2. 2. Comparison of the residual stress measurement techniques [2004Osm].....	32
Table 3.1. Substrate thickness.	42
Table 3.2. Physical properties of the substrates [URLCoe, URLMe].....	43
Table 3.3. Powder composition.....	43
Table 3.4. Parameters used for thermal spraying.	44
Table 3.5. Sample dimensions used for the analysis.....	45
Table 3.6. Elastic constants of the different materials.	50
Table 3.7. Instrument settings used for different reflections in neutron diffraction.	53
Table 3.8. Parameters used for heat treatment.	57
Table 4.1. Porosity and mean grain size of the coatings.	65
Table 4.2. Measured properties of the coatings.	66
Table 4.3. Residual stresses in WC coatings deposited on different substrates.....	70
Table 4.4. Residual stresses in WC coatings deposited on different substrates.....	72
Table 4.5. Yield strength, abrasive wear results and average residual stress of the coated samples.....	79
Table 4.6. Properties of the WC-Co coatings on various substrates.	84
Table 4.7. Summary of materials and residual stress values determined in the substrates and HVOF coatings.	103
Table 4.8. Comparison of residual stresses in WC coatings determined under different thermal conditions (experimentally measured directly and predicted from stress balance using the measured through thickness stress profiles in the substrates).....	105
Table 4.9. Properties of the as-sprayed and annealed WC-17Co coatings.	115
Table 4.10. Residual stress and abrasive wear results of coatings and different substrates subjected to various conditions.....	120

CHAPTER ONE

1.0 INTRODUCTION

Hardmetals are very hard, wear resistant materials made by powder metallurgical techniques. Generally, they consist of fine carbide particles dispersed in a binder metal. They are used extensively in industry against different types of environmental load. This is due to the good mechanical, physical and chemical properties. The most commonly used hardmetals consist of tungsten carbide (WC) in a cobalt (Co) matrix, where the WC is the hard phase and promotes wear resistance and Co is the binder and adds some ductility. Cemented carbides, best known for their superior wear resistance, have a range of industrial uses which are diverse compared to other powder metallurgy products. Common uses include mining tools, metalworking tools, and wear resistant components. All these applications have one mechanical property in common: the ability to resist wear.

Hardmetals are also used as coatings, and this retains the toughness of the substrate with the good wear resistance of the WC-Co coating. A commonly used method for coatings is thermal spraying. Thermal spray techniques are a collective term that embraces a group of coatings processes. In thermal spray coatings, micro-size metallic or nonmetallic surfacing materials are deposited in a molten or semi-molten condition onto a prepared grit-blasted substrate. The resulting coating imparts desired surface properties to the substrate while maintaining the substrate's unique properties.

Thermal spraying techniques started at the beginning of 1900 [1996Sie]. During that period until today, many different thermal spray systems have been developed. All are fundamentally based on the same principle [1996Sie]. A heat source liquefies the coating material (powder) and splashes it onto the surface of the workpiece (substrate) that has to be coated. Depending on the heat source (combustion flame or thermal plasma) temperatures from 100 to 10000 °C can be reached. Velocities from 100 to 1000 m/s can be reached by the injected particles. This high kinetic energy leads to plastic deformation of the droplets at the surface to be coated, whilst shrinkage and fast cooling make the droplets clamp onto the surface profile.

Thermally sprayed coatings based on tungsten carbide are widely used in industry. Many authors have conducted research on the different types of deposition methods, the effect of

powder morphology and spray parameters on microstructure evolution and coating properties [1996Jen, 1998Vil]. However, not all aspects are fully understood. Thermal spray coating technology is extensively used for the protection of components from abrasive, adhesive and erosion wear, and corrosion. As demand for engineering application increases, the requirements for composite coatings that protect the substrate is also increased [2010Rob]. In wear-resistant applications, the coated layer provides the resistance to wear, while the substrate supports the impact to which the system (coating and substrate) is subjected. Advances in thermal spraying make possible the replacement of bulk components in paper milling [2000Fri] or the replacement of chromium plating in aircraft manufacturing [2001Str, 2001Nas], or automobile industry [1997Khe, 1998Cha], as well as the deposition of thermal sprayed coatings on critical parts in petroleum drilling [1993Kes].

Residual stresses are self equilibrating internal stresses existing in a free body which has no external forces or constraints on its body [1982Mur]. During thermal spray manufacturing of layer composites, residual stresses are formed in coatings and substrates due to the different stages of the manufacturing process. The most important stress generating effects, which can superpose on each other are the following:

- Substrate pre-treatment [1998Lug],
- Solidification and shrinkage of spray particles [2006Wen],
- Phase transformation during temperature changes [1991Kur],
- Heat transfer between coating and substrate towards thermal equilibrium (which may be influenced by simultaneous surface cooling) [2001Wit],
- Impulse transfer from impinging particles [2006Wen], and
- Heat transfer to the environment during cooling of the composite to room temperature.

This research aimed at investigating the techniques for determining the residual stresses in WC-Co thermal sprayed coatings and discussing their suitability for the evaluation of stresses in thermal sprayed coatings, as well as studying the effect of the stresses on the abrasion resistance of the coating. Four substrates, namely aluminum, brass, 304L stainless steel and super-invar for batch A (commercial samples) and five substrates for batch B (Samples procured from Good fellow, UK, which had mild steel in addition) were investigated. The samples were thermally sprayed with coating of 200 μ m thickness deposited on their

substrate. These materials were chosen to have a range of coefficients of thermal expansion in addition to being different to that of coating material.

In this research, the feedstock powder was produced by sintering and spray-drying, characterized for size and size distribution, morphology and phase composition. Coatings were deposited by a high velocity oxy-fuel (HVOF) spraying system and characterized by evaluating the microstructures, phase composition, grain size, wear resistance and the residual stress determined via different non-destructive methods.

1.1 MOTIVATION

- Thermal sprayed WC-Co coatings help to protect the base material against different environmental conditions, e.g. abrasive wear, high temperature, chemically aggressive fluid, hot gas corrosion etc.[1995Paw].
- Residual stresses exert a large influence on coating and composite properties. They lead to crack formation or influence on coating's hardness and adhesion strength [1999Sto].
- Since the formation of residual stresses cannot be avoided, they can be prevented/or reduced by using proper process parameters during coating manufacturing.
- In order to obtain information about the characteristic generation of residual stresses for specific process conditions, the reliability of residual stress analysis methods is important.
- The results from this project will assist the user of coatings in matching substrates and coatings and/or in deciding whether to change the deposition procedure to cater for any residual stresses.

1.2 RESEARCH QUESTIONS

- How can a systematic investigation of residual strains associated with thermally sprayed WC-Co coatings on metal substrates be achieved?
- What are the microstructural characteristics of HVOF sprayed WC-Co coatings on metal substrates?
- How can the effects of heat treatment on the abrasive wear of thermally sprayed WC-Co coatings be determined?
- What influence can residual stress have on the wear resistance of the coating?

1.3 HYPOTHESIS

Coatings can be improved if the mechanism which leads to residual stresses, such as spraying techniques, substrate properties and cooling rate can be optimised. Therefore, the aim of this investigation was to compare residual stress profiles before and after heat-treatment, and relate these changes to the microstructural transformations after heat-treatment of relatively thin thermal spray cermet coatings, as well as the abrasion resistance of annealed coated samples.

1.4 AIMS AND OBJECTIVES

The main aim of this research work was to study the effect of residual stress on the abrasion resistance of thermal spray coatings. This was achieved through the following objectives:

- (1) Reviewing the present knowledge of the coating technology.
- (2) Identification of the residual stress state in the coating and substrate.
- (3) Analysis and comparison of the results obtained from the given coated substrate samples, and
- (4) Assessment of the wear resistance of the material.

CHAPTER TWO

2.0 LITERATURE REVIEW

2.1 INTRODUCTION

This chapter reviews the selected information on WC-Co and properties of the WC-Co thermally spray coatings. This chapter includes a brief survey of the effect of residual stress and the wear resistance of the WC-Co. The review on coatings highlights the current observations and understanding on the interaction of powder processing and coating deposition technologies on coating properties.

2.2 WC-Co

WC-Co, whether sintered or coatings, is a composite material consisting of grains of hard WC phase cemented together by a Co binder. Henry Moissan (1852-1907), a Nobel Laureate (1906), is best known as the inventor of the electric furnace and for his unsuccessful attempts to prepared artificial diamonds. It was in his laboratory at the School of Pharmacy at the University of Paris, that the two carbides of tungsten were discovered, namely W_2C (1896) by Moissan himself and WC by Williams [1996Gur].

Tungsten carbide-cobalt (WC-Co) based materials are extensively used in industry in their sintered, as well as thermally sprayed, forms for applications requiring abrasion, sliding, fretting, and erosion resistance [1981Sar, 1997Woo, 2001Gui]. The hard WC particles form the major wear resistance constituent of this material, while the cobalt binder provides toughness and support. Properties such as hardness, wear resistance, and strength are influenced primarily by the WC grain size and volume, also by varying the porosity and (often unintentionally) the carbide and binder phase composition. In the sintered material, the WC grains tend to touch one another and form a continuous “skeleton” of carbide, with a cobalt binder occupying the spaces between the carbide grains [1979Exn]. The properties can also be tailor-made for specific applications by changing the grain size of WC and the amount of binder [1970Gur].

2.3 PHASE EQUILIBRA IN THE W-C-Co SYSTEM

Tungsten combines with carbon to form hexagonally closed packed (hcp) carbides, namely WC and W_2C (Figure. 2.1).

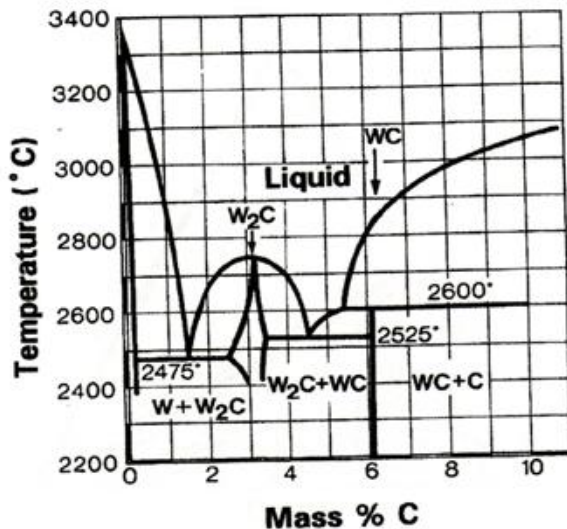


Figure 2.1. Simplified equilibrium phase diagram for the binary W-C system [1988Sch].

The W_2C phase also has other allotropic forms as can be seen in Figure 2. 2. WC contains 6.13 wt% C and has a microhardness of about 2400kg/mm², while W_2C contains 3.16 wt% C and has a microhardness of about 3000kg/mm², but is more brittle than WC [1988Sch]. Of the more commonly used metal carbides, only WC and Mo_2C have an hcp crystal structure, while most of the others (e.g. TiC, TaC, NbC, and VC) are face-centred cubic (fcc). Nevertheless, the hcp WC lattice can transform to an fcc lattice by means of small atomic displacements [1966San, 1988Sch].

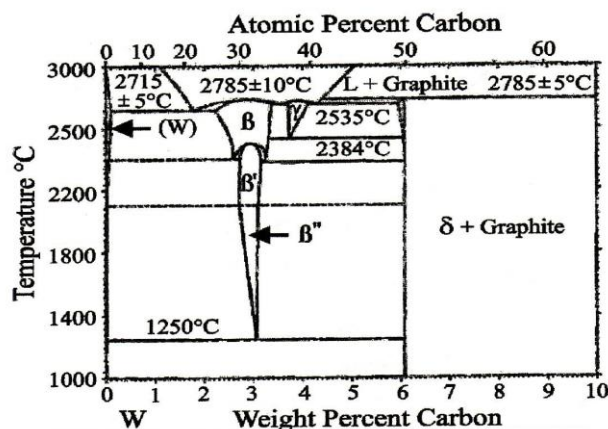


Figure 2.2. Partial equilibrium phase diagram for W-C, showing three allotropic forms of W_2C , β , β' and β'' , with metastable γ , WC_{1-x} [1990Mas, 1992Bak].

The wet ability of WC by most binder metals is better than that of the other carbides [1990Mas, 2008Vil]. This, along with its relative toughness, makes it the most widely used carbide for sintered hard metals. Cobalt is the most commonly used binder because the excellent carbide wetting improves the adhesion properties. Cobalt is hcp below 425°C and fcc above, but a significant amount of fcc phase is often retained in sintered WC-Co hard metals at room temperature [1966San, 1988Sch], as well as in coatings. Pure WC, in the absence of cobalt, does not melt under standard atmospheric conditions, but instead decomposes into a liquid phase and graphite above about 2780°C, as can be seen from the peritectic reaction phase diagram for the W-C system (Figure 2.2).

The properties of sintered WC-Co composites are critically dependent on their final composition [1981Sar]. Slight deviations from the ideal carbon content allow the occurrence of either the eta ternary compound or graphite. Most of these phases are usually undesirable, and results in degradation of mechanical properties. Nagender [1991Nag] and Baker [1992Bak] reported that the W-C-Co ternary system has nine phases present at 1300°C. These include η phases ($\text{Co}_6\text{W}_6\text{C}$, $\text{Co}_3\text{W}_3\text{C}$ and (W_2C) , and the intermediate μ phase (Co_7W_6). These are typically found in the metallic matrix. However, the most common transformations in WC-Co coatings are $\text{WC} \leftrightarrow \text{W}_2\text{C}$ and $\text{WC-Co} \leftrightarrow \text{Co}_3\text{W}_3\text{C}$ [2000Ste].

2.4 WC-Co THERMAL SPRAY COATINGS

2.4.1 Introduction

Thermal spray coatings are extensively used for the protection of components from abrasive, adhesive and erosion wear, and corrosion. As the demand for engineering applications increases, the requirements for composite coatings that protect the substrate, to retain the physical and chemical properties, and enhance the resistance of the substrate to wear and corrosion are increasing [2010Rob].

WC-Co coatings composed of hard ceramics particles embedded in a metallic binder have good tribological properties, due to their excellent adherence to the substrate, good cohesion, low porosity, high levels of retained WC during spraying, as well as good mechanical properties [1997Usm, 2001Gui, 2003Yan]. The main types of spray processes available are wire spraying, powder flame coating, D-gun coating (a form of high pressure/high velocity flame spraying), air plasma spraying (APS), controlled atmosphere plasma spraying (CAPS),

low pressure/vacuum plasma spraying (LPPS/VPS), and high velocity oxygen fuel (HVOF) coating [1995Paw]. HVOF spraying has been shown to be one of the best methods for depositing WC-Co powders, because of the higher velocity and lower temperatures experienced by the powder particles compared to other deposition methods, which result in less decomposition of the WC during spraying [1995Paw, 2003Yan]. However, even during HVOF spraying, the WC-Co powder has to be exposed to a high temperature flame jet for heating and acceleration.

According to Luiz [1998Lui], when the coating sprayed by HVOF system (CDS of plasma Technik) and Plasma (VPS) are compared in terms of wear resistance, it was discovered that the protection against wear is three times higher when the WC-Co is applied by the hypersonic process. Provot *et al.* [1993Pro] showed that HVOF (CDS) produced decarburizing effects inferior to those produced by plasma spraying (APS). Due to the high temperature involved in the plasma process, some immediate phase changes happen, so the carbon (e.g. in WC-17%Co), can be oxidized and/or diffused into the matrix. However, HVOF operates at temperatures below air plasma spraying and the powder is kept in contact with the flame for a short time, so that the original characteristics of the WC are better retained, and consequently the microstructure is not melted and is more resistant to wear.

The control of coating properties is complex because, as shown in Figure 2.3, the properties derive from an interaction of various factors. For each process, powders are needed. There are many kinds of commercially available powders which are usually produced by several different manufacturing methods including cast-crushed, sintered-crushed, agglomerated, aggregated and coated [1996Li, 2005Mac]. The process route determines the morphology and phase composition of the powder. The main variables for thermal spraying are powder particle size, powder morphology and size distribution and crystal structure. Depending mainly on the manufacturing method, the powder flow varies during spraying [1996Ber] and the spraying techniques determine the phases that occur in the coating [1955Gur, 1996Kha, 1996Li, 1985Ara, 1989Dor].

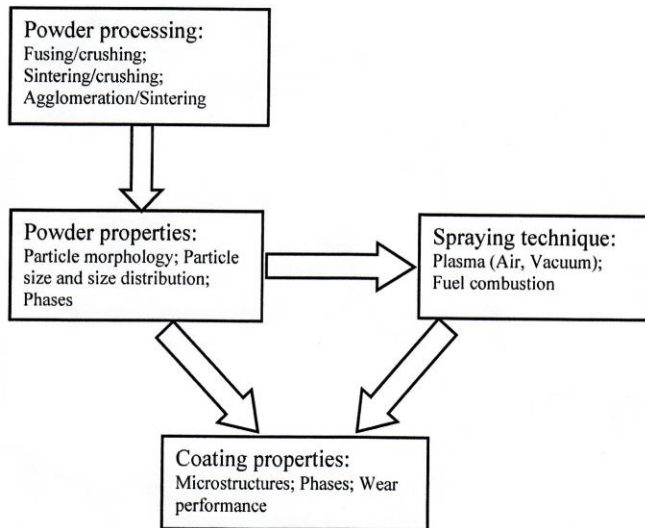


Figure 2.3. Relationship between powder properties, spraying technique and coating properties [2005Mac].

The structure of a thermally sprayed coatings is very sensitive to the structure of the starting powder and spraying techniques [1955Gur, 1996Li, 1998Vil], which also affect the performance of the coatings. Hence, knowledge of powder characteristics is important to help explain the resulting coatings.

For tungsten carbide cobalt cemented alloys, the carbon content, cobalt and carbide grain size are the important factors which influence the mechanical performance and structure of cemented carbide material [1955Gur, 1996Li]. The decomposition of tungsten carbide depends greatly on powder type produced by different manufacturing methods [1985Vin, 1989Ram, 1996Li]. Five representative types of WC-Co powders were selected by Li *et al.* [1996Li], to clarify the dependence of the structure of sprayed coatings on the structure of the initial powders. The WC-Co powders were sprayed with the Jet-Kote process of plasma spraying. The decomposition of tungsten carbide after passing through the flame depended greatly on the structure of the powder, in particular, the pre-existence of complex carbides $\text{CO}_3\text{W}_3\text{C}$ and W_2C .

Thermal spraying techniques were invented by Schoop in the early 1900s after observing how lead cannon balls adhered to vertical surfaces after firing. The continuous detonation spray process was invented in 1958 by Union Carbide. However, it was Browning in 1983 who first patented the high velocity oxygen fuel process [1983Bro]. Table 2.1 presents some highlights of different types of thermal spray techniques, which are based on the same

principle: all impacting both thermal and kinetic energy to the powder particles being sprayed, thus leading to plastic deformation of the droplets at the surface to be coated [1996Sie]. Each technique has a unique velocity/temperature combination, as a result, the coatings deposited by different techniques have different microstructures and phases, and so different responses to wear. HVOF processes are characterized by low flame temperatures and high particle velocities. HVOF-WC-Co coatings have been successfully used as internal sealing faces valves to overcome tribological and tribo-corrosion issues associated with leakage and jamming [1988Viv].

Table 2. 1. Thermal spray process comparison [2004Dav].

Attribute	Flame spray	High-velocity oxyfuel	Detonation gun	Wire arc	Air plasma	Vacuum plasma	Radiofrequency plasma
Jet							
Jet temperature. K	3500	5500	5500	>25,000	15,000	12,000	10,000
Jet velocities. m/s (ft/s)	50 - 100 (160 - 300)	500 - 120 (1600 - 4000)	>1000 (>3300)	50 - 100 (160 - 300)	300 - 1000 (1000 - 3300)	200 - 600 (700 - 2000)	20 - 80 (70 - 300)
Gas flow. SLm	100 - 200	400 - 1100	N/A	500 - 3000	100 - 200	150 - 250	75 - 150
Gas type	O ₂ , acetylene	CH ₄ , C ₃ H ₈ , H ₂ , O ₂	O ₂ , acetylene	Air, N ₂ , Ar	Ar, He, H ₂ , N ₂	Ar, He, H ₂	Ar, He, H ₂
Power input. KW	20	150 - 300	N/A	2 - 5	40 - 200	40 - 120	40 - 200 (plate)
Particle feed							
Particle temperature (max). °C (°F)	2500 (4500)	3300 (6000)	N/A	>3800 (>6900)	>3800 (>6900)	>3800 (>6900)	>3800 (>6900)
Particle velocities. m/s (ft/s)	50 - 100 (160 - 300)	200 - 1000 (700 - 3300)	N/A	50 - 100 (160 - 3000)	200 - 800 (700 - 2600)	200 - 600 (700 - 2000)	20 - 50 (70 - 160)
Material feed rate. g/mn	30 - 50	15 - 50	N/A	150 - 2000	50 - 150	25 - 150	20 - 50
Deposit/coating							
Density range (%)	85 - 90	>95	>95	80 - 95	90 - 95	90 - 99	95 - 99
Bond strength. Mpa (Ksi:)	7 - 18 (1 - 3)	68 (10)	82 (12)	10 - 40 (1.5 - 6)	<68 (<10)	>68 (>10)	>68 (>10)
Oxides	High	Moderate to dispersed	Small	Moderate to high	Moderate to coarse	None	None

2.4.2 Microstructure of HVOF WC-Co

The nature of the microstructure phases and their percentage in HVOF coatings depend mostly on the heat and mass transfer between the gas jet and the in-flight particles prior coating formation [2000Ste]. The nature and the stoichiometry of the fuel and the corresponding combustion gases are crucial operating conditions that tune the microstructure, and thus the coating properties [1986Has, 2010Sah]. The extent of the WC transformation depends on the starting powder (size, morphology, carbide size distribution), the amount of oxygen in the environment, and the spray parameters.

HVOF coatings have a low porosity due to high velocities during spraying [1983Bro, 1996Li]. One of several sources of porosity is shadowing due to the angle of impingement of the spray stream. Shadowing is generally associated with coatings sprayed at 45° angle from the optimal normal angle of incidence [2005Cra]. Coating porosity decreases (i.e. density increases) as the angle of spraying approaches 90° (i.e. normal to the surface being coated). Porosity is an important coating feature that strongly influences coating properties. As with oxide inclusions, porosity can be a desirable characteristic. It is generally considered that porosity is undesirable. Porosity creates poor coating cohesion and allows for higher wear and corrosion rates, and is generally associated with a higher number of unmelted or resolidified particles that become trapped in the coating. Poor splat or particle cohesion leads to premature coating cracking, delamination, or spalling. For hardface or wear-resistant coatings, porosity lowers coating hardness and contributes to poor surface finishes, thus decreasing wear resistance. Porosity in wear coatings can also lead to the generation of coating fragments that break away and become abrasive cutting agents, increasing coating wear rates [2005Cra].

Most researchers examined the coating microstructures in cross section using optical and/or scanning electron microscopy (SEM). The features were usually porosity, and sometimes the size and size distribution of the carbide phase. Some authors [1993Tom, 1996Kor] used Murakami's reagent to reveal the other phases than WC and cobalt in the coating. The microstructures were also characterized by variations in grey level contrast of the binder phase in BSE micrographs, a result of variations in composition [2000Sta]. In backscattered electron (BSE) SEM images, the higher the tungsten content, the lighter the phase appears. due to the higher average atomic number of tungsten than carbon [1996Gui]. For example, WC appears lighter than cobalt, and W_2C appears lighter than WC [1990Var]. The W_2C and η phases also often have a characteristic dendritic morphology [1998Vil]. Powders are usually examined using XRD, TEM, SEM, and both surface morphology and cross sections can be characterized [1979Exn, 1996Li, 1998Vil].

2.4.3 Phase Compositions in WC-Co Coatings

HVOF spraying of WC-Co powders produces phase changes, since spraying is done in the presence of oxygen [1986Has, 2010Sah]. Fewer or no phase changes occur when oxygen is replaced by air. Up to 50% of the WC-Co starting material is known to decompose and transform during spraying process [2010Rob]. The WC may decompose to W_2C , or even to

metallic tungsten, and the decomposition products may dissolve into metallic cobalt to form an amorphous or nanostructured Co-W-C phase, or complex carbides such as $\text{Co}_3\text{W}_3\text{C}$, $\text{Co}_2\text{W}_4\text{C}$, $\text{Co}_6\text{W}_6\text{C}$ and $\text{Co}_3\text{W}_9\text{C}_4$.

A decarburization mechanism that most likely occurs in thermal spraying process is [1989Dor, 1990Ner]:



Stage 3 only occurs only in the very high thermal energy spraying processes, including HVOF [1995Vuo]. Eta phases such as $\text{Co}_3\text{W}_3\text{C}$, $\text{Co}_2\text{W}_4\text{C}$, $\text{Co}_6\text{W}_6\text{C}$ in the powders have been found to increase the amount of W_2C in coatings [1996Kha, 1996Li], while W_2C in powder favours stage 2, and leads to the occurrence of free W in coatings.

The amorphous of the binder phase after spraying is thought to be caused by the dissolution of W and C and W_2C in the binder [1996Li, 1998Vil]. The complex carbide binder evidently is more brittle than cobalt based binder, the lack of a pure metallic phase, such as cobalt in WC-Co coating, provides the coating with superior corrosion resistance against molten metal alloy baths [2012Cha2]. Tomi *et al.* [1993Tom] found that $\eta\text{-W}_3\text{CO}_3\text{C}$ binder phase based exhibited excellent corrosion resistance against molten zinc in comparison with cobalt binder based WC-Co. However, when the WC-Co powder contains complex carbides, $\text{Co}_3\text{W}_3\text{C}$ and $\text{Co}_6\text{W}_6\text{C}$, the M_6C and M_{12}C phases will be found in the coating, which make the phase constituents more complicated [1988Bar].

Another problem associated with the structure of WC-Co coatings is concerned with the cobalt related phases in the coating. The cobalt phase cannot easily be recognised by X-ray diffraction analysis [1996Li]. Instead, a broad shallow peak in the X-ray diffraction pattern is observed, due to variation in cobalt matrix composition [1989Ram].

The W_2C accounts for a considerable amount of material in the Diamalloy 2003 WC-12%Co powder and is also found in the resulting deposits [1991Ner2]. This phase has a melting temperature of about 2860°C , whereas WC-Co has a melting temperature of about 2780°C [1991Bhu]. The melting of such high temperature phases as W_2C is uncertain with HVOF and is reliant on the amount of powder entering the HVOF gun for combustion. The existence

of W_2C (which might have remained unmelted during spraying) is detrimental to the coating and the component properties.

2.5 COATING MICROHARDNESS

It has been shown [1997Mil] that within the temperature range of 196 to 900°C, the hardness of WC 10 vol. % Co alloys decreased with increasing WC grain size according to:

$$H = H_0 + K_y d^{0.5} \dots [1951Hal] \quad \text{Equation 2.4}$$

according to Hall-Petch type relationship [1951Hal], where H is the hardness, H_0 is the intrinsic stress resisting dislocation motion, d is the mean WC grain size and K_y is the hardening coefficient.

The hardness of thermal spray WC-Co coatings deposited by any deposition technique increases with increased retained WC [1995Vuo, 1996Kha, 2005Mac], and for lower porosity in the coating. As already noted, the amount of retained WC depends on the level of decarburization. Complete decarburization of WC to W reduced the amount of retained WC and lowers the hardness, while partial decarburization to W_2C increased hardness [1991Ner1, 1995Vuo]. It is reasonable that the hardness values increased with increasing W_2C content in the coatings, because W_2C (HV = 29.4 GPa) is harder than WC (HV = 23.5 GPa) [1985Vin]. Jacobs *et al.* [1999Jac] also reported that the hardness values increased largely with increased W_2C in the coatings, and was much higher when the matrix phase of the coatings was Co_6W_6C instead of metallic cobalt.

Yang *et al.* [2003Yan] determined the hardness values of a cross-sections of WC-12%Co coatings under loads of 1.96 N, 9.8 N and 49 N. At 1.96 N, the indentation was small and usually within a single splat containing no porosity. The hardness increased with decreasing carbide size, because of the higher degree of decomposition of WC in the finer coating, and the Hall-Petch relationship [1951Hal]. In contrast, when the load was 9.8 N or 49 N, hardness decreased with decreasing carbide sizes in the coatings. This is because the indentations included pores and several splats during measurement. However, porosity and splat cohesion may strongly influence the hardness values at higher loads. A higher porosity and weaker splat cohesion in the finer coatings may result in lower hardnesses under higher loads.

There are numerous factors that may affect the measured hardness of coatings, including the preferred orientation, grain size, porosity, residual stress and densification of coatings [1997Mil, 2010Rob], as well as the starting powder chemistry and coating process parameters.

2.6 SURFACE PREPARATION AND MEASUREMENT

Surfaces for thermal spraying have to be chemically and mechanically well-prepared for good adhesion [1988Wig, 1996Gri, 2009Cha]. Among the different possibilities for surface preparation, grit blasting is an efficient way to produce cost-effective and reproducible results [1995Var, 1996Sie].

Grit-blasting is a process in which angular shaped metallic or ceramic grits are carried by pressurised air stream and hurled against the surface of the material [2009Cha]. The sharp grits erode the surface and a rough surface suitable for thermal spraying is created. Common grits are alumina, silicon carbide and chilled iron grits. It is necessary to make the substrate rough before thermal spraying to generate sufficient surface roughness, which ensures mechanical anchorage between the coating and substrate [2000Sta]. Abrasive grit blasting, shown schematically in Figure 2.4, is used to clean and prepare metallic substrates. The grit is sucked into the nozzle, accelerated in a compressed air stream and sprayed onto the substrate surface. Where the surface is smooth, grit blasting increases surface roughness, but where the surface is coarse, grit blasting will make it smoother.

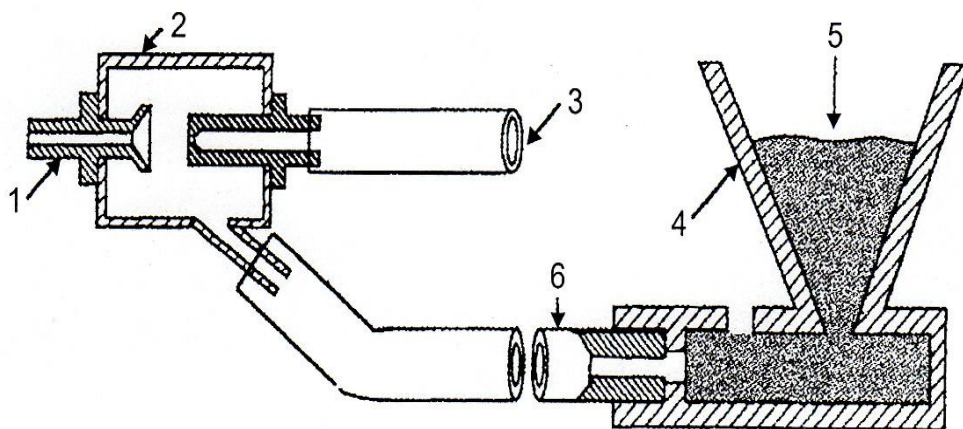


Figure 2.4. Representation of abrasive grit blasting where: (1) nozzle; (2) suction chamber; (3) compressed-air inlet; (4) grit feeder; (5) abrasive grit; (6) hose [1995Paw].

Surface roughness will be enhanced after grit-blasting the substrate material and this strongly influences the adhesion of the coating to the substrate. An increase in the roughness results in an increase in the adhesion. The influence of the blasting parameters, such as blasting duration, pressure and angle, on the coating bond strength or surface roughness has been tested [1974App, 1987Wig, 1995Paw].

The grits also undergo surface damage during blasting [1988Wig, 2009Cha]. The grits are brittle, and during collision with the substrate, the sharp edges of the grits are broken up. In addition, collisions occur between the impacting and ricocheting grits. With each collision, grits wear from the surface by microbrittle fracture [2009Cha].

Surface topography plays an important part in understanding the nature of coatings. No matter how finely finished, most rubbing surfaces in machinery are rough microscopically. As a result, the microtopography of a single surface and the nature of a contact between two surfaces are important to understand the nature of friction between the coating and substrate. The best parameter to optimise the grit-blasting is the roughness. The techniques for measuring the surface roughness value of grit blasted material and coatings can be divided into two broad categories: contact types and non-contact types. On the microscopic scale of surface measurements, a contact type stylus profiler (SP) using electronic amplification is the most popular. In SP, the stylus is loaded on the surface to be measured, and then moved across the surface at a constant velocity to obtain surface height variation [1982Tho, 1994Whi]. More recently, a non-contact optical profiler (NOP) [1984Wya, 1985Bhu, 1986Wya, 1988Bhu, 1988Lan] based on the principle of two-beam optical interferometry was developed, and is now widely used in industry.

On the ultramicroscopic scale of surface measurement, scanning tunnelling in microscopy (STM) and atomic force microscopy (AFM) give fine details of surfaces on a molecular scale. AFM can also be used for other measurements associated with forces, such as magnetism, electrostatic attraction, chemical attraction, adhesions, friction, wear and lubrication [1984Wya, 1995Bhu].

AFM was used to measure the surface roughness of coated substrates [1995Poo]. Roughness can be characterized by many parameters, such as R_a (equivalent to average roughness (AA)) or central-line average (CLA) or R_{max} . R_a describes the overall quality of polishing, while

R_{\max} is useful in describing a polished surface with no valleys or holes. It is commonly observed that the roughness parameters of engineering surfaces change with scan size, which is due to increased wavelength features that are included as the scan size is increased [1978Say]. Thus, in practice, the scan size should be related to the bandwidth covered by the normal contact width of the physical surface involved.

2.7 RESIDUAL STRESS

A stress state which exists in the bulk of a material without application of an external load (including gravity) or other source of stress, such as thermal gradient, is called a residual or internal stress [1987Noy]. All residual stress systems are self-equilibrating; the resultant force and the moment which they produce must be zero. Generally, three main kinds of residual stress can be distinguished, according to the distance or range over which they can be observed. The first kind of residual stress, Type I, is macroscopic, long-range, and extends over at least several grains of the material [2013Kra]. The second kind, Type II, often called residual microstress, covers one grain or part of grain, while the third kind, Type III, is very short range, over several atomic distances with the grain, and is equilibrated over a small part of the grain. It results from plastic deformation.

Stress is an extrinsic property, and must be calculated from a direct measurable property such as strain, or force and area [1987Noy]. The available methods of residual stress measurement may be classified into two groups: those that calculate stress from strain, assuming linear elasticity, and those that monitor other nonlinear properties. The residual stress state that develops in a deposit depends largely on the thermal conditions to which system has been subjected, and is a combination of quenching stresses that arise during deposition and cooling stresses post-deposition (Figure 2.5).

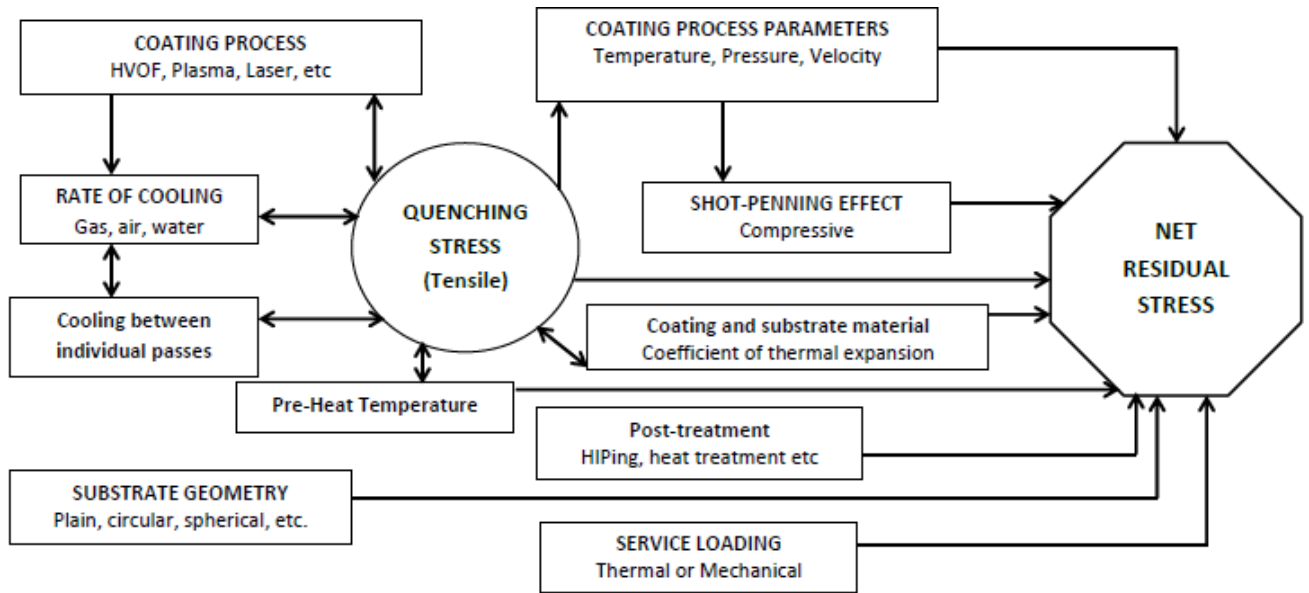


Figure 2.5. Origins of residual stress during coating processes [2011Azi].

2.7.1 Residual Stress Development in Formed Components

In the HVOF thermal spraying system, individual molten or semi-molten particles impinge on a substrate or pre-existing molten material at a speed of up to 850 m/s [1990Kow]. Despite their low mass, the effect of particles striking a surface at this speed causes certain deformations to the pre-existing material (substrate and particles already on the surface) [1982Zuk]. The impingement of each particle causes a stress field which depends upon the solid state of this pre-existing material.

In addition to the mechanical effect of impact, temperature effects are also relevant in stress development [2002God, 2007Ahm, 2009Mar]. These include the effects of both local and global temperature changes. Each particle is heated in the combustion chamber of the HVOF gun, and projected towards the substrate or die as a liquid. On impacting the substrate, it forms lamellae that cool down to their melting range and solidify, as shown in Figures 2.6 and 2.7. The combustion temperature approaches 3000°C [1989Met], but using forced cooling, the spraying temperature at the substrate for WC-Co is ~500°C [1999Sto]. Therefore, the temperature decrease experienced by the particle is very large. This leads to the formation of quenching stresses in the individual lamella, formed from the particles. These stresses are only alleviated by the introduction of micro-cracks in the material, or debonding from the substrate.

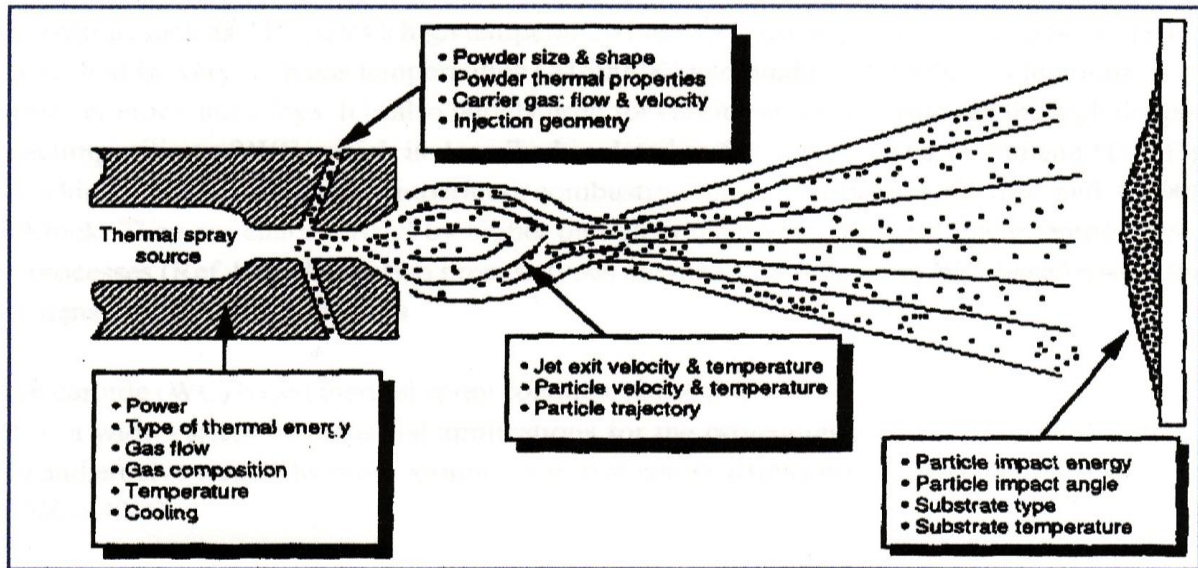


Figure 2.6. Schematic representation of the thermal spray process, listing the primary variables that influence the quality of thermal spray coatings [2004Dav].

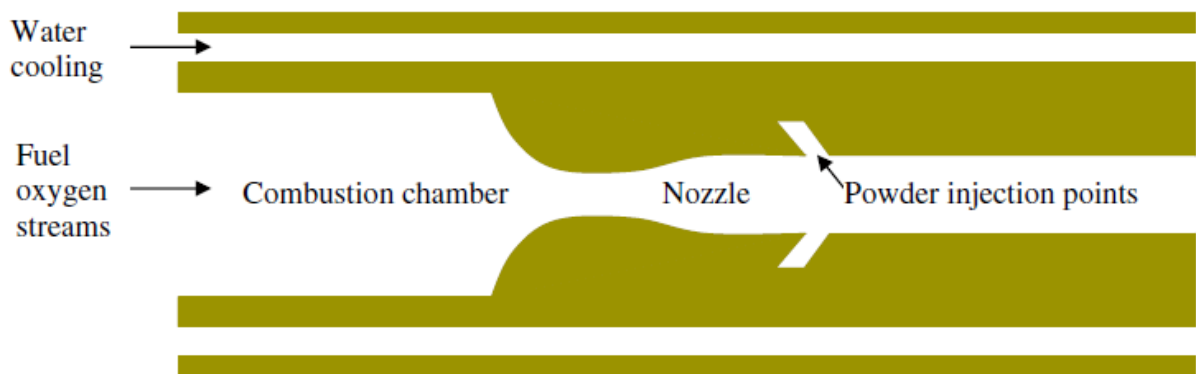


Figure 2.7. Schematic representation of the HVOF thermal spray process [2009Kam].

The single pass of a Diamond Jet HVOF gun produces a thickness of about 30 μm of deposited material, and five or six lamellae may exist at such depths [1995Paw]. As the lamellae solidify, they contract, but are constrained by each other and the substrate, thus generating high tensile stresses in the individual lamellae as shown in Figure 2.8. This tensile quenching stress in the lamellar is unavoidable, and may be estimated by the expression for thermal stress. Some authors have also emphasised the effect of the release of kinetic energy and associated it with peening stresses [1996Cly]. Quenching stresses were suggested to be dominant in processes where the particles are completely molten in the spray gun, as in APS [1998Kur2]. The particles spread upon impact, but the contraction during cooling and solidification is constrained by the underlying material and tensile stresses are generated inside each sprayed particle.

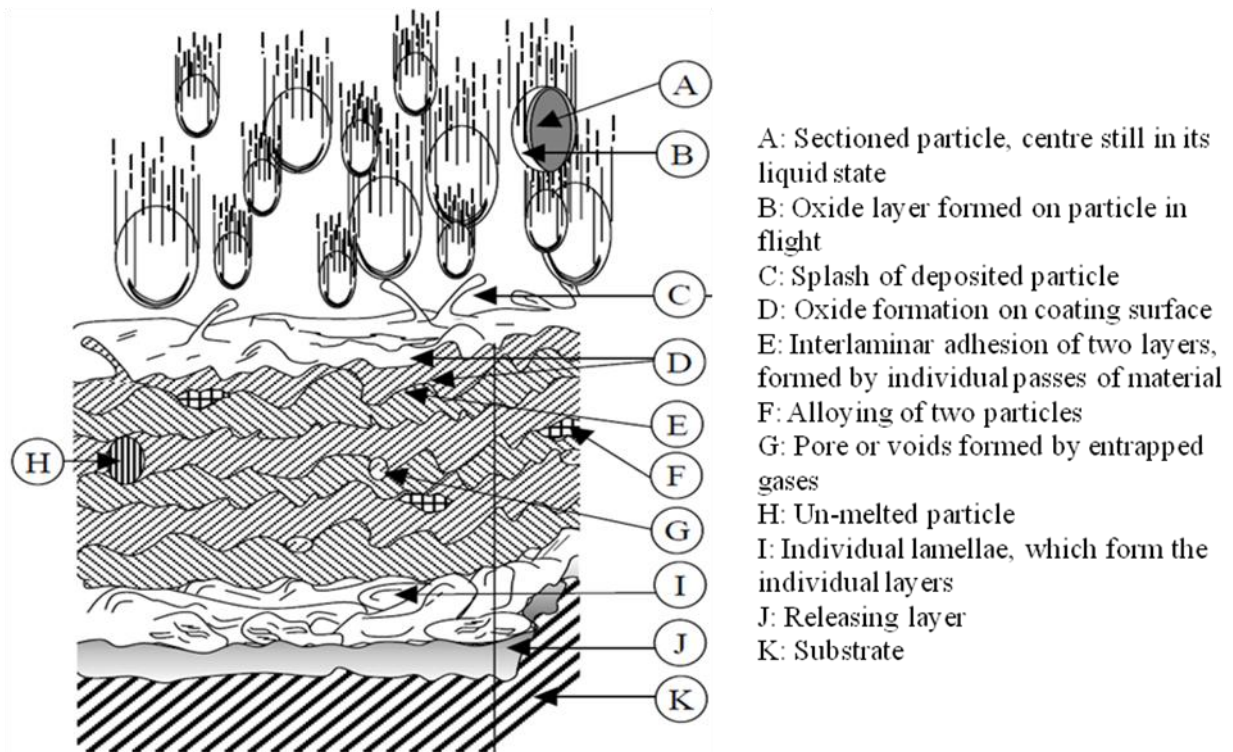


Figure 2.8. Schematic representation of the formation of a thermal spray coating, showing the coating is built up as droplets of semi-molten powder are flattened onto the substrate by the force of impact, with typical features: splat-like structure, pores, partially melted or unmelted powder particles and oxidised particles [1999Sto, 2004Dav].

Conversely, peening stresses may be generated in the surface layers where partially fused particles impact at high velocity onto the substrate. [1998Kur1, 1998Kur2]. The surface of the target is plastically deformed, inducing a significant level of compressive stresses which are cumulative with the previous quenching stresses. The magnitude of such quenching stresses implies that several relaxation mechanisms are activated [1981McP, 1987Gru, 1989Fau]. These can include plastic yielding, creep, microcracking and interfacial sliding [1995Kur]. Neither the degree of relaxation nor the local stress value are accessible to experimental measurement, but the effects of the quenching stresses were observed by monitoring the curvature induced in relatively thin substrate-deposit pairs [1990Kur, 1990Gil, 1991Kur1, 1991Kur2, 1994Gil]. The results showed that the residual stresses were 10-100 MPa and were insensitive to the substrate material and the spraying conditions, as long as the coating thickness exceeded 10 μ m [1990Kur], although they were affected by the substrate temperature, especially when metallic materials were sprayed [1995Kur, 1998Mat].

A second kind of stress arises during cooling, particularly after spraying. Some experiments have shown decreases in the curvature of specimens or even an inversion of form [1990Kur, 1990Gil]. Since they occur during cooling to room temperature, these stresses were named cooling stresses [1991Kur2]. They are attributed to the mismatch of thermal expansion between coating and substrate materials [1998Kur2], and can be either tensile or compressive [1990Tak, 1991Kur1]. Thermal mismatch strains between coating and substrate generated later during the cooling to room temperature can be accommodated in the coating flaws, porosities or microcracks, and only a limited zone will be affected in the interface with the substrate. Cooling stress affects coatings with a very dense structure, inducing a through thickness residual stress gradient. For such coatings, the residual stress state at the top surface can change from tensile to compressive as the temperature increases, due to different proportions of the quenching and thermal mismatch components [1998Mat].

In HVOF sprayed coatings, surface preparation played a crucial role in stress formation of the coating. Generally, a grit-blasted surface is under compressive stress [2009Cha]. Mellali *et al.* [1997Mel] used the curvature method to measure the compressive residual stress on a grit-blasted surface. He found that stress increased with blasting pressure and grit size. The effect of blasting process parameters on substrate surface residual stress was studied using a statistically designed experiment [2009Cha]. For this purpose, the Barkhausen noise analysis (BNA) of the blasted surface was measured. He reported that on grit-blasting, the surface undergoes work hardening. The compressive residual stress on the surface and subsurface hardness increases with blasting pressure and blasting angle.

The final overall stress at the coating surface can be obtained by adding the quenching stress result to the cooling stress. Verbeek [1998Ver] recognised three stages in the formation of residual stresses in plasma sprayed coatings. The first stage concerned solidification of the particles. The second stage involved heating of the substrate during the cooling process, caused by the heat transport from the coating to the substrate. This resulted in expansion of the substrate, causing tensile stress in the already deposited parts of the coating. Next to this, the newly deposited layers solidified on the substrate. The third stage concerned the stresses caused by cooling down of the substrate and the coating together, after the coating process had been completed. Whether the cooling stress in the coating was tensile or compressive depended upon the relative values of the expansion coefficients of substrate and coating. If, as the temperature decreased, the coating contracted more than the substrate ($\alpha_c > \alpha_s$), a tensile

stress was generated in the coating, where α_c = coefficient of thermal expansion of the coating, and α_s = coefficient of thermal expansion of the substrate. This sometimes led to adhesion loss and cracking of the coating or formed material [1995Ito]. If the coefficients of thermal expansion were equal, no cooling stress developed. However, if the coating contracted by a smaller amount than the substrate ($\alpha_c < \alpha_s$), the resulting cooling stress was compressive [1995Ito].

The cooling stress is superposed upon the tensile quenching stress of the coating. The nature of the overall residual stress is determined by the following criteria [2000Sto]:

- $\alpha_c < \alpha_s$ stresses in the coating may be either tensile or compressive,
- $\alpha_c > \alpha_s$ stresses in the coating are tensile, and
- $\alpha_c = \alpha_s$ stresses in the coating are tensile.

The possibility of either tensile or compressive stress when $\alpha_c < \alpha_s$, arises because tensile stress remains in the deposited material if the compressive cooling stress is less than the tensile quenching stress. However, if the cooling stress is greater, then the resultant is compressive. The implication is that high tensile quenching stresses can be negated by the compressive cooling stresses, through appropriate selection of the deposited material and substrate.

2.7.2 Residual Stresses of WC-Co coatings

WC-Co is a composite with WC as the major phase and Co as a binder which is more ductile. The stress determined by various techniques focussed on the WC phase in the coating. The measured values of the WC stress is the sum of all contributions, e.g., coating macrostress, bulk microstress, and surface treatment/condition, and surface relaxation effects very close to the surface. Thus, the macrostress in the coating cannot be presumed to be due only to the WC stress [Kra2013]. Theoretical models and experimental observations showed that thermal residual stress was compressive in the WC particles and tensile in the Co [1965Gur, 1989Kra, 1990Maj, 1990Seo, 1995Lav, 1996Mar]. Many researchers have determined the residual stress of as-sprayed WC-Co thermal spray coatings employing different techniques. Researchers working with a WC-12Co coating deposited on a stainless substrate reported tensile stresses of 259 MPa and 37 MPa (i.e. principal stress values) which were determined by X-ray diffraction measurements [1997Ahm]. Pina *et al.* [2003Pin] also evaluated the

residual stresses of a HVOF WC-12Co coating by the same technique, employing the $\sin^2\psi$ method and reported tensile stresses of 165 MPa. Wang *et al.* [2004Wan] also with X-ray diffraction, reported a similar value of 112 MPa. Stokes and Looney [2004Sto] determined the residual stresses in WC-Co coatings by an analytical method similar to that of Clyne *et al.* [1996Cly], and reported tensile surface stresses of 82 MPa and 15 MPa for coatings of thicknesses of 200 and 600 μm , respectively. However, the measurements conducted on the surface of coatings by X-ray diffraction, and hole drilling indicated tensile residual stresses of 63 MPa and 60 MPa, respectively. The residual stress changed from tensile on the surface to compressive at the coating-substrate interface [2005Voo]. Pejryd *et al.* [1995Pej] determined the residual stress profile of different WC-Co coatings deposited by HVOF employing a modified layer removal method, and also found that the residual stress changed from compressive at the surface, to tensile at the substrate.

In general, the magnitude and orientation of residual stress depend not only on the technique and deposition parameters, but also on the method employed for deposition, which can also have different phases, resulting in residual stresses as volume changes due to thermal expansion.

2.7.3 Measurement of Residual Stress

Residual stress in thermally sprayed coatings may be measured by many techniques, which may be categorised into two methods:

- (1) Destructive method e.g. hole drilling techniques and layer removal (surface grinding, electropolish, etching, etc.),
- (2) Non-destructive method which includes:
 - ▶ XRD residual stress techniques,
 - ▶ Synchrotron X-ray stress techniques,
 - ▶ Neutron diffraction method.

In the present research, non destructive methods were used to determine the residual stress in the coatings i.e. XRD, synchrotron and neutron diffraction.

2.7.4 X-Ray Residual Stress Measurement

The application of XRD stress measurement to practical engineering problems began in the early 1950s. The advent of X-ray diffractometers and the development of the plane-stress residual stress model allowed its successful application to hardened steel [1952Ogi, 1959Koi]. By the late 1970s, XRD residual stress measurement was routinely applied in aerospace and nuclear applications involving fatigue and stress corrosion cracking of nickel and titanium alloys, as well as aluminium and steels. Today, it is applicable to materials that are crystalline, relatively fine grained, and produce diffraction for any orientation of the sample surface. Samples may be metallic or ceramic, provided a diffraction peak of suitable intensity and free of inference from neighbouring peaks can be produced in the high back-reflection region with the radiations available. X-ray diffraction residual stress measurement is unique in that macroscopic residual stresses can be determined non-destructively, but the limitation is that X-ray penetration is extremely shallow ($<3\ \mu\text{m}$ into WC) [1987Noy]. It is used to analyse a surface layer whose thickness depends both on the sample material and the incident beam wavelength. Usually, this thickness is not high enough to cover the entire thickness of the thermally sprayed coating. Nevertheless, this hindrance can be an advantage for studying possible stress gradients in the cross section by using suitable surface removal methods or different wavelengths. The technique has been extensively applied to the study of thermally sprayed coatings [1987Ric, 1999Pin]. It gives reliable results of the final residual stress state of the material [1991Kur1, 1994Gre].

Obtaining stress-free interplanar spacings can be problematic. In cemented carbide with WC as the carbide, the WC is a reliable reference phase because it remains stoichiometric and does not dissolve the solute in solution. However, the metal binder does take W and C into solution during sintering, so that the starting binder cannot be used as a stress-free reference [2013Kra]. For applied stress (*in situ*) measurements, changes in binder stress can be readily measured relative to the starting-unstressed value regardless of any uptake of W or C. In-situ measurements are simpler with respect to stress-free reference values, because the strains are derived relative to the initial values of the interplanar spacings, regardless of the residual stress state [2013Kra].

High temperature measurement may be particularly problematic as compositional changes can occur, in which case the initial values of d -spacings are no longer meaningful. Creep or other time-dependent changes with temperature (e.g. phase changes, precipitation,

composition) are problematic with respect to the direct measurement of the change in the binder phase [2009Mar].

The problem with using X-rays to study thermal residual stresses in cemented carbides is the high absorption by W. It leads to shallow beam penetration and the inability to properly measure the bulk, i.e. volumetric stress state. It takes 4.8 mm of W to absorb half the intensity of a thermal neutron beam and 2.1 μm for Cu X-rays. This illustrates the difficulty of using X-rays to study heavy elements, which is a problem with synchrotron radiation. Clyne *et al.* [1996Cly] highlighted some difficulties in using X-ray measurements to determine the coating stress, including:

- (1) Limitation of the range of ϕ , since large values would require the incidence X-ray beam to penetrate appreciable thicknesses of coating and/or substrate.
- (2) The penetration depth of X-ray diffraction is proportional to the surface roughness of as-sprayed coating only, as well as
- (3) Error from variation in stress levels.

An attempt to explore these factors by successive layer-removal techniques [1991Kin] was inconclusive, since such removal itself changes the stress distribution, even if it can be effected without inducing any deformation or damage in the underlying material.

However, the greater penetration of neutrons offers several advantages:

- (1) Surface effects, such as deformation due to grinding or polishing, or oxidation are avoided;
- (2) X-rays are largely confined to the relaxation region near the surface for microstresses, whereas this is not an issue for neutrons;
- (3) Complete rotation of the sample is achieved, giving more thorough sampling.

It is apparent from the above that diffraction and the sampling capacity of neutrons offer an improved measurement of the micro- and macro- behaviour of cemented carbides. However, the quantification and roles of micro-scale plasticity behaviour in these carbides also benefited from the application of microstructural finite element modelling (FEM). This technique allows independent assessment of both elastic and plastic strain components developing during thermal and mechanical loading. Such modelling would enable both

prediction of macroscopic response and interpretation/validation of diffraction results [1996Wei, 2013Kra].

Probably the most informative method of residual stress evaluation, for thermally sprayed coatings, involves measuring the curvature of the substrate/deposit couple. Curvature can be measured by a variety of contacting and non contacting techniques [1996Cly]. In general, curvatures down to about 0.1 m^{-1} (10m radius) are easy to measure, whereas much lower values require more care and specialized equipment. However, while curvatures can be easily measured, the interpretation in terms of stress state is a more complex task. This is partly because the curvature adopted by a system with a given stress state is unique and predictable, but a given curvature does not correspond to a unique stress state. However, it is possible to infer a stress distribution from a curvature, provided certain boundary conditions are assumed [1996Cly].

2.7.5 Principles of X-ray diffraction residual stress measurement

Residual stress magnitudes are determined through measurement of changes in the material lattice spacing, d -spacing, due to the presence of a stress. Based on the knowledge of the non-stressed lattice spacing, any stresses present in the sample or material can be calculated using the established $\sin^2\psi$ equation from Noyan [1987Noy]. In this method, a collimated X-ray beam of wavelength similarly to the interplanar spacing is focussed onto a specimen and the number of X-rays diffracted is counted as the angle between the X-ray detector and X-ray tube is varied [URLRes]. This allows a plot of diffracted intensity versus 2θ to be achieved. From these peaks, the lattice spacing, which varies from stressed to non-stressed material can be determined using the Bragg equation. Figure 2.9 indicates the impinging and diffracted X-ray beam on a magnified level. The angle ψ is the angle between the surface normal and the bisector of the incident and diffracted X-ray beam. It is also the normal between the diffracted lattice planes and the sample's surface. Figure 2.9a) shows the sample orientated so that the diffracting lattice planes are parallel to the surface. The compressive stress observed would not affect this lattice spacing, as they are acting parallel to the diffracting lattice planes. The sample has been rotated through a known angle ψ in Figure 2.9b). The presence of compressive stress causes the lattice spacing to be smaller than in the non-stressed state, which can be measured through determination of the shift in the diffracted intensity peaks. Once the shift is measured for at least two orientations of ψ (the rotation of axis), then the lattice spacing, and hence residual stresses, can be resolved.

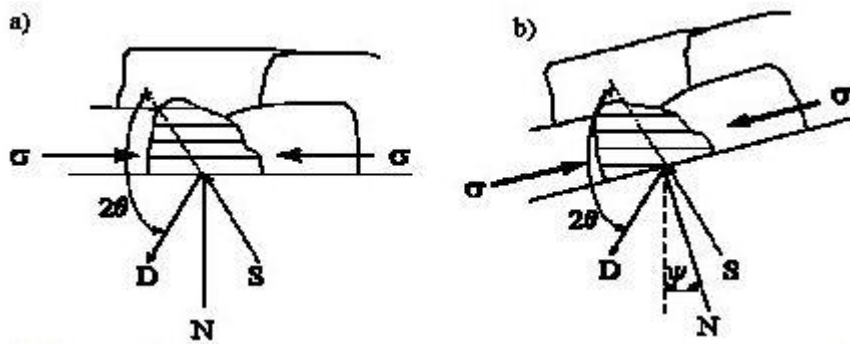


Figure 2.9. Sample and laboratory coordinate systems [URLRes]: a) $\psi = 0$ and b) $\psi = \psi_i$ (sample is rotated through some known angle ψ_i), where D = X-ray detector, S = X-ray source, and N = Surface normal.

Using the Bragg equation:

$$n\lambda = 2d\sin\theta \quad \text{Equation 2.5}$$

where λ = wavelength (nm), n = constant, θ = Diffraction angle (2 Theta in $^\circ$).

The strain is obtained as the change in d -spacings between crystallographic planes and is given by:

$$\frac{d_{\varphi\psi} - d_o}{d_o} = \frac{1+\nu}{E} \sigma_\varphi \sin^2 \psi - \frac{\nu}{E} (\sigma_{11} + \sigma_{22}) \quad \text{Equation 2.6}$$

This predicts a linear variation of strain or interplanar spacing variation with $\sin^2 \psi$ so that stress σ_φ can be obtained from the slope of a plot of strain vs $\sin^2 \psi$. The geometry for the biaxial stress is shown in Figure 2.9.

where σ_φ is the stress component along the $S_\varphi S_\varphi$ direction in the plane, and is given by:

$$\sigma_\varphi = \sigma_{11} \cos^2 \varphi + \sigma_{12} \sin^2 \varphi + \sigma_{22} \sin^2 \varphi \quad \text{Equation 2.7}$$

$d_{\varphi\psi}$ = spacing in the direction defined by φ and ψ (m);

ν = Poisson ratio and E = Young's modulus (Pa),

σ_φ = Surface stress defined by the angle φ (Pa)

A graph of $d_{\varphi\psi}$ vs $\sin^2 \psi$ is plotted with the stress value determined from the slope [1987Noy]. This approach is called the $\sin^2 \psi$ technique.

The slope m , is given by:

$$m = (1+\nu)/E \cdot \sigma_{\phi} \cdot d_0 \quad \text{Equation 2.8}$$

The parameters $-\nu/E$ and $(1+\nu)/E$ are generally known as S_1 and $1/2S_2$ respectively, and are referred to as the X-ray elastic constants. A linear behavior of $d_{\phi\psi}$ vs $\sin^2\psi$ is predicted by Equation 2.6 [1987Noy].

2.7.6 Sources of Error

Since XRD residual stress determination requires precision in the measurement of the angular position of diffraction peaks of the order of 1 part in 10^5 , many sources of error must be controlled. The sources of error of primary importance may be placed on the following categories: sample dependent errors, instrumental and position errors, effect of sample geometry and X-ray elastic constant.

Sample dependent errors: The preparation of the sample surface depends on the nature of the residual stresses to be determined. If the stresses of interest are produced by surface treatments such as machining, grinding, or shot peening, the residual stress distribution is usually limited to less than 500 μm below the sample surface [1996Pre]. Therefore, the sample surface must be carefully protected from secondary abrasion, corrosion, or etching. Samples should be oiled to prevent corrosion and packed to protect the surface during handling. If the stresses of interest are those produced by carburizing or heat treatment, it may be advisable to electropolish the surface of the sample, which may have undergone finish grinding or sand blasting after heat treatment. Thus, state of sample surface plays a crucial role in determined stress on the material.

Instrumental and position error: The principal sources of error in X-ray diffraction residual stress measurement are related to the high precision with which the diffraction-peak position must be located [1996Pre]. Instrumental alignment requires coincidence of the θ and ψ axes of rotation and positioning of the sample such that the diffracting volume is centered on these coincident axes. If a focusing diffractometer is used, the receiving slit must move along a true radial line centred on the axes of rotation. All these features of alignment can be checked

readily using a stress-free powder sample. If the diffraction apparatus is properly aligned for residual stress measurement, a loosely compacted powder sample producing diffraction at approximately the Bragg angle to be used for residual stress measurement should indicate not more than ± 14 MPa apparent stress. Alignment and positioning errors result in systematic additive error in residual stress measurement.

Effect of sample geometry: Excessive sample surface roughness or pitting, curvature of the surface within the irradiated area, or interference of the sample geometry with the diffracted X-ray beam can result in systematic errors similar to sample displacement [1996Pre]. Coarse grain size, often encountered in as-cast materials, can lessen the number of crystals contributing to the peaks which become asymmetrical, resulting in random errors in the diffraction-peak location and hence residual stress measurement. Residual stress generally cannot be measured reliably using X-ray diffraction in samples with coarse grain sizes.

X-ray elastic constant: A major source of potential systematic proportion error arises in determination of X-ray elastic constants $(E/1+\nu)_{(hkl)}$ [1996Pre]. The residual stress measured is proportional to the value of the X-ray elastic constants, which may differ by as much as 40% from the bulk value, due to elastic anisotropy. The X-ray elastic constant must be determined empirically by loading a sample of the material to known stress levels and measuring the change in the lattice spacing as a function of applied stress and ψ tilt.

2.7.7 Neutron Diffraction

The use of neutrons for the study of residual stresses in composite materials is complementary to the use of X-rays [1985All, 1986Coh, 1987Noy, 1990Kra]. The advantages are derived from the greater penetration depth of neutrons in most engineering materials as compared to X-ray of around 0.2mm down to bulk measurements of up to 250 mm in aluminium or 37mm in steel [1975Bac]. This makes surface penetration less critical, enabling the study of systems containing heavy elements and/or large diameter fibres or particles, and allows the $\psi = 90^\circ$ orientation to be easily reached using transmission geometry and the ψ -goniometer configuration. Neutrons also provide bulk volume averages that enable sampling of entire cross sections of tension/compression test specimens for example. Thus, neutrons are well-suited to the study of the inherently volumetric microstress states found in composites. Furthermore, subsurface macro- or micro-stress gradients may be separated, but the approach followed only gave microstress. In neutron stress analysis, in order to obtain

strain values which are representative of the bulk, the domains of the different constituents have to be small compared to the penetration depth, if the material is composed of fibres or grains which are several microns thick or even larger, X-ray results will be strongly affected by surface effects, whereas neutron results are not. For the investigation of grain interaction stresses, the large penetration depths of neutrons may be helpful, because they allow the determination d vs $\sin^2\psi$ distributions up to $\sin^2\psi=1$, i.e. in-plane strain components can be measured directly.

2.7.8 Biaxial state condition for neutron diffraction

In order to determine the stress state at a certain position in the substrate or deposit, strain values for both normal and in-plane directions has to be determined, and always from the same sample volume element [1986Coh, 1987Noy, 2004Kel, 2005Hut]. For the investigated thermal sprayed deposits, the spraying angle perpendicular to the substrate surface suggested isotropy within the surface plane of the deposits. With most specimen/symmetry conditions and thickness of coatings, an in-plane biaxial stress state is assumed. Also, the normal component of stress (through thickness direction) in any thin coating has to be zero (boundary condition). The basic equations governing the biaxial stress condition in neutron measurement can be expressed as [1987Noy, 2004Kel]:

$$\sigma_{\parallel} = \frac{1}{1/2S_2(hkl)} \left\{ \varepsilon_{\parallel} - \frac{S_1(hkl)}{1/2S_2(hkl) + 3S_1(hkl)} (2\varepsilon_{\parallel} + \varepsilon_{\perp}) \right\} \quad \text{Equation 2.9}$$

$$\sigma_{\perp} = \frac{1}{1/2S_2(hkl)} \left\{ \varepsilon_{\perp} - \frac{S_1(hkl)}{1/2S_2(hkl) + 3S_1(hkl)} (2\varepsilon_{\parallel} + \varepsilon_{\perp}) \right\} = 0 \quad \text{Equation 2.10}$$

$$\varepsilon_{\parallel} = \frac{d_{\parallel} - d_o}{d_o} \quad \varepsilon_{\perp} = \frac{d_{\perp} - d_o}{d_o} \quad \text{Equation 2.11}$$

$$d_o = \left(1 + 2 \frac{S_1(hkl)}{1/2S_2(hkl)} \right) d_{\perp} - 2 \frac{S_1(hkl)}{1/2S_2(hkl)} d_{\parallel} \quad \text{Equation 2.12}$$

$$\sigma_{\parallel} = \frac{1}{1/2S_2(hkl)} \left(\frac{d_{\parallel} - d_{\perp}}{d_{\perp}} \right) \sigma_{\perp} = 0 \quad \text{Equation 2.13}$$

where σ_{\parallel} = in-plane stress component and σ_{\perp} = normal stress component,

d_{\perp} and d_{\parallel} = lattice plane in the normal and parallel direction to the coated, respectively,
 ε_{\perp} and ε_{\parallel} = strain component respectively in the normal and parallel directions,
 hkl = Miller indices of the Bragg reflection used,
 S_1 and S_2 = X-ray elastic constants, and
 d_0 = unstressed lattice spacing of crystallographic planes described by Miller indexes hkl .

2.7.9 Synchrotron Radiation XRD

The control of the residual stress is a primary issue in the coating industry. Both the deposition process and the service conditions may produce a residual stress, which may be particularly critical in applications where a large mismatch exists between structural, thermal and mechanical properties of layer and substrate.

XRD is known to be a valuable technique to measure residual strain in a non-destructive way [1987Noy]. However, the shallow penetration of X-rays and the need for suitable diffraction geometry for careful control of several possible error sources limits the applications of this technique. Errors may be especially relevant when studying low stress levels. In addition, as traditional XRD methods involve the measurement of high angle reflections, it may be necessary to use different wavelengths to study different materials or polyphasic components. Therefore, the use of synchrotron X-rays may help to overcome some of these limitations. Even though it was designed for high resolution power diffraction, the parallel beam geometry is perfectly suited to the X-ray Residual Stress Analysis (XRSA), being almost unaffected by the typical errors arising from sample positioning and roughness.

Synchrotron radiation is produced by the acceleration of electrons or positrons. Electron are accelerated to near the speed of light (energies of up to 7 GeV at the advance photon source (APS).). They are then injected into storage ring where they are steered by 1097 magnet in a vacuum. The positrons are guided by magnets that bend them and can also wiggle.

The principal advantages offered by synchrotron XRD are essentially [1987Noy]:

► Exceptional high fluence

The high X-ray flux permits detection of even very weak reflections that frequently occur when studying thin films,

- An appropriate wavelength may be selected in a wide range, by simply changing the angle of the Si double crystal monochromatic radiation, but a white beam of X-ray energies were used for this investigation
- The goniometer geometry gives a narrow instrumental profile, even at high 2θ angles, which is the angular region where data for XRSA are collected.

There are two basic approaches to stress determination: modelling and measurement. The model, analytical or numerical [1990Els, 1990Tak], can provide a valuable insight to the coating build-up and trace certain phenomena that may not be observable *a posteriori*. However, their general applicability is limited, due to the complex nature of the process and imprecise knowledge of the constituent's properties. The use of modelling has two primary purpose: To evaluate whether a proposed measurement is feasible; To design such a measurement. It is especially the coating property variation with processing parameters that underlines the importance of experimental methods [1996Per, 1998Maj]. The experimental methods of residual stress determination that are commonly applied to thermally sprayed coatings were shown in Table 2.2 [2004Osm].

Table 2. 2. Comparison of the residual stress measurement techniques [2004Osm].

Technique	PROs	CONs
X Ray Diffraction	Versatile, widely available Wide range of materials Portable systems Macro and micro RS*	Basic measurements Lab-based systems, small components
Hole Drilling	Quick, simple, Widely available Portable. Wide range of materials Deep hole drilling for thick section components	Interpretation of data Destructive Limited strain sensitivity and resolution
Synchrotron	Improved penetration & resolution of X-rays Depth profiling Fast Macro and micro RS	Specialist facility only Lab-based
Neutron Diffraction	Excellent penetration & resolution 3D maps Macro and micro RS	Specialist facility only Lab-based
Magnetic	Very fast Wide variety of magnetic techniques Portable	Only ferromagnetic materials Need to separate the microstructure signal from that due to stress
Ultrasonic	Generally available Very fast Low cost Portable	Limited resolution Bulk measurements over whole volume
Raman/Fluorescence	High resolution Portable systems available	Surface measurements Interpretation Calibration Limited range of materials

*RS: Residual stress

2.8 WEAR RESISTANCE

An extensive economic benefit could be achieved by reducing the loss of material from the action of wear [1986Han, 1989Von], because abrasive wear reactions account for more than 50% - 60% of the total of all wear forms. Thermal spray coatings have shown favourable properties to protect substrate surfaces.

Wear resistance of powder materials and coatings depends to a large extent on structural peculiarities (heterogeneity of the composite structure, porosity of materials, state of stress of surface etc.) and qualitative properties (hardness, toughness). Abrasive wear of materials depends on testing conditions: properties of abrasive (hardness, particle size and shape), wear parameters (impact velocity, impact angles) and other testing conditions (temperature, testing media etc.) [2005Kul]. Many different researchers [1974Blo2, 1989Kul, 1994Res, 1996Kal, 1997Res] have demonstrated that conventionally-manufactured hardmetals and similar coatings of different types and compositions behave differently under the conditions of abrasive wear. In wear-resistance applications, the coated layer provides the wear resistance, while the substrates support any impact to which the component (coating and substrate) is subjected.

HVOF processes were developed primarily for protective coatings against severe abrasive wear. They are commonly used to spray wear resistant WC coatings of high quality and density. The abrasion resistance is also better for coatings having high inter-splat bond strengths [1987Noy, 1990Ner, 1995Vuo]. The inter-splat bond strength for HVOF spray processes is high because the high powder particle velocities produce high impact energy when the semi-molten powder particles strike the substrate surface [1990Var]. Kim *et al.* [1994Kim] reported that wear mechanisms in abrasion are influenced by the inter-splat bond strength. Low bond strength coatings wear by a process of splat delamination, due to the formation of subsurface micro-cracks. On the other hand, high bond strength coatings wear by selective removal of the binder followed by the removal of carbide grains [1994Kim], much the same way as observed in bulk cemented carbide.

2.8.1 Types of Wear

There are four main types of wear, besides a few marginal processes that are often classified under these forms of wear. Each wear process obeys its own laws, and to confuse matters, on

many occasions wear of different types is combined. It is then difficult to disentangle a complex situation and to find the primary cause of the wear. The major types of the wear are:

- (1) Abrasive wear,
- (2) Adhesive wear,
- (3) Fretting, and
- (4) Erosion.

This research evaluated some abrasive wear mechanisms.

2.8.2 Three-Body Abrasion

WC-Co coatings work particularly well in abrasive conditions [1974Blo2, 2000Vil]. It works for both in two-body abrasive wear, where wear is caused by hard protuberances of the counterface, and three-body abrasive wear is that caused by the hard particles that are free to roll and slide between two surfaces, acting as interfacial elements. The most commonly used three-body abrasion test ASTM G65 and its variations has as the third body a standard rubber wheel rotating against the surface being abraded. This test is usually referred to as the Dry Sand Wheel (DSRW) test and is shown schematically in Figure 2.10.

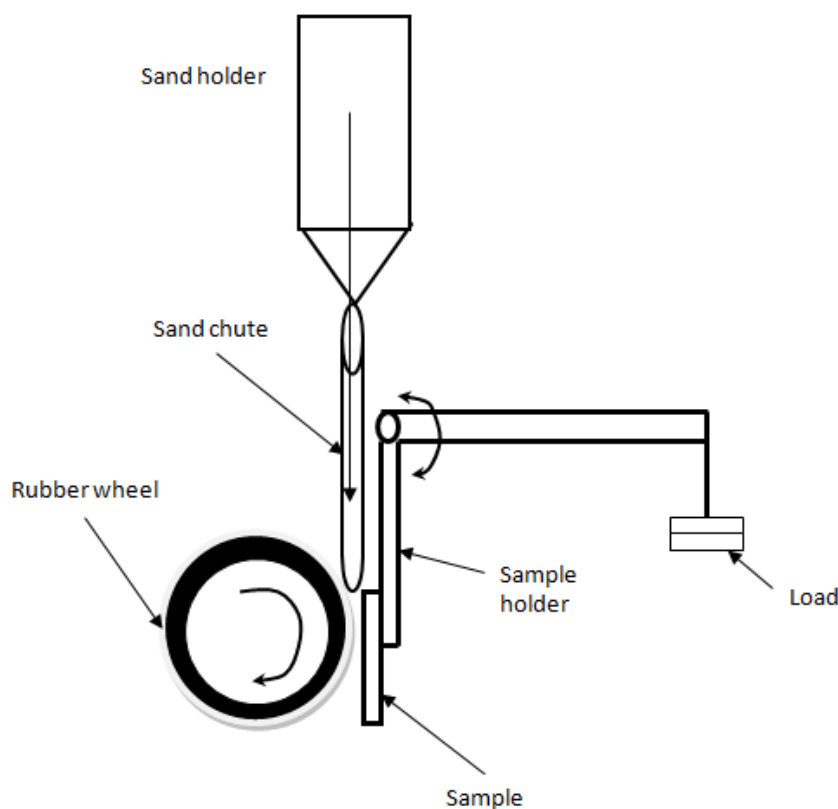


Figure 2.10. Schematic diagram of ASTM-G65 wear test machine [2010Mab].

2.8.3 Abrasion Wear Mechanism of Sintered WC-Co Alloys

Abrasive wear occurs when a rough hard surface, or soft surface containing hard particles, slides on a softer surface and ploughs a series of grooves [1992Hut]. The material from the grooves is displaced in the form of wear particles, which are generally loosened and lost.

Abrasive wear of WC-Co hardmetals has been extensively examined in the last decades with a particular focus on the determination of the abrasion wear resistance [2007Kra]. With the conventional WC-Co material, the wear resistance of WC-Co coating increased with decreasing of carbide particle size [1995Gur, 1995Ste, 1996Li, 2004Li]. This trend has been observed using standard test methods utilizing high loads and coarse abrasives a few hundred micrometers in size [1955Gur, 1996Li, 1998Kre, 2001Ska].

Microstructure and wear performance of WC cermet coatings can be influenced by many factors, including spray processing methods, spray parameters and structure of feedstock [1989Ram, 1996Li, 1996Ka1, 1998Kre]. Nevertheless, as demonstrated by several recent researchers [1998Vil, 2007Kra], ultrafine grades may demonstrate higher wear rates in comparison with the conventional micron grades. Thus, the rate of material removal by ploughing observed for the ultrafine grades may be higher than for the preferable binder removal following by WC grains pull-out, studied for the micron-scale grade [2007Kra].

A WC-Co component is said to be wearing in the “hard abrasive regime” when the abrasive particles are harder than the WC phase in the abrading component, while a “soft abrasive regime” occurs in the converse case [1992Hut, 2007Kra]. In the “hard abrasive regime”, the harder abrasives cause mass loss of both the WC and Co phases. Grooves form on the abrading surface and material loss is by plastic deformation [1986Lar]. The scale of each removal event is dependent on the size of the abrading particles, which are generally one or more orders of magnitude greater than the WC grain size. In the “soft abrasive regime”, the abrading particles cause mass loss via a process in which first the binder is lost, followed by the loss of WC grains. The loss of the binder phase, which leaves surface depressions and faceted pits [1974Blo1], is an extrusion process caused by repeated loading of adjacent carbide grains by frictional shear stresses [1978Lar, 1986Lar]. The preferential loss of the binder phase changes the properties of the surface compared to the bulk, and depending on the application, pre-disposes the component to secondary processes, e.g. cracking in case of rotary WC-Co drill bits used for mining [1974Blo1].

The influence of hardness on the abrasive wear is not decisive alone, and the relationship between hardness and erosion resistance of hardmetals differs substantially from the linear relationship found for metals. At the same level of hardness, the wear resistance of WC-Co hardmetals may differ by up to 50% [2007Kim]. At the same time, an increase in hardness does not always result in an increased of wear resistance due to its spraying distance.

The tribological behaviour of different sprayed coatings compared with the bulk sintered WC-Co is complicated by the inhomogeneous microstructure and the phase transformations of the starting material, which lead to a wide variation in mechanical properties [2010Rob]. Up to 50% of the WC-Co starting material is known to decompose and transform during the spraying process. The effect of these phase transformations has been shown by Stewart *et al.* [1998Ste] to be generally deleterious to the abrasive wear performance of HVOF WC-Co coatings. The transformations also contribute to the scatter in tribological properties, and therefore testing of these coatings at relevant service conditions is advisable in order to determine the range of wear rates, friction, and damage mechanism present for particular coatings under consideration for specific applications.

Wayne *et al.* [1990Way] suggested that cobalt extrusion, followed by carbide removal, or carbide fracture, is the dominating wear mechanism. According to Larsen-Basse and co-workers [1979Lar, 1985Lar], this mechanism acts mainly in the mild wear regime for sintered carbides, since the hard phases (WC, W_2C) yield only a small displacement from the normal and tangential stress applied by the abrasive particles. Thus, deformation mainly occurs in the soft and ductile matrix, so that it is forced to protrude outside the surface of the material by the compressive stress of the abrasive particles, due to poor deformability of the hard phases. After the removal of the soft matrix, macrocracking or detachment of the hard phase occurs when the support and compressive loading of the matrix are no longer present. A similar explanation was made by Yan *et al.* [2003Yan], after the examination of the sliding wear behaviour of HVOF-sprayed WC-12%Co coatings. Based on their results, they proposed that when two surfaces are brought into sliding contact at the beginning, the soft ductile cobalt matrix between WC particles undergoes severe deformation. The deformed cobalt is extruded by the compressive stress of the protruding asperities of alumina. Microcracking and/or pull-out of WC particles then occurs when there is no longer support of the matrix, leading to the original formation of the wear debris.

The tribological performance (abrasion, sliding wear and erosion) of thermal spray coatings depends on numerous properties such as coating composition, nature of phases and their distribution, microstructure, porosity and residual stress [2010Rob]. All these properties, in turn, affect the hardness of the coating, which is conventionally used as the primary correlating parameter for evaluating wear resistance. Another factor that strongly influences the tribological performance of HVOF WC-Co coatings is adhesion of the coating to the substrate [2000Ste]. This is largely influenced by the pre-spraying surface preparation, which normally requires grit blasting to roughen the surface to allow mechanical interlocking of the initial splats, with grossly textured shot blasted surfaces with re-entrant features to enhance coating bonding. The strength of the coating-substrate interface can be compromised by embedment of any grit remnant prior to deposition. The grit particles act as stress raisers and encourage interfacial crack propagation and delamination of the coatings when stresses induced by tribological contacts are large enough to act at the interface. Thus, care in the substrate preparation is paramount to good coating performance.

Wang *et al.* [2004Wan2] reported that, in order to achieve a nanostructure WC-Co coating with superior wear resistance, it is important that spray parameters should be optimized to obtain appropriate flame temperatures, velocities and chemistries during the HVOF spraying process. They investigated the effect of flame conditions on abrasive wear performance of HVOF sprayed nanostructured WC-12Co coatings, and found that the decarburization of WC particles in spraying and bonding among WC particles in the nanostructured coating significantly affected the wear performance. Examination of the worn surfaces of the nanostructured coatings revealed that the dominant wear mechanism was spalling from the interface of WC-Co splats when the spray particles experienced limited melting under the oxygen/fuel flow ratio 1:20. While the melting state of the spray particles improved under the oxygen/fuel flow ratio of 16, the dominant wear mechanism was plastic deformation and ploughing of the matrix and spalling of WC particles from the matrix.

2.8.4 Hardness of Abrasive material

The abrasion rate depends on material hardness, or more precisely, on the material hardness/abrasive hardness ratio (H_m/H_a) [1992Hut, 2005Kul]. If the material hardness is lower than abrasive hardness, microcutting of the surface may take place. If material hardness is higher than abrasive hardness ($H_m > H_a$), clear removal of the material usually does not take place, and the entire process has the nature of fatigue. The hardness of coatings must be

maximum, and higher than that of the abrasive, depending on the erosion conditions to guarantee high abrasion-erosion wear resistance at small impact angles [2005Kul].

2.9 HEAT TREATMENT OF WC-Co

The HVOF deposited coatings contain low porosity and low oxide content [1992Ner]. To improve the density and homogeneity of sprayed coatings, post-spray treatments, such as laser remelting, shot peening, HIP or furnace treatment have been used. Mathew *et al.* [2009Mat] reported that the as-sprayed coatings were in a metastable state, therefore when they were exposed to elevated temperature, microstructural and compositional transformations could occur. The most probable changes are the precipitation of fine carbides or possibly oxide, accompanied by recrystallisation of the matrix and pore and void reduction. Post-treatment of thermal spray coatings has been shown to refine the microstructure, e.g. by eliminating porosity and microcracks, and to promote beneficial phase transformations and metallurgical bonding within the coating microstructure [1994Kho, 1997Gho]. It has been reported by several researchers [1975Tay, 1994Kho, 1998Ste] that heat treatment could beneficially modify any WC-Co deposit. Nerz *et al.* [1991Ner2] showed that there was an exothermic reaction in the WC-Co coatings at the approximately 860°C, which did not occur in the powder. This might be related to recrystallisation of the amorphous matrix into eta phase carbides [1991Ner2]. Richert *et al.* [2011Ric] studied the effect of annealing on the microstructure of HVOF deposited coatings, and found that homogenization of the microstructure occurred. After annealing WC-Co coatings at 500°C, voids and pores almost completely disappeared.

Heat treatment probably causes changes in the coatings' properties, in particular microhardness [1975Tay]. Richet *et al.* [2011Ric] showed that annealing increased the microhardness of the HVOF WC-Co coating. After annealing at 500°C and 24 h, the average microhardness was 1488 HV_{0.2}, which compared to the initial state (1240HV_{0.2}), was an increase of about 20%. This probably resulted from the reduced porosity, as well as formation of eta phase after heat treatment. However, Stewart *et al.* [1998Ste] reported decreased hardness after heat treatment above 700°C, which was probably due to the gross cracking of the sample dominating any residual stress effects. Recrystallisation of the amorphous binder above 700°C also alters the hardness of the sample.

Heat treatment significantly improved the wear performance of WC-Co coatings [1990Len, 1990Ito, 1998Ste]. Nerz *et al.* [1991Ner2] showed increased abrasive wear resistance after heat treatment of HVOF sprayed WC-Co coatings at 900°C, but concluded that this was due to the increased carbide content, as the amorphous binder recrystallised to form eta phase. Heat treatment of the coatings significantly improved the erosion resistance under high velocity impact conditions which had improved the inter-splat cohesion [2009Mat]. It also caused microcracking in the WC-Co coating, due to different coefficients of thermal expansion. Therefore, microcracking and reduction in residual stresses in the coating were seen as beneficial in promoting abrasive wear resistance of the coating. However, large scale cracking of the coating, caused by high-temperature heat treatment at 1100°C, lead to preferential wear within the coating, while low-temperature treatment of 250°C gave significantly increased coating abrasive wear resistance [1998Ste].

The XRD patterns of the coatings after heat treatment showed a decrease in the amount of the WC, which could be due to the dissolution of tungsten carbide in cobalt and formation of eta phase [1998Ste]. Heat treatment at 800°C and 950°C caused no significant phase transformations. on the other hand, high temperature heat treatment (1100°C) completely transformed the amorphous phases to crystalline eta phases [2006Kha].

The studies relating to the relative changes in the residual stress profile due to post treatment have been limited. This is due to the fact that although experimental techniques such as change in curvature, deep hole drilling have all long been applied to measure the residual stress profiles in thermal spray coatings, the methodology of these measurements makes them destructive for the WC cermet coatings [2007Ahm]. However, due to the difficulties in depositing the coating, little work was found on non-destructive techniques. The influence of vacuum heat treatment on the residual stress of thermal spray cermet coatings via neutron and X-ray diffraction was studied by Ahmed *et al.* [2007Ahm]. The neutron diffraction results indicated that the stress in coating materials was compressive, with an average of -553 MPa for the as-sprayed and -492 MP for the heat-treated coating, which was mainly due to the higher value of the coefficient of thermal expansion of the substrate material.

The residual stress value in the substrate was therefore tensile in the as-sprayed coatings, whereas it varied from compressive to tensile within the substrate of the heat-treated coating. The X-ray diffraction measurements results indicated compressive stress values, with an

average of -785 ± 40 MPa for the as-sprayed coatings and -815 ± 60 MPa for heat-treated coatings. Lenling *et al.* [1990Len] reported that post heat treatment of WC based coatings increased the compressive residual stress of the coatings, whereas Stewart *et al.* [1998Ste] showed that heat treatment at all examined temperatures reduced the residual stress of the coating. Notwithstanding compressive stresses generally being beneficial, substantially large compressive residual stress in the thermal spray coatings can be detrimental since they can lead to delamination due to spalling. On the whole, residual stress is one of the major problems in thermal spray layers, especially in thick coatings. The effect of heat treatment on the state of the stresses in WC-Co HVOF coatings was studied by Khameneh *et al.* [2004Kha] by using XRD, the compressive residual stress of a WC-17Co coating decreased after heat treatment. Stewart *et al.* [1998Ste] showed that heat treatment caused changes in the residual stress state of the coating and its integrity, because of the thermal expansion mismatch between the coating and substrate. Heat treatment caused reduction in the residual tensile stress of the coating by cracking in the coating, which could be useful in wear resistance of the coating.

CHAPTER THREE

3.0 EXPERIMENTAL PROCEDURE

3.1 Introduction

This chapter describes the materials, methodology and equipment employed in this research. The methodology is divided into three parts:

- Characterization of the powders used for the coating,
- Deposition of coatings, and
- Characterization and testing of the coatings.

3.2 Materials

The samples used for this work were produced in two batches, A and B (Table 3.1), with the substrate properties listed in Table 3.2. The differences between A and B are the latter being fine grained with minimal texture differences to allow better comparison with diffraction experiments. Batch A samples were commercial samples of thickness 9 mm, whilst the set B samples of thickness 6 mm was procured from Goodfellow, UK, with mild steel samples (SABS 1431 grade 300WA) in addition. The choice of the substrate was to give a wide range of coefficients of thermal expansion, and the different thicknesses were selected because one was used industrially (Batch A), whereas the other was smaller. This would allow the effect of thickness to be ascertained.

For the aluminium alloy, a 2xxx series was used, which is alloyed with copper, and is used in aerospace. It is normally used because of its high strength and good to excellent machinability, although the corrosion resistance is poor. It is relatively strong and it is the only aluminium alloy group that significantly naturally ages. This reduces ductility over time, as well as abrasion resistance [1996Sta]. Whilst the annealing temperature for the aluminium alloy would have been suitable for most low-alloyed aluminium alloys, it was actually below that normally used for this alloy, and would have allowed some precipitation which subsequently affected the wear resistance. It is usually annealed at 450°C for 2 hours.

Super-invar alloy has been the metal of choice for low expansion applications for years, because it has a near-zero coefficient of thermal expansion, over a limited temperature range.

It is easily formed, deep drawn, fabricated, tough and adhesive, but not hard or abrasive [2003Kir].

Brass is any alloy of copper and zinc, the proportion of zinc and copper can be varied, to create a range of brasses with varying properties. The malleability and acoustic properties of brass made it the metal of choice for brass musical instruments. The relatively low melting point of brass (depending on composition), and its flow characteristics, make it a relatively easy material to cast [1986Die].

Mild steel is a very common structural material that is often coated to improve its corrosion resistance. It is the most versatile, least expensive and widely used engineering material, which has found extensive application in various industries. It is used in large tonnage in marine application, nuclear power and aerospace [1971Uhl].

Stainless steels have high strength grades with good combinations of strength, fatigue resistance, and ease of forming and joining [1999Bed]. They have excellent corrosion resistance in oxidising acid media. Other good properties include easy maintenance, high ductility and high work hardening rate [2002Net].

The aluminium and brass alloys were chosen in order to find the effect of stress relaxation on the substrates, since their melting points are low. Conversely, the substrates with high melting points, 304L stainless steel, Super-invar and mild steel, were selected to derive the effect of stress relaxation on the coating. The sample size and measurement positions used for the strain analysis during X-ray analysis are shown in Figure 3.1.

Table 3.1. Substrate thickness.

Batch	Substrate	Thickness (mm)
A	Aluminum 2xxx alloy 304L stainless steel Brass (Cu63/Zn37) Super-invar (Fe64/Ni36)	9
B	Aluminum 2xxx alloy 304L stainless steel Brass (Cu63/Zn37) Super-invar (Fe64/Ni36) Mild steel (SABS 1431 grade 300WA)	6

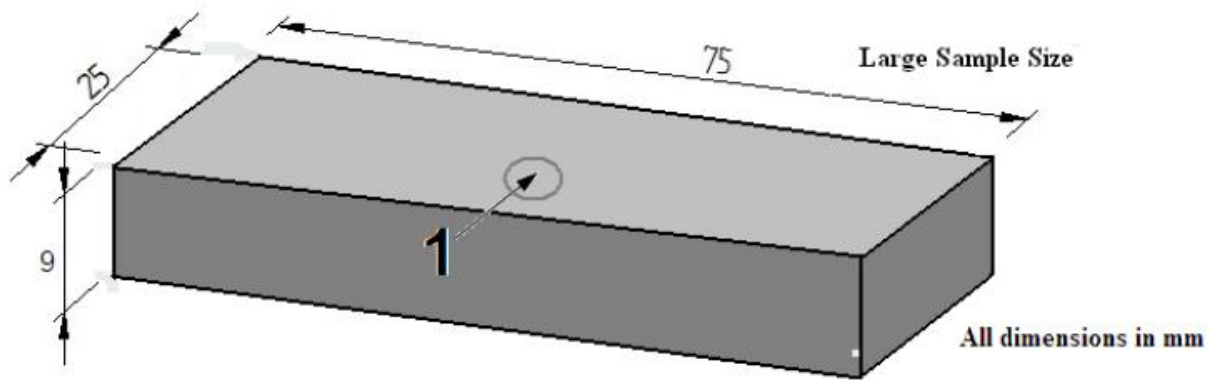


Figure 3.1. Sample geometry and measurement positions for the strain analyses.

Table 3.2. Physical properties of the substrates [URLCoe, URLMel].

Substrate	Melting point (°C)	Specific heat capacity (J/g °C)	Coefficients of thermal expansion [10 ⁻⁶ /K]
Aluminium alloy	660	0.900	23
Brass	930	0.380	19
304L stainless steel	1365	0.460	17.3
Super-invar	1454	0.123	1.2
Mild steel	1500	0.620	11

3.3 Powder

The powder used for depositing coatings was supplied by H.C. Starck, Germany. It was produced by spray drying and sintering. Table 3.3 gives the nominal composition in weight and equivalent volume fractions. The powder particle size was given by the manufacturer as ranging between 15 and 45 microns. This is similar to the powder reported by Macho [2005Mac].

Table 3.3. Powder composition.

Powder	Nominal composition (wt %)	Equivalent volume fraction (vol.%)
WC-17Co	83WC-17Co	73WC-27Co

3.4 Powder characterization

The powder was characterised in the as-received state to determine its morphology and elemental composition. Chemical characterization of the powder was done using XRD, and scanning electron microscopy (SEM) with energy dispersive X-ray spectroscopy (EDX).

A Bruker AXS D-8 Advanced Diffractometer with cobalt radiation, and set at 20 mA and 40 kV, was used to determine the phase compositions of the powder. The surface was analysed in the as-deposited condition, without any metallographic preparation.

3.5 Coating procedure

Coatings were done on large plates that were cut into smaller sections for the respective investigations. The surface of the substrate was machined, grit blasted using 24 μm alumina grit before deposition. Coating deposition was carried out under industrial conditions using a High Velocity Oxyl Flame (HVOF) JP5000 thermal spraying system. Coatings of about 200 μm thickness were deposited on all the substrates (batches A and B). Deposition parameters were the same on all the coated samples, using spray parameters optimised for WC-Co powder and are shown in Table 3.4. Thus similar to the parameters reported by Luyckx [2007luy].

Coatings were deposited for three sets of test:

- (1) Residual stresses (XRD, Synchrotron and Neutron) investigation,
- (2) Abrasion wear test,
- (3) Heat-treatment test. The dimensions sizes of the substrate used for different test are given in Table 3.5.

Table 3.4. Parameters used for thermal spraying.

Parameter	Setting used for all the coatings
Gun barrel	102 mm
Spraying distance	380 mm
Kerosene flow rate	0.0227 m ³ /h
Oxygen flow rate	56.6 m ³ /h

Table 3.5. Sample dimensions used for the analysis.

Test	Substrate dimension for batch A (mm)	Thickness (mm)	Substrate dimension for batch B (mm)	Thickness (mm)
Dry abrasion	75 x 25	9	75 x 25	6
X-ray diffraction	75 x 25	9	25 x 25	6
Synchrotron	Not measured	-	25 x 25	6
Neutron	Not measured	-	25 x 25	6
Coating characterization	12 x 10	9	12 x 10	6

3.6 Coating characterization

For microstructural analysis, coatings of about 200 μ m thickness were deposited on substrates of 12 x 10mm in size (Table 3.5) cut from the larger samples of 100 x 100mm. The cross-sectional sections of the coatings were prepared by mounting samples, in a chuck device, where they could be polished using sequentially finer grades of SiC abrasive paper: 120, 320, 400, 600, 800, and 1200 (microns). They were then polished with a cloth sequentially using fines diamond paste: 6 μ m, 3 μ m and 1 μ m. The polished samples cross-sectional surface were characterized by optical microscopy using a Zeiss AxioTech reflected light microscope, scanning electron microscopy (SEM) on a FEI Quanta 200 equipped with a 3D backscatter electron imaging (BSE) attachment and an atomic force microscope (AFM) using a Veeco Dimension 3100. This enabled study of the to study microstructural features and coating characteristics.

X-ray diffraction (XRD) patterns were obtained using a Bruker AXS D8 Advance Diffractometer with Cu-K α radiation at 20 mA under a voltage of 40 kV. The specimens were scanned with a scanning speed of 2°/min in 2 θ range of 25-140° and the intensities were recorded. The diffractometer interfaced Bruker DIFFRAC PLUS and EVA software enabled qualitative chemical phase identification based on the *d*-spacings and intensities on the diffraction pattern with the aid of JCPDS data cards [2009Mah].

The average grain size and distribution were measured on the coating cross sections by a metallographic technique of linear and planar analysis [1953Ful, 1963Gur]. The porosity of the coatings was measured on the cross section by dot counting.

Coating hardness was obtained as macrohardness using a Vickers hardness tester at an applied load of 5 kg. Five measurements were made for each coating and the average hardness value determined. Hardness was calculated from the relation:

$$HV_{load} = 1854.4 \times F/d^2 \quad \text{Equation 3.1}$$

where F = load in g, and d = diameter of the indenter in μm .

The atomic force microscope with a tip radius less than 10 nm was employed to measure the surface roughness of the coatings within a surface area of $25.4 \mu\text{m}^2$. The coating characterization procedure was the same for both as-sprayed coatings and heat-treated coated samples.

3.7 Test procedures

The coatings were tested for residual stresses, abrasive wear and coating characterization. The procedures of these tests are given in the following sections. This was done on both as-sprayed and heat-treated samples.

3.7.1 Residual stresses analyses

Non-destructive techniques used to determine the residual stresses in this research were:

- (a) X-ray diffraction,
- (b) Neutron measurement, and
- (c) Synchrotron X-rays.

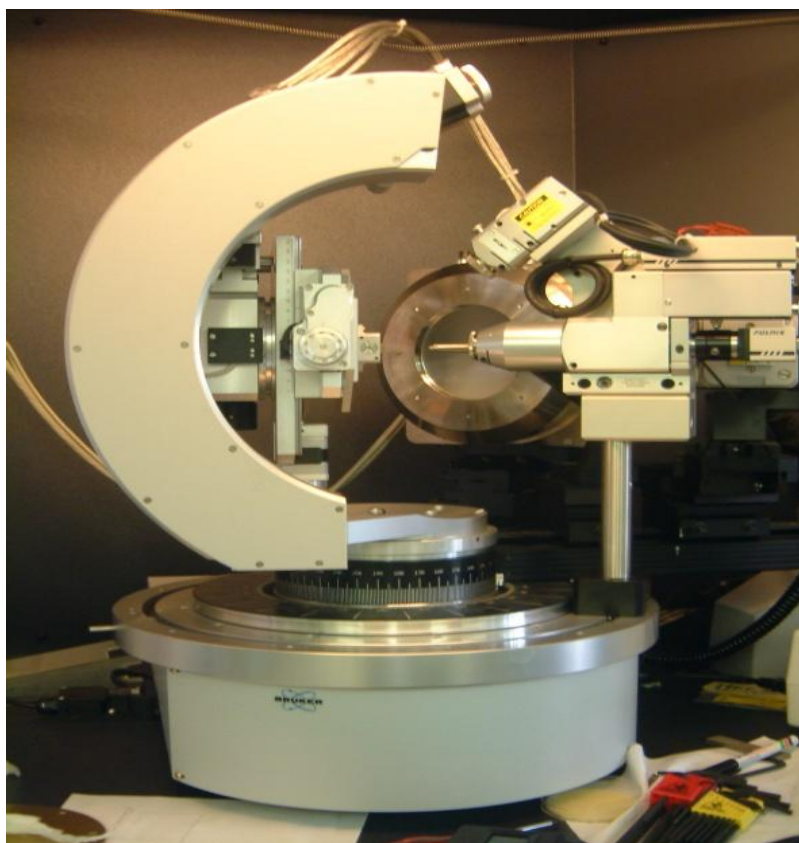
The residual stresses of as-sprayed coatings on Batch A samples (Table 3.1) were determined by X-ray diffraction only; these samples were not suitable for neutron and synchrotron X-ray measurements due to larger grain sizes and crystallographic texture. For the Batch B samples (Table 3.1), X-ray diffraction was used to determine residual stresses on the grit-blasted material, as-sprayed coatings, annealed coatings, annealed grit-blasted material and abrasive wear surfaces. A synchrotron and neutron facility in France [European Synchrotron Radiation Facility and Institut Laue-Langevin] was used to determine stresses on the parent materials, grit-blasted materials and as-sprayed coatings for the brass and

super-invar substrates. This was done to find the contribution of each process during the thermal spray procedure, as well as to investigate if there is correlation between synchrotron and neutron measurements. Other neutron measurements were done at Kowari (ANSTO, Australia) to determine residual stresses on grit-blasted material, as-sprayed coatings, annealed grit-blasted material and annealed coatings for brass, mild steel, super-invar and aluminium. This was done to investigate the contribution of each step of the coating process as well, and to ascertain if any correlation existed between X-ray analysis and neutron diffraction results, as well as the contribution of coating process. All efforts to determine residual stresses on as-sprayed and annealed coatings on 304L stainless steel using neutron and synchrotron X-rays proved abortive due to higher absorption of their substrate properties with neutron radiation, as well as the limited beam time allocated at Kowari (ANSTO, Australia).

3.7.2 X-ray diffraction measurement

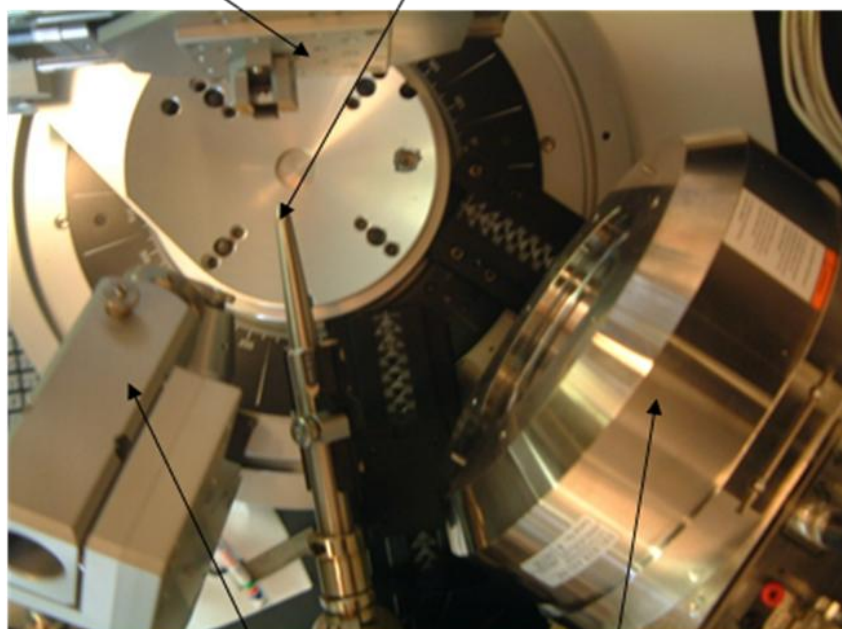
The diffraction based techniques (Figure 3.2) are non destructive and mostly do not require surface preparation. Brass, aluminium, 304L stainless steel, super-invar (Batch A), as well as Batch B samples which included mild steel were used as the substrates. The samples sizes are given in Table 3.5. The sizes of Batch B samples were changed in order to determine if correlation existed between X-ray and neutron diffraction measurements. The measurements were conducted by using Co-K α radiation with a wavelength of λ Co-K α = 1.78897Å and energy = 7 keV. The anode settings were 40 kV and 40 mA. A Laser video camera system on the instrument was used to align the sample position at the centre of the goniometer. The instrument included a graphite monochromator and 0.8mm diameter collimator on the instrument primary side. Diffraction collection was done using a two-dimensional High Star (Bruker AXS) detector. Measurements were taken with the samples oriented in six different azimuth angles; 0°, 180°, 90°, 270°, 45° and 225° to determine the full stress tensor using the side-inclination geometry define by tilt around the projection of the projection of incident beam.

Since WC-Co is a composite with WC as the major phase, stresses measured by X-ray diffraction focused only on the WC phase near the surface region of the coatings (as done by other authors [2001Mur]) since cobalt peak was weak. The residual stress measurements comprised following the shift of the WC Bragg peaks. A high angle peak was selected to be free of interference from other peaks. This was chosen to provide highest possible accuracy.



Sample stage

collimator



Laser video camera

detector

Figure 3.2. Side and top view of the D8 Discover for measuring residual stresses at Necsa.

The coated samples were fine grained, typically with micron grain size. The lattice strain was obtained from the shift of the hkl Bragg peak position when compared with that of an unstrained specimen. The residual stress measurement was performed in ψ geometry using $\sin^2\psi$ for both positive and negative ψ angles. With the $\sin^2\psi$ techniques, the strain-free lattice parameter was obtained from the $\psi = 0$ value. The lattice strain in the WC coating was obtained from the shift of the defined Bragg peak positions shown schematically in Figure 3.3 [1996Cly]. The strain in the WC coating were measured using the $\{112\}$ and $\{202\}$ reflections. The instruments settings and reflections used are summarised in Table 3.6.

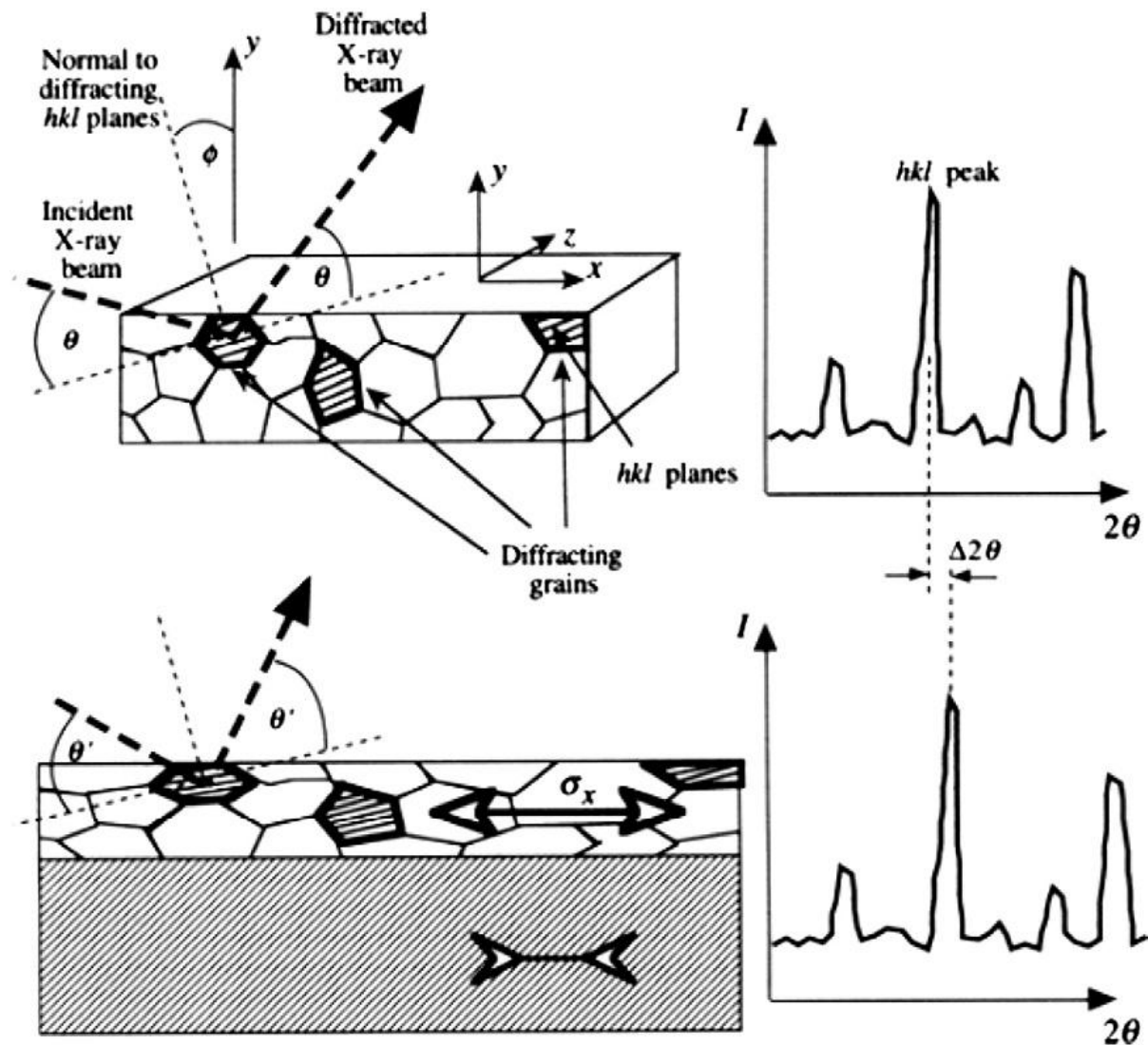


Figure 3.3. Schematic diagram of the XRD strain measurement $\sin^2\psi$ technique for measurement of the residual stress [1996Cly]. The top diagrams show the experimental conditions at $\psi = 0^\circ$ with the bottom diagrams showing the conditions at inclined ψ values.

Table 3.6. Elastic constants of the different materials.

Reflection	S_1 (MPa ⁻¹)	$1/2S_2$ (MPa ⁻¹)	Poisson's ratio, ν
$\{112\}_{\text{WC}}$	-2.564×10^{-7}	1.859×10^{-6}	0.16
$\{202\}_{\text{WC}}$	-3.247×10^{-7}	1.948×10^{-6}	0.20
$\{311\}_{\text{Al}}$	-4.784×10^{-6}	1.928×10^{-6}	0.33
$\{211\}_{\text{Fe-}\gamma}$	-1.429×10^{-6}	6.190×10^{-6}	0.30
$\{311\}_{\text{Ni}}$	-1.844×10^{-6}	8.936×10^{-6}	0.30
$\{311\}_{\text{Cu}}$	-3.197×10^{-6}	1.351×10^{-5}	0.31

The above diffraction elastic constants were calculated using the Neeffeld-Hill's module [1987Noy]. Data were analysed for residual stress determination using Bruker AXS software (Leptos, version 6). A video (Laser) camera system was used to align the sample measurement position to the centre of goniometer. The instrument set-up included a graphite monochromator and 0.8mm diameter collimator on the primary side. Data collection was done using two dimensional High Star (Bruker AXS) detector.

3.7.3 Fundamental equations for stress measurement with 2D XRD

The fundamental principle of 2D measurement is based on the relationship between stress tensor and diffraction cone distortion. The merit of the 2D system is that each point on diffraction Debye-Scherrer cones are used to analyse the result, leading to quick with data collection times. The fundamental equation for strain and stress measurement by diffraction, using 2D detectors is [2003Bob]:

$$f_{11}\epsilon_{11} + f_{12}\epsilon_{12} + f_{22}\epsilon_{22} + f_{13}\epsilon_{13} + f_{23}\epsilon_{23} + f_{33}\epsilon_{33} = \ln\left(\frac{\sin \theta_0}{\sin \theta}\right) \quad \text{Equation 3.2}$$

where f_{ij} = the strain coefficient, while $\ln\left(\frac{\sin \theta_0}{\sin \theta}\right)$ determines the diffraction cone distortion at the particular $(\gamma, 2\theta)$ position. The material for this investigation was considered to be isotropic. Therefore, two independent elastic constants, Young's modulus, E , and Poisson ratio, ν , or macroscopic elastic constants were taken into consideration, as related by:

$$1/2S_2 = (1 + \nu)/E \quad \text{Equation 3.3}$$

and

$$S_1 = -\nu/E. \quad \text{Equation 3.4}$$

The equation for stress measurement, using 2D detector is given by [2003Bob]:

$$P_{11}\sigma_{11} + P_{12}\sigma_{12} + P_{13}\sigma_{13} + P_{22}\sigma_{22} + P_{23}\sigma_{23} + P_{33}\sigma_{33} = \ln\left(\frac{\sin\theta_0}{\sin\theta}\right) \quad \text{Equation 3.5}$$

$$\text{where } P_{ij} = \begin{cases} (1/E)[(1+\nu)f_{ij} - \nu] = \frac{1}{2}S_2f_{ij} + S_1 & \text{if } i = j \\ (1/E)(1+\nu)f_{ij} = \frac{1}{2}S_2f_{ij} & \text{if } i \neq j \end{cases} \quad \text{Equation 3.6}$$

Yu *et al.* [2004Yu] stated that for biaxial stress state, i.e. only in-plane stress components,

Equation 3.5 becomes:

$$P_{11}\sigma_{11} + P_{12}\sigma_{12} + P_{22}\sigma_{22} + \frac{1-2\nu}{E}\sigma_{ph} = \ln\left(\frac{\lambda}{2d_0'\sin\theta}\right) \quad \text{Equation 3.7}$$

The biaxial stress state corresponds to the straight line of the $d - \sin^2\Psi$ plate.

3.7.4 The mean penetration depth

The mean penetration depth was calculated by [1987Noy]:

$$\tau = \frac{\sin\theta\cos\Psi}{2\mu} \quad \text{Equation 3.8}$$

where τ = mean penetration depth, μ = linear absorption coefficient, ψ is the tilt angle and θ = Bragg peak position in degrees, with the linear absorption coefficients determined according to Hubbell *et al.* [1974Hub].

3.7.5 Neutron diffraction stress measurement

Test specimens (Table 3.2) coated on the 25 x 25 mm face were used for these measurements. The extremely small coating thickness of 200 μm (for neutron diffraction stress experiments) meant that accurate measurements on a fine through thickness mesh were done to obtain the coating stress indirectly, through stress balance in the coating/substrate system. High accuracy and many datapoints were required to compensate for the unfavorable ratio of the

thicknesses of the coating (0.2 mm) to that of the substrate (e.g. 8.3 mm). In addition, an attempt was made to directly measure the stresses in coatings. These two approaches gave a good countercheck on each other for reproducibility.

A sub-millimetre gauge volume was chosen in order to balance different competing factors, such as through-thickness spatial resolution (to be able to measure sharp stress distribution from grit blasting, possibly over the stress from the substrate production process, and to avoid edge effects [1997Spo]), statistical uncertainty (to achieve strain accuracy better than 50 μ strain) and total measurement time, limited by the length of the experiment. The neutron diffraction residual stresses measurements were carried out using the residual stress diffractometer Kowari (ANSTO, Australia) shown in Figure 3.4. The measurements were done in multiple through-thickness locations to cover the entire sample thickness, forming a line profile with usually 0.3 mm spacing between points. In the locations close to the surface (where high stress gradients were expected due to peening from grit-blasting), some extra points were measured. In order to optimise localisation of the gauge volume, the take-off angle $2\theta_M$ of the Si (400) monochromator was varied to maintain a geometry close to 90°. The instrument settings for the reflection used are given in Table 3.7. For each location, d -spacings were measured in the two principle directions namely, in-plane and normal to the surface. The balanced biaxial plane stress assumption was used to recalculate stresses from the measured d -spacings and the diffraction elastic constants, used for the stress calculations, were computed using the self-consistent method of Kröner [1958Kro], and are given in Table 3.7.



Figure 3.4. KOWARI neutron strain scanner at ANSTO, Australia.

To separate stresses originating from the spray process from pre-existing stresses (e.g. residual stress from cold rolling of the substrates and/or the grit-blasting process) neutron stress measurements were done on the uncoated substrate samples. They were treated as separate samples and measured using the same procedure. The crucial part of the measurements was the high positioning accuracy, because of the necessity to combine multiple sets of data from different samples and directions. Position accuracy of 0.01 mm was maintained throughout of the experiment. For measurements in the substrate materials, this was sufficient to ensure that positioning errors were smaller than counting statistical errors, but for stress measurements in 0.2 mm WC coatings in conditions of partial illumination, the positioning error are larger, reaching $\sim 100 \mu$ strain. In this case, the error was included in the analysis as a significant part of the reported total errors. Figure 3.6a shows the sample geometry and set-ups on the instrument. This procedure was the same for the heat treated samples.

Table 3.7. Instrument settings used for different reflections in neutron diffraction.

Reflection	$2\theta_m$	$\Lambda(\text{\AA})$	$2\theta_B$	Gauge volume (actual)(mm)	Sample thickness (mm)	S_1 (TPa) ⁻¹	$1/2S_2$ (TPa) ⁻¹
$\{211\}_{\text{Fe-}\gamma}$	76.0°	1.67	91.3°	0.3x0.3x15	8.3	-1.26	5.72
$\{311\}_{\text{Cu}}$	69.0°	1.55	89.5°	0.3x0.3x15	6.4	-2.88	11.06
$\{311\}_{\text{Ni}}$	67.0°	1.52	89.0°	0.3x0.3x15	6.4	-2.33	9.34
$\{112\}_{\text{WC}}$	64.0°	1.44	90.0°	0.3x0.3x15	0.2	—	1.65
$\{211\}_{\text{WC}}$	67.0°	1.50	92.1°	0.4x0.4x15	0.2	—	1.82

3.7.6 Synchrotron stress measurements at ESRF

This study included the parent material, as-received being the reference state, prior to and after the grit-blasted surface roughening preparation, as well as the final as-coated samples shown in Figure 3.5.

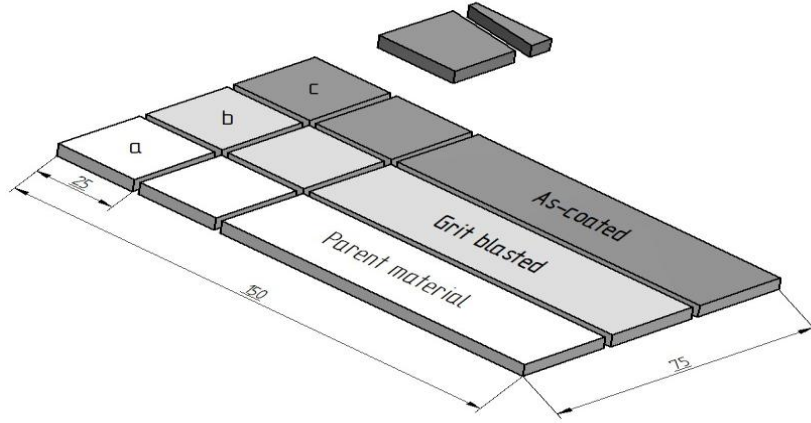


Figure 3.5. Schematic diagram showing the locations where samples were extracted from the as-procured plates, designated as parent material (reference state throughout this study), grit-blasted substrate and coated sample.

The high atomic number of W limits the penetration depth achievable with laboratory based X-ray instruments utilizing Co-K α to typically 2 μm , which is similar to the surface roughness. By exploiting the penetration depth of high energy synchrotron radiation (SR), depth resolved information was possible. The approach used here utilized 80-200 keV white beam synchrotron X-rays from the ID15A instrument at the ESRF (France), employed in the energy dispersive mode. The brilliance and high energy of the synchrotron X-rays enabled approximately 2% transmission through 2.5 mm of a sample, sufficient to collect a powder diffraction pattern. Beam sizes (depth x in-plane dimensions) of 0.03 x 0.6 mm² were used for this investigation, in conjunction with sample sizes of 25 x 25 mm³ and wedge shaped samples (cut by EDM) containing the coating for synchrotron measurement.

Exploratory measurements at different beam path lengths showed that a 2.3 mm depth of WC rendered data of sufficient accuracy for strain determination. The coatings were extensively mapped with SR using the WC {101} peak. Measurement time per position was 1200 s for WC, and 60 s for the substrate. For the Co face-centred cubic structure in the substrate, the {311} peaks were used for the strain determinations. Strains in the substrate were referenced to the parent materials, and WC to flakes of coating chipped from the substrates.

Figure 3.6b shows the sample geometry and set-up of the instruments. The use of two detectors with the SR investigations allowed simultaneous measurement of the in-plane and

normal strain components. For the ND investigations, the samples had to be re-oriented for the different strain directions. The schematic diagrams (Figure 3.6) show the radial collimation geometry that minimized surface aberration contributions [2004Kel].

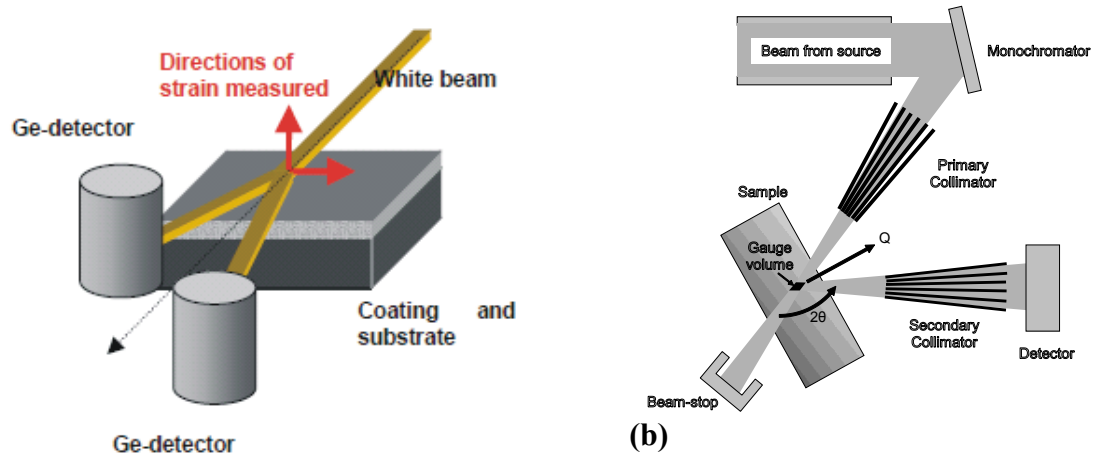


Figure 3.6. Measurement geometries employed with (a) Synchrotron and (b) Neutron diffraction investigations [2004Kel].

3.8 Abrasion wear testing

Dry abrasion testing was done using Dry Sand Rubber Wheel test rig (Figure 3.7) in accordance with standard ASTM G65-04 [2010ASTM] at ambient temperature and humidity.

Silica sand procured from Rolfes Silica of size 300-600 μm was used as the abrasive material. The abrasive sand was characterized using sieves analysis and SEM/EDX. Test specimens (Table 3.5), coated on the 70 x 25 mm face, were pressed against the rubber wheel under an applied load of 25 N. The rotational speed of the rubber wheel was kept at 140 r/mins and the sand flow rate at 4.3 g/s. The total test duration was 30 minutes. At 5 minute intervals, the samples were ultrasonically cleaned and then weighed using a Mettler Toledo Pb503S weighing machine.



Figure 3.7. General set-up of Dry Sand Rubber Wheel test rig showing vibratory feeder, testing chamber silo for the abrasive particles, flow rate meter and hook for loading.

For each coating, three specimens were used and the average value was used to indicate the mass loss and wear rate. Mass losses from the test specimens were determined to an accuracy of 0.1mg at the 5 minute intervals. The same procedure was employed for the parent material (substrate), grit-blasted samples, as-sprayed coating and heat treated coated samples. The wear scars were examined using SEM and EDX.

3.9 Heat treatment procedure

Stress relieving heat treatments were conducted on all the as-sprayed samples (Table 3.8), to relieve residual stresses generated during the spraying process. The research on heat treated Batch A samples was carried out by two undergraduate students, Mr Lucas Mabotja [2010Mab] and Mr Ntakadzeni Makhwathana [2010Nta] as their final year honours project at the University of the Witwatersrand, whilst research on the heat treated Batch B samples was carried out under this project. The polished specimens (from the coating characterization and wear tests) and unpolished samples (from residual stress measurements) were annealed in an ELITE Thermal Systems Limited tube furnace. The samples were placed in a ceramic container which was then placed inside the furnace. The process was done according to the parameters given in Table 3.8. The annealing temperatures, apart from that for mild steel,

were taken as 40% of the melting temperature of the substrate material. In the case of mild steel, an annealing temperature of 700 °C was taken to ensure that the low carbon phase transition was not activated. Annealing was carried out for one hour under argon atmosphere.

Table 3.8. Parameters used for heat treatment.

Coated substrate	Annealing temperature (°C)	Heating rate (°C.minute ⁻¹)	Dwell time (h)	Cooling rate (°C.minute ⁻¹)
Brass	375	6	1	5
Aluminium	375	6	1	5
Mild steel	700	6	1	5
304L stainless steel	875	6	1	5
Super-invar	875	6	1	5

CHAPTER FOUR RESULTS

4.1. BATCH A (COMMERCIAL SAMPLES)

4.1.1. Effect of Substrates on the Microstructure of Thermally Sprayed WC-17 wt%Co Coatings

4.1.1.1 Introduction

The objective of this work was to examine the effect of the substrate on the microstructure of WC-Co coatings sprayed by the HVOF process after deposition. The work was also done to gain a better understanding of the decomposition process of tungsten carbide during thermal spraying and the microstructures of the coatings.

4.1.1.2 Results

The typical morphology and components of the powder is shown in Figure 4.1.

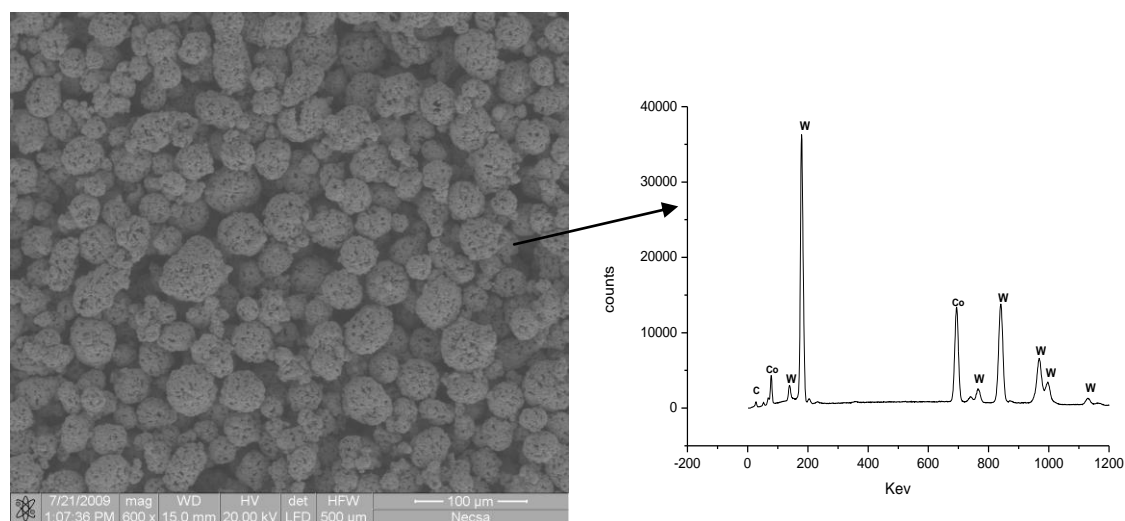


Figure 4.1. SEM-SEI micrograph and EDX spectrum of starting WC-17wt%Co powder.

4.1.1.3 X-ray diffraction

Figure 4.2 shows the X-ray diffraction spectra of the powder and as-coated surfaces. The starting powder comprised only WC and Co, but different phases were found on the different coated samples. All the coatings had a broad peak at $2\theta \approx 44^\circ$. The XRD results of the coated aluminium sample showed WC and metallic Co, with only a small amount of W_2C . The

coating on 304L stainless steel revealed the presence of WC only, with no Co. Detection of cobalt can be slightly compromised as XRD using Cu radiation tube can be insensitive to the detection of cobalt [2003Dal]. For super-invar, the XRD spectrum was significantly different from the others and was of a poorer quality, with broader peaks. There were large Co peaks, as well as small W_3C peaks. The brass sample showed WC and the possibility of some free Co by the slight peak at $2\theta \approx 44^\circ$. Two different carbides were found: W_2C in the aluminium sample, and W_3C in the super-invar sample.

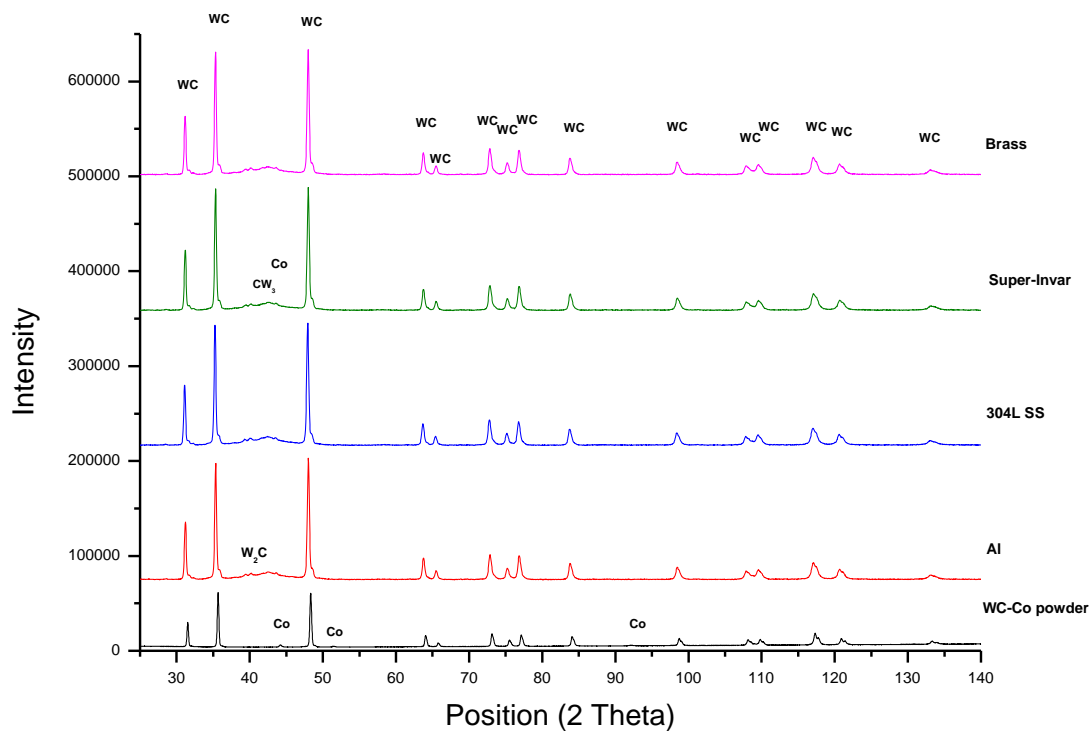


Figure 4.2. XRD patterns of the starting WC powder and as-sprayed coatings.

The optical micrographs of the as-sprayed coating cross-sections are presented in Figures 4.3 to 4.5. The microstructures show how well the coatings fitted on to the roughened substrate surfaces to create good mechanical bonds. Porosity was also seen. For the as-sprayed coating on the aluminium substrate, Figure 4.3, porosity was seen, with a good fit between coating and the regular surface of the substrate. No peeling was observed at the interface between coating and the substrate.

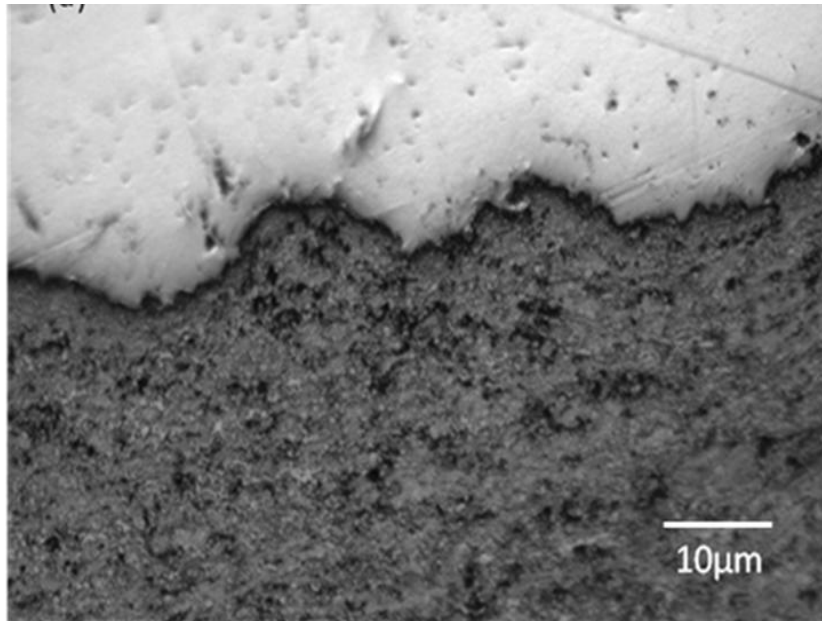


Figure 4.3. Optical micrograph of WC-17wt% Co coatings (bottom) on aluminium.

The as-sprayed coating on 304L stainless steel substrate shown in Figure 4.4 had porosity, as well as a good fit between coating and the regular surface of the substrate. The black area in the coating-substrate interface is the alumina used for the grit-blasted, which is similar to the work reported by Machio [2005Mac].

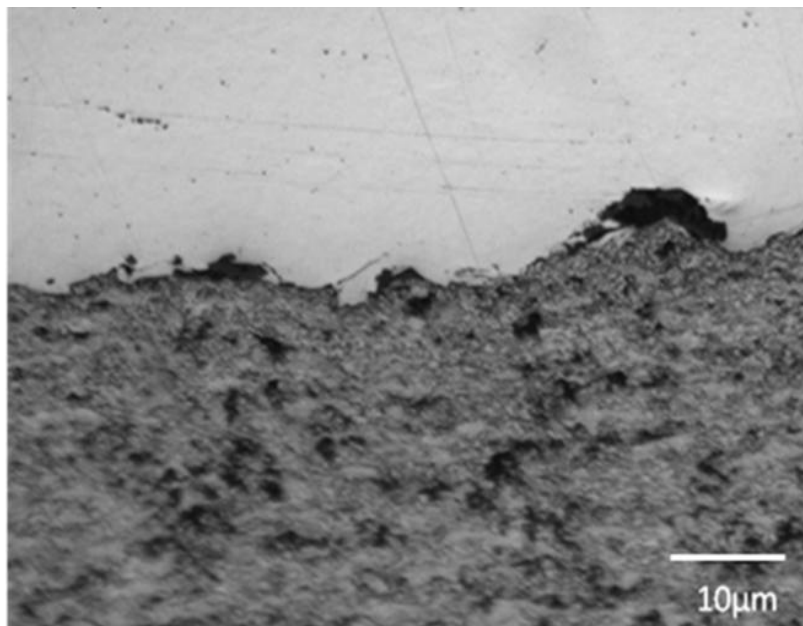


Figure 4.4. Optical micrograph of WC-17wt% Co coating (bottom) on 304L stainless steel showing coating and holes.

Figure 4.5 shows the as-sprayed coating on the brass substrate, with porosity and a good interface between the coating and the regular surface of the substrate. No peeling was observed at this interface.

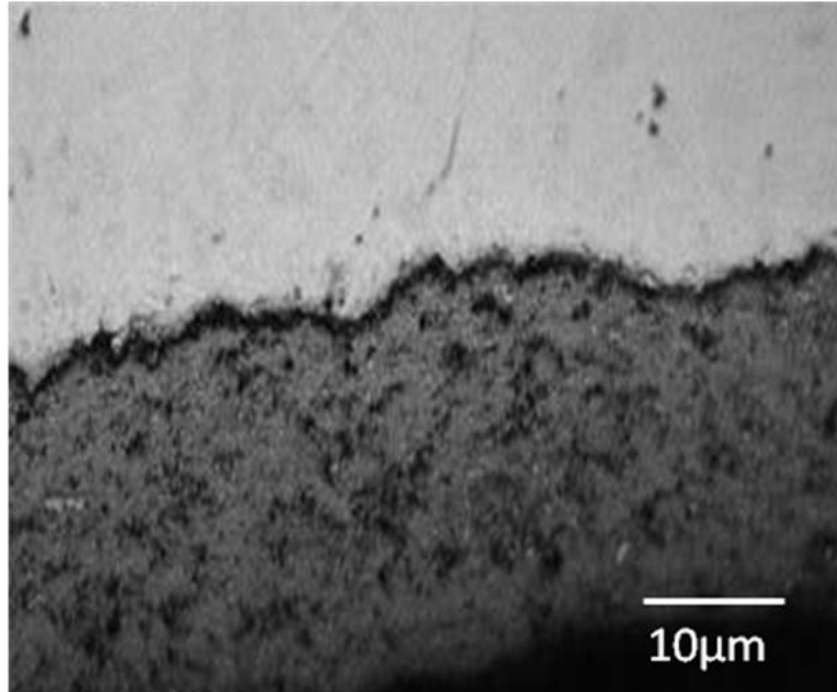


Figure 4.5. Optical micrograph of WC-17wt% Co coating (bottom) on brass.

The SEM/BSE micrographs of the WC-17 wt% Co coatings are shown in Figures 4.6-4.9. At higher magnification, the coatings showed pores and mainly equiaxed WC grains of different sizes in a Co matrix. The typical thermal sprayed coating microstructure observed in the as-sprayed coatings on aluminium substrate is shown in Figure 4.6. The noticeable features were the lamellar structure, due to individual splats forming a layered structure, pores and different WC particle sizes within the Co matrix.

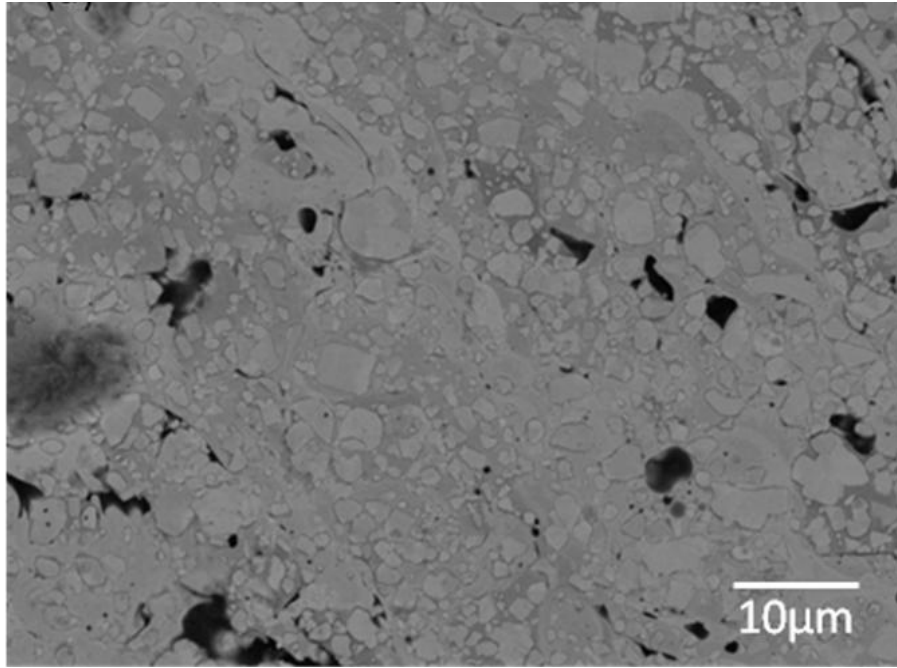


Figure 4.6. SEM-BSE image of WC-17 wt% Co coating on the aluminum substrate, showing WC (light), cobalt binder (medium), and pores (black).

From the microstructure of the as-sprayed coating on brass substrate shown in Figure 4.7, the most noticeable features were the lamellar structure from individual splats forming the layered structure, pores and different sized WC particles within the Co matrix.

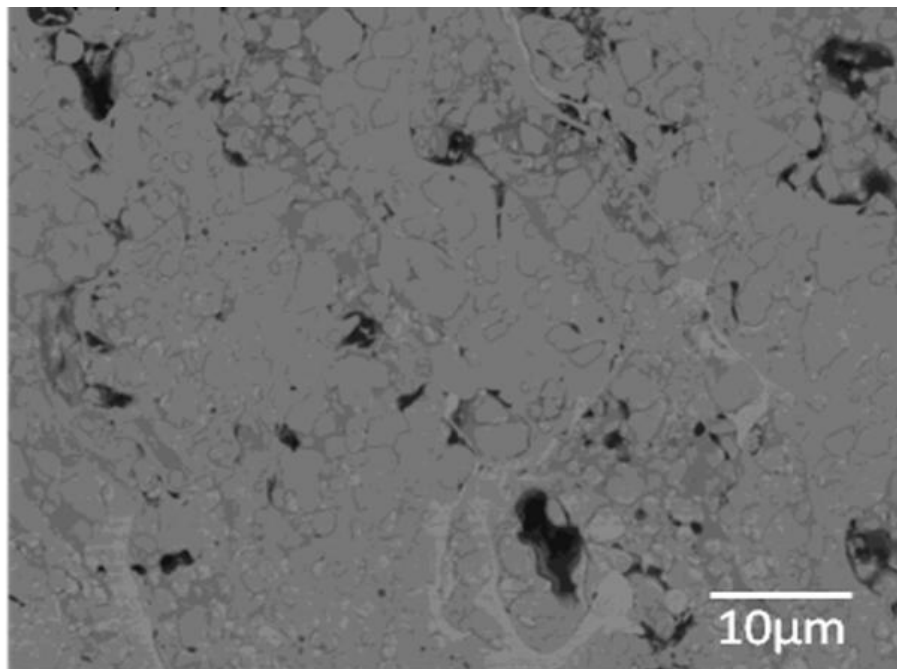


Figure 4.7. SEM-BSE image of WC-17 wt% Co coating on brass substrate, showing WC (light), cobalt binder (medium), and pores (black).

The microstructure of the as-sprayed coating on the 304L stainless steel substrate shown in Figure 4.8 had a lamellar structure (from the individual splats forming the layers), smaller pores and more similar sized WC particles than for brass.

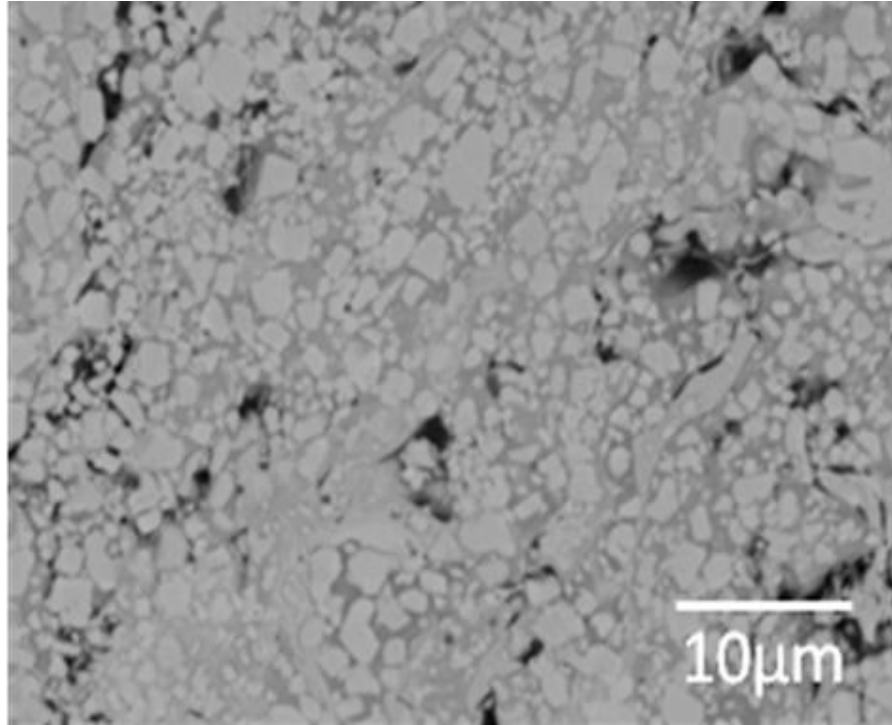


Figure 4.8. SEM-BSE image of WC-17 wt% Co coating on 304L stainless steel, showing WC (light), cobalt binder (medium), and pores (black).

The microstructure of the as-sprayed coatings on the super-invar substrate (Figure 4.9) shows a lamellar structure (from the individual splats), pores, microcracks and a range of WC particle sizes within the Co matrix. These cracks are thought to result from the residual stress relaxation during deposition, as the yield strength of the WC was exceeded during the thermal contraction when the hot splats experienced quick thermal quenching as they encountered the surface. However, this did not weaken the bonding between coating and substrate because the cracks were perpendicular to the coating thickness.

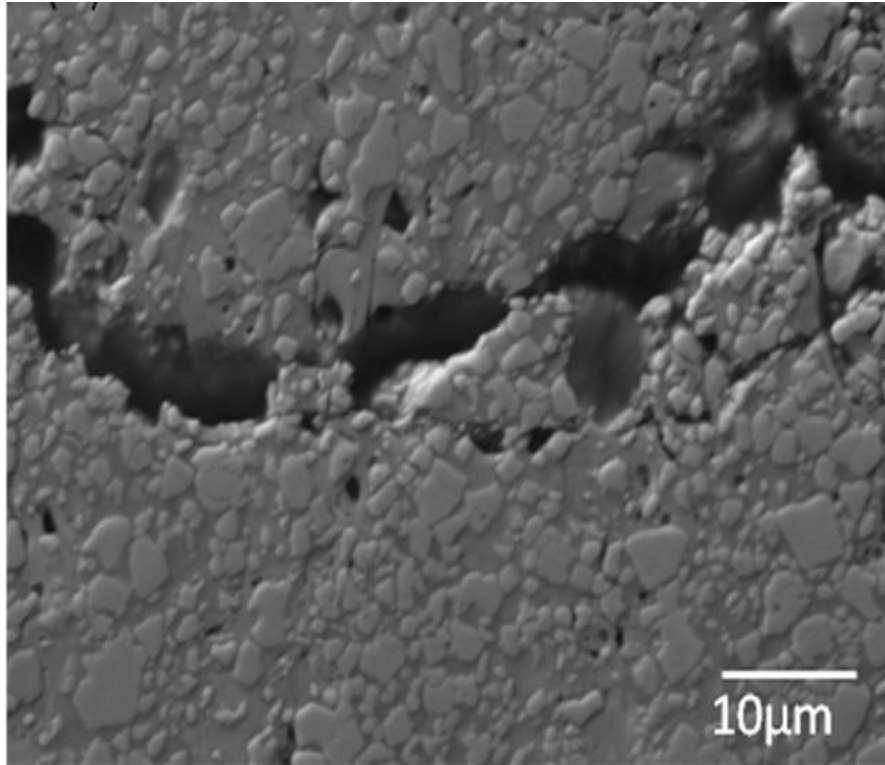


Figure 4.9. SEM-BSE image of WC-17 wt% Co coating on super-invar substrate, showing WC (light), cobalt binder (medium), pores (black), and microcracks.

EDX analyses showed that all the coatings were composed of W, Co and C, with the 304L stainless steel sample containing Al in addition. The presence of aluminium at the interface was attributed to the alumina grit blast preparation of the substrate before deposition of the coating. The phases identified from EDX analyses were in agreement with X-ray diffraction results. The porosities observed in the microstructures were very low, except for super-invar which had a slightly higher porosity.

The initial WC grain size of the starting powder was $1.2 \pm 0.3\mu\text{m}$, and the mean WC grain sizes in the coatings are given in Table 4.1, with the substrates properties given in Table 3.2.

Table 4.1. Porosity and mean grain size of the coatings.

Substrate	Porosity (%)	WC grain size (μm)
Aluminium	0.5149 ± 0.001	0.150 ± 0.01
Brass	0.4581 ± 0.002	0.127 ± 0.01
304L SS	0.5596 ± 0.001	0.185 ± 0.02
Super-invar	0.7529 ± 0.001	0.133 ± 0.02

The mean grain sizes were in general similar and small. It might be expected that less porosity would be associated with smaller grain size, but this was not the case. The grain size distribution in Figure 4.10 shows a homogeneous distribution for coated stainless steel and brass substrate, whereas more irregular grain sizes are seen in aluminium and super-invar. Table 4.1 shows that the porosity of the super-invar coating was a little higher than the rest of the samples, which agreed with the SEM images. The brass sample had slightly lower porosity.

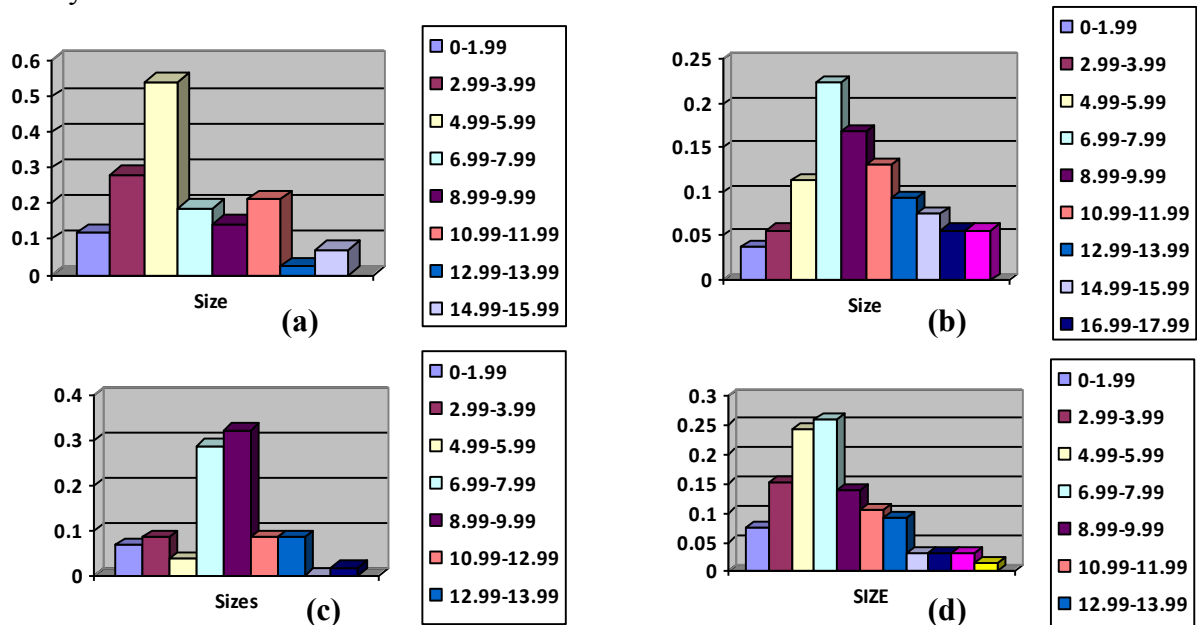


Figure 4.10. Grain size distribution of the coatings on different substrates: (a) aluminium, (b) 304L stainless steel, (c) super-invar, and (d) brass.

Table 4.2. Measured properties of the coatings.

Substrate	Surface roughness Rq (nm)	H _V coating (GPa)	H _V substrate (GPa)
Aluminium	35	10.22±0.02	0.09±0.01
Brass	32	10.04±0.01	1.40±0.01
304L SS	10	9.41±0.01	2.71±0.01
Super-Invar	24	7.91±0.01	1.53±0.01

The three-dimensional surface roughness measurements on the coatings by atomic force microscopy are shown in Figure 4.11, and the results are given in Table 4.2. The aluminium and brass samples had similar roughness values. The surface profiles showed periodic high peaks, scratches and low valleys corresponding to the machining marks

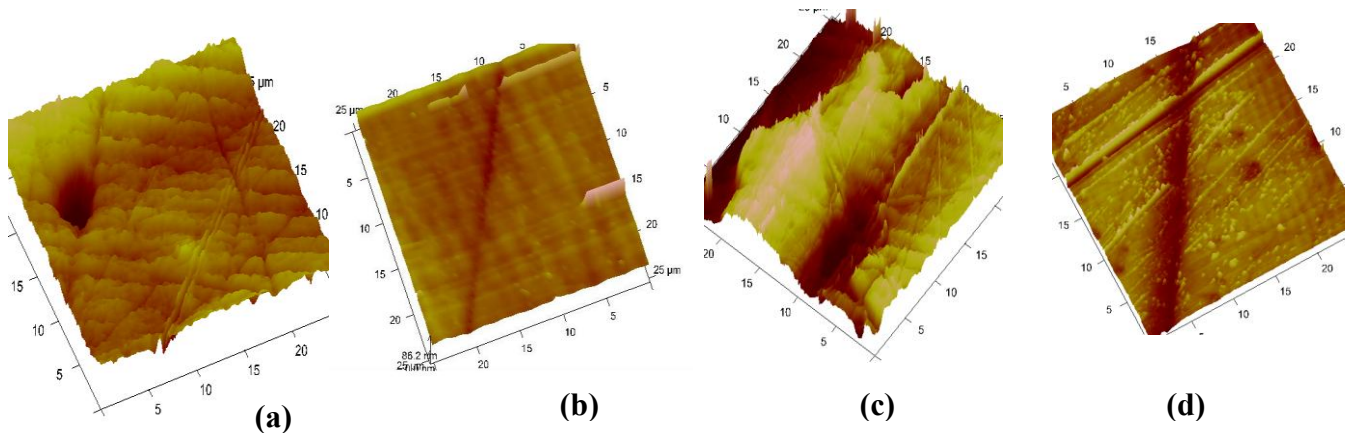


Figure 4.11. AFM surface profiles of WC-17wt% Co coatings on different substrates: (a) aluminium, (b) 304L stainless steel, (c) super-invar, and (d) brass.

The microhardness values of both coatings and substrates are shown in Table 4.2 and Figure 4.12. The results indicated a higher microhardness in the coating compared to the substrates, which was expected. The value for the coated aluminum sample was slightly higher than the other coated samples, due to the occurrence of W₂C.

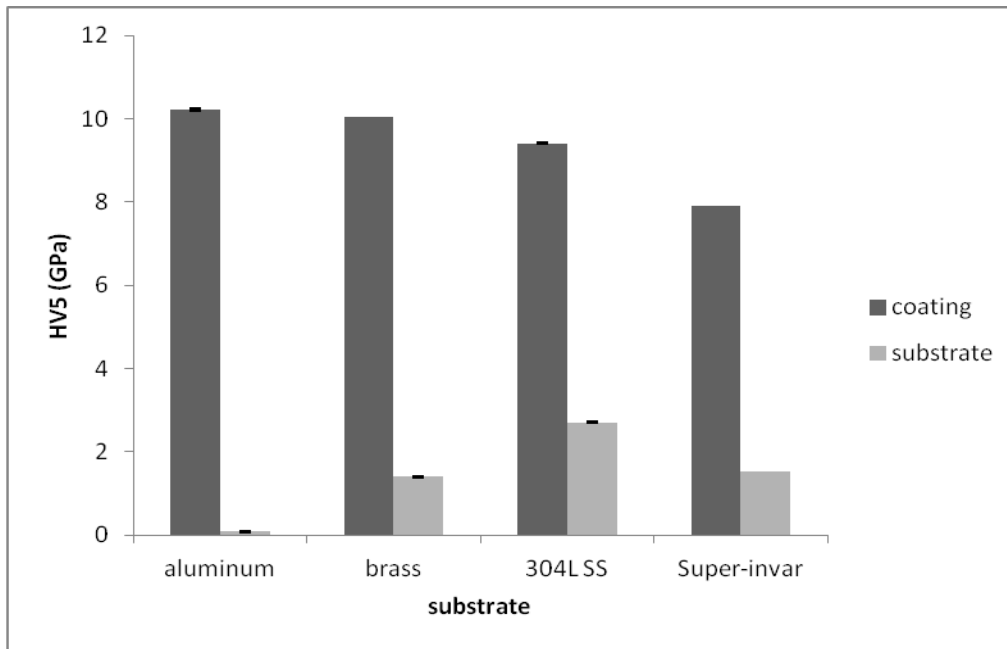


Figure 4.12. Microhardness values of WC-Co coatings and the different substrates.

The relationships between the coating results (Table 4.2), as well as the substrate properties (Table 3.2), are shown in Figures 4.13-4.18 (with no error bars shown, as the errors were small (Table 4.2)). The microhardness decreased with increasing grain sizes (Figure 4.13), and increasing porosity (Figure 4.14), increased with increasing coefficient of thermal expansion (Figure 4.15) and increasing surface roughness (Figure 4.16). The surface roughness decreased with increasing substrate melting point (Figure 4.17), whilst the surface roughness increased with increasing coefficient of thermal expansion (Figure 4.18).

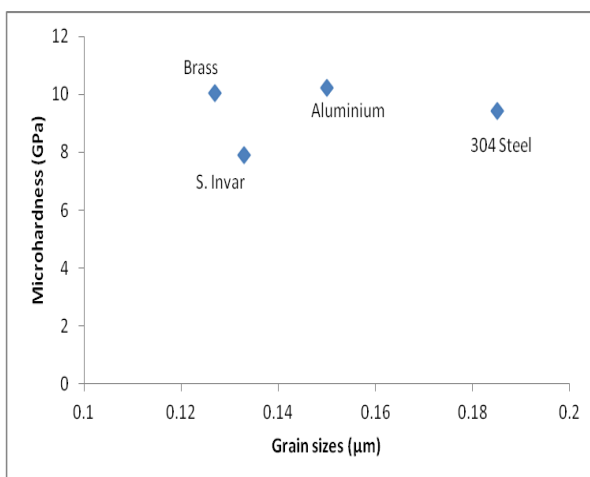


Figure 4.13. Correlation between the grain sizes and microhardnesses of the WC-17Co coatings on the different substrates.

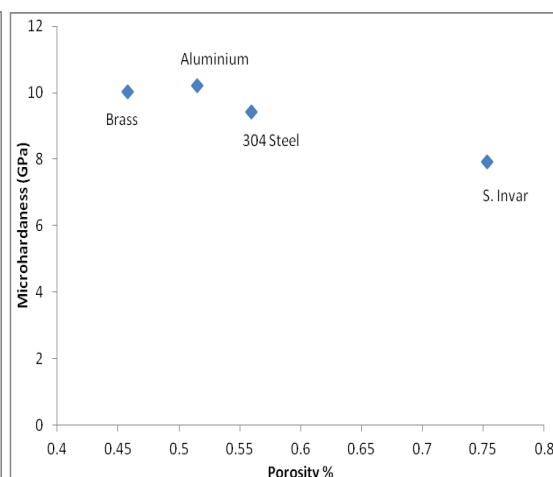


Figure 4.14. Correlation between the porosity and microhardnesses of the WC-17Co coatings on the different substrates.

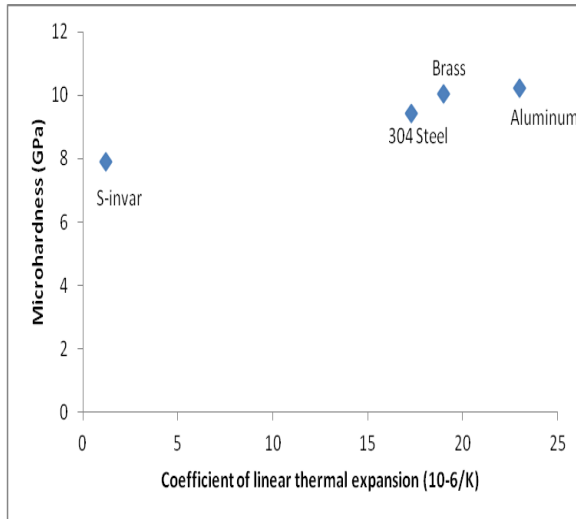


Figure 4.15. Correlation between the substrate coefficients of linear thermal expansion and microhardness of the WC-17Co coatings on the different

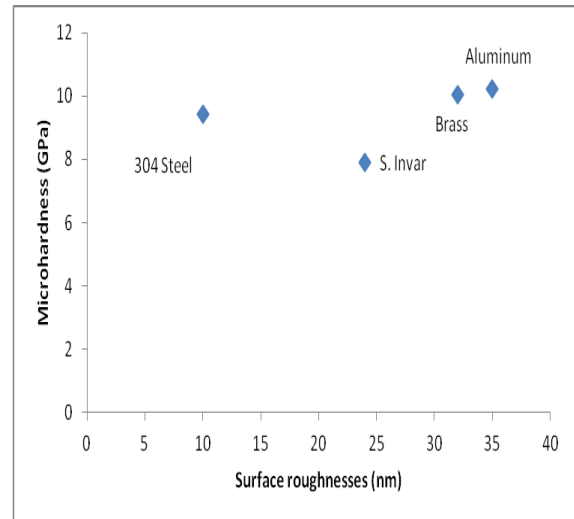


Figure 4.16. Correlation between the surface roughness and microhardness of the WC-17Co coatings on the different substrates.

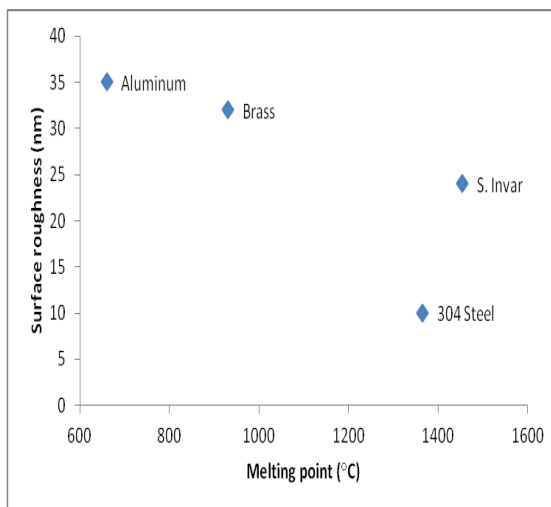


Figure 4.17. Correlation between the melting point and surface roughness of the WC-17Co coatings on the different substrates.

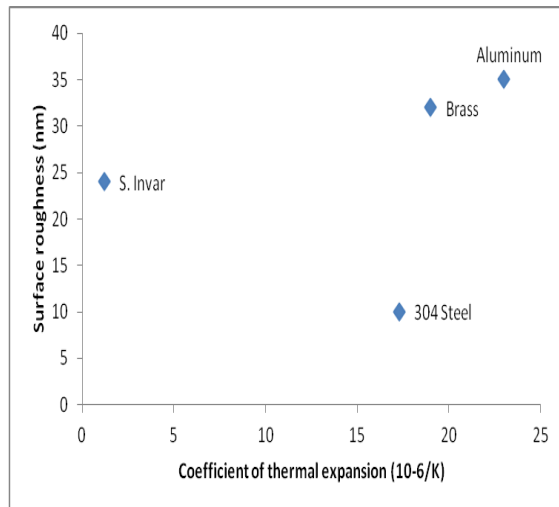


Figure 4.18. Correlation between the coefficient of thermal expansion and surface roughness of the WC-17Co coatings on the different substrates.

4.1.2. X-ray diffraction measurements of residual stress in WC-Co thermally sprayed coatings onto metal substrates

4.1.2.1. Introduction

The objective of this portion of the work was to further explore the use of X-ray diffraction to determine the residual strain in WC-17wt% Co HVOF coating on different substrates, and to extend it to investigate the influences of hardness and coefficients of thermal expansion on the nature of the residual stress.

4.1.2.2. Results

A representative plot of strain against $\sin^2\psi$ typically observed for the investigation of the as-sprayed coatings is shown in Figure 4.19. The $-\sin^2\psi$ of the sample showed a negative slope for as-sprayed coatings on aluminum and brass, and coated super-invar showed positive slopes.

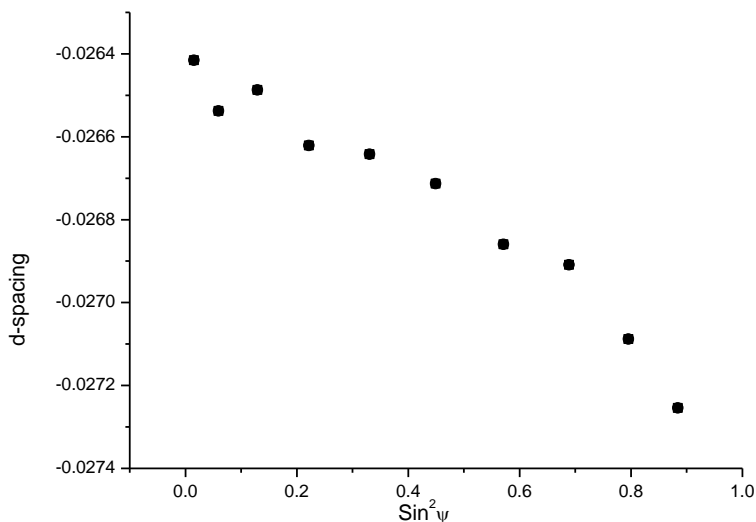


Figure 4.19. Plot of d -spacing against $\sin^2\psi$ for as-sprayed coating on the brass substrate.

The residual stresses determined under the assumption of planar stress conditions using a reflection of $\{202\}_{\text{WC}}$ are given in Table 4.3 and Figure 4.20. The residual stresses were determined to be compressive in the as-sprayed coatings on aluminium, 304L stainless steel and brass, whilst they were tensile on the coated super-invar sample. Notwithstanding the nature of the stresses, they were all of relatively low magnitudes which could be due to flaws.

Table 4.3. Residual stresses in WC coatings deposited on different substrates.

Coated Substrate	Residual stress measured with Co-K α (MPa)
Brass	53.5 \pm 28.0
Aluminum	-129 \pm 26.2
Super-Invar	74 \pm 30.6
304L stainless steel	-51.2 \pm 18.3

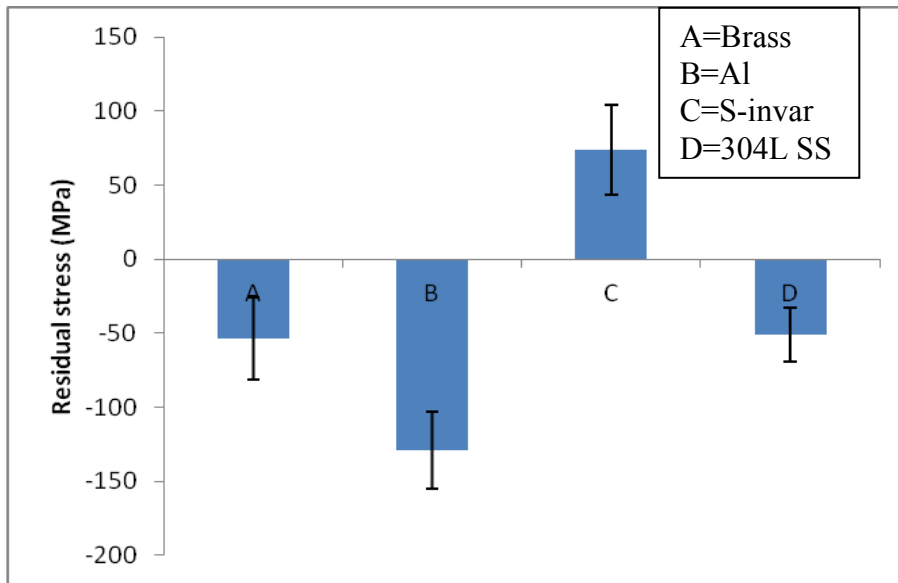


Figure 4.20. Residual stresses in as-coated WC-Co coatings deposited on the different substrates.

The relationships between the residual stresses values of the coating against microhardness, coefficient of thermal expansion of the substrate, as well as specific heat capacity are shown in Figures 4.21 to 4.23. The residual stress decreased with increasing microhardness (Figure 4.21), increasing coefficient of thermal expansion (Figure 4.22) and increasing specific heat capacity (Figure 4.23).

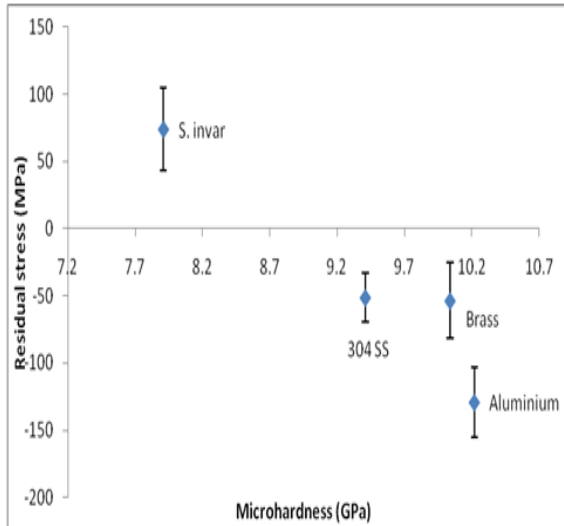


Figure 4.21. Correlation between the coating microhardness and residual stresses values of the WC-17Co coating on the different substrates.

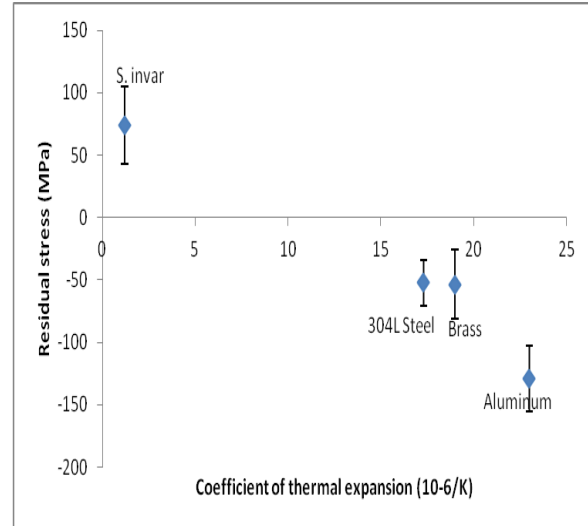


Figure 4.22. Correlation between the coefficient of thermal expansion of the substrates and residual stresses values of the WC-17Co coating on the different substrates.

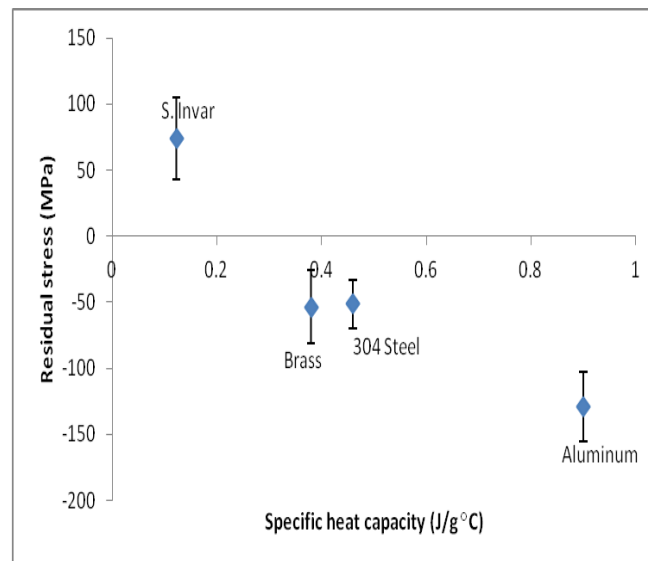


Figure 4.23. Correlation between the substrate specific heat capacity and residual stresses of the WC-17Co coatings on the different substrates.

Residual stress investigations by X-ray diffraction, were also done for the reflection of $\{112\}_{WC}$ but not necessarily corresponding to the same position of the $\{202\}_{WC}$. The stresses were compressive, as shown in Table 4.4.

Table 4.4. Residual stresses in WC coatings deposited on different substrates.

Coated Substrate	Residual stress measured by Co-K α (MPa)
Brass	-47.5 \pm 43.1
Aluminum	-149.8 \pm 50.2
Super-Invar	-17.6 \pm 44.6
304L stainless steel	-17.6 \pm 44.6.

The relationships between the residual stresses (Table 4.4), as well as the substrate properties (Table 3.2), are shown in Figures 4.24-4.26. The residual stress do not show a discernable relationship with substrate melting point (Figure 4.24), residual stress increased with increasing coefficient of thermal expansion (Figure 4.25) and with increasing specific heat capacity (Figure 4.26).

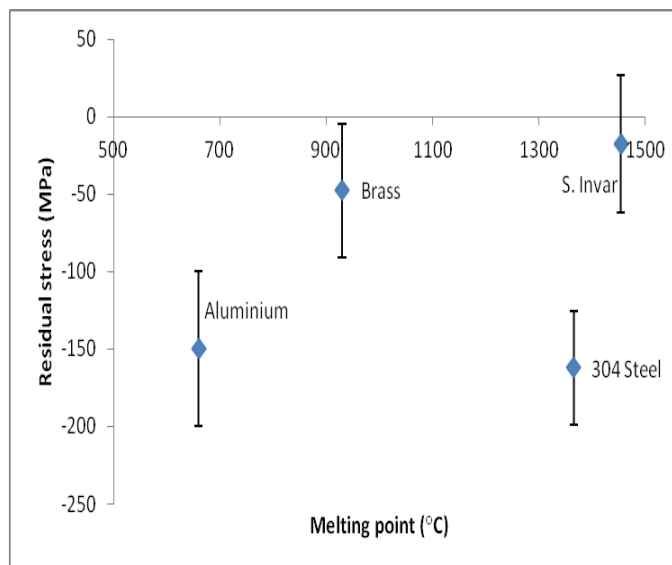


Figure 4.24. Correlation between the substrate melting points and residual stresses of the WC-17Co coatings on the different substrates.

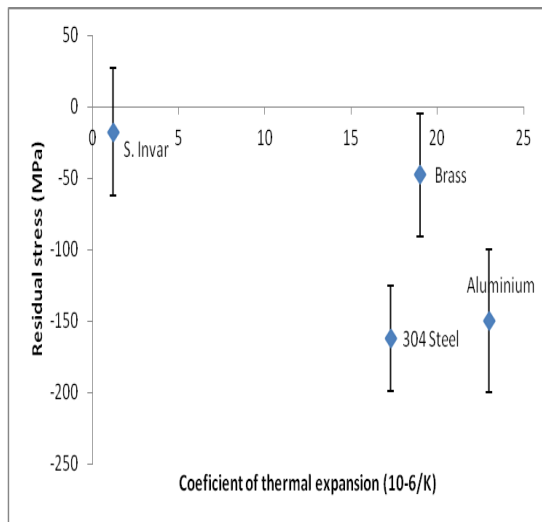


Figure 4.25. Correlation between the substrate coefficients of thermal expansion and residual stresses of the WC-17Co coatings on the different substrates.

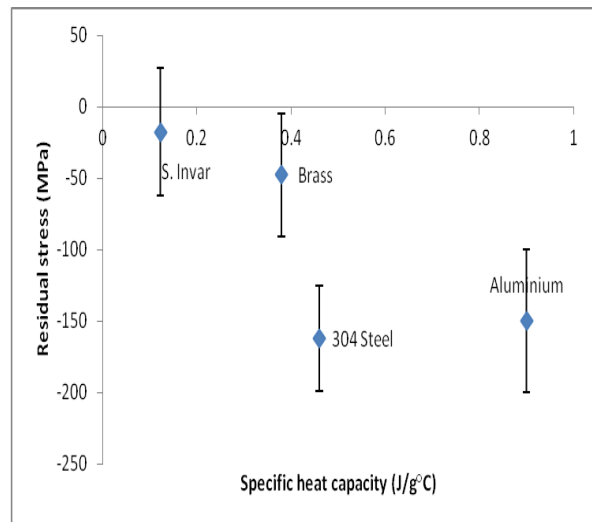


Figure 4.26. Correlation between the substrate coefficients of thermal expansion and residual stresses of the WC-17Co coatings on the different substrates.

4.1.3. Effect of substrate on the 3 body abrasion wear of HVOF WC-17wt%Co coatings

4.1.3.1. Introduction

The objective here was to evaluate the abrasive wear resistance of WC-17wt%Co thermal spray coatings deposited onto four different substrates, in order to assess the effect of substrate on the coatings' wear behavior. The wear mechanisms were identified and related to the coating microstructure and hardness.

4.1.3.2. Results

The morphology of the silica abrasive is presented in Figure 4.27 which shows the angular nature of the particles, with a particle size distribution between 300-600 microns.

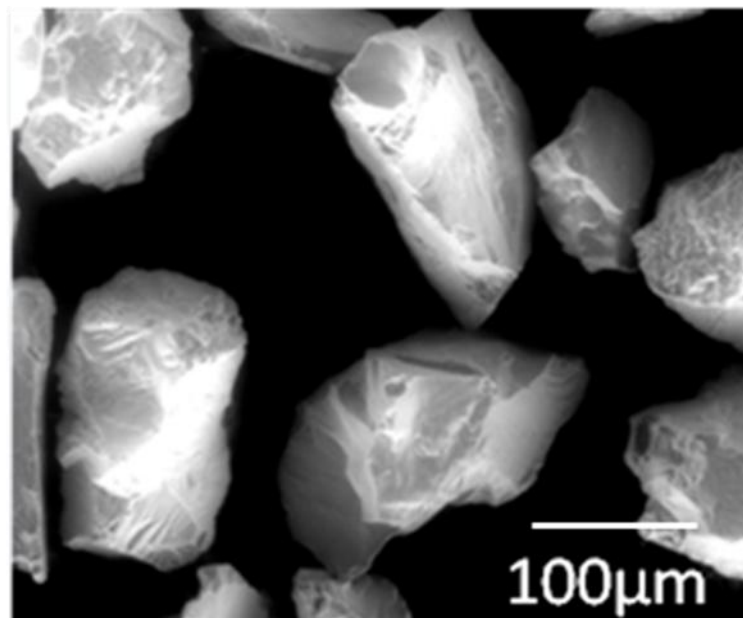


Figure 4.27. Morphology of silica abrasive procured from Rolfes Silica, South Africa.

The results of the average cumulative mass loss for each coated substrate during the 30 minute test are shown in Figure 4.28, with the wear rates for each coated substrate after 30 minutes shown in Figure 4.29 (where the errors were too small to plot i.e. ± 0.001). The general trend of increasing mass loss as time progresses was seen for all coated substrates. The coated aluminium consistently had the highest average mass loss, despite having the highest hardness. The coated brass and super-invar samples showed similar mass loss trends. The coated 304L stainless steel had the lowest mass loss after 20 minutes, even though it had the second lowest hardness value. These results do not follow the known trend of increasing

hardness being associated with decreased wear rate [2007Kim]. This implies that additional factors are determining the wear response of the coated substrates.

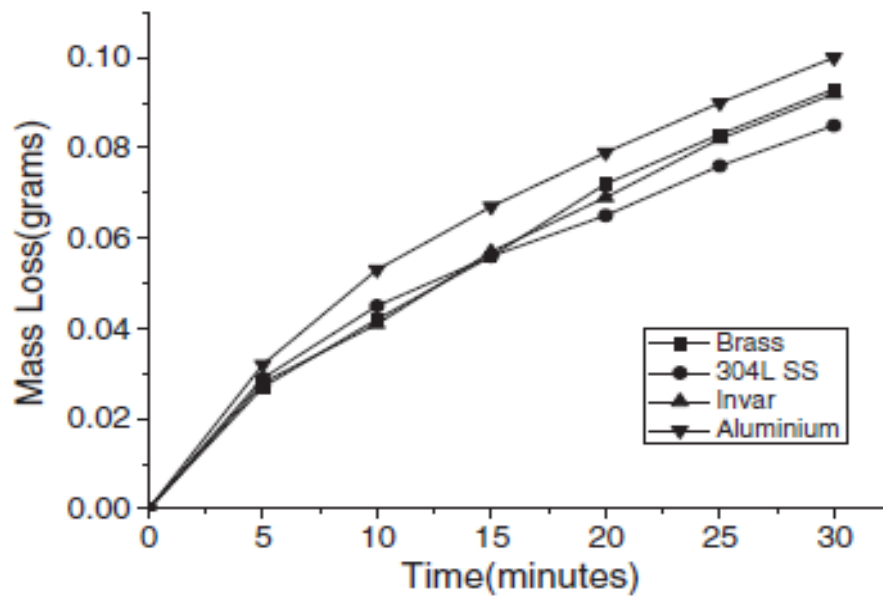


Figure 4.28. Average cumulative mass loss for each coated sample on abrasive wear testing.

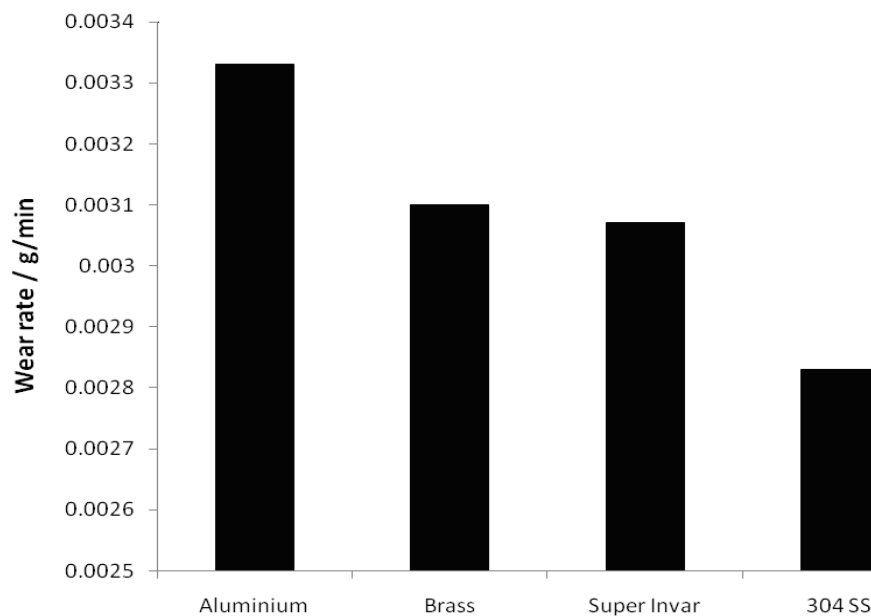


Figure 4.29. Wear rates of as-received coated substrates after 30 minutes of abrasive wear testing.

To understand the wear behaviour, the wear scars were examined using the SEM. Figures 4.30-4.33 show SEM images of the worn surfaces for each coated substrate. Similar wear features were observed on all four worn coated substrates. However, the degree of damage differed among the different substrates. The worn coated aluminium substrate sample (Figure 4.30) revealed extensive cracking of the carbide grains, as well as fragmenting of the carbides. Also, there was Co binder removal in the selected areas, leaving the carbide grains in higher relief and unsupported. Rounding of the carbide grain edges was observed, as well as micro-crack paths and multi-grain pull-out. A deep wear groove was visible.

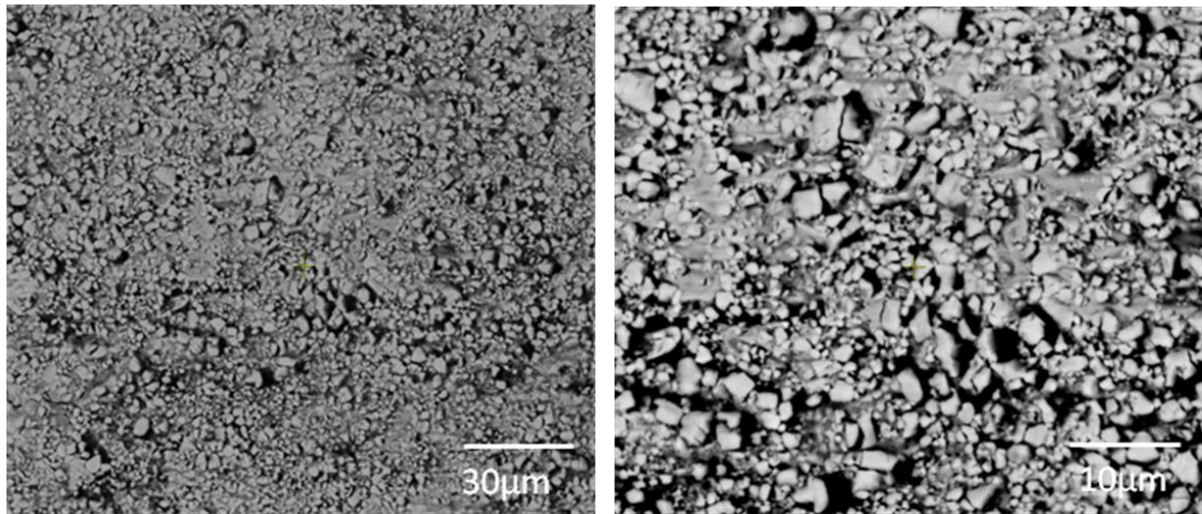


Figure 4.30. SEM-BSE micrographs of the worn WC-17Co coating surfaces on the aluminum substrate, showing extensive cracking and fragmentation of the carbides (WC (light) and Co (dark)).

The worn coated brass substrate sample (Figure 4.31) had fewer cracked and fragmented carbides. There was Co binder removal in selected areas, leaving the carbide grains in higher relief and unsupported, whereas less Co binder removal was seen on the coated 304L stainless steel substrate (Figure 4.33). Rounding of the carbide grain edges was observed, as well as micro-crack paths and multi-grain pull-out. A deep wear groove was visible.

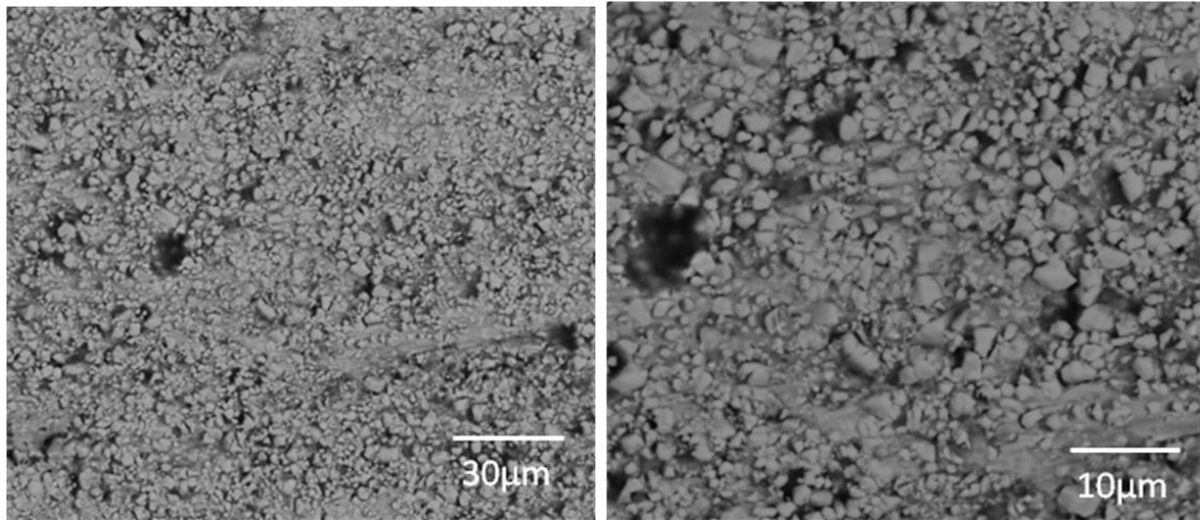


Figure 4.31. SEM-BSE micrographs of the worn WC-17Co coating surface on brass, showing cracks, individual pull-out of carbides and binder removal around the harder carbides standing prone (WC (light) and Co (dark)).

Figure 4.32 shows the worn coated super-invar substrate sample. The noticeable features were fewer cracked and fragmented carbides. Some of the Co binder had been removed, leaving the carbide grains in higher relief and so unsupported. Rounding of the carbide grain edges, micro-crack paths, multi-grain pull-out and a deep wear groove were also observed.

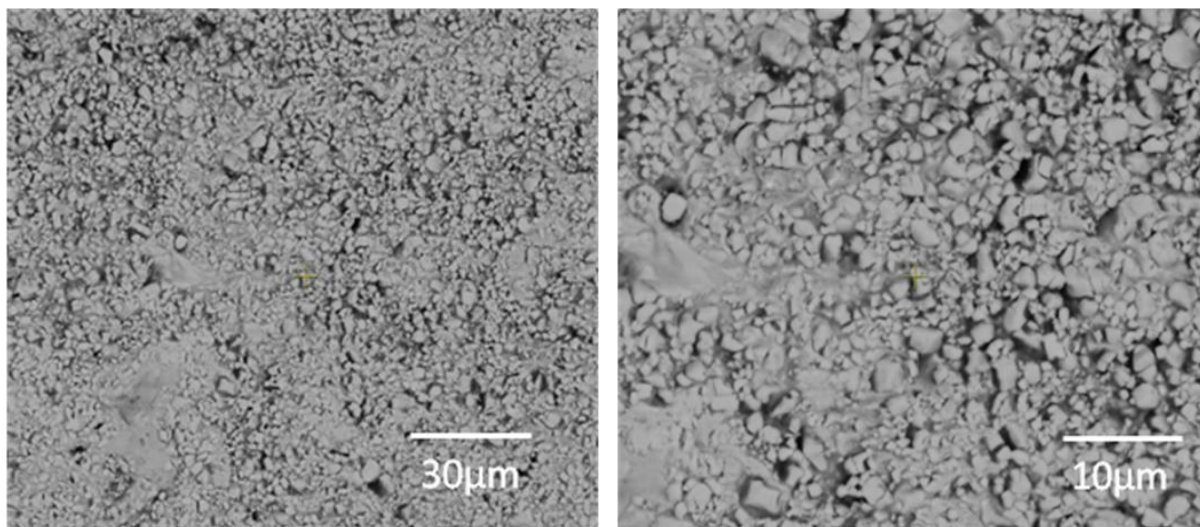


Figure 4.32. SEM-BSE micrographs of the worn WC-17Co coating surface on super-invar, showing cracks and preferential binder removal around harder carbides standing prone (WC (light) and Co (dark)).

The worn coated 304L stainless steel substrate sample (Figure 4.33) revealed fewer cracked and fragmented carbides. It also showed limited binder removal with microcracking in the selected areas, leaving the carbide grains in higher relief and unsupported, while the coated aluminium (Figure 4.30) showed the highest level of binder removal. Rounding of the carbide grain edges, micro-crack paths, multi-grain pull-out and deep wear grooves were visible.

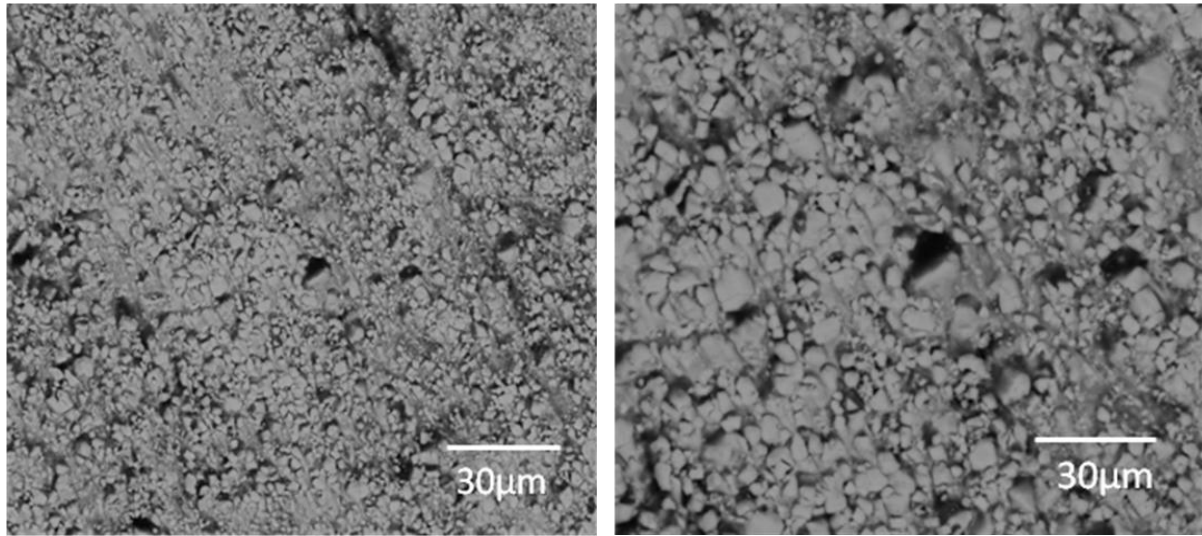


Figure 4.33. SEM-BSE micrographs of the worn WC-17Co coating surface on 304L stainless steel, showing few cracks, pull-out of carbides and preferential binder removal around free standing carbide grains (WC (light) and Co (dark)).

To understand the correlation between the wear loss, residual stress and yield strength, residual stresses were determined on the abrasive samples, with their average stress values given in Table 4.5. The yield strength of each coating was calculated using the formula of Cahoon *et al.* [1971Cah], with n assumed to be 0.15 [1986Die] and the values are listed in Table 4.5.

$$\sigma_o = \frac{HV(0.1)^n}{3}$$

Table 4.5. Yield strength, abrasive wear results and average residual stress of the coated samples.

Substrate	Aluminum	Brass	304L Stainless Steel	Super-invar
Coating Yield strength (GPa)	2.41	2.37	2.22	1.87
Wear mass loss (g)	0.10 ± 0.01	0.093 ± 0.01	0.085 ± 0.01	0.092 ± 0.01
Average residual stress (MPa)	-224.23 ± 42.3	-149.3 ± 42.7	-93.06 ± 43.8	-78.86 ± 41.2

4.2. BATCH B RESULTS (SUBSTRATES PROCURED FROM GOODFELLOW, UK)

4.2.1. Microstructural characteristics of HVOF sprayed WC-Co coatings on metal substrates

4.2.1.1. Introduction

The choice of a metal substrate for thermal spraying needs adequate attention for good properties. The substrates of the Batch B samples were specifically sources to be fine grained with minimal crystallographic texture to enable residual stress investigation with different techniques. The goal of this portion of the work was to demonstrate the dependency of the coating microstructures and mechanical properties on the coated substrate.

4.2.1.2. Results

Figure 4.1 shows the morphology of the feedstock powder. The powder was identified to be tungsten carbide grains in a cobalt matrix by EDX. The scanning electron microscope backscattered electron images of the coatings are presented in Figures 4.34 to 4.39. These figures show the main features of the coatings, highlighting the differences between them at higher magnification. The higher magnifications revealed the carbides better, with a typical microstructure of thermal spraying. The microstructure of the as- sprayed coatings on

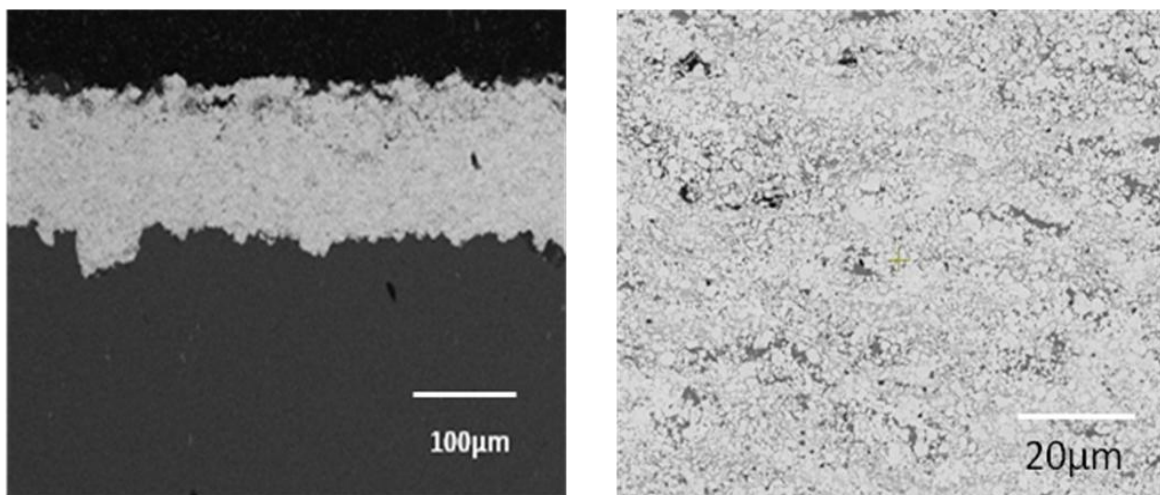


Figure 4.34. SEM-BSE images of cross-sections of WC-17%Co coating on aluminum, showing WC (light), cobalt binder (medium), and pores (black).

The aluminium substrate, Figure 4.34, had mainly finer, equiaxed WC particles, as well as coarser, elongated WC particles, and pores.

The microstructure of the as-sprayed coating on brass substrate is presented in Figure 4.35. The main features were the pores, microcracks, and mainly equiaxed WC particles of different sizes.

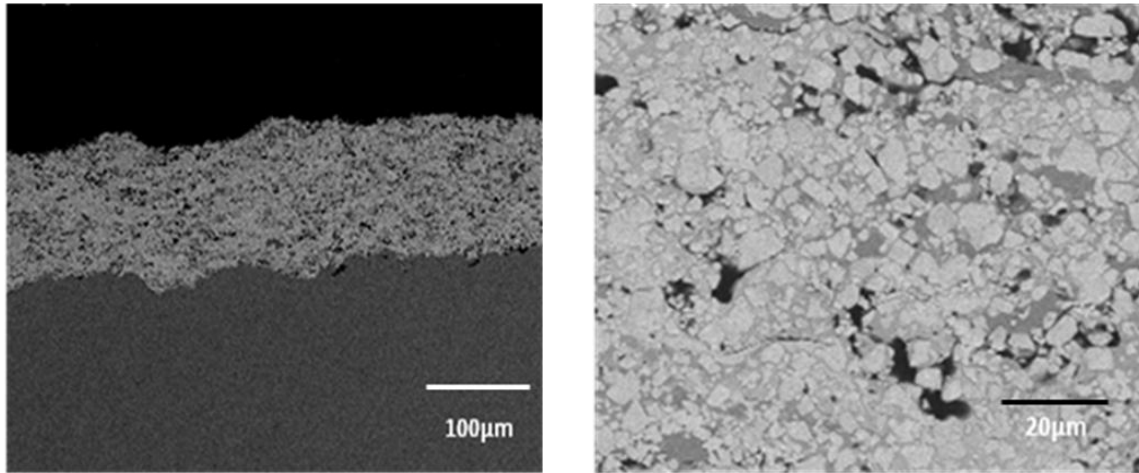


Figure 4.35. SEM-BSE images of cross-sections of WC-17%Co coating on brass, showing WC (light), cobalt binder (medium), pores (black) and microcracks on the right hand image.

The as-sprayed coating on the mild steel substrate, shown in Figure 4.36, had a microstructure with pores, finer, elongated carbide with more pronounced micro-cracking with distinct differences in WC particle size embedded within the Co matrix. The long crack found in the coating is roughly parallel to the interface. It is thought that, the crack does not weaken the bonding between the coating and the substrate, because they are perpendicular to the coating thickness.

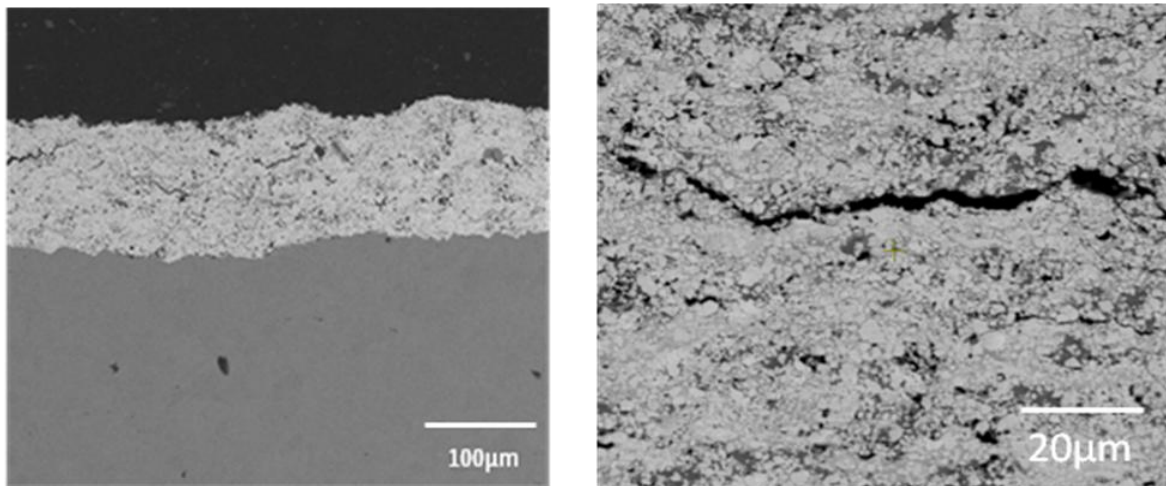


Figure 4.36. SEM-BSE images of cross-sections of WC-17%Co coating on mild steel, showing WC (light), cobalt binder (grey), pores (black), with microcracks on the left hand image.

Figure 4.37 shows the microstructure of the as-sprayed coatings on the super-invar substrate. The major features were the pores, microcracks, and mainly equiaxed carbides in the Co matrix.

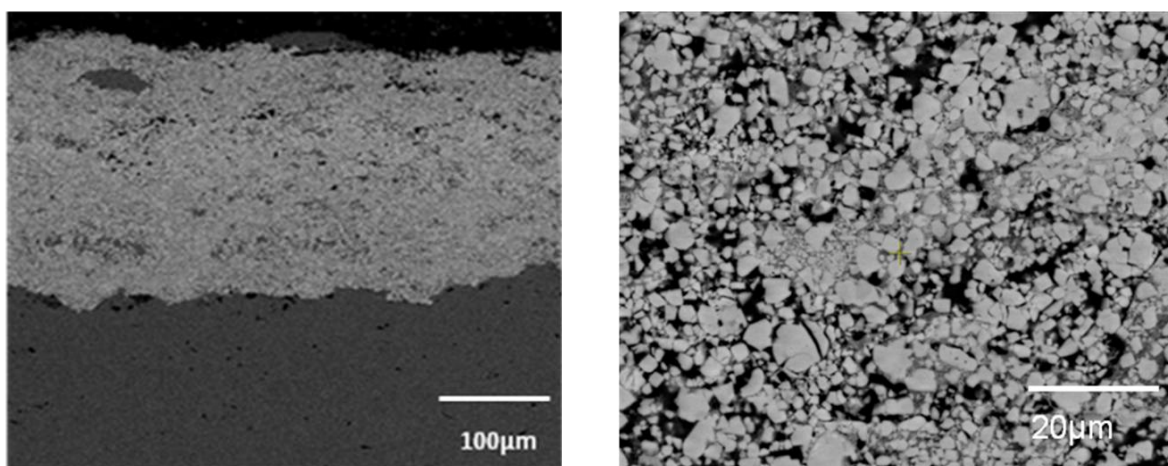


Figure 4.37. SEM-BSE images of cross-sections of WC-17%Co coating on super-invar, showing WC (light), cobalt binder (grey), and pores (black).

The microstructure of the as-sprayed coatings on 304L stainless steel substrate (Figure 4.38) had a lamellar structure, with pores, microcracks, finer and some elongated carbides, with a range of WC particle sizes.

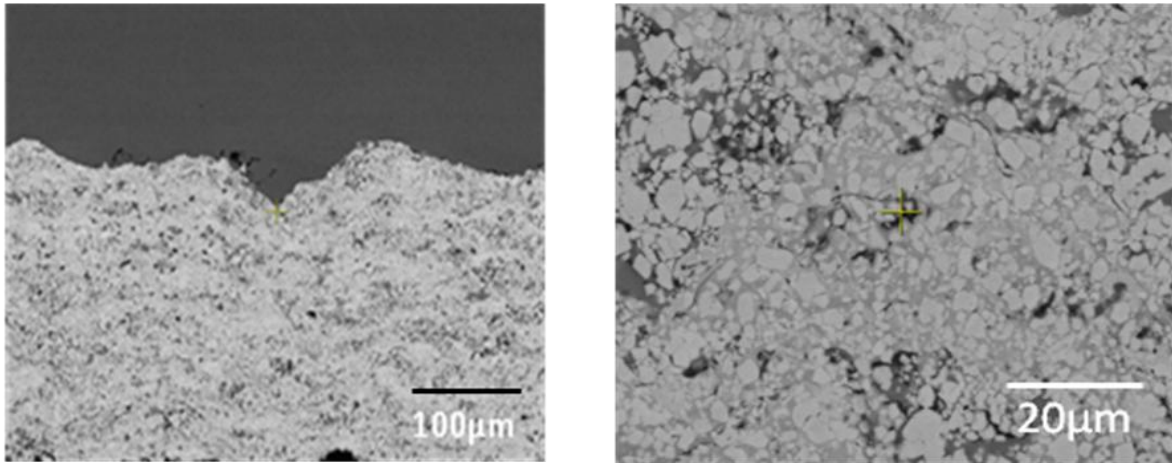


Figure 4.38. SEM-BSE images of cross-sections of WC-17%Co coating on 304L stainless steel, showing WC (light), cobalt binder (medium), and pores.

A typical SEM-BSE image of a Vickers hardness indentation on a cross-section of a WC-17% Co coating is shown in Figure 4.39. No cracking was seen from the indentation, which showed that the coating integrity was good, despite the localised microcracks observed (Figure 4.36).

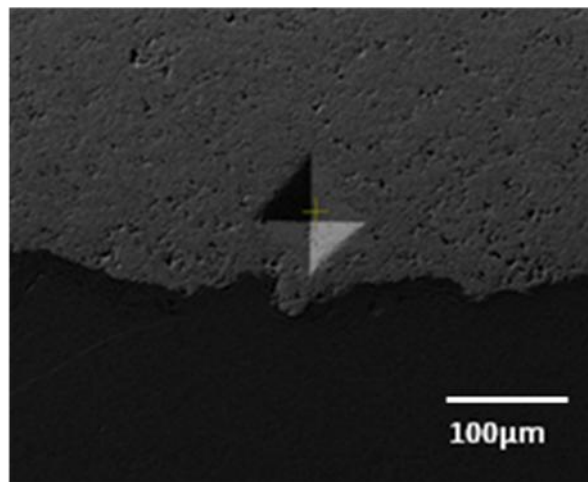


Figure 4.39. SEM-BSE image of a Vickers hardness indentation on the cross-section of WC-17%Co coating on super-invar.

The results of metallographic characterization of the coatings to determine the mean carbide size are shown in Table 4.6. The mean grain sizes were small and generally similar. Table 4.6 shows that porosity of the as-sprayed super-invar was a little higher than the rest of the

samples, which is in agreement with the observations on the microstructures. As-sprayed 304L stainless steel had slightly lower porosity than the other samples.

Table 4.6. Properties of the WC-Co coatings on various substrates.

Substrate	Coating Porosity (%)	WC grain size (μm)	Residual stress (MPa)	Coating HV ₅ (GPa)	Substrate HV ₅ (GPa)
Aluminum	0.618 \pm 0.100	0.94 \pm 0.20	-15.7 \pm 17.0	8.55 \pm 0.01	1.45 \pm 0.01
Brass	0.630 \pm 0.100	1.00 \pm 0.20	36.0 \pm 17.5	6.60 \pm 0.01	1.29 \pm 0.01
304L SS	0.463 \pm 0.200	1.14 \pm 0.20	24.6 \pm 18.6	9.11 \pm 0.01	1.74 \pm 0.02
Super-invar	0.762 \pm 0.200	0.82 \pm 0.20	111.1 \pm 17.3	7.63 \pm 0.01	1.35 \pm 0.01
Mild steel	0.570 \pm 0.100	1.07 \pm 0.02	30.5 \pm 19.1	7.01 \pm 0.01	1.25 \pm 0.01

Figure 4.40 shows comparisons of the starting powder (which was the same for both A and B batches) and diffraction patterns of as-sprayed coatings on the different substrates. The XRD patterns were very similar, indicating that the coatings comprised primarily of WC with only a small signal of Co, suggesting that Co was only slightly crystalline. A small amount of Co₆W₆C was found on the as-sprayed coating on mild steel, despite the same powder being used for the feedstock.

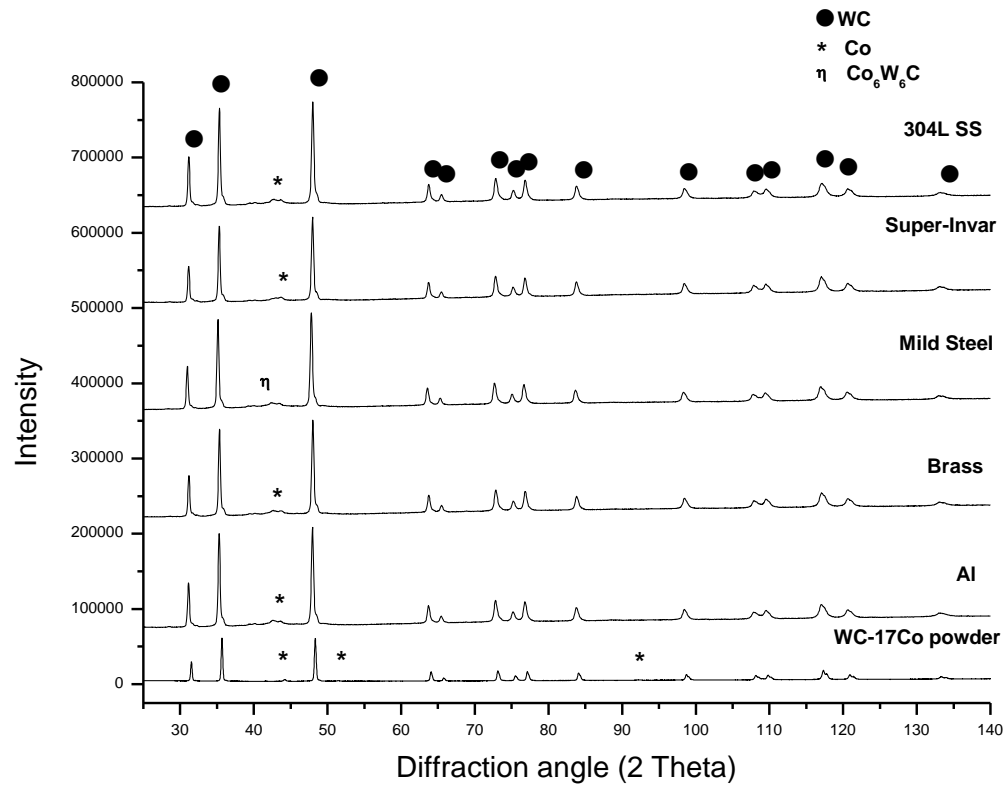


Figure 4.40. XRD patterns of the starting powder and as-sprayed coatings.

The macrohardness values of both substrate and coatings are shown in Table 4.6 and Figure 4.41. The results indicate a higher macrohardness in the coatings compared to the substrates. The value for the as-sprayed coating on 304L stainless steel was slightly higher, followed by coated aluminium substrate. The as-sprayed coating hardnesses were (in decreasing order): 304L stainless steel > aluminium > super-invar > mild steel > brass.

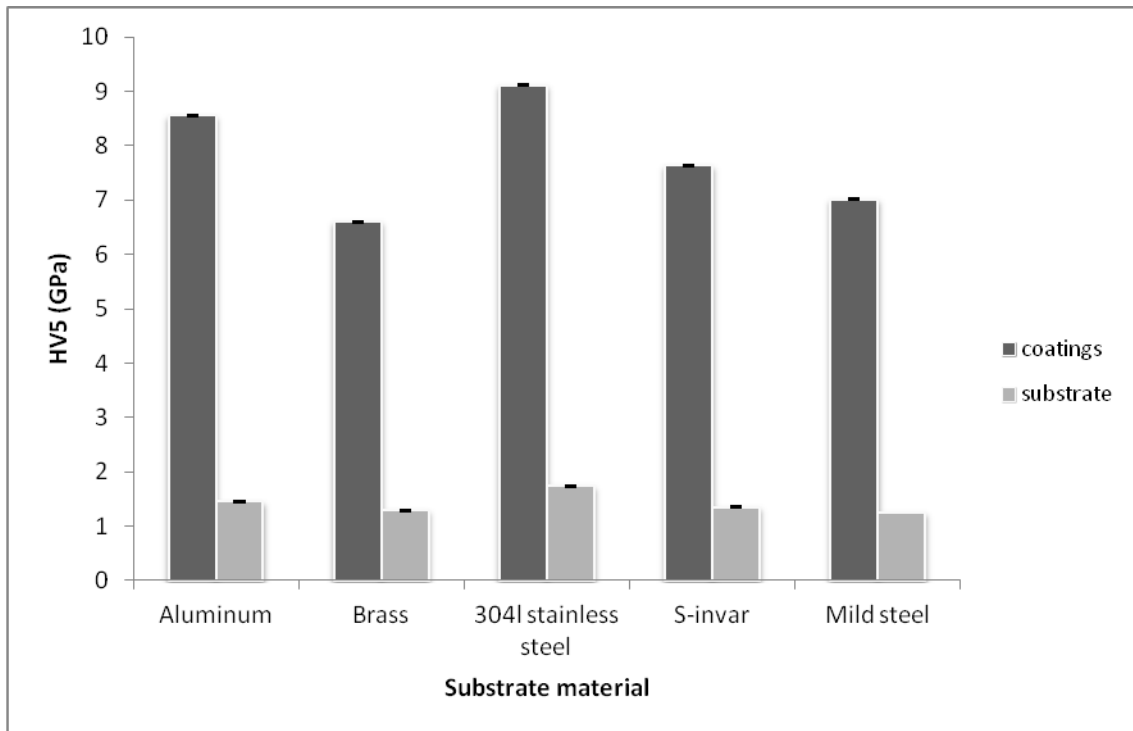


Figure 4.41. Macrohardness values of WC-17Co coatings on the different substrates.

The relationships between coating macrohardness with grain size, porosity and substrate microhardness are shown in Figures 4.42-4.46. The macrohardness showed a slight increase with increasing grain size (Figure 4.42), and decreased with increasing porosity (Figure 4.43). With increasing substrate macrohardness, the coating hardness increased (4.44). The microhardness showed a slight increase with increasing substrate melting point (4.45). With increased coefficient of thermal expansion, the macrohardness increased (Figure 4.46).

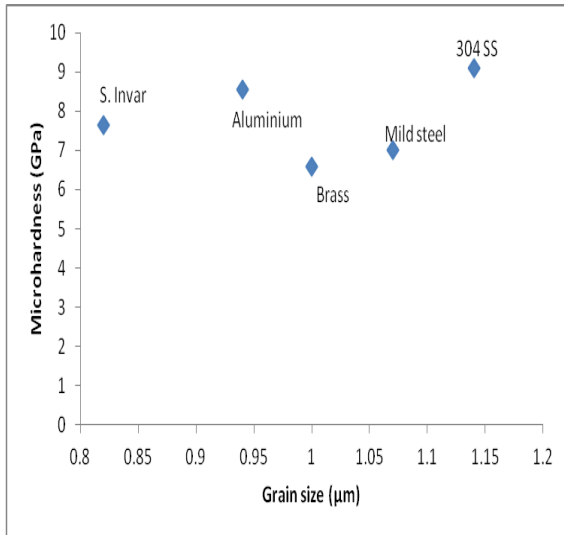


Figure 4.42. Correlation between the grain sizes and microhardness of the WC-17Co coatings on the different substrates, showing slight decreases of hardness but scattered.

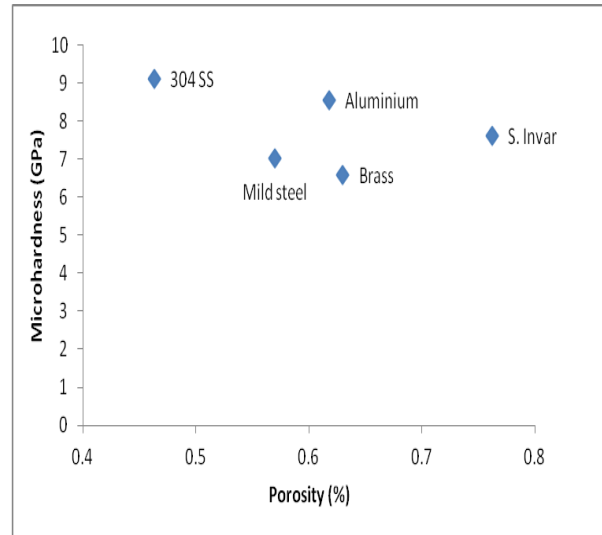


Figure 4.43. Correlation between the porosity and microhardness of the WC-17Co coatings on the different substrates, showing hardness decreased with increasing porosity.

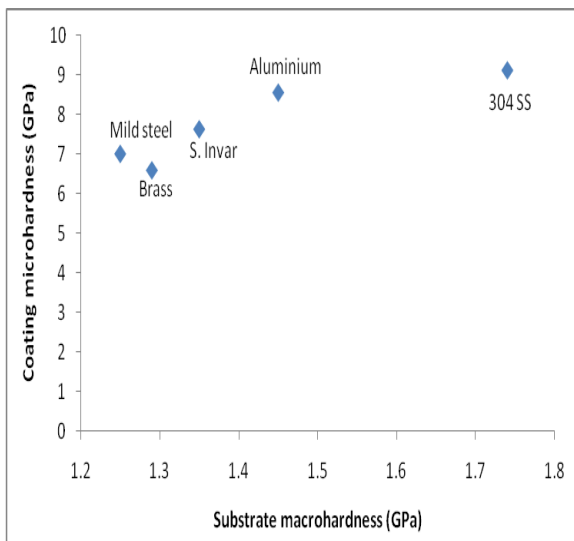


Figure 4.44 Correlation between the substrate and coating microhardness of the WC-17Co coatings on the different substrates, showing increasing coating hardness with substrate hardness.

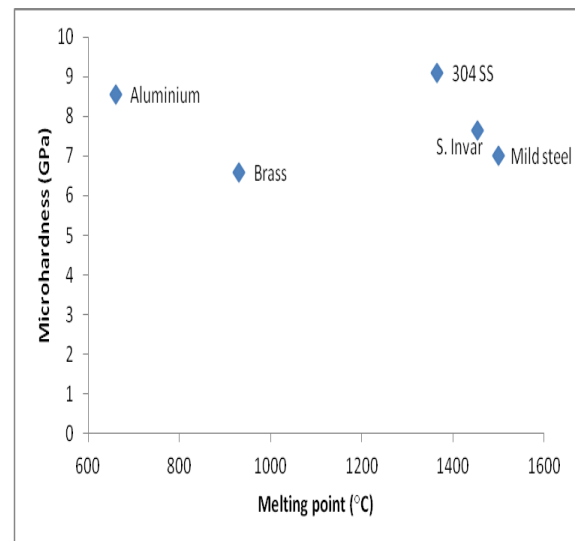


Figure 4.45. Correlation between the substrate melting point and microhardness of the WC-17Co coatings on the different substrates, showing a slight increase.

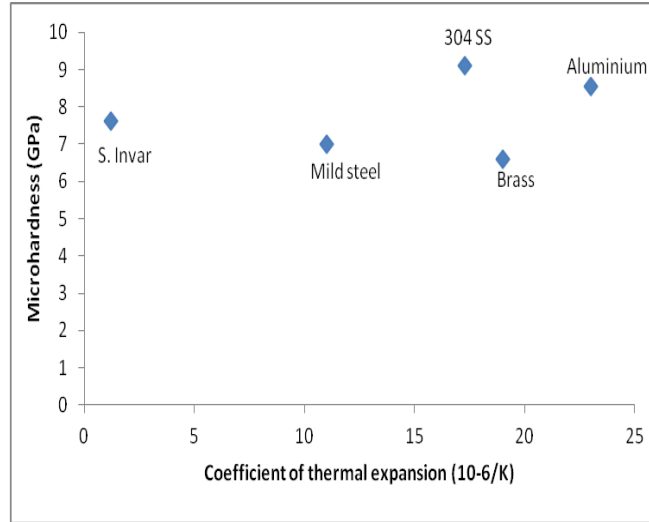


Figure 4.46. Correlation between the substrate coefficient of thermal expansion and microhardness of the WC-17Co coatings on the different substrates, showing a slight increase.

The typical lattice plane spacings, $d\psi$, were calculated and plotted as a function of $\sin^2\psi$, as shown in Figures 4.47–4.51. The total residual stress is obtained from the slope of this plot by applying Equation 2.6. The negative slope observed in Figure 4.47 corresponds to a compressive residual stress in the WC-Co coating. The positive slopes observed in Figures 4.48-4.51 correspond to tensile stresses in the WC-Co coating.

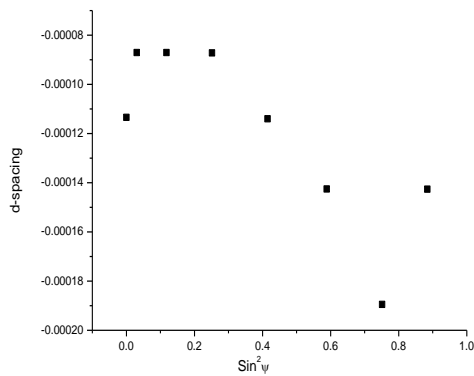


Figure 4.47. Plot of d -spacing versus $\sin^2\psi$ for the as-sprayed WC-17Co coating on aluminum substrate.

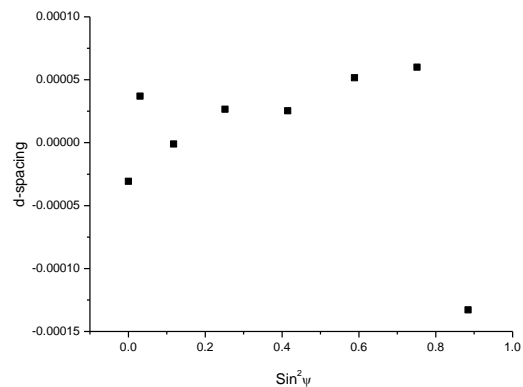


Figure 4.48. Plot of d -spacing versus $\sin^2\psi$ for the as-sprayed WC-17Co coating on brass substrate.

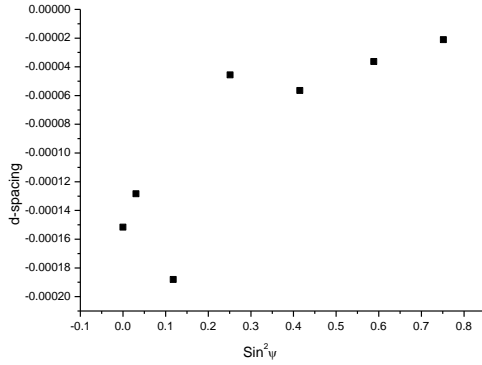


Figure 4.49. Plot of d -spacing versus $\sin^2\psi$ for the as-sprayed WC-17Co coating on mild steel substrate.

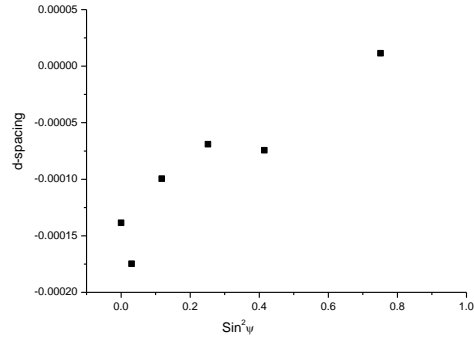


Figure 4. 50. Plot of d -spacing versus $\sin^2\psi$ for the as-sprayed WC-17Co coating on 304L stainless steel

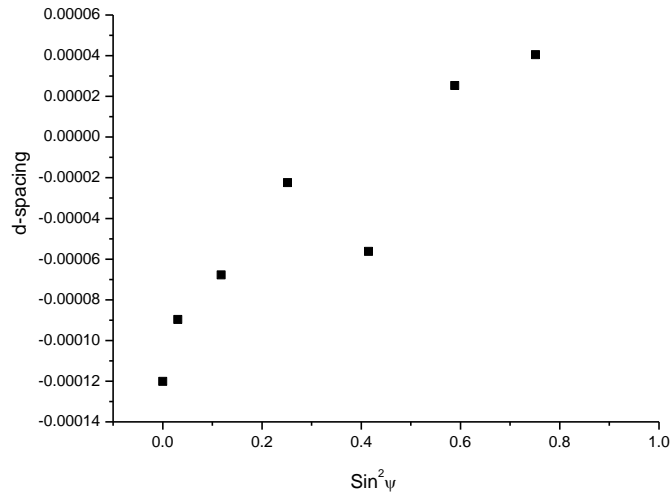


Figure 4.51. Plot of d -spacing versus $\sin^2\psi$ for the as-sprayed WC-17Co coating on super-invar substrate.

The stress values were calculated and reported in Figure 4.52. The residual stresses determined from the $\{112\}_{\text{WC}}$ reflection with the assumption of planar stress conditions are given in Table 4.6 and Figure 4.52. The residual stresses were tensile in the as-sprayed coatings on super-invar, mild steel, 304L stainless steel and brass, whilst they were

compressive on the as-sprayed coating on aluminium. However, all the residual stress values were very low.

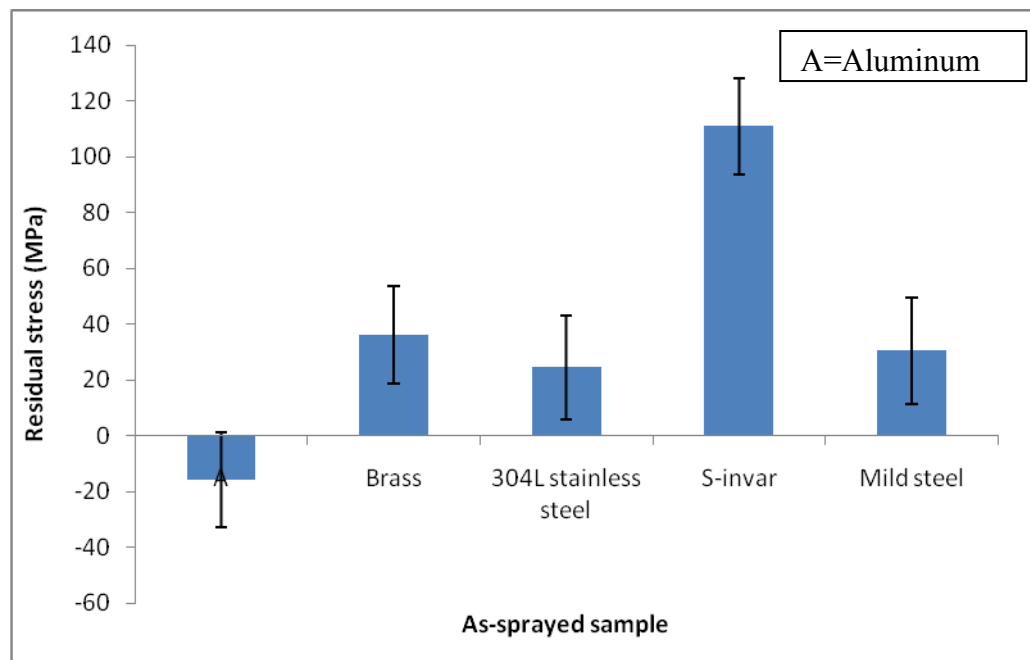


Figure 4.52. Summary of residual stresses determined in for the as-sprayed WC-Co coatings deposited on the different substrates of this study. The results for aluminum is given by the first bar plot that is not labelled.

4.2.2. Systematic investigation of residual strains associated with WC-Co coatings thermal sprayed onto metal substrates

4.2.2.1. Introduction

This part of the study investigates the potential role that differences in the coefficients of thermal expansion (CTE) between different substrates and WC-Co coatings could have, in order to improve the functional properties of the substrate-coating combination. If successful, these coatings could potentially replace bulk sintered carbides in some wear applications. The integrity of these sprayed deposits is strongly influenced by the residual stress profiles in the deposit as well as the substrate. A systematic characterisation of the residual stresses originating from the various process steps involved in the HVOF process were investigated. The study included the parent material (the as-received condition being the reference state) prior to and after the grit-blasted surface roughening preparation, as well as the final as-coated samples. This investigation was primarily on the influences of the substrate materials, supplemented by results of the coatings where possible.

4.2.2.2. Results

The coating characterization of the as-sprayed starting powder and as-sprayed coating on brass, super invar and 304L stainless steel has been discussed in Section 4.2. The depth resolved residual strain results for the brass samples are shown in Figures.4.53 and 4.54 respectively for the synchrotron and neutron investigations, and correspondingly for the invar samples in Figures.4.55 and 4.56. The depth resolved residual strain results for the 304L stainless steel sample are shown in Figure 4.57 for the synchrotron only. The neutron measurement for 304L stainless steel was not investigated as we did not have beam time. Also, because its duplex phase makes stress investigations more difficult to measure. Since the neutron diffraction and X-ray diffraction analyses were possible subsequently, all data processing was done on the same Bragg peaks (Table 3.7), for the synchrotron investigation throughout to enable direct comparison of results irrespective of the technique used.

Data were taken at all measurement positions with fully submerged gauge volumes where the sample surface positions were determined from entry or wall scans. No surface aberration effects were observed in the data included in the analyses. Results are for the parent material (left hand), the grit blast substrate (centre) and HVOF as-coated sample (right hand). The

substrate coating interface is at 0 mm. The graphs on the lower line in Figures 4.53 to 4.57 show an enlarged view of the results near surface region. The error bars indicate the systematic error associated with the measurements with the lines through the symbols serving as guides to the eye.

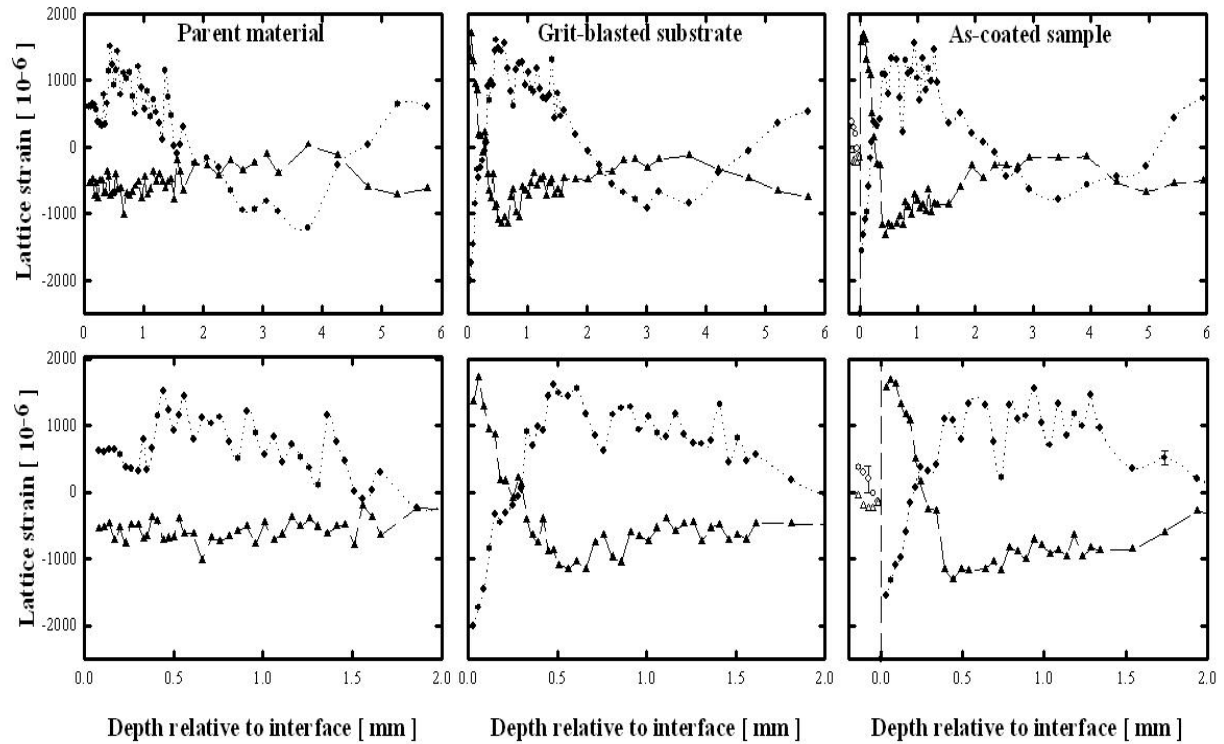


Figure 4.53. Residual strain depth dependence determined from the lattice plane spacing of the $\{311\}_{\text{Cu}}$ and $\{101\}_{\text{WC}}$ Bragg peaks measured with synchrotron X-ray diffraction on the thinned wedge brass sample. The bottom figures show an enlarged view of the results at the near surface region. Legend: \bullet = substrate in-plane component; \blacktriangle = substrate normal component; \circ = WC in-plane component; Δ = WC normal component.

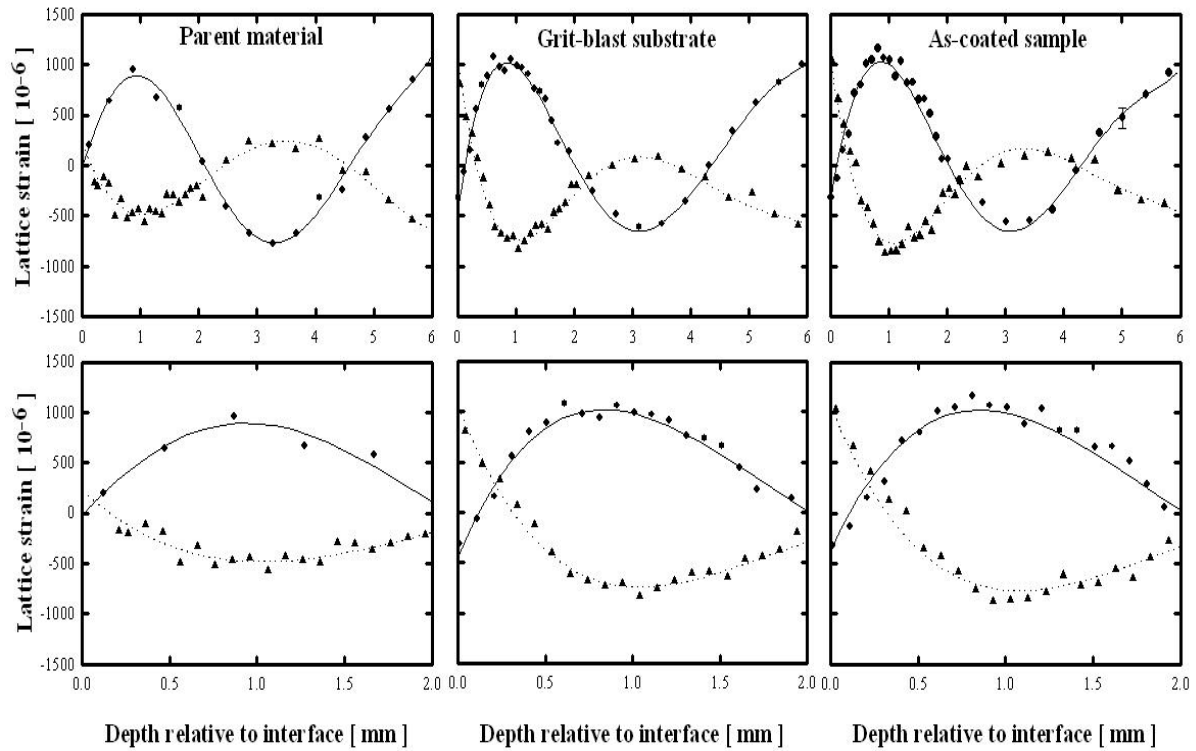


Figure 4.54. Residual strain depth dependence determined from the lattice plane spacing of the $\{311\}_{\text{Cu}}$ Bragg peak measured with neutron diffraction on brass sample. The bottom figures show an enlarged view of the results at the near surface region. The lines through the symbols represent polynomial curve fits to enable stress calculations at corresponding depth values. Legend: ● = substrate in-plane component; ▲ = substrate normal component.

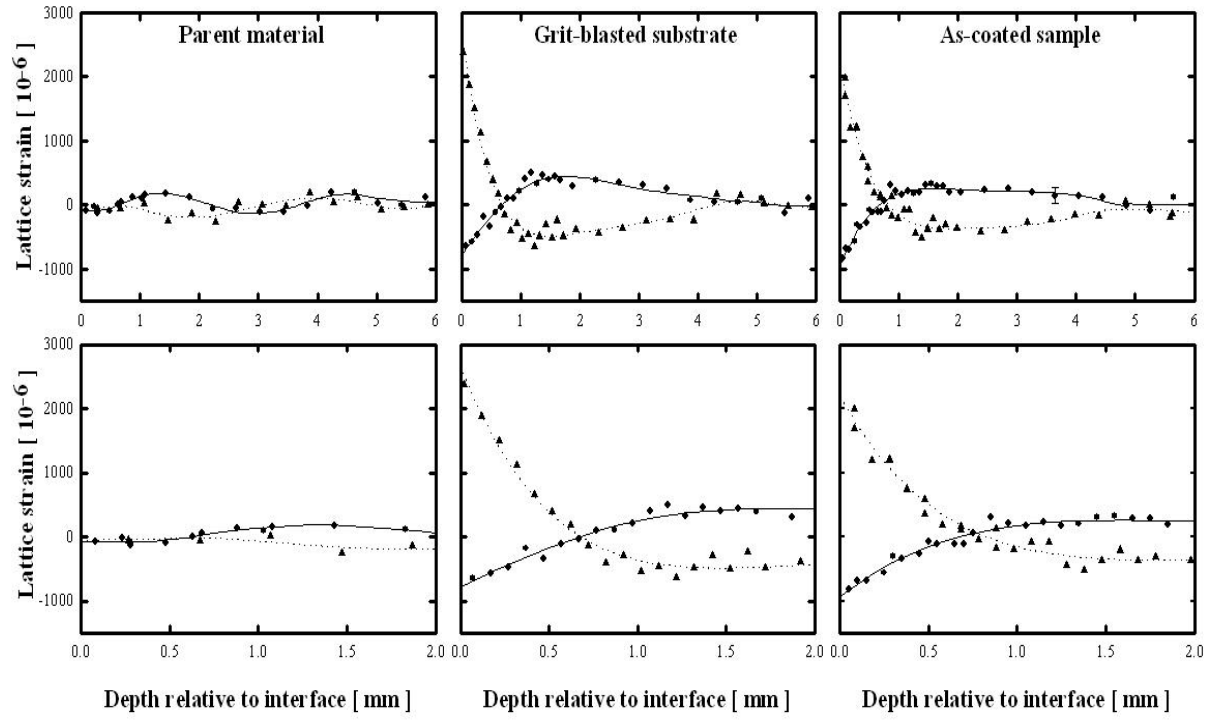


Figure 4.55. Residual strain depth dependence determined from the lattice plane spacing of the $\{200\}_{\text{Ni}}$ and $\{101\}_{\text{WC}}$ Bragg peaks measured with synchrotron X-ray diffraction on the thinned wedge invar sample. The bottom figures show an enlarged view of the results at near surface region. Legend: ● = substrate in-plane component; ▲ = substrate normal component; ○ = WC in-plane component; △ = WC normal component.

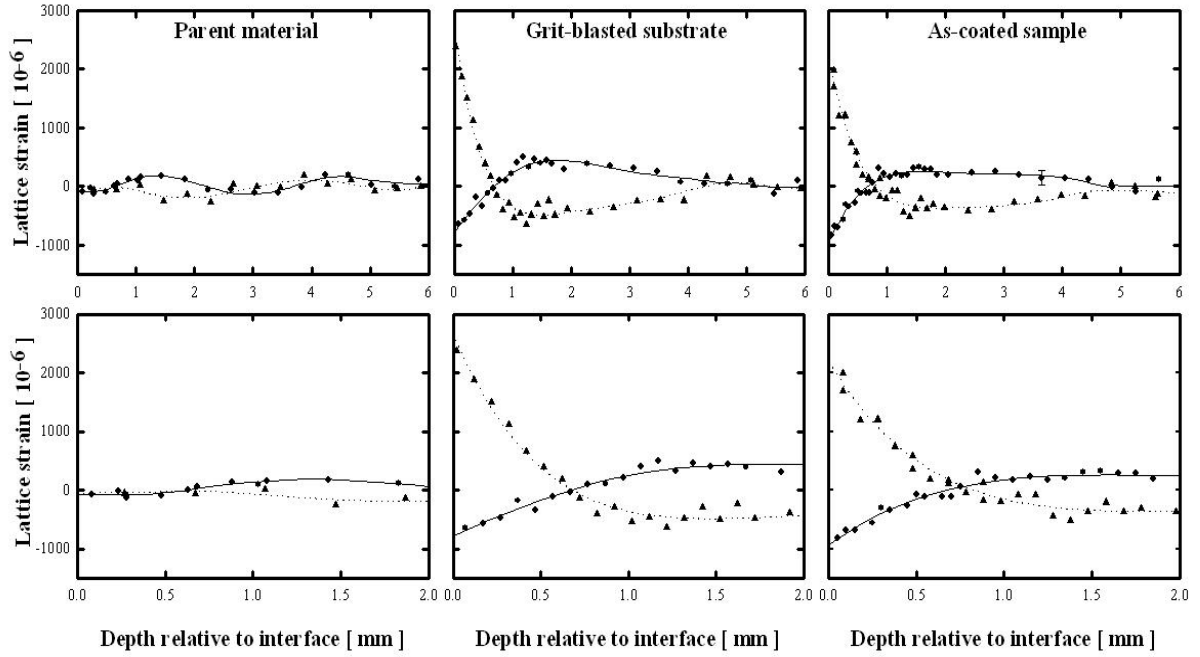


Figure 4.56. Residual strain depth dependence determined from the $\{200\}_{\text{Ni}}$ Bragg peak measured with neutron diffraction on invar sample. The bottom figures show an enlarged view of the results at the near surface region. The lines through the symbols represent polynomial curve fits to enable stress calculations at corresponding depth values. Legend: \bullet = substrate in-plane component; \blacktriangle = substrate normal component.

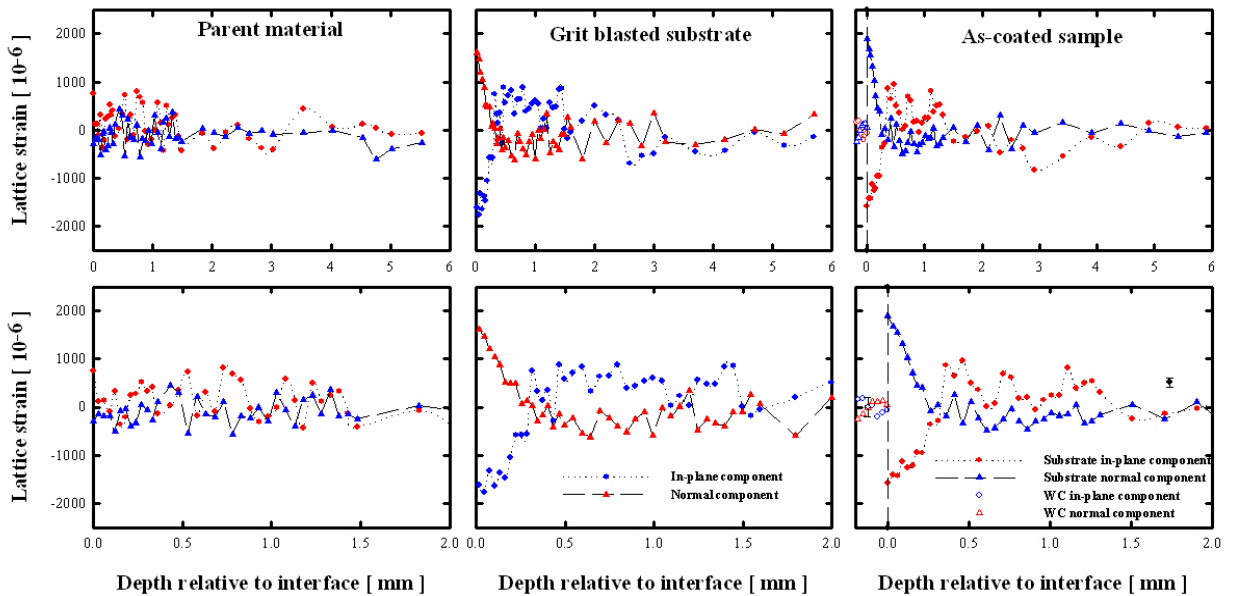


Figure 4.57. Residual strain depth dependence determined from the $\{311\}_{\text{Fe-}\gamma}$ reflection in the 304L stainless steel substrate and $\{101\}_{\text{WC}}$ Bragg peaks measured with synchrotron X-ray diffraction. The bottom set of figures show an enlarged view of the results at the near surface regions. Legend: \bullet = substrate in-plane component; \blacktriangle = substrate normal component; \circ = WC in-plane component; Δ = WC normal component.

The in-plane residual stresses measured in the samples using biaxial stress assumption are displayed in Figures 4.58–4.62. Since the synchrotron investigations were taken simultaneously with the same sample setup, direct conversion of the strains to stresses for each depth position could be done from the in-plane and normal components of strains. The neutron diffraction measurements necessitated different reorientations of the samples, and were measurements not taken at coincident depth positions. To enable stress determinations, 6th order polynomial curves were used, which rendered good fits to the strain (lattice parameter) profiles as shown in Figures 4.56 and 4.58 respectively. Stresses were then determined from the fitted curves, rendering the smooth curves shown in Figures 4.59 and 4.61.

A bi-axial stress condition, discussed in Section 2.7.8, was used to determine the lattice parameter. The elastic constants used in the determination of the stress values are shown in Table 3.7. Results are for the parent material (left set), the grit blast substrate (centre set) and HVOF as-coated sample (right set). The substrate coating interface was set at 0 mm. The bottom figures show an enlarged view of the results at the near surface region. The error bars indicate the systematic error associated with the measurements. The lines through the symbols are guides to the eye.

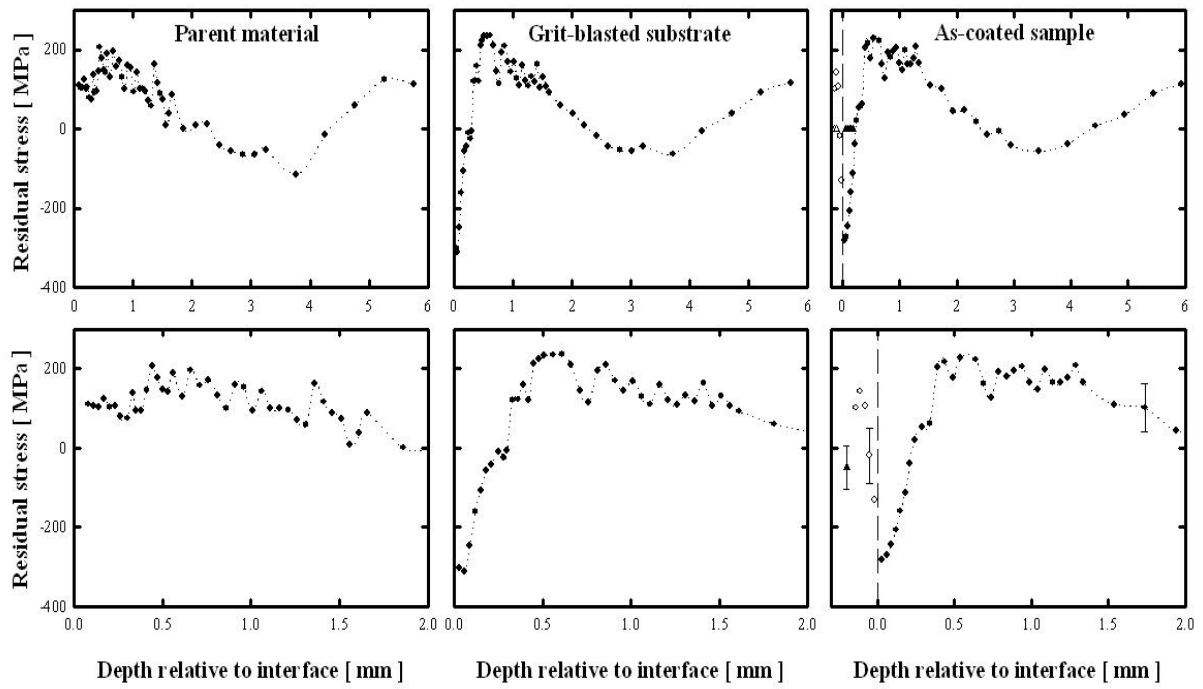


Figure 4.58. In-plane residual stress depth dependence determined from the lattice strain results of the $\{311\}_{\text{Cu}}$ and $\{101\}_{\text{WC}}$ Bragg peaks measured with synchrotron X-ray diffraction on the thinned wedge brass sample. The near surface residual stress of the WC determined with laboratory X-rays (Co radiation) is also indicated [2012Ola]. Legend: ● = substrate in-plane stress; ○ = WC in-plane stress; ▲ = WC near surface stress (laboratory X-rays).

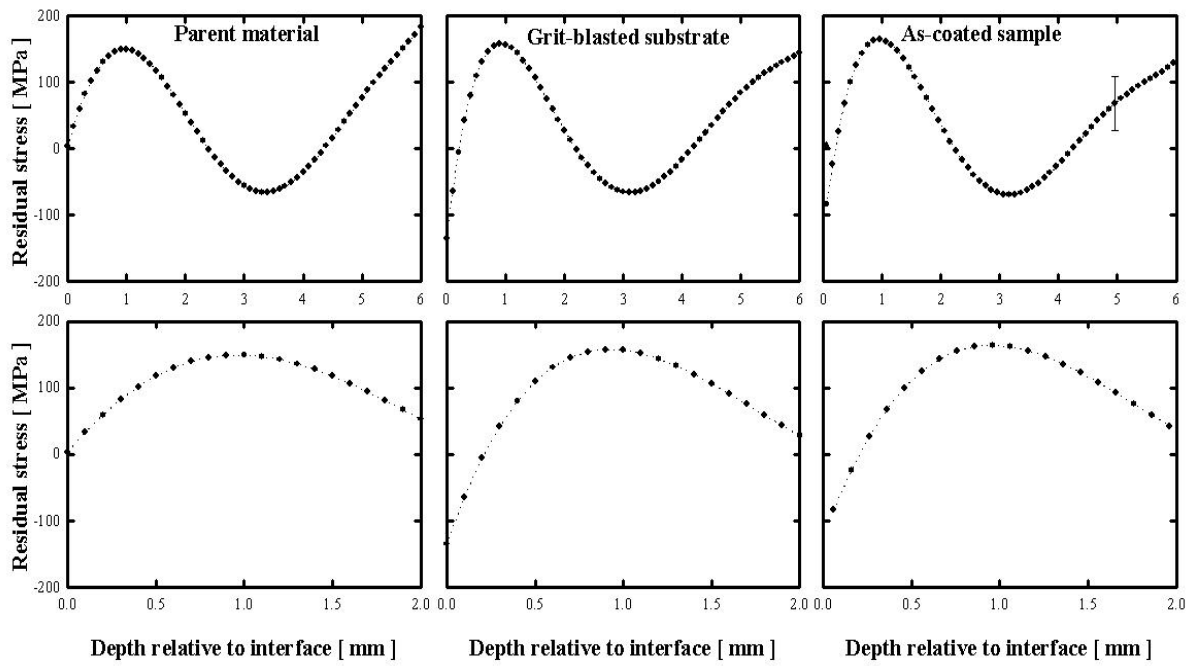


Figure 4.59. In-plane residual stress depth dependence determined from the fitted lattice strain results of the $\{311\}_{\text{Cu}}$ Bragg peak measured with neutron diffraction on the 25 x 25 mm² brass sample.

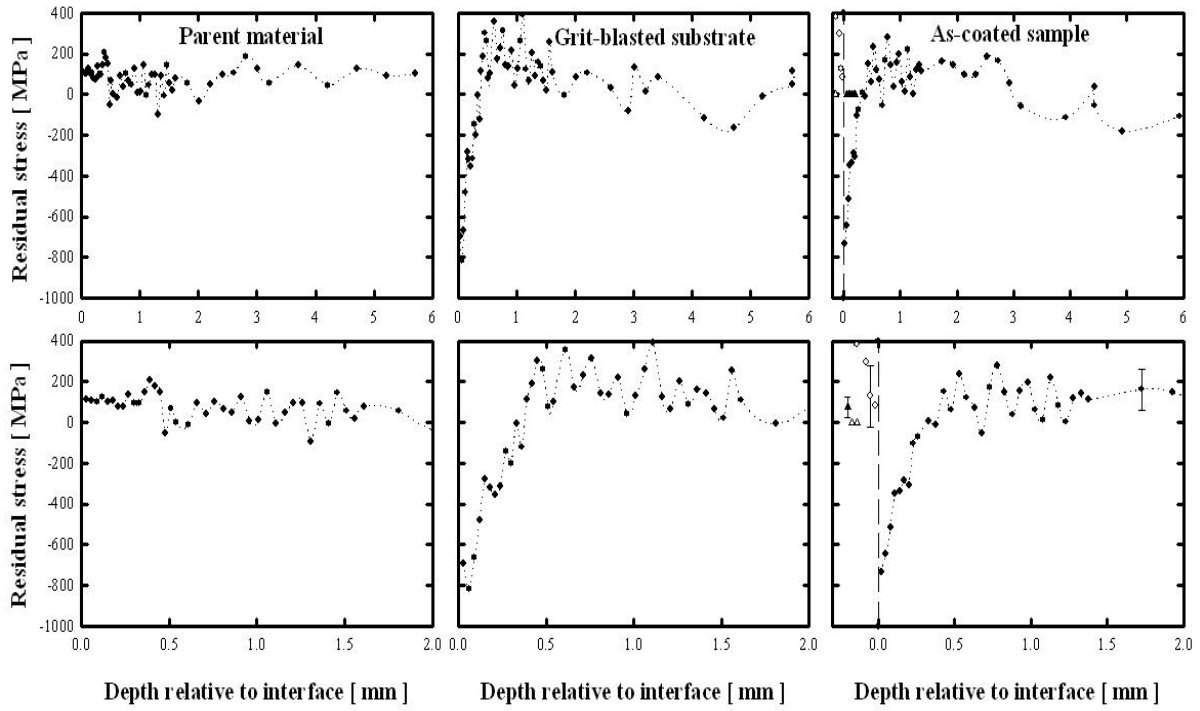


Figure 4.60. In-plane residual stress depth dependence determined from the lattice strain results of the $\{200\}_{\text{Ni}}$ and $\{101\}_{\text{WC}}$ Bragg peaks measured with synchrotron X-ray diffraction on the thinned wedge invar sample. The near surface residual stress of the WC determined with laboratory X-rays (Co radiation) is also indicated [2012Ola]. Legend: ● = substrate in-plane stress; ○ = WC in-plane stress; ▲ = WC near surface stress (laboratory X-rays).

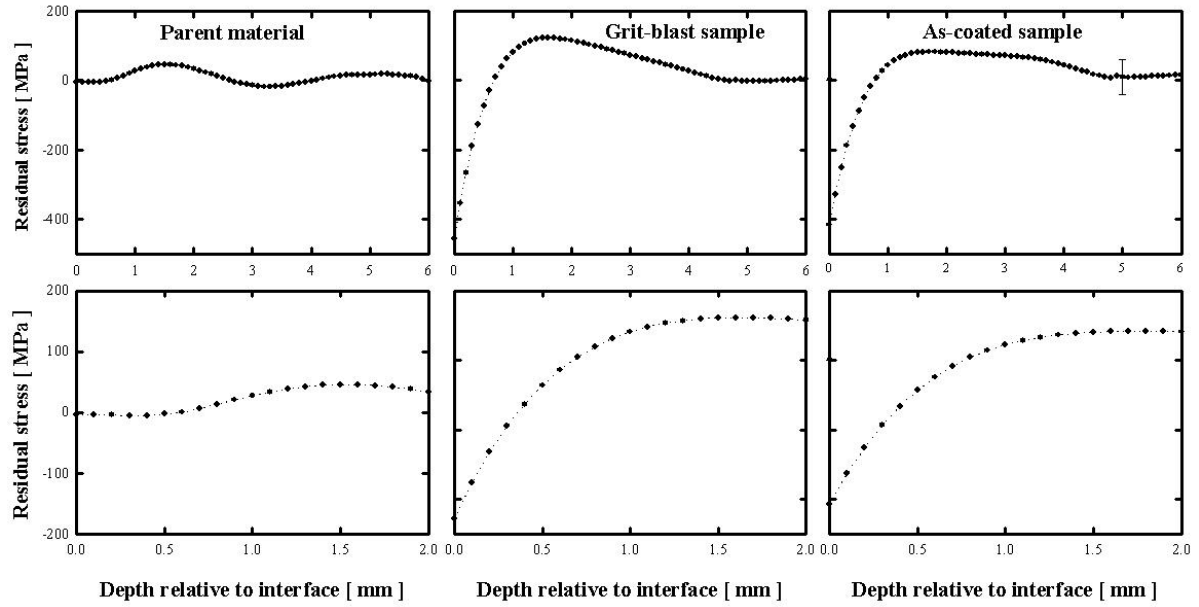


Figure 4.61. In-plane residual stress depth dependence determined from the fitted lattice strain results of the $\{200\}_{\text{Ni}}$ Bragg peak measured with neutron diffraction on the 25 x 25 mm² super invar sample.

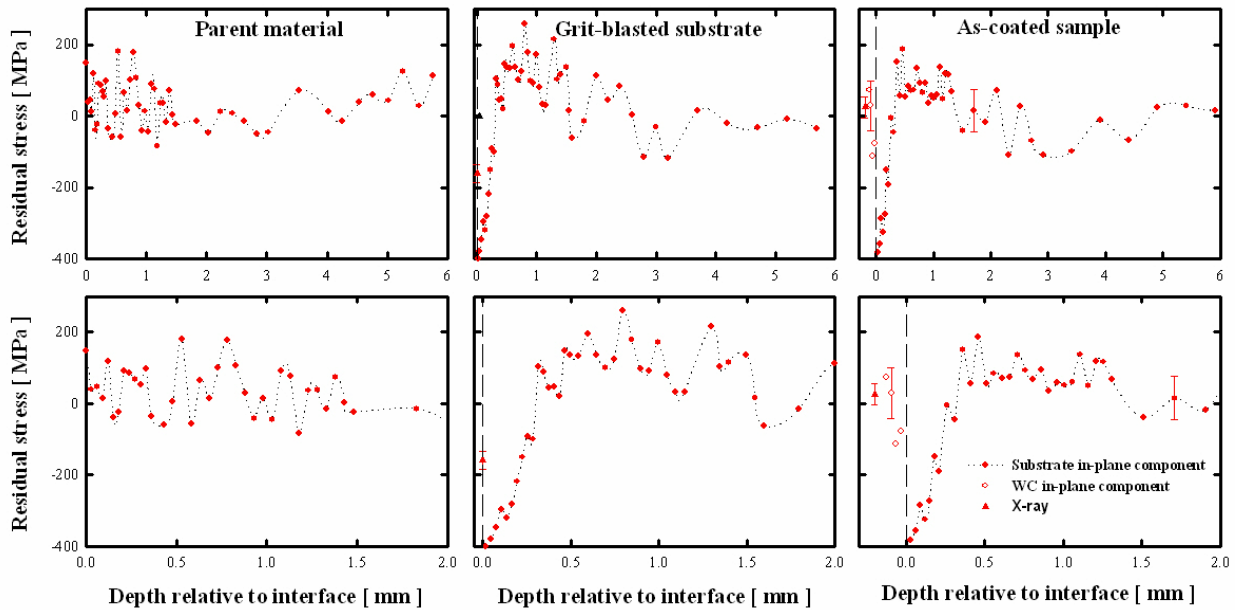


Figure 4.62. In-plane residual stress depth dependence determined from the lattice strain results of the $\{311\}_{\text{Fe-}\gamma}$ and $\{101\}_{\text{WC}}$ Bragg peaks measured with synchrotron X-ray diffraction. The near surface residual stress of the WC determined with laboratory X-rays (Co radiation) is also indicated [2012Ola]. The substrate coating interface was set at 0 mm.

Legend: ● = substrate in-plane stress; ○ = WC in-plane stress; ▲ = WC near surface stress (laboratory X-rays).

To quantify the different contributions associated with the two dominant processing steps, the plastic depth strain profiles (eigenstrains) were considered in Figures 4.63-4.65 for the respective grit-blasted substrates. The eigenstrain approach is a sensitive parameter, since the strain profiles in the samples contain both the elastic strains constrained by the plastic deformation, especially near the grit-blast and coated surfaces. Inherent to the systematic approach, the eigenstrain for each process contribution could be individually determined by subtracting the measured through-thickness residual elastic strain profiles in the as-received parent material from each of these samples. The curve (Figures 4.63-4.65) show the plastic strain (eigenstrain) profiles associated with the different processing steps for the samples. The profile shows similar trend for both grit-blast and as-coated sample on both techniques (neutrons and synchrotron X-ray diffraction).

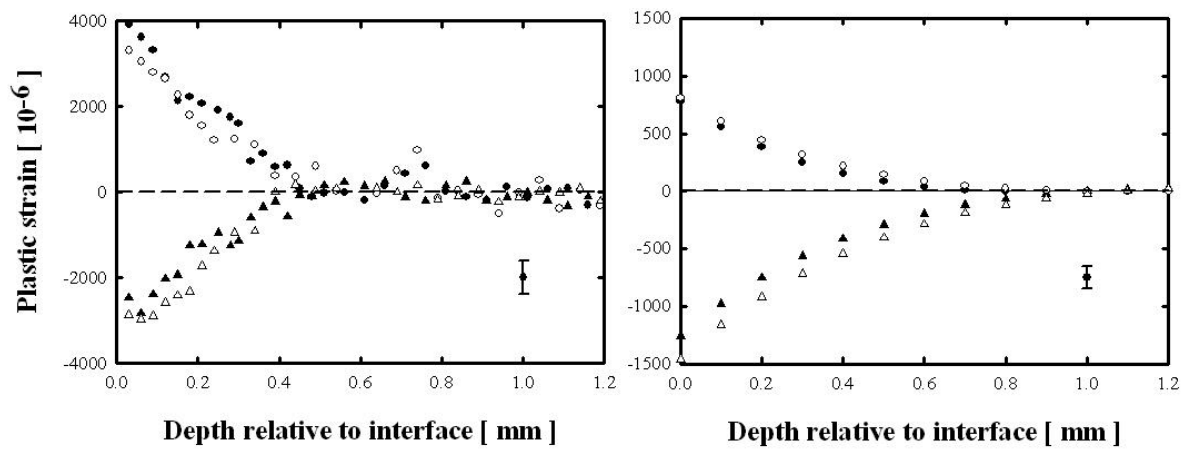


Figure 4.63. Plastic strain profiles (eigenstrains) for brass determined from strain results of X-ray synchrotron (left) and neutron diffraction (right). Legend: ● = grit blast in-plane component; ▲ = grit blast normal component; ○ = as-coated in-plane component; △ = as-coated normal component.

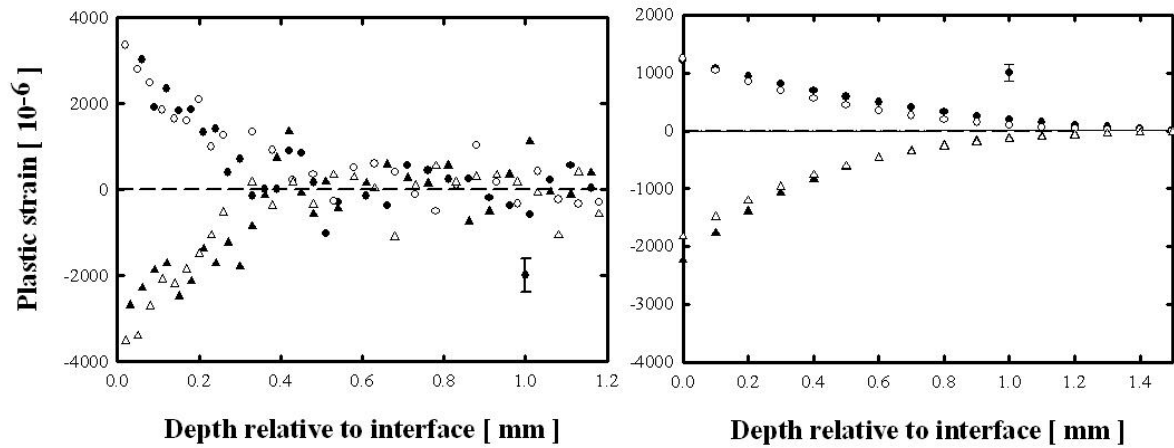


Figure 4.64. Plastic strain profiles (eigenstrains) for super invar determined from strain results of X-ray synchrotron (left) and neutron diffraction (right). Legend: ● = grit blast in-plane component; ▲ = grit blast normal component; ○ = as-coated in-plane component; Δ = as-coated normal component.

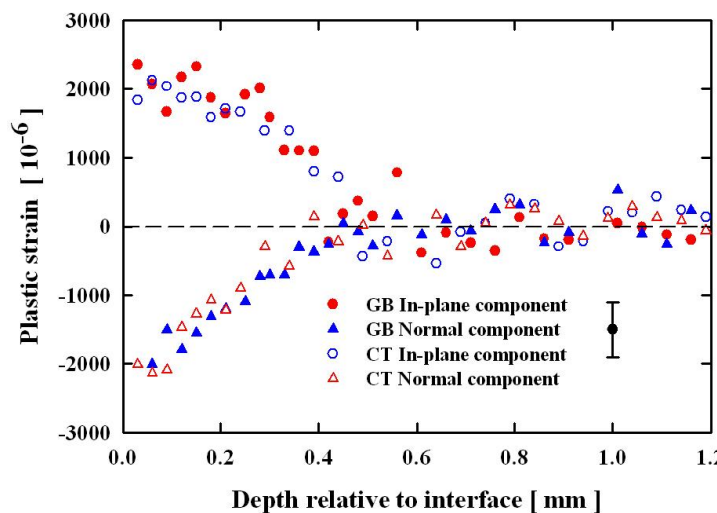


Figure 4.65. Plastic strain profiles (eigenstrains) for 304L stainless steel determined from strain results of X-ray synchrotron investigations. Legend: ● = grit blast in-plane component; ▲ = grit blast normal component; ○ = as-coated in-plane component; Δ = as-coated normal component.

Table 4.7 summarises the residual stress results for all the samples of this study determined from X-ray diffraction (Table 4.6) and synchrotron XRD. The characteristic of the residual stresses are similar. The difference in the respective values is ascribed to the respective probing depths. The synchrotron results shown are the average values determined for the WC

coating thickness. The X-ray method was limited for the measurement of residual stresses on the surface of materials (limited to 2 microns penetration in WC), whilst high energy synchrotron X-rays (100 keV enabled at least 2.5mm penetration), with a good gauge volume definition to enable depth resolved information. The gauge volume is a trade-off between the spatial resolution requirement within the expected strain field and the time available for data collection [2012Ros].

Table 4.7. Summary of materials and residual stress values determined in the substrates and HVOF coatings.

Material	CTE ($10^{-6}/\text{K}$)	Reflection	DEC (TPa^{-1})		Residual stress in grit-blast substrates (MPa)		Residual stress in as-coated coatings (MPa)	
			S_1	$\frac{1}{2}S_2$	XRD	SR	XRD	SR
WC WC-17Co	5.2	$\{101\}_{\text{WC}}$	-0.321	1.707	----	----	----	----
Aluminium	23	$\{311\}_{\text{Al}}$	-5.05	19.462	-160 ± 10	-200 ± 25	-15.7 ± 17	-160 ± 50
Brass	19	$\{311\}_{\text{Cu}}$	-2.902	11.106	-123 ± 10	-303 ± 25	-53.5 ± 28	-40 ± 25
304LStainless steel	17	$\{311\}_{\text{Fe-}\gamma}$	-1.598	7.034	-159 ± 36	-458 ± 25	24.6 ± 19	22 ± 50
Super invar	≤ 1	$\{200\}_{\text{Ni}}$	-1.910	7.539	-251 ± 10	-695 ± 25	74 ± 31	288 ± 25

4.2.3. Residual stress in thin WC-Co coated systems studied by high-precision neutron diffraction

4.2.3.1 Introduction

The aim of this part of the study was to systematically derive the residual stress conditions in a system of thin WC-Co coatings on mild steel substrates where the two coefficients of thermal expansion were different. The neutron strain scanning investigations were done on the KOWARI neutron strain scanner, using a sub millimeter sized gauge volume and paying special attention to gauge volume localisation accuracy and treatment of edge effects. Investigations were extended to the annealed counterpart samples to examine experimentally whether heat-treatment is beneficial for stress relaxation/alteration procedure.

4.2.3.2. Results

Typical stress profiles measured in the as-prepared grit-blasted, as-sprayed coatings and its stress-relieved annealed counterpart are shown in Figures 4.66-4.69. The residual stresses in the WC phase coating (Table 4.8) determined under the different conditions were compressive, but quite different, for the as-sprayed and heat-treated coated samples. However, low tensile stresses were found on the as-sprayed mild steel sample. The results show that within the grit-blasted and as-coated sample, the predominant contribution of the shot blast surface roughening treatment was clearly evident at the coated near-surface position (surface at 0 mm). After annealing, the residual stress due to the cold-work action had been completely relaxed. Differences in the gradients of the two curves would be ascribed to the influence of the thermal interaction associated with the differences in coefficient of thermal expansion (CTE) between the coating and the substrate.

Table 4.8. Comparison of residual stresses in WC coatings determined under different thermal conditions (experimentally measured directly and predicted from stress balance using the measured through thickness stress profiles in the substrates).

Substrate	Condition	Experimental stress (MPa)	Predicted stress, (MPa)	Average stress (MPa)
Steel	as-sprayed	28 ± 334	-36 ± 118	-34 ± 118
Steel	Annealed	-490 ± 407	-340 ± 80	-341 ± 29
Brass	as-sprayed	-44 ± 107	-47 ± 48	-46 ± 48
Brass	Annealed	-367 ± 86	-339 ± 27	-340 ± 26
Invar	as-sprayed	N/A	N/A	N/A
Invar	Annealed	N/A	-61 ± 22	N/A
Aluminium	as-sprayed	-600 ± 100	-378 ± 50	-379 ± 50
Aluminium	Annealed	-880 ± 100	-814 ± 50	-815 ± 50

Figure 4.66 show the residual stress of as-sprayed and heat treated coatings on mild steel. The compressive stress induced by the grit-blasting was clearly seen at the near surface region, while in the heat treated sample, this feature was eliminated, i.e. stress relieved.

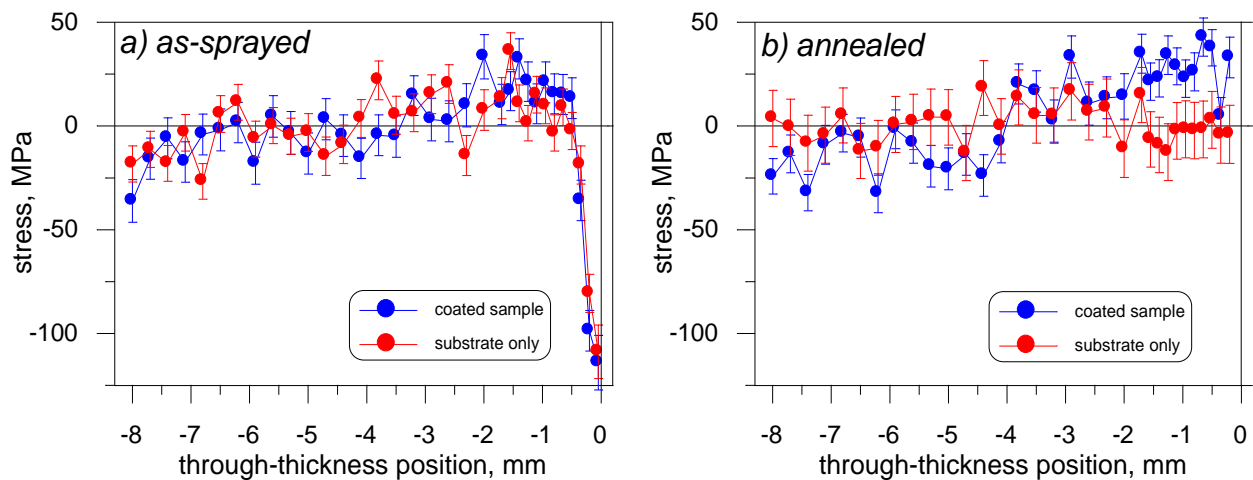


Figure 4.66. Experimentally measured through-thickness stress profiles for steel samples in: a) as-sprayed and b) annealed conditions at 700°C, also with the profiles measured on the substrates only.

The actual residual stresses present in the as-sprayed WC coating on the mild steel was determined by the precise point-by-point subtraction of the stress in the “substrate alone” grit-blasted sample from the stress profile “coating substrate” system shown in Figure 4.67. Stress results of the as-sprayed condition were tensile, while larger compressive stresses were

established in the WC coating after heat treatment, because the thermal strains are greater for heat-treatment than the as-sprayed condition.

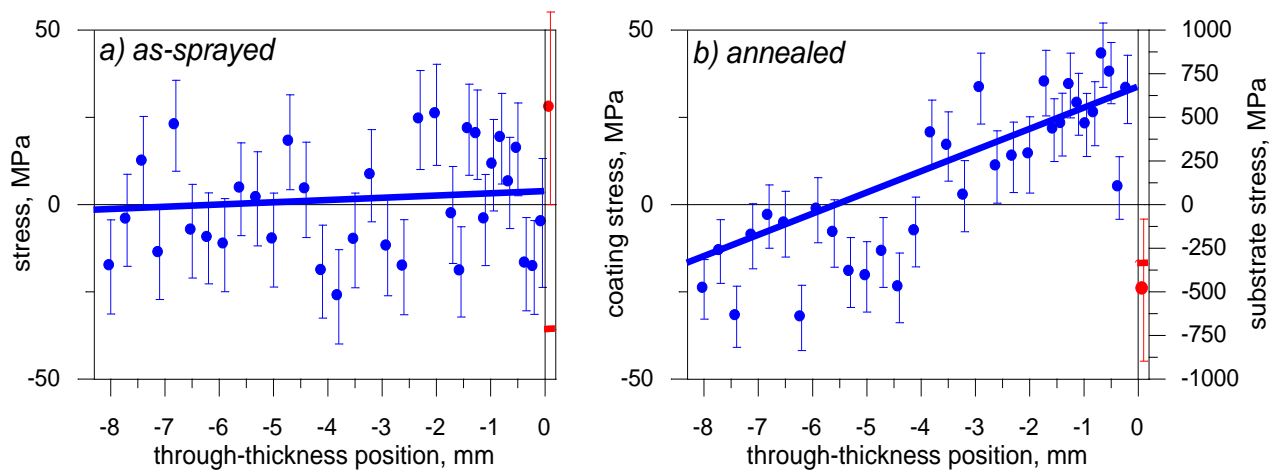


Figure 4.67. Experimentally determined through-thickness stress profiles for mild steel samples in: a) as-sprayed and b) annealed conditions and model fit of the experimental data.

The typical depth resolved in-plane stress in the as-sprayed and heat treated samples are shown in Figure 4.68 for the grit-blasted aluminium substrate. The compressive stress induced by the grit-blasting was clearly seen at the near surface region, while it eliminated, by stress relieving, in the heat treated sample.

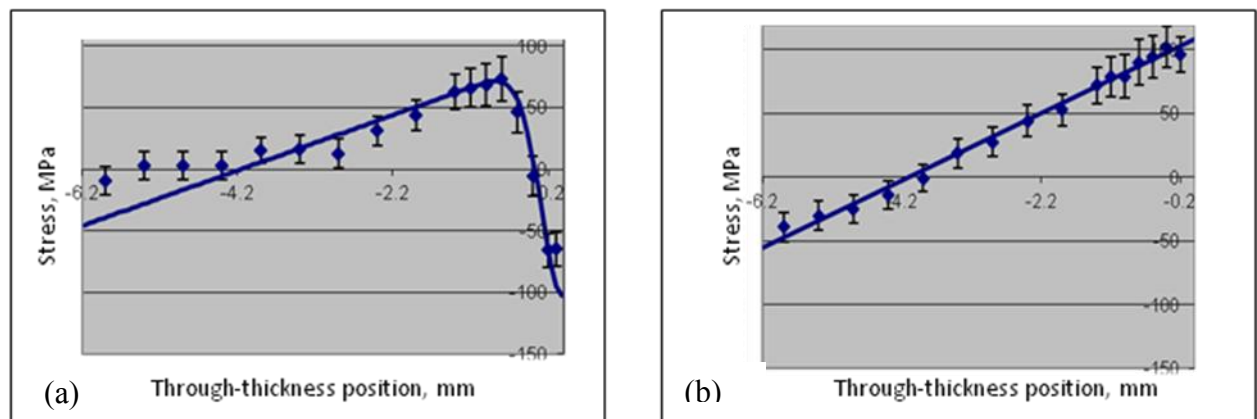


Figure 4.68. Measured in-plane residual stresses (MPa) in the aluminium substrates: (a) Grit-blast only sample preparation stage; (b) Grit-blast sample, annealed at 375°C.

Figure 4.69 shows the through-thickness stress profile measured on the WC-coated aluminium sample. Compressive stresses were found in the as-sprayed condition, whilst larger compressive stresses were found in the WC coating after heat treatment.

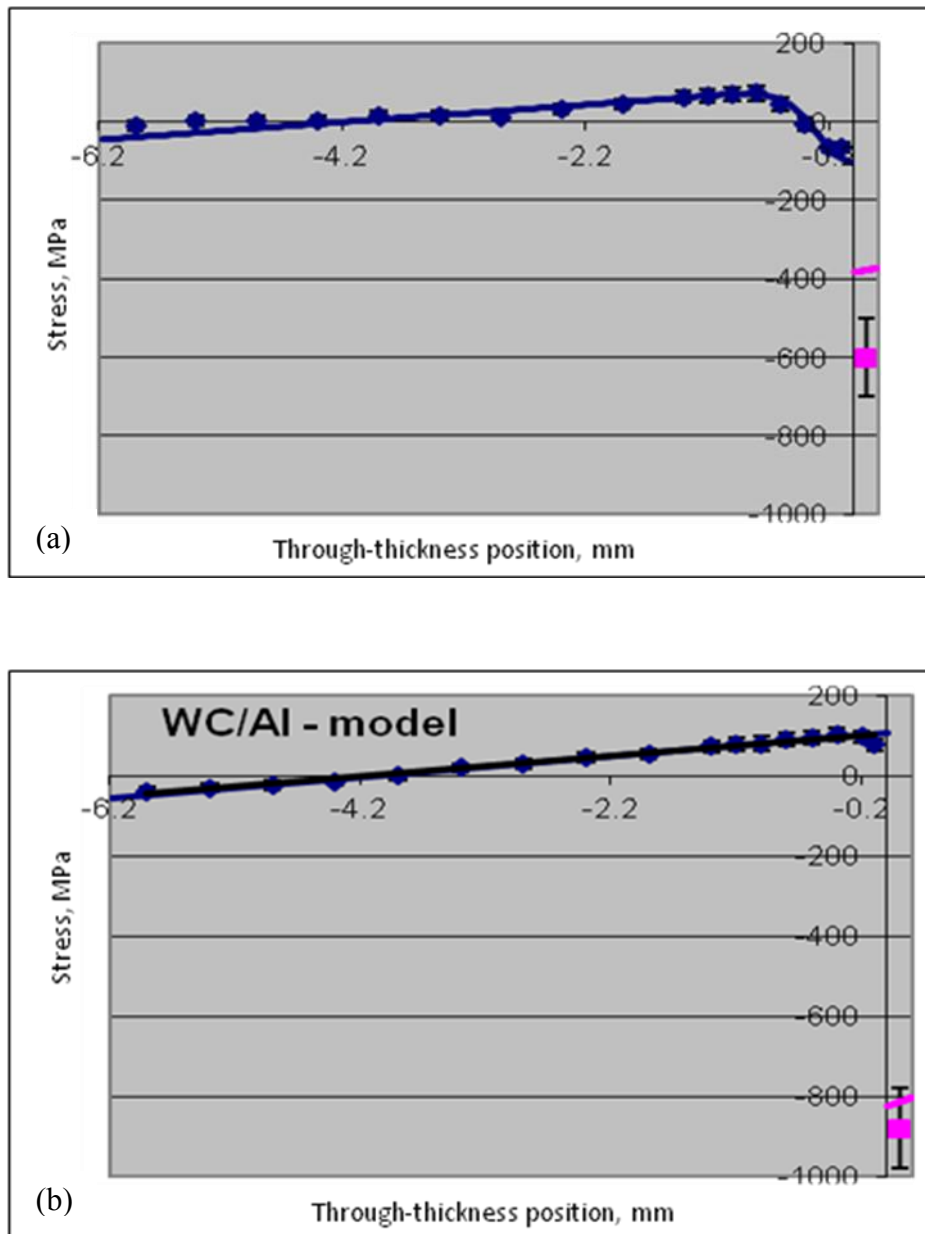


Figure 4.69. Measured in-plane residual stresses (MPa) in WC-coated aluminium samples: (a) As-coated condition; (b) Annealed at 375°C.

In Figure 4.70, the coating stress values are expressed in terms of strain, so that strain can be correlated with thermal mismatch originating from the differences of the thermal expansion of the coating and substrate. The coating strains were all negative, and some of the errors were very large due to time frame used for the measurement.

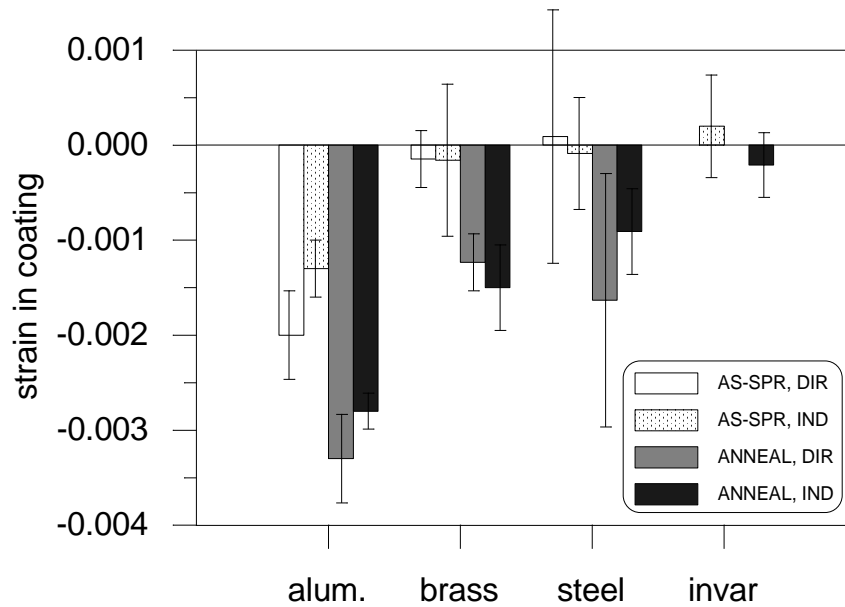


Figure 4.70. Strains in coated samples of different substrate materials.

4.2.4. Effect of heat treatment on the abrasive wear of samples with thermally sprayed WC-Co coatings

4.2.4.1. Introduction

The results reported on here are for the Batch B samples. The aim of this investigation was to compare the abrasive wear resistance of as-sprayed HVOF to heat treated HVOF WC-17wt% Co coatings on different substrates.

4.2.4.2. Results

The optical micrographs of the heat-treated coatings cross-sections are presented in Figures. 4.71-4.73. The microstructure of all the coatings was similar and typical for spray coatings. The microstructure of the heat-treated coating on the brass substrate shown in Figure 4.71 showed no gap between the coating and an irregular interface, with a good fit between coating and the irregular surface of the substrate. No peeling was observed at the interface between the coating and the substrate. The porosity of these coatings was very low, and no unmelted particles were observed.

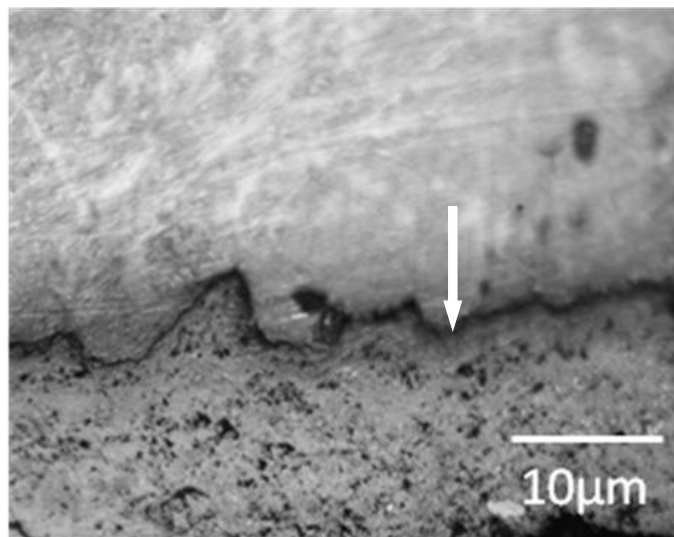


Figure 4.71. Optical micrograph of cross-section of the annealed WC-17wt% Co coating (bottom) on brass, showing the no gap between the coating and irregular surface (shown by arrow).

For the heat-treated coating on the mild steel substrate shown in Figure 4.72, the main features were holes, microcracks and a good fit between the coating and the irregular surface.

The black region in the coating-substrate interface is the alumina used for the grit-blasting, which was also found by Machio [2005Mac]. Long cracks were seen in the coating, roughly parallel to the coating-substrate interface. These cracks caused the relaxation in residual stress after heat treatment, although they did not weaken the bonding between coating and substrate because they are perpendicular to the coating thickness. In-addition, the coating thicknesses were very even. No peeling was observed at the interface between the coating and the substrate. The porosity of these coatings was very low, and no unmelted particles were observed.

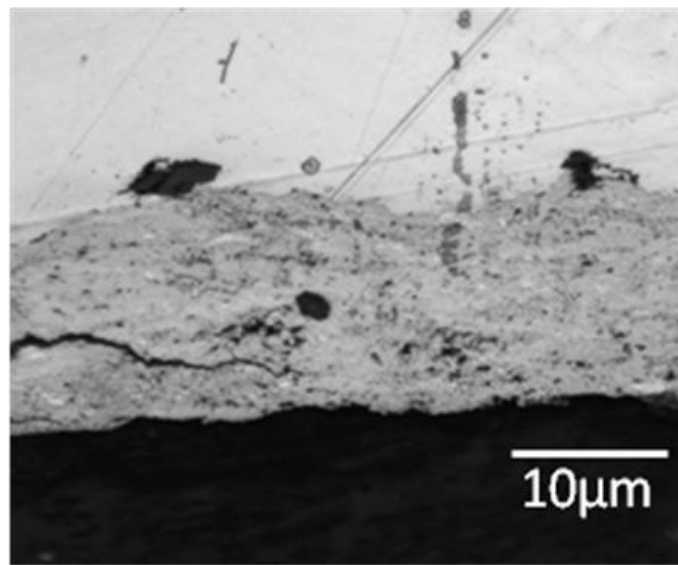


Figure 4.72. Optical micrograph of cross-section of annealed WC-17wt% Co coating (bottom) on mild steel substrate, showing holes, microcracks and the good fit between coating and irregular surface. The black area on the image is the alumina used for grit-blasted.

The microstructure of the heat-treated coating on super-invar substrate (Figure 4.73) had holes, microcracks and the good fit between the coating and the irregular substrate surface. The black area in the coating-substrate interface was alumina that was used for grit-blasting, as also observed by Machio [2005Mac]. No peeling was observed at the interface between the coating and the substrate. The porosity was very low, and no unmelted particles were observed.

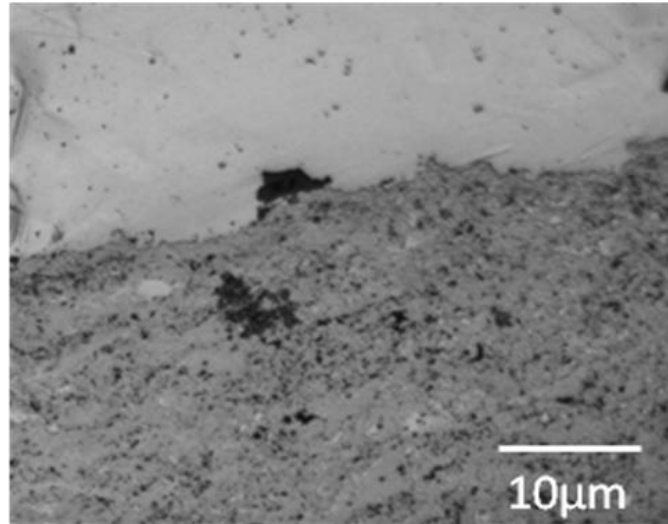


Figure 4.73. Optical micrograph of cross-section of annealed WC-17wt% Co coating (bottom) on super-invar, showing holes and good fit between coating and irregular surface. The black area in the coating-substrate interface is the alumina used for grit-blasted.

Typical thermal spray microstructures were captured by the scanning electron microscope (Figures 4.74-4.78). These figures show main features of the coatings, highlighting the difference between them. Unlike in optical micrographs, the WC can be differentiated by its brighter contrast. EDX analyses showed that all the annealed coatings were composed of W, Co and C. The annealed coating on aluminium is shown in Figure 4.74. The noticeable features showed pores (black), equiaxed WC embedded in a Co binder, and fine particles.

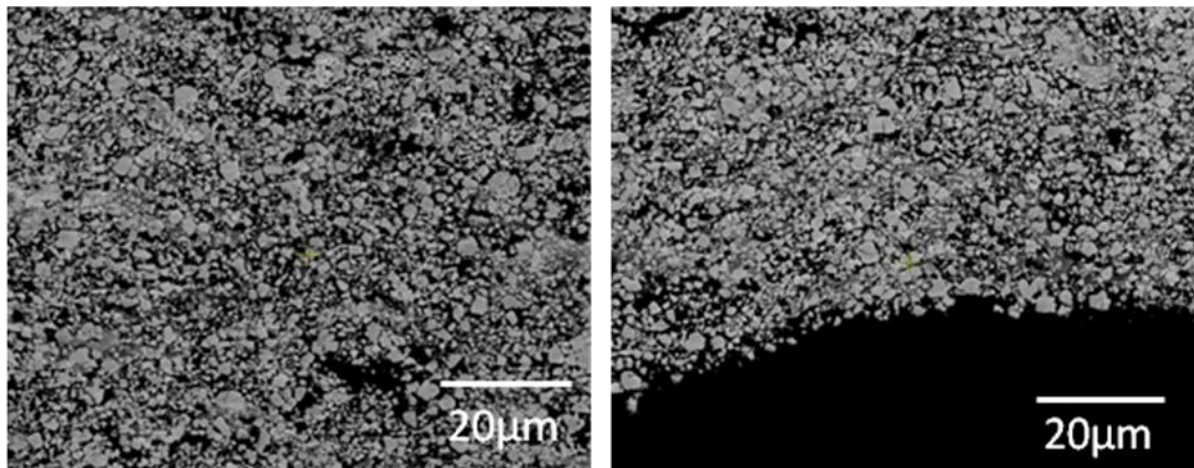


Figure 4.74. SEM-BSE images of cross-sections of annealed WC-17% Co coating on aluminum, showing WC (light), cobalt binder (medium), pores (black), microcracks and coating interface (right side).

Figure 4.75 shows the microstructure of the annealed coating on the brass substrate. Major features included holes, microcracks and a good coating-substrate fit. There was no peeling at the interface. The porosity was fairly low, with no discernable unmelted particles.

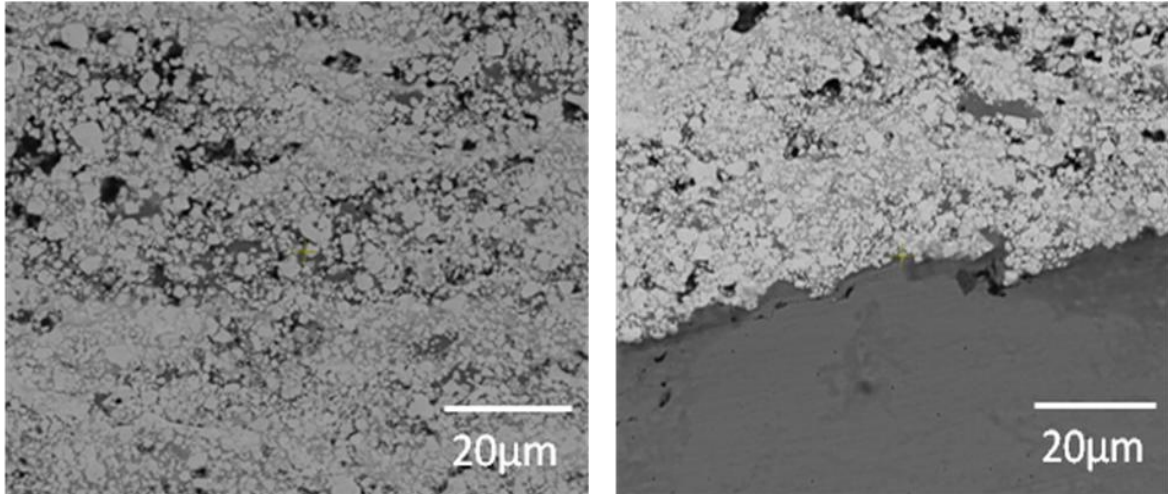


Figure 4.75. SEM-BSE images of cross-sections of annealed WC-17% Co coating on brass, showing WC (light), cobalt binder (medium), pores (black), microcracks and coating interface (right side).

The microstructure of the annealed coating on the mild steel substrate is shown in Figure 4.76. It had the following noticeable features: holes, lamellar structures, microcracks, carbide pull-out and a good fit between the coating and the irregular substrate surface. No peeling was observed at the interface. There was fairly low porosity, and no unmelted particles were observed.

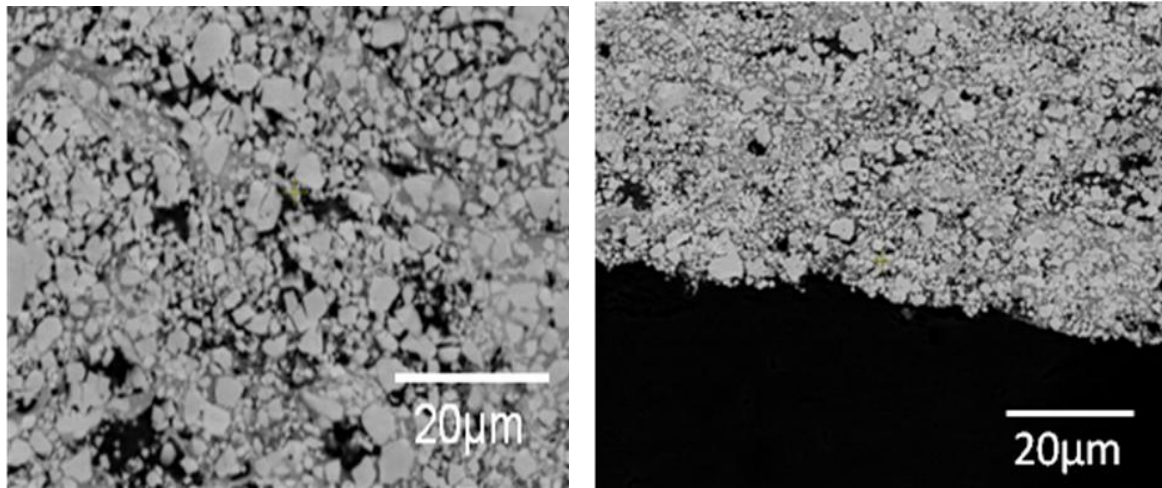


Figure 4.76. SEM-BSE images of cross-sections views of annealed WC-17% Co coating on mild steel, showing WC (light), cobalt binder (medium), pores (black), microcracks, carbide pull-out and coating interface (right side).

From the microstructure of the annealed coating on the super-invar substrate shown in Figure 4.77, the main features were microcracks, carbide pull-out and a good fit between the coating and irregular surface of the substrate. The carbide pull-out was determined as being due to the combined effect of temperature and coefficient of thermal expansion of the coating. No peeling was observed at the coating-substrate interface. There was some porosity, with no discernable unmelted particles.

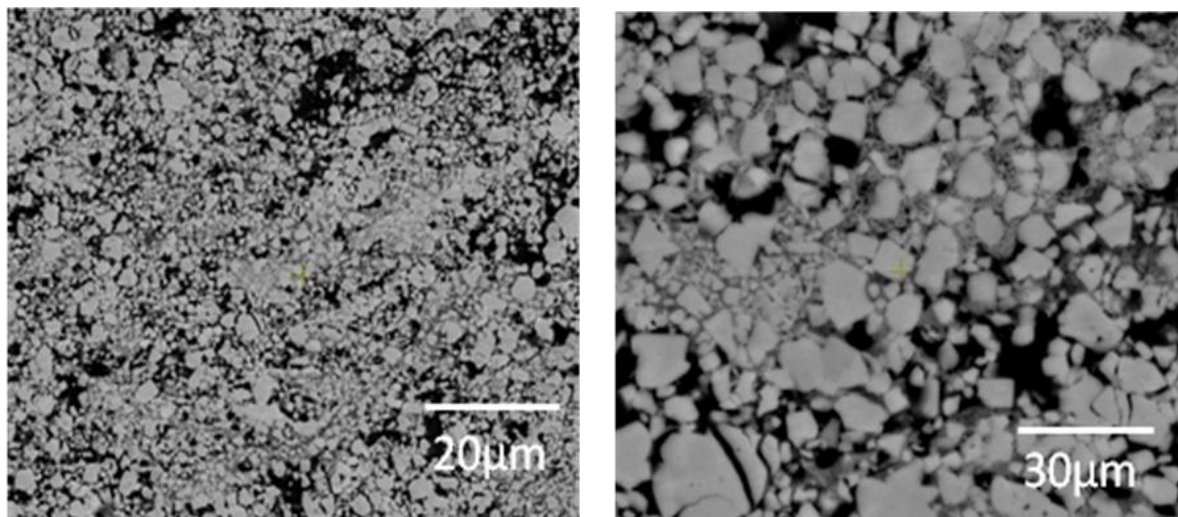


Figure 4.77. SEM-BSE images of cross-sections of annealed WC-17% Co coating on super-invar, showing WC (light), cobalt binder (medium), pores (black), microcracks, carbide pull-out (right side).

The microstructure of the annealed coating on the 304L stainless steel substrate (Figure 4.78) had finer carbide distribution, microcracks and a good fit between the coating and the irregular surface. No peeling was observed at the interface between the coating and the substrate. The porosity of these coatings was low, and no unmelted WC particles were observed.

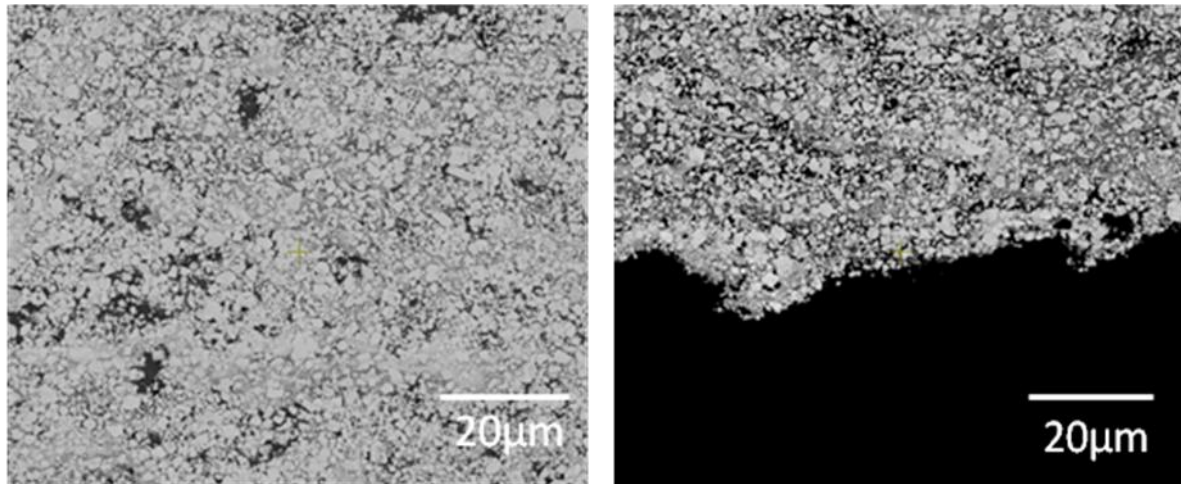


Figure 4.78. SEM-BSE images of cross-sections of annealed WC-17% Co coating on 304L stainless steel substrate, showing WC (light), cobalt binder (medium), pores (black), microcracks, carbide pull-out and coating interface (right side).

The grain sizes of the as-sprayed and annealed coatings are shown in Table 4.9. They were generally small, but different. Noticeable reductions in size after heat-treatment were found, despite the same starting powder having been used as the feedstock.

Table 4.9. Properties of the as-sprayed and annealed WC-17Co coatings.

Material	Conditions	Hardness HV ₅ (GPa)	Substrate HV ₅ (GPa)	Porosity (%)	WC grain size (μm)
304L Stainless steel	As- sprayed coating	9.11±0.01	1.74±0.02	0.463±0.200	1.14±0.20
	Annealed coating	6.35±0.01	1.69±0.01	0.163±0.020	0.98±0.20
Super- invar	As- sprayed coating	7.63±0.01	1.35±0.01	0.863±0.200	0.82±0.20
	Annealed coating	7.54±0.01	1.34±0.01	0.762±0.010	0.63±0.20
Mild steel	As- sprayed coating	7.01±0.01	1.25±0.01	0.570±0.100	1.07±0.20
	Annealed coating	7.80±0.01	1.21±0.01	0.368±0.020	1.01±0.20
Aluminum	As- sprayed coating	8.55±0.01	1.45±0.01	0.618±0.100	0.94±0.20
	Annealed coating	5.73±0.01	0.74±0.01	0.408±0.010	0.76±0.20
Brass	As- sprayed coating	6.60±0.01	1.29±0.01	0.630±0.100	1.00±0.20
	Annealed coating	6.14±0.01	0.86±0.02	0.427±0.010	0.83±0.20

Figures 4.79-4.81 show XRD patterns of the as-sprayed (bottom spectrum), and heat-treated WC-Co coating (top spectrum) for the different substrates. The layers in both conditions had similar phases to the feedstock (Figure 4.2), the main peaks being tungsten carbide (WC) and cobalt (Co), while more secondary eta phase was found on heat-treated mild steel.

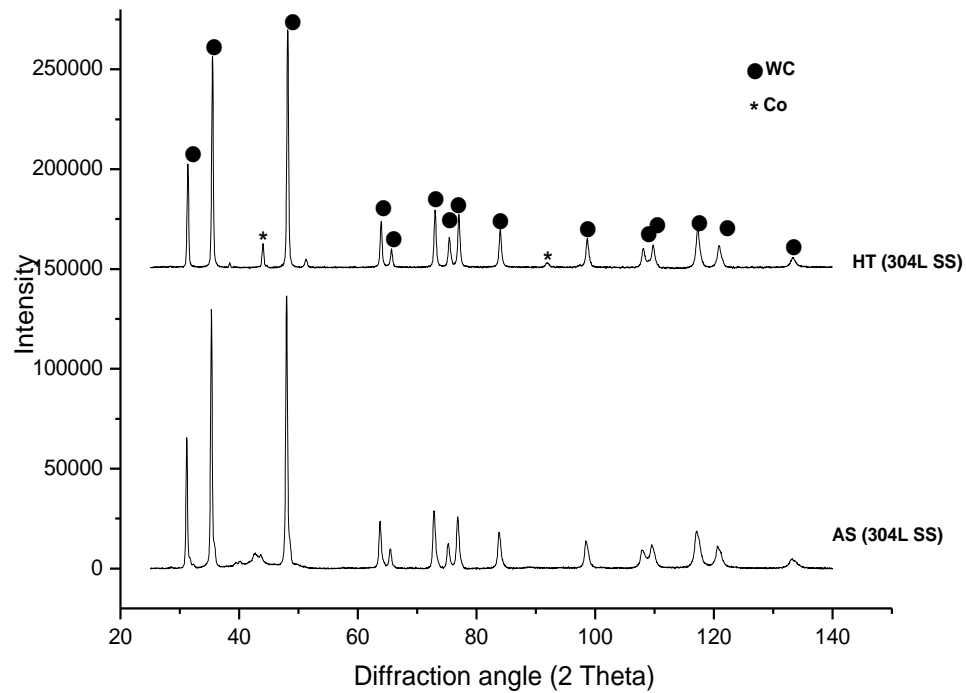


Figure 4.79. XRD patterns of the as-sprayed and annealed WC-17Co coatings on 304L stainless steel.

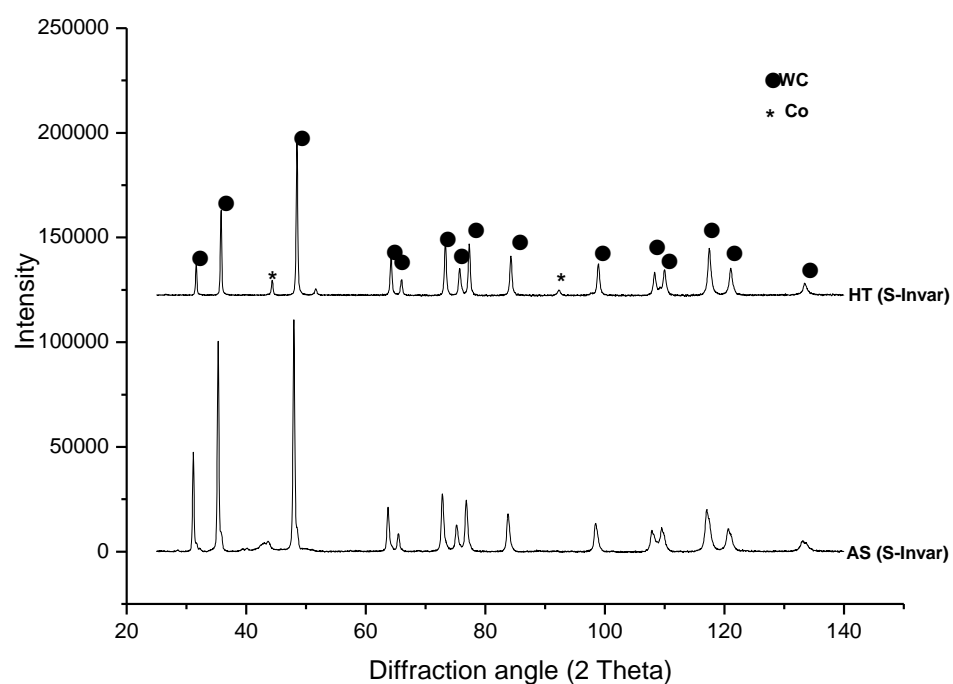


Figure 4.80. XRD patterns of the as-sprayed and annealed WC-17Co coatings on super-invar.

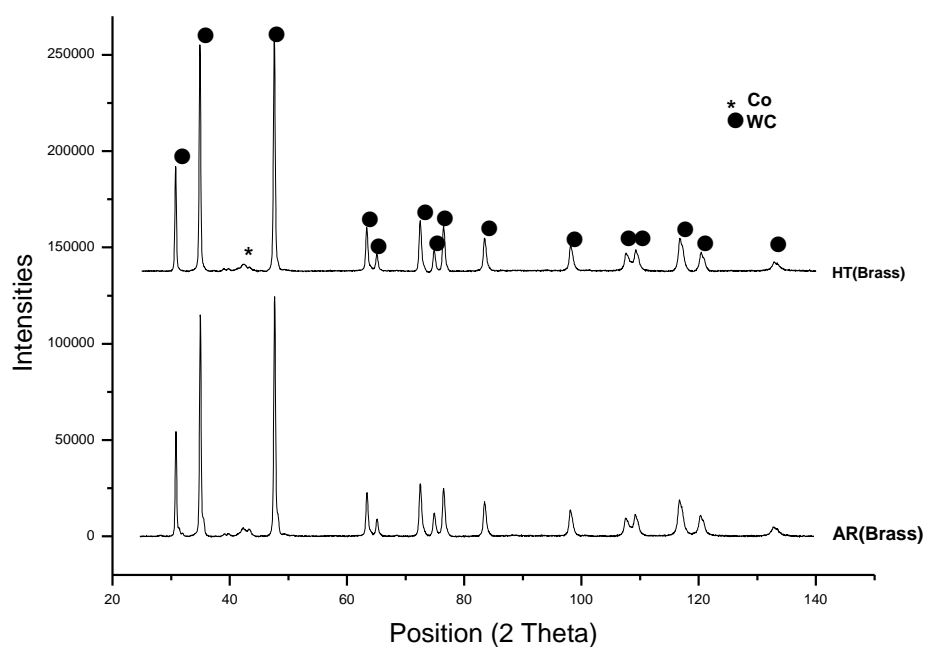


Figure 4.81. XRD patterns of the as-sprayed and annealed WC-17Co coatings on brass.

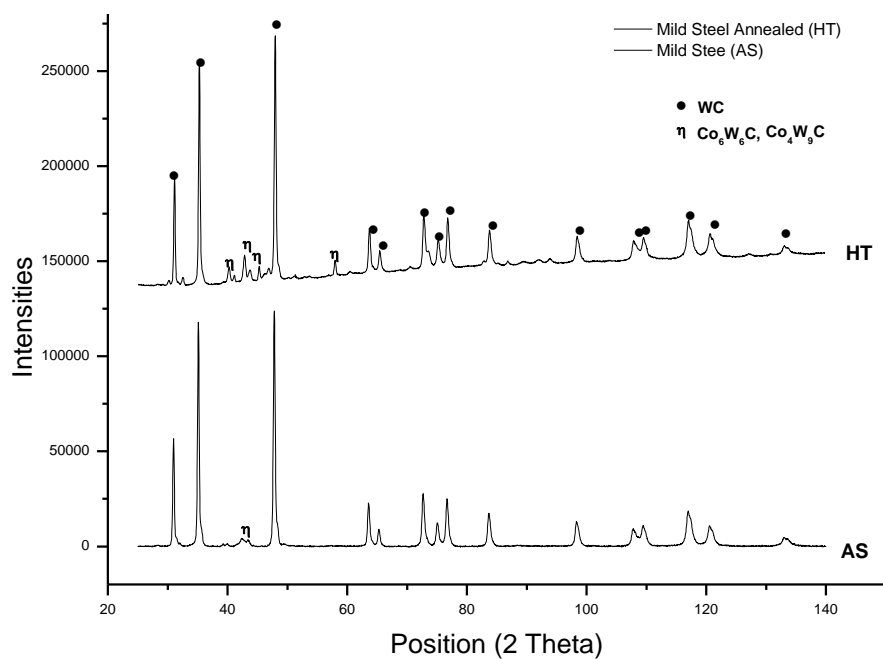


Figure 4.82. XRD patterns of the as-sprayed and annealed WC-17Co coatings on mild steel.

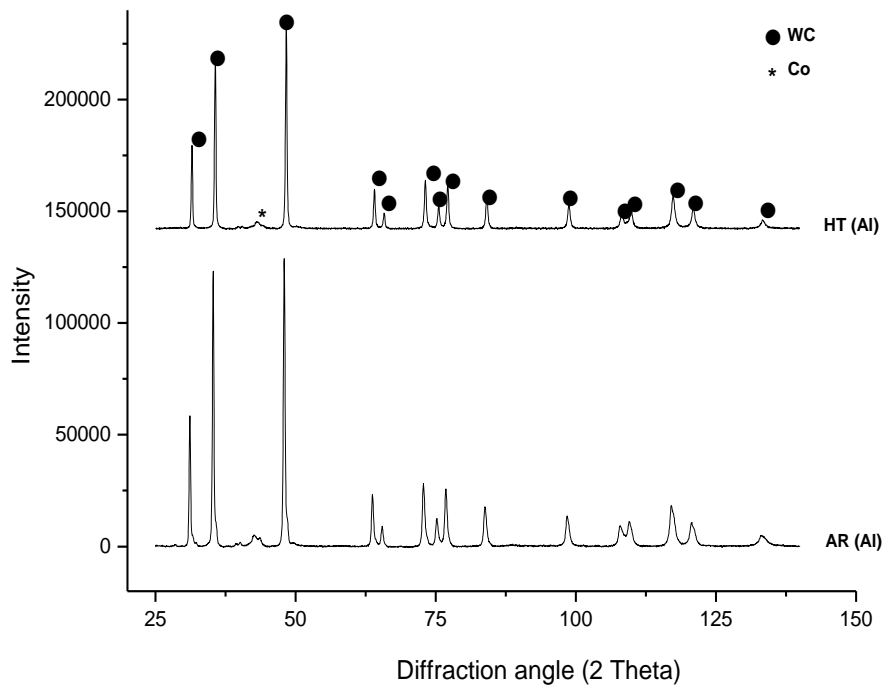


Figure 4.83. XRD patterns of the as-sprayed and annealed WC-17Co coatings on aluminum.

A summary of the coating and substrate hardness values for the as-sprayed and annealed conditions are shown in Table 4.9 and Figure 4.84. The results indicate a much higher macrohardness for the coatings compared to the substrates, as expected since these are hardmetal coatings. In the as-sprayed coatings, the coating on 304L stainless steel was harder than the other coated samples. After annealing, a noticeable reduction of macrohardness was found in all the samples except for the as-sprayed mild steel. This is ascribed to the eta phase being present on the as-sprayed coating on mild steel.

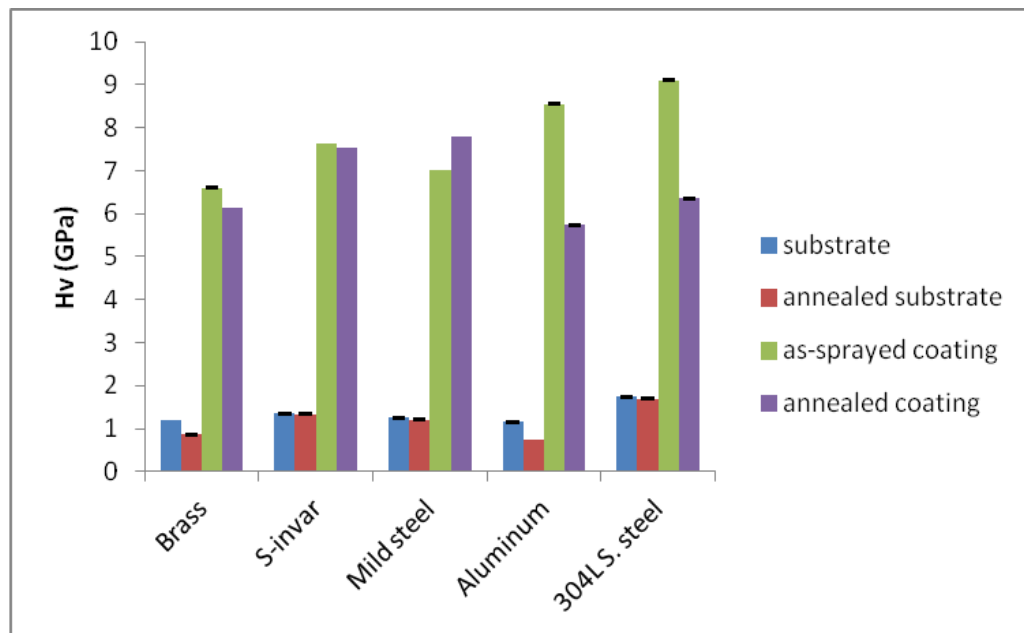


Figure 4.84. Macrohardness values of as-received substrate, as-sprayed and annealed WC-Co coating and the different substrates.

Figures 4.85 and Table 4.10 present the residual stress results measured by X-ray diffraction of the grit-blasted substrate, annealed grit-blasted substrate, as-sprayed coatings, and annealed as-sprayed coatings. The elastic constants used in the determination of the stress values are shown in Table 3.6. Analyses of the different conditions were carried out to identify the contribution of each process in the coating. The natures of the residual stresses were tensile in the as-sprayed coatings except for coated aluminum that is compressive, whilst compressive were found in other conditions. These results indicate that the residual stress in the as-sprayed coatings changed significantly due to the annealing treatment.

Table 4.10. Residual stress and abrasive wear results of coatings and different substrates subjected to various conditions

Substrate	Conditions	Residual Stress (MPa)	Wear mass loss (g)
304L Stainless steel	Grit blasted sample	-158.5±35.8	0.602±0.010
	Annealed grit blasted	-174.9±18.1	Not measured
	As-sprayed coating	24.6±18.6	0.066±0.010
	Annealed coating	-206.9±18.4	0.035±0.010
	Substrate	Not measured	1.430±0.010
Super-invar	Grit blasted sample	-250.9±7.7	0.569±0.010
	Annealed grit blasted	-53.1±7.5	Not measured
	As-sprayed coating	111.1±17.3	0.161±0.010
	Annealed coating	-106.5±15.1	0.138±0.010
	Substrate	Not measured	1.183±0.010
Aluminum	Grit blasted sample	-160±8.4	0.278±0.010
	Annealed grit blasted	-83±17.9	Not measured
	As-sprayed coating	-15.7±17.0	0.057±0.010
	Annealed coating	-113.4±18.4	0.039±0.010
	Substrate	Not measured	0.471±0.010
Brass	Grit blasted sample	-123.6±2.7	0.653±0.010
	Annealed grit blasted	-67.0±5.9	Not measured
	As-sprayed coating	36.0±17.5	0.073±0.010
	Annealed coating	-11.8±15.3	0.081±0.010
	Substrate	Not measured	1.558±0.010
Mild steel	Grit blasted sample	-171.5±22.5	0.617±0.010
	Annealed grit blasted	-40.3±35.2	Not measured
	As-sprayed coating	30.5±19.1	0.084±0.010
	Annealed coating	-95.6±18.6	0.179±0.010
	Substrate	Not measured	1.129±0.010

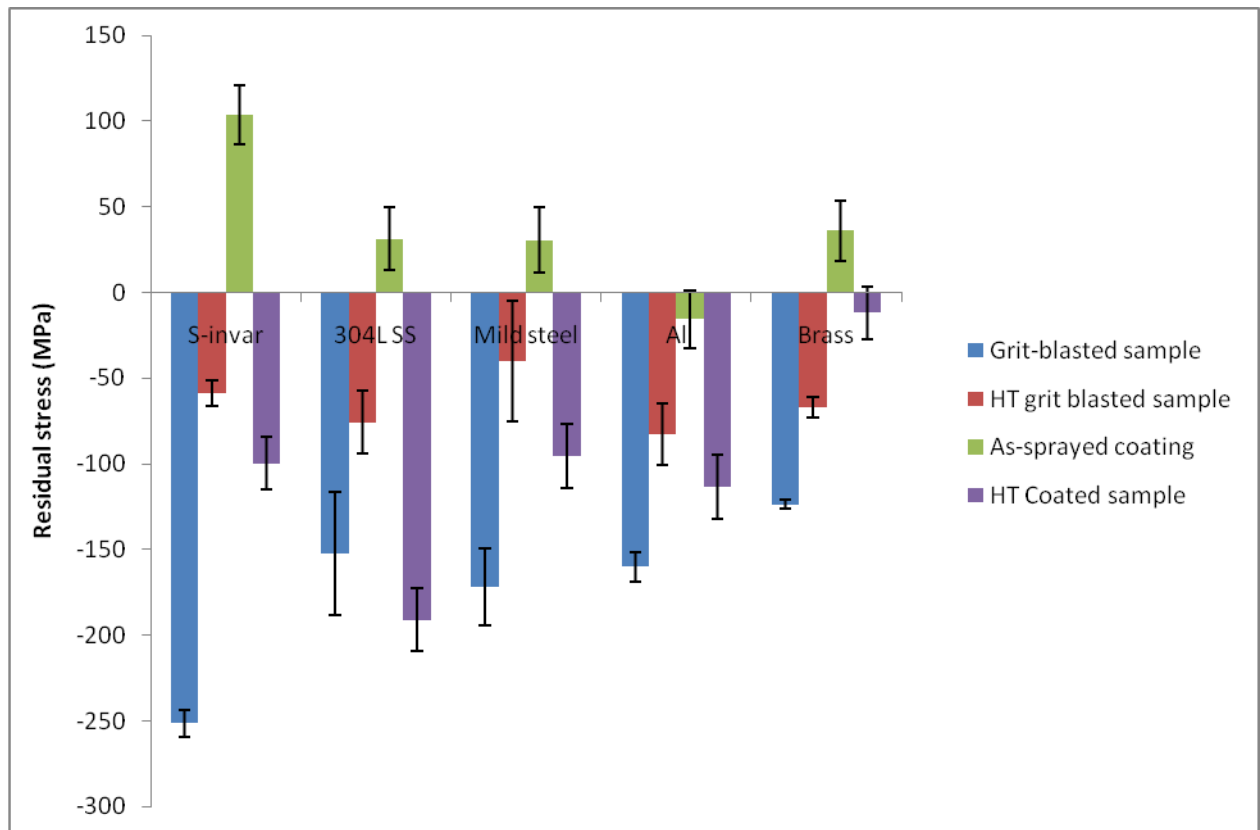


Figure 4.85. Residual stress of WC-17Co coating and substrate under different conditions.

Figures 4.86-4.89 show the abrasive wear mass loss of the as-received substrates, grit-blasted substrate, as-sprayed coatings, annealed coatings with the final wear rates shown in Figure 4.90 (with no error bars shown, as the errors were small [Table 4.10]). This was done to systematically characterize the integrity of the coating after the wear measurements, as well as to investigate the effect of silica sand on the coated surfaces. The results (Table 4.10) show the contribution of each process step to the wear resistance of the coating. A 45 - 50% reduction in the wear resistance of the substrate in the grit blasted condition compared to the as-received substrates were found, whereas the wear resistance of the as-coated substrates a reduction of about 80 - 95% in compared to the as-received substrate was found.

The substrate wear is shown in Figure 4.86 and the wear rates in Figure 4.90. The investigation was done on the substrate to ascertain the support given by the substrate to the wear resistance. The wear mass losses increased with time, and were parabolic. The brass substrate had the highest mass loss, with an apparent peak in pull-out before 10 minutes, followed by the 304L stainless steel substrate. The peak in mass loss in the brass specimen is most likely a measurement error, since it is highly unlikely that materials would be removed

and then replaced. The aluminum substrate gave the best wear resistance, due to precipitation hardening in the alloy, while super-invar and mild steel substrate were in the middle.

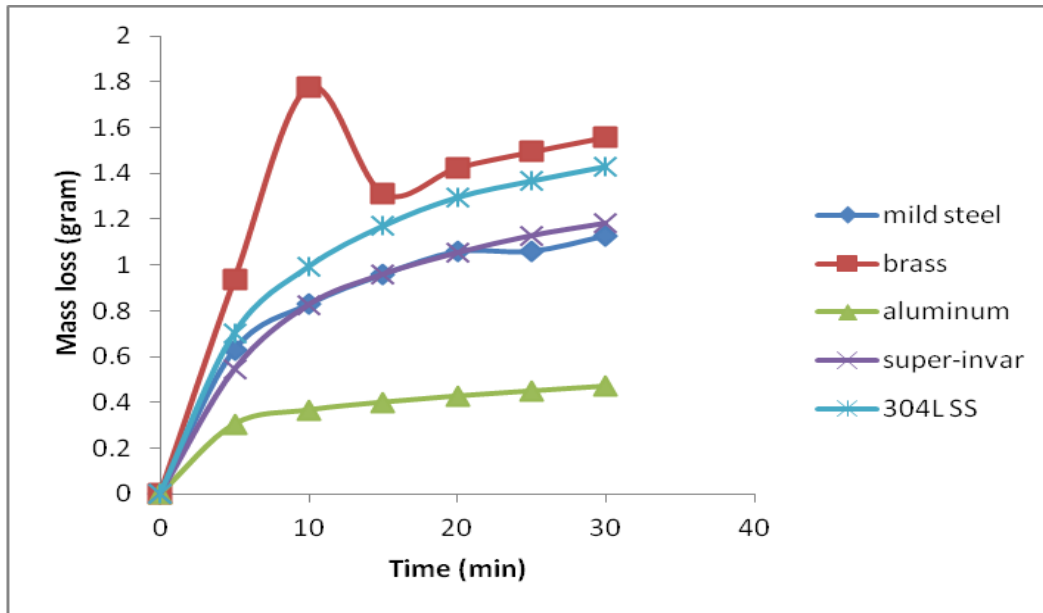


Figure 4.86. Abrasive wear mass loss of the as-received substrates.

The effect of grit-blasting on the wear resistance of the substrate samples was studied. A general trend of increasing mass loss with time, in a parabolic mode (Figures 4.87 and 4.90) was seen for all the grit-blasted substrate samples. The grit-blasted brass consistently had the highest average mass loss. Grit blasted 304L stainless steel, mild steel and super-invar substrate samples showed similar trends of parabolic wear rate. The grit-blasted aluminum substrate had the lowest mass loss after 30 minutes.

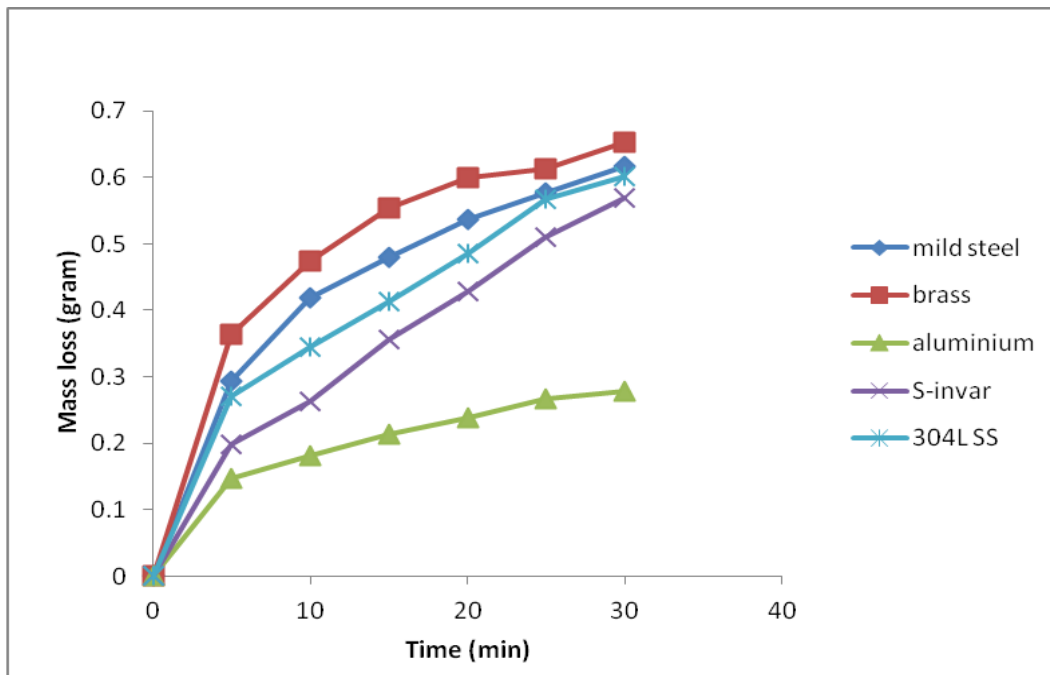


Figure 4.87. Abrasive wear mass loss of the grit-blasted substrates.

The abrasion resistance of the as-sprayed coatings on the different substrates is shown as mass loss results in Figure 4.88. The highest mass loss was recorded for the coated super-invar substrate. The coated mild steel substrate and brass substrates had similar mass losses within experimental error. The mass losses for the coated aluminium and 304L stainless steel substrates were similar, and lowest.

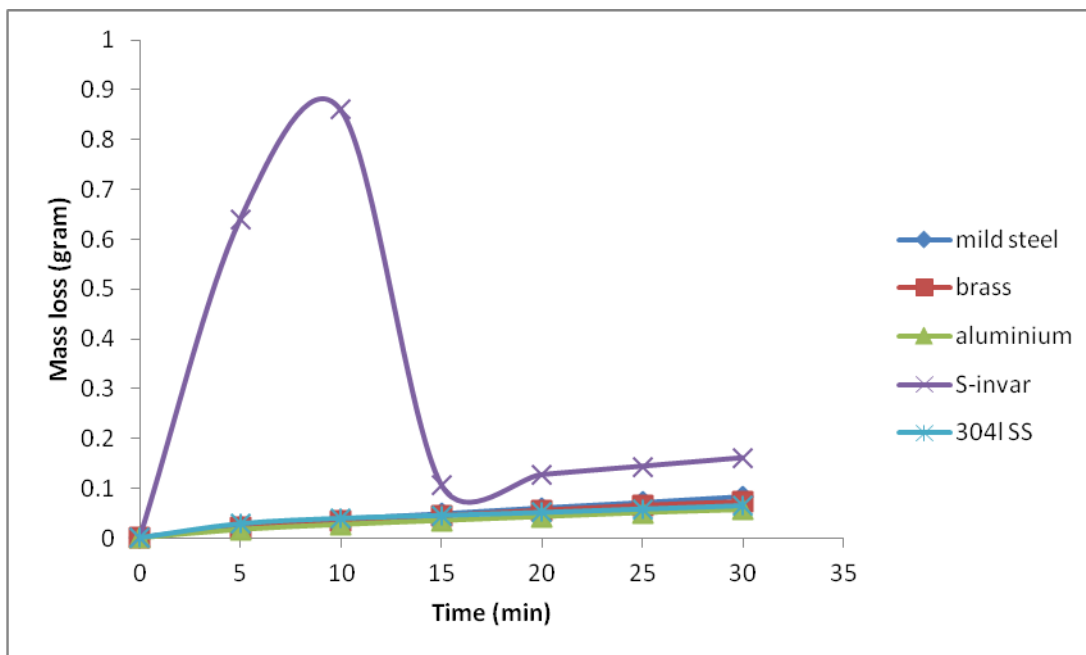


Figure 4.88. Abrasive wear mass loss of the WC-17Co as-coated deposits substrates.

The mass loss results of the annealed coated samples are shown in Figure 4.89, with a similar trend of increasing mass loss with time. The annealed coatings on mild steel had the highest average mass loss, and annealed coatings on brass and super-invar had similar trends, lying in the middle, despite their differences in hardness. The annealed coatings on 304L stainless steel and aluminium gave the best wear resistances, despite the differences in their hardness.

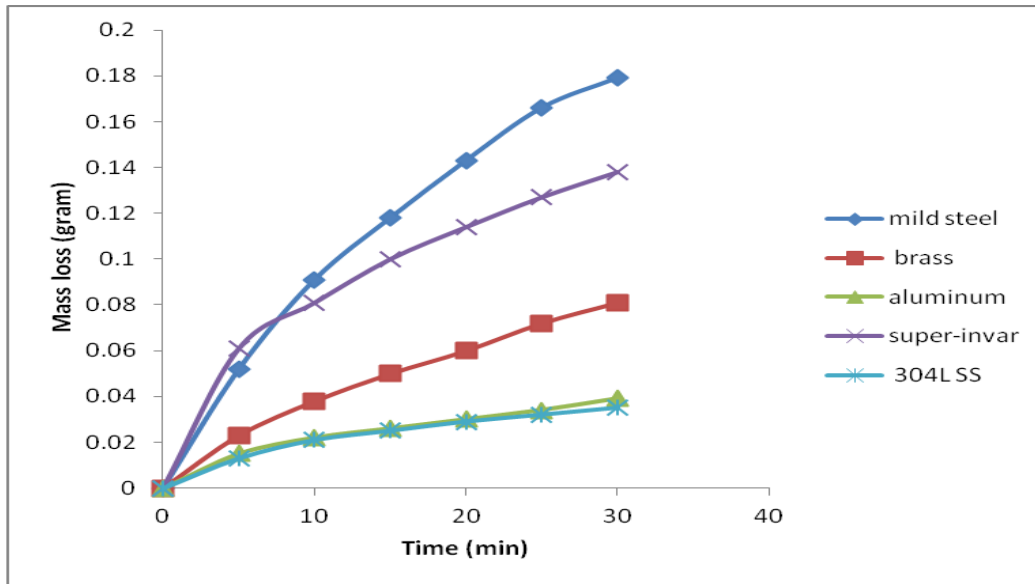


Figure 4.89. Abrasive wear mass loss of the annealed WC-17Co coatings on the different substrates.

The wear rates of the substrates of different conditions are shown in Figure 4.90. There was a 45 - 50% reduction in the wear resistance of the substrate in the grit-blasted condition compared to as-received condition, whereas the coated substrates showed a wear resistance which was about 80 – 95% better than the substrate.

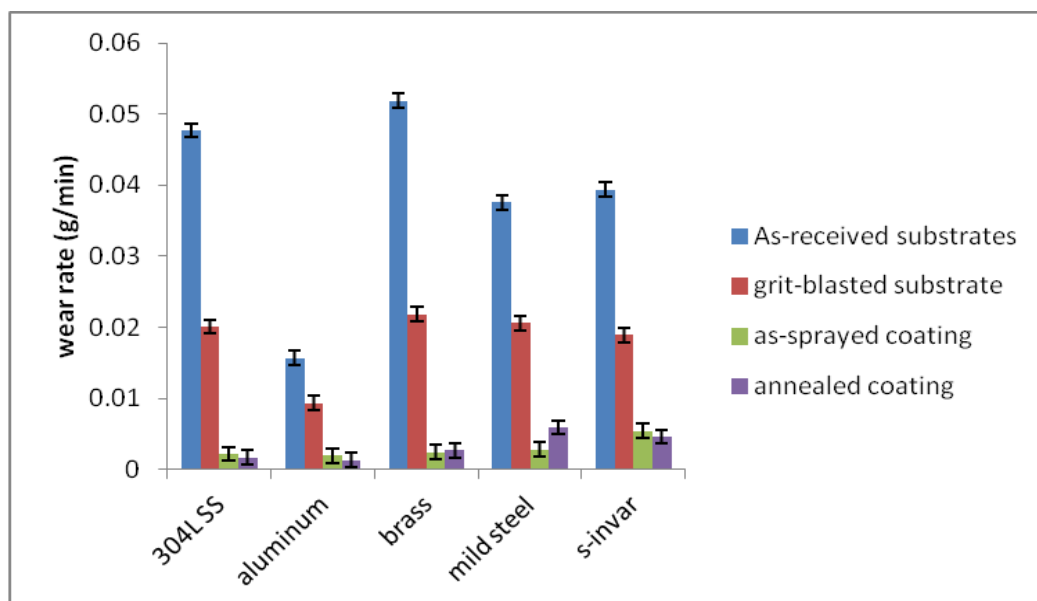


Figure 4.90. Summary of the wear rates of the different as-received substrates and WC-Co coatings under different conditions.

To understand the wear behaviour of the coatings, the wear scars of samples under different conditions were examined using SEM-SE, and the worn surfaces are shown in Figures 4.91 to 4.110. Similar wear features were observed on the five worn substrate surfaces (Figures 4.91-4.95). The damage was largely by plastic deformation. EDX showed that SiO_2 particles had become embedded in the substrate. The worn surface of the super-invar as-received substrate is shown in Figure 4.91, with plastic deformation, embedded silica sand (e.g. shown by arrow) small pits and deep grooves.

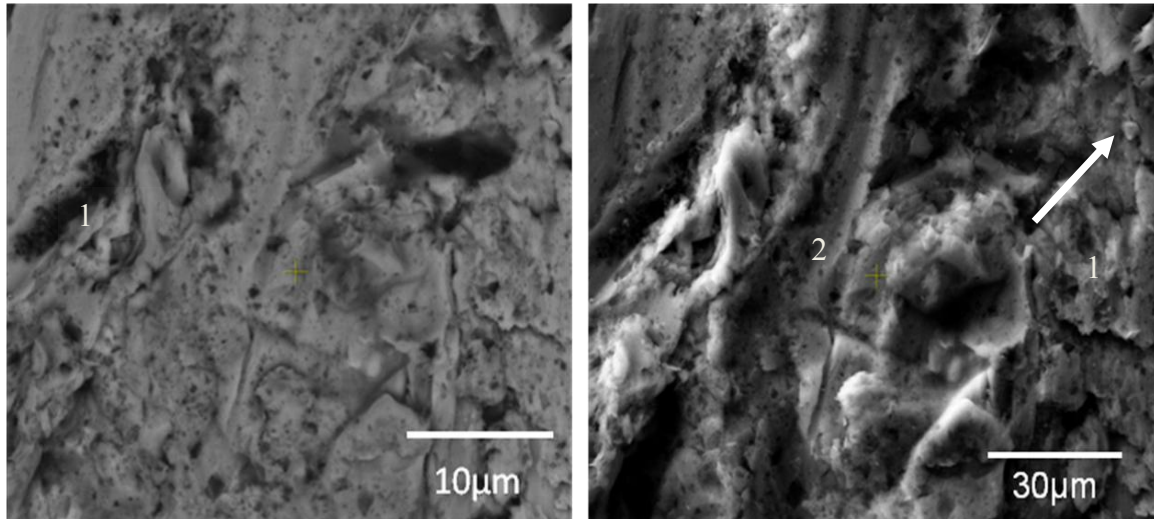


Figure 4.91. SEM-SE micrographs of the worn super-invar as-received substrate, revealing plastic deformation (1), silica sand (shown by arrow) with small pits and deep grooves (2).

Figure 4.92 shows the surface of the worn mild steel as-received substrate. There was plastic deformation, with trapped silica sand (shown by arrow), small pits and deep gauges.

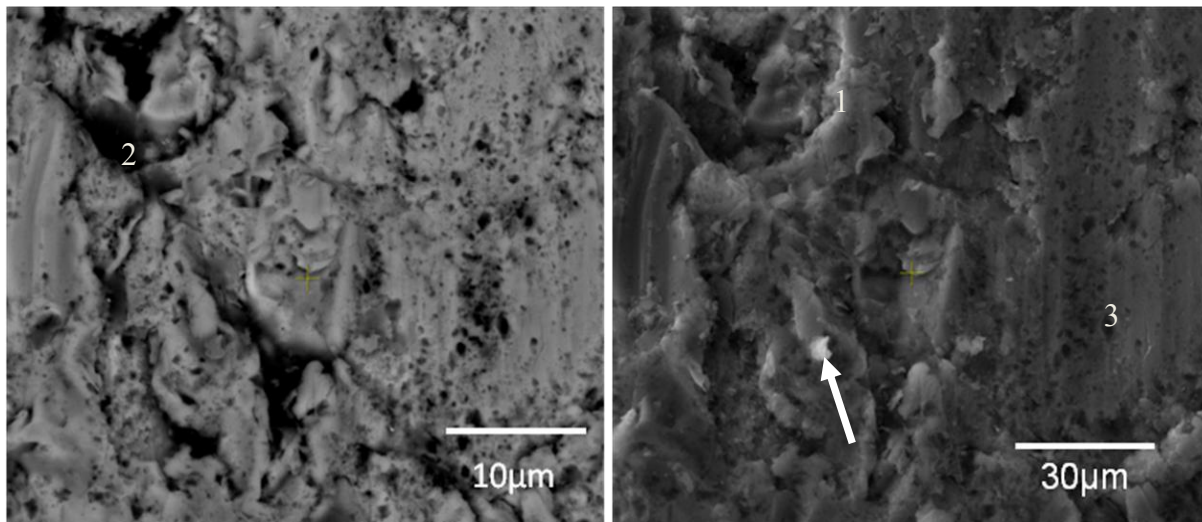


Figure 4.92. SEM-SE micrographs of the worn mild steel as-received substrate, revealing plastic deformation (1), silica sand (shown by arrow) with small pits (2) and grooves (3).

Similar to the other samples, the worn surface of the brass as-received substrate, Figure 4.93, had plastic deformation, embedded silica sand (arrow), with small pits and deep gauges.

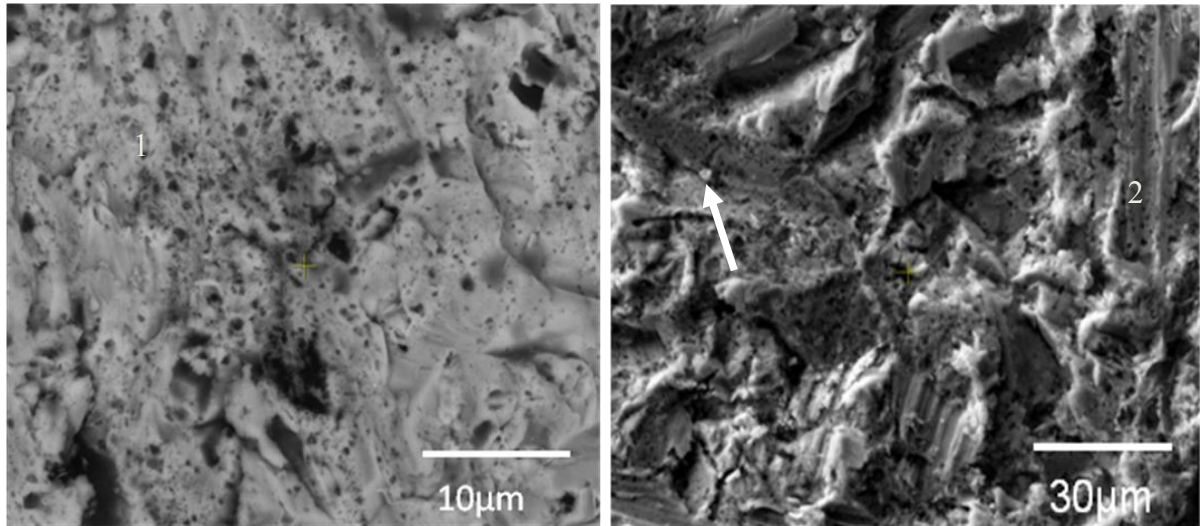


Figure 4.93. SEM-SE micrographs of the worn brass as-received substrate, revealing plastic deformation (1), silica sand (indicated by arrow), deep grooves (2) and small pits.

The surface of the worn 304L stainless steel as-received substrate is shown in Figure 4.94. The major features were plastic deformation, entrapped silica sand abrasive (shown by arrow), together with small pits and deep grooves.

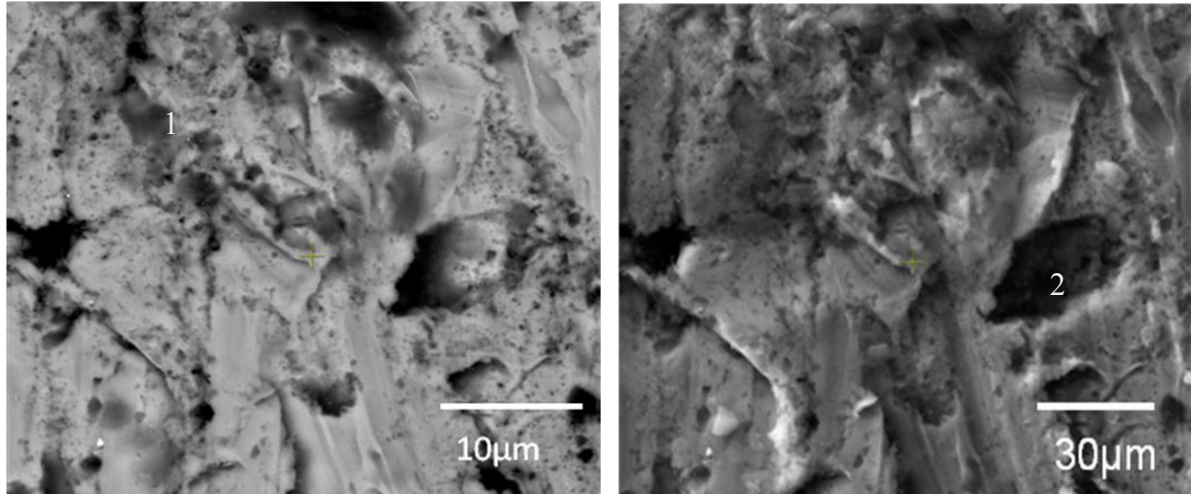


Figure 4.94. SEM-SE micrographs of the worn 304L stainless steel as-received substrate, revealing plastic deformation (1), deep grooves and small pits (2).

The worn surface of the aluminium as-received substrate (Figure 4.95) had plastic deformation, embedded silica sand abrasive (indicated by arrow), small pits and deep grooves.

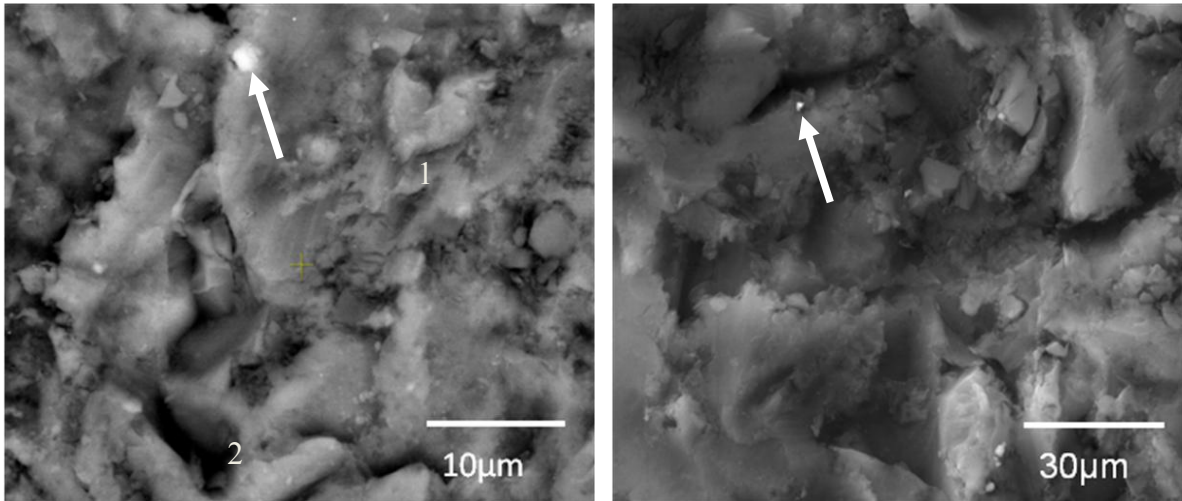


Figure 4.95. SEM-SE micrographs of the worn aluminium as-received substrate, revealing plastic deformation (1), silica sand (shown by arrow) with small pits (2).

Figures 4.96-4.100 show the worn surfaces of the grit-blasted samples, which experienced plastic deformation. Some SiO_2 particles were embedded into the substrates of all the grit-blasted samples. The abraded surfaces of the grit-blast samples indicated extensive damage, with large patches of the abraded surface beginning to delaminate. Figure 4.96 shows the worn surface of the grit-blasted mild steel substrate. There was plastic deformation and embedded silica, although the degree of plastic deformation was less than the worn surface of the as-received substrate due to the effect of work hardening of the grit-blasted surface.

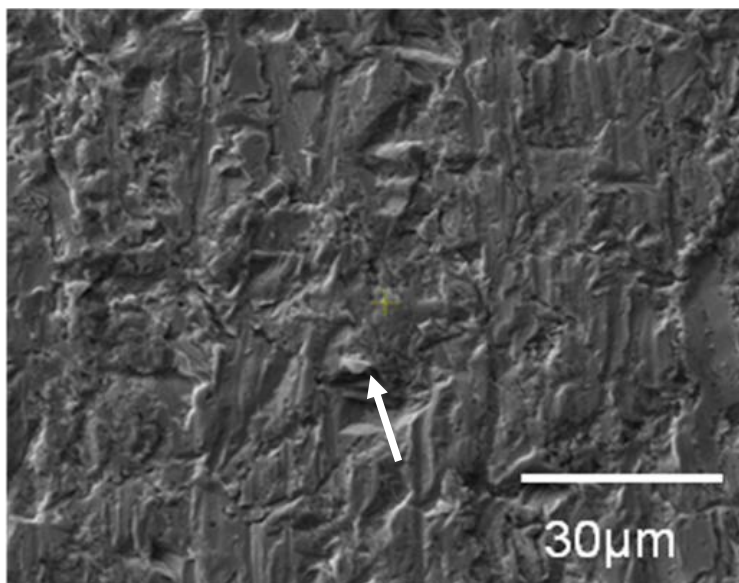


Figure 4.96. SEM-SE micrograph of the worn grit-blasted mild steel substrate, revealing plastic deformation and silica sand (shown by arrow).

The worn surface of the worn grit-blasted 304L stainless steel substrate is shown in Figure 4.97. The noticeable features were plastic deformation and embedded silica sand.

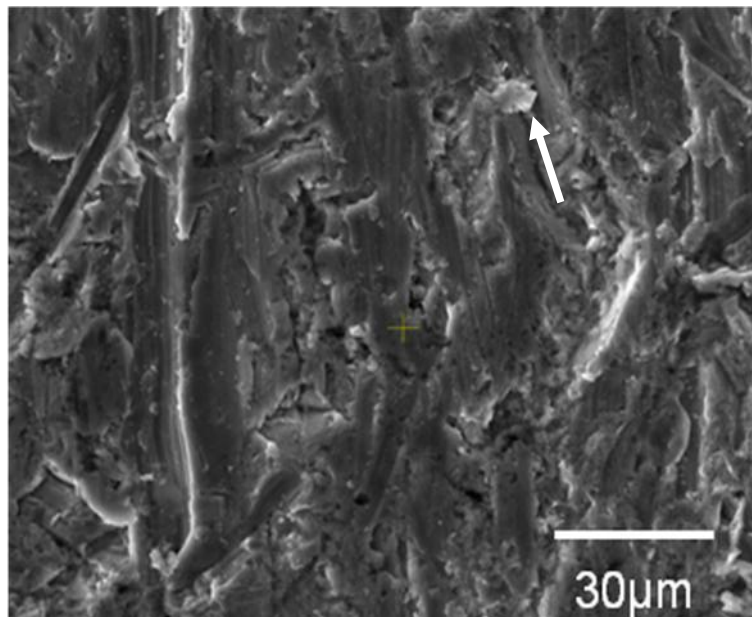


Figure 4.97. SEM-SE micrograph of the worn grit-blasted 304L stainless steel substrate, revealing plastic deformation and silica sand (shown by arrow).

The worn surface of the grit-blasted brass substrate shown in Figure 4.98 exhibited plastic deformation and trapped silica sand.

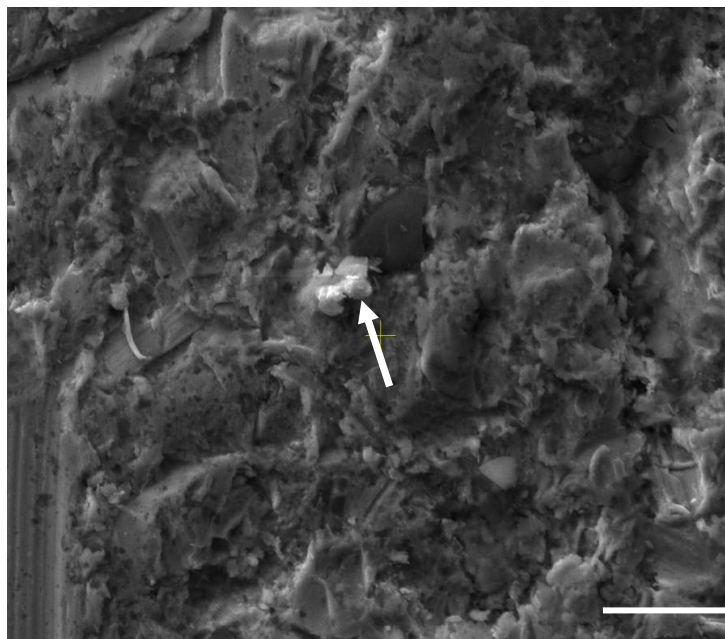


Figure 4.98. SEM-SE micrograph of the worn grit-blasted brass substrate, revealing plastic deformation, deep grooves and silica sand (shown by arrow).

The worn surface of the grit-blasted aluminium substrate (Figure 4.99) had plastic deformation, entrapped silica sand, and a small pit.

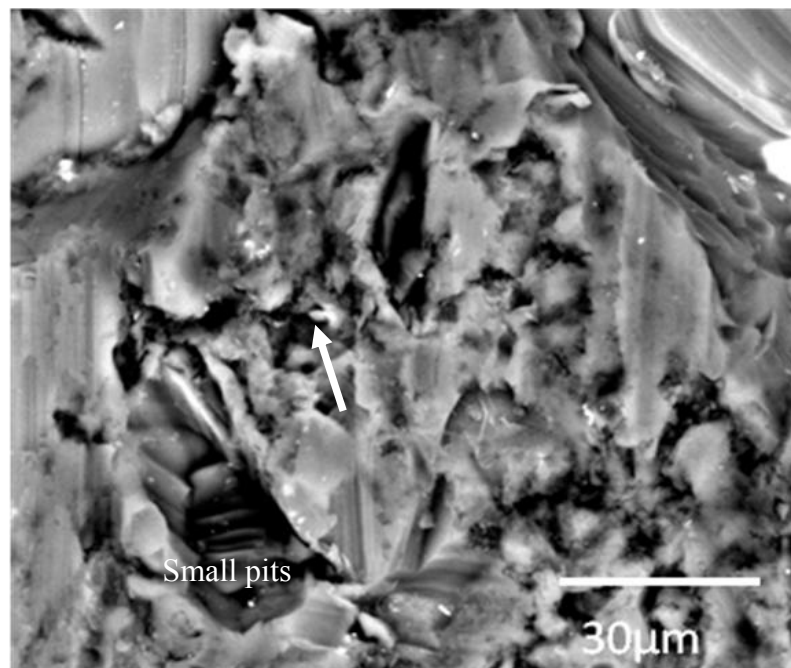


Figure 4.99. SEM-SE micrograph of the worn grit-blasted aluminum substrate, revealing plastic deformation, deep grooves, silica sand (shown by arrow) with small pits.

The worn surface of the worn grit-blasted super-invar substrate is shown in Figure 4.100. The noticeable features were plastic deformation.

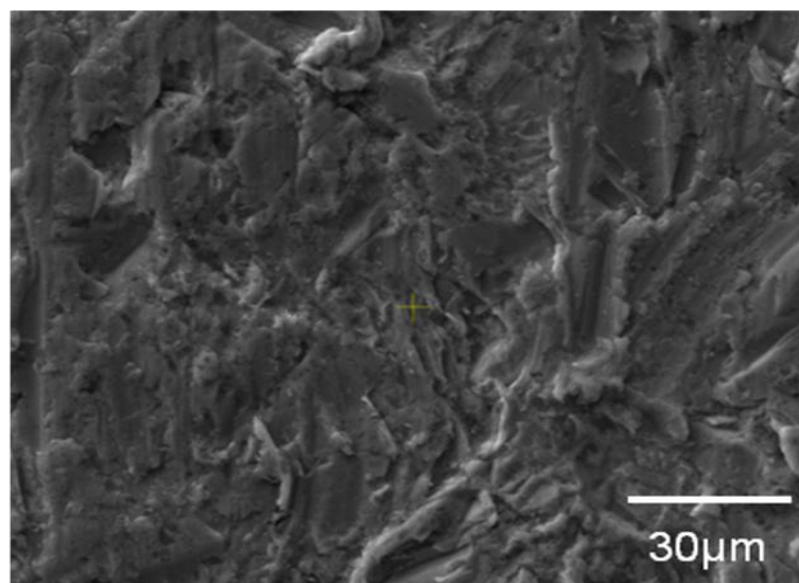


Figure 4.100. SEM-SE micrograph of the worn grit-blasted super-invar substrate, revealing plastic deformation.

On the as-sprayed coatings, similar wear features were found on the worn surfaces (Figures 4.101-4.105). The worn surface of the coated 304L stainless steel substrate (Figure 4.101) had fragmented carbides and fewer cracked carbides than the other samples, as well as fewer gauges in the abrasion direction. The gauges were made by the SiO₂ abrasive.

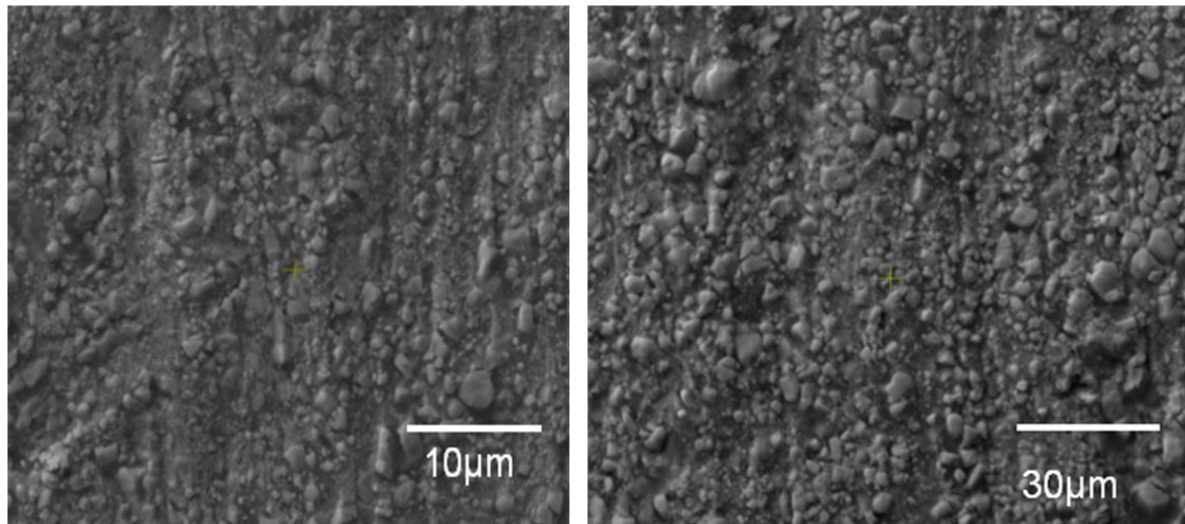


Figure 4.101. SEM-SE micrographs of the worn WC-17Co coating surface on 304L stainless steel, showing fragmentation of carbides, and pull-out of carbides as a result of binder removal.

Figure 4.102 shows the worn surface of the coated aluminium substrate. The following were observed: fragmented carbides, microcracking, pull-out of carbides as a result of binder removal, and parallel gauges in the direction of abrasion.

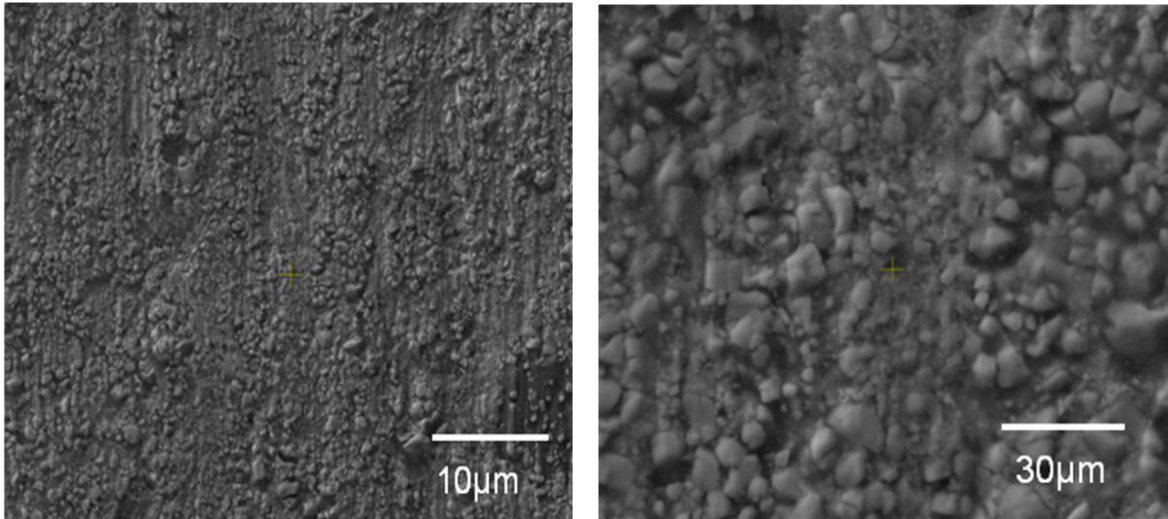


Figure 4.102. SEM-SE micrographs of the worn WC-17Co coating surface on aluminium substrate, showing fragmentation of carbides, microcracking and pull-out of carbides as a result of binder removal.

The worn surface of the coated mild steel substrate is presented in Figure 4.103. The noticeable features were fragmentations of high relief carbides, cracking, and pull-out of carbides as a result of binder removal.

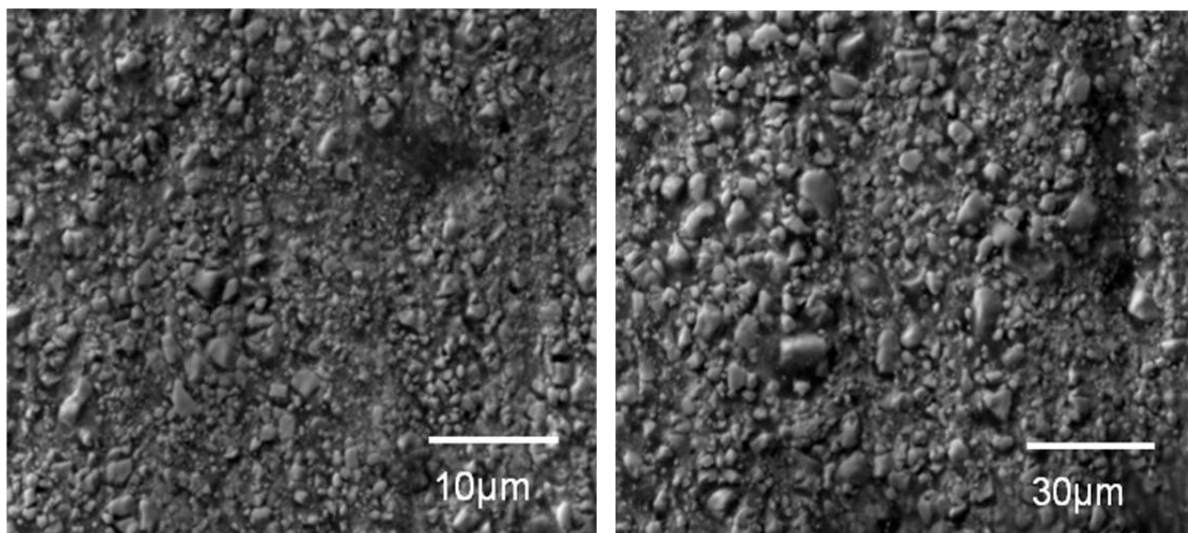


Figure 4.103. SEM-SE micrographs of the worn WC-17Co coating surface on mild steel, showing fragmentation of high relief carbides, cracking, pull-out of carbides due to binder removal.

The worn surface of the coated brass substrate (Figure 4.104) had fragmented carbides, microcracking, pull-out of carbides due to binder removal, high relief carbides and holes.

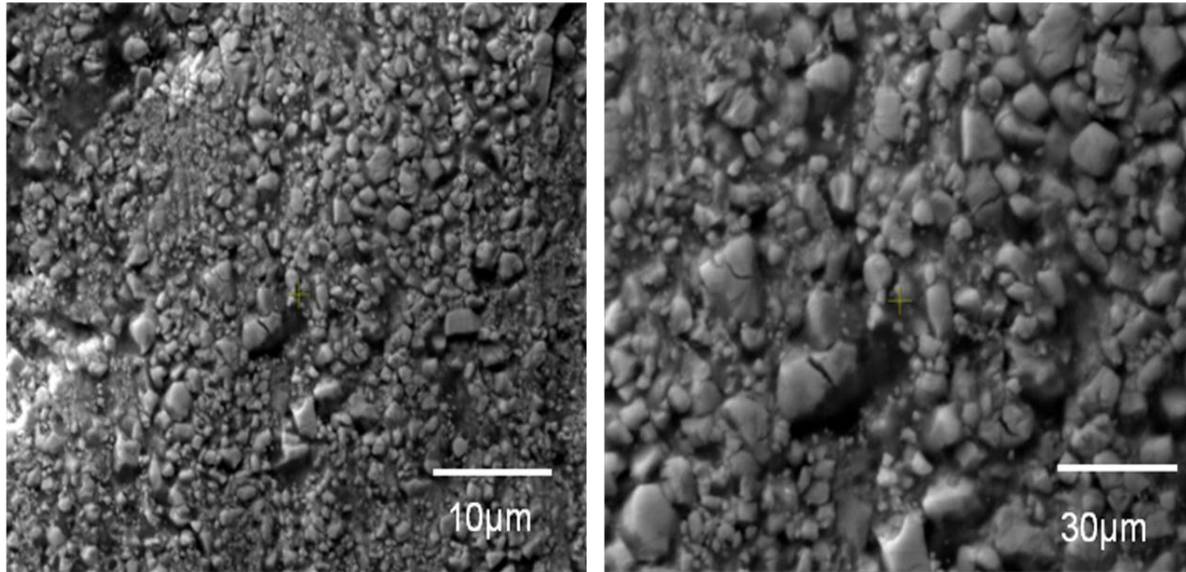


Figure 4.104. SEM-SE micrographs of the worn WC-17Co coating surface on brass, showing fragmentation of carbides, microcracking, pull-out of carbides due to binder removal, high relief carbides and holes.

The worn surface of the coated super-invar substrate shown in Figure 4.105, had microcracking, fragmented carbides, pull-out of carbides as a result of binder removal and gauges. The gauges were from the SiO₂ particles used as abrasive, or possibly the WC debris.

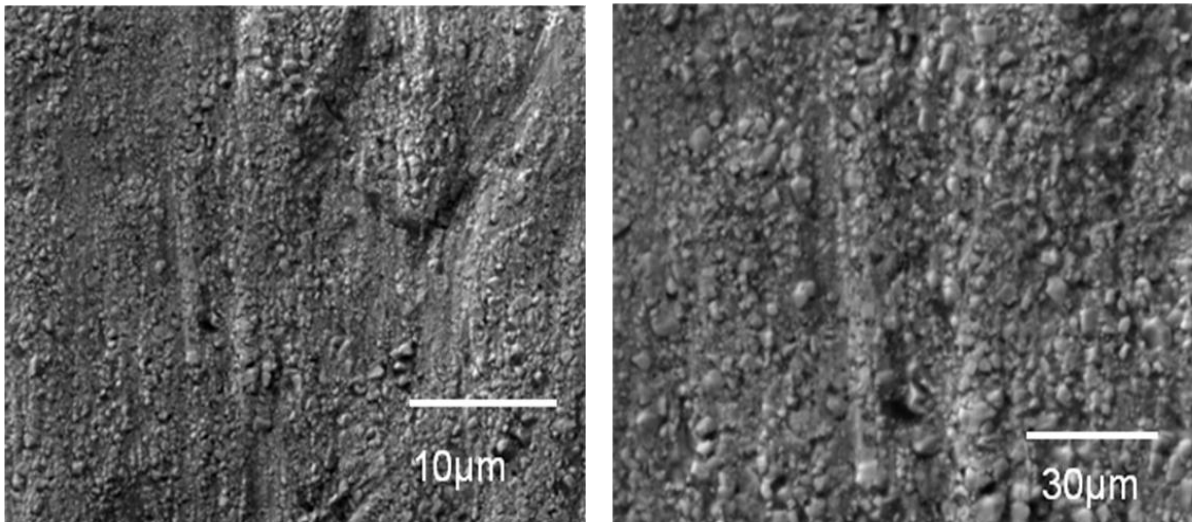


Figure 4.105. SEM-SE micrographs of the worn WC-17Co coating surface on super-invar, showing fragmentation of carbides, cracking and pull-out of carbides due to binder removal and groove formation.

In order to assess the abrasive wear behavior of the annealed thermal sprayed WC-Co coatings, the samples were examined using SEM. Figures 4.106-4.110 provide typical SEM micrographs of abraded surfaces of WC-17Co coatings. The worn surface of annealed coated sample of aluminum (Figure 4.106) shows in relief WC, fragmentation of carbides and microcracking.

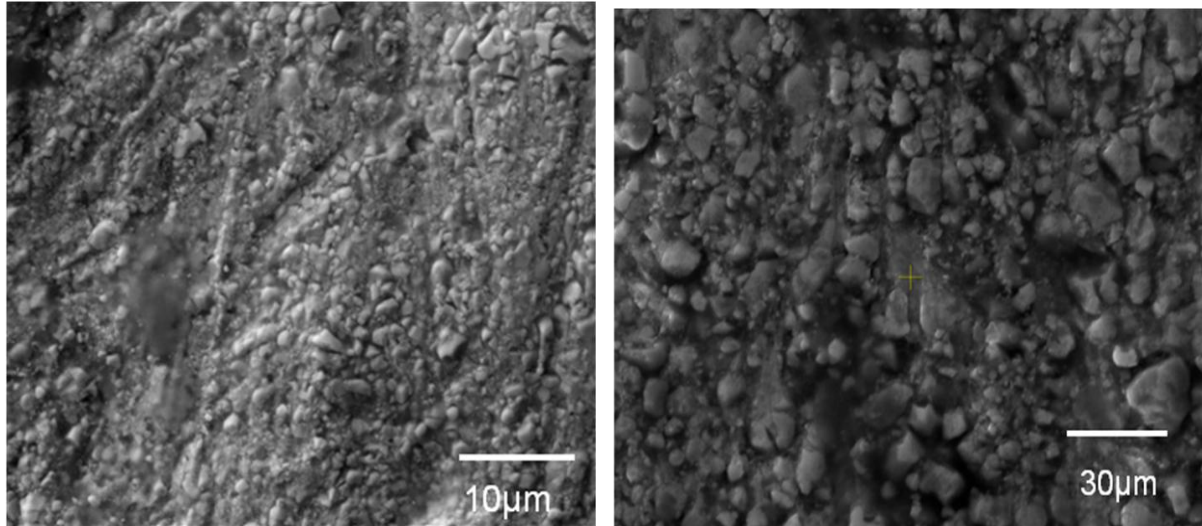


Figure 4.106. SEM-SE micrographs of the worn annealed WC-17Co coating surface on aluminum, showing fragmentation of carbides, cracked WC grains, and pull-out of carbides due to binder removal.

The worn surface of annealed coated 304L stainless steel (Figure 4.107) showed fragmentation of WC, cracked WC grains and pull-out of carbides, due to binder removal.

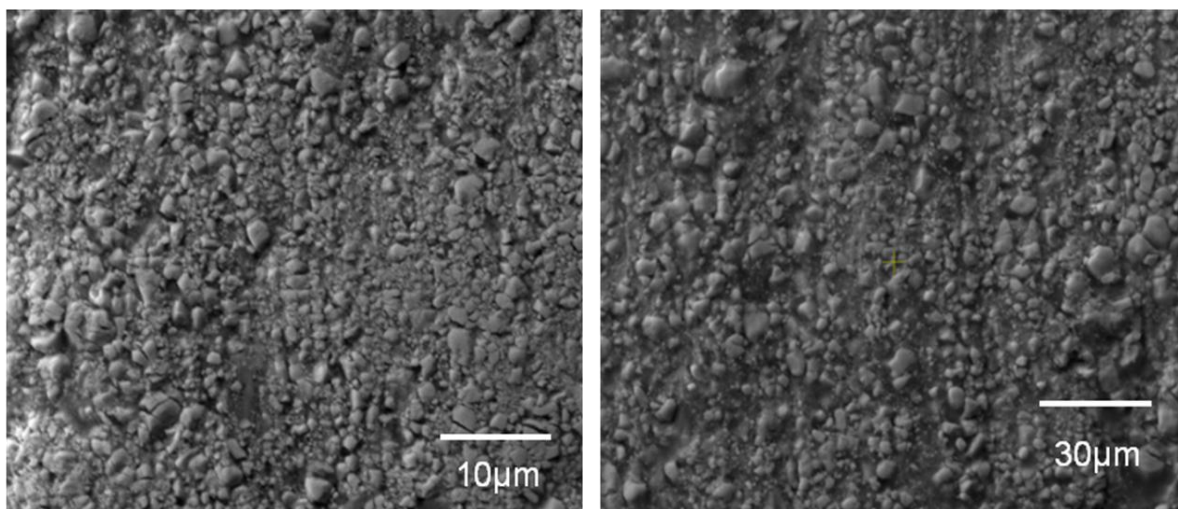


Figure 4.107. SEM-SE micrographs of the worn annealed WC-17Co coating surface on 304L stainless steel, showing fragmentation of carbides, cracked WC grains and pull-out of carbides due to binder removal.

The worn surface of annealed coated brass (Figure 4.108) had more fragmentation of carbides, smearing, pull-out of carbides, microcracking and trapped SiO₂ particles.

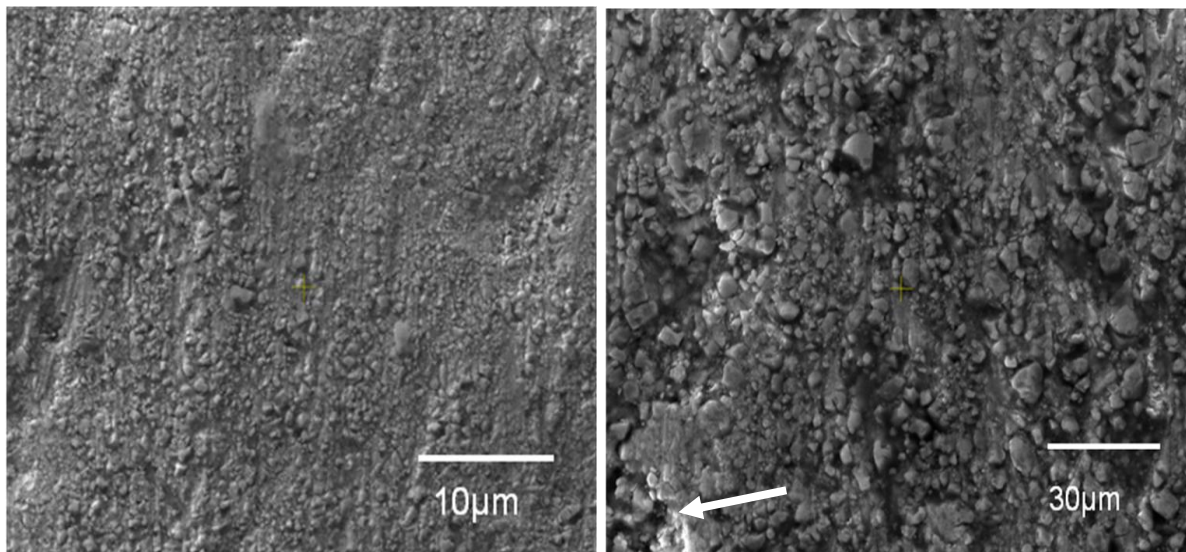


Figure 4.108. SEM-SE micrographs of the worn annealed WC-17Co coating surface on brass, showing fragmentation of carbides, cracking, smearing (shown by arrow), high relief carbides and pull-out of carbides due to binder removal.

Figure 4.109 shows the worn surface of the annealed coating on mild steel. The noticeable features were fragmentation of carbides, smearing, microcracking, and pull-out of carbides due to binder removal.

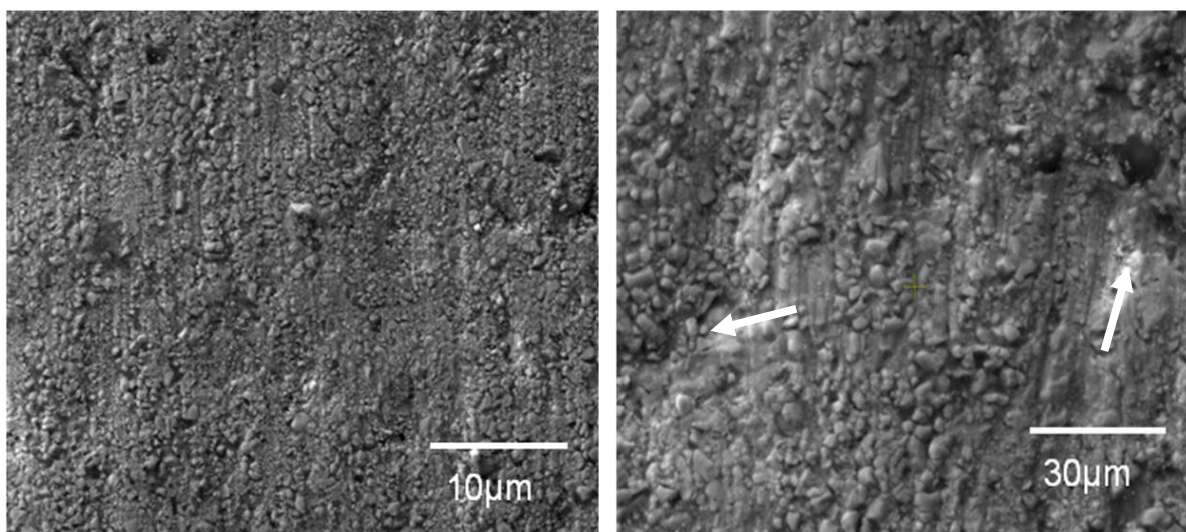


Figure 4.109. SEM-SE micrographs of the worn annealed WC-17Co coating surface on mild steel, showing fragmentation of carbides, microcracking, smearing (shown by arrow), pull-out of carbides due to binder removal.

Figure 4.110 shows the worn surface of the annealed coating on super-invar. There was fragmentation of the carbides, microcracking, and pull-out of the carbides due to binder removal.

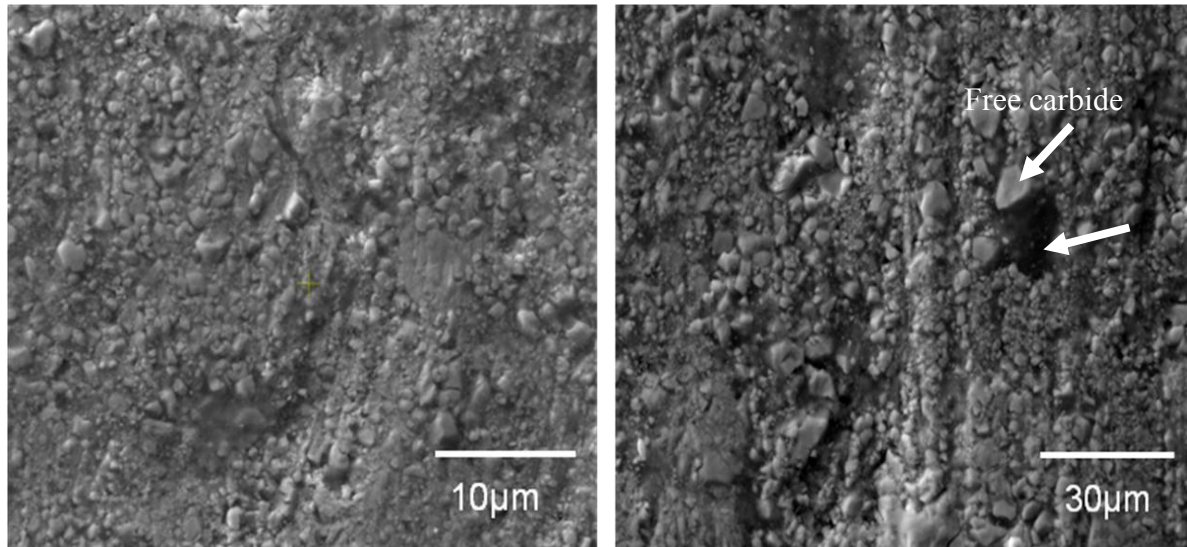


Figure 4.110. SEM-SE micrographs of the worn annealed WC-17Co coating surface on super-invar, showing fragmentation of carbides, microcracking and pull-out of carbides (shown by arrow) due to binder removal.

Overall, the abraded surfaces of the annealed coated samples were very similar, except that the WC particles were cracked, and sometimes pulled-out (shown by arrows in Figures 4.108 - 4.110). In the case of cracking in the coatings, the soft Co binder was first preferentially removed by the abrasion, resulting in the WC standing proud. At this stage, the abrasive particles repeatedly impacted the WC, and these repeated stressing caused the WC to crack, rather than the carbides being pulled out of the matrix. The probable reason could be that the bonding between the WC and Co binder in those regions was very strong. As a result, the fragments of WC were continuously removed as debris and the rate of removal of the WC controlled the overall abrasion rate. However, in the regions where pull-out was observed, the bonding between the WC and Co binder phase was weaker (due to the porosity) in the coatings. Thus, repeated stressing of the WC by abrasive impact causes pull out of the entire WC well before the WC can be cracked (2010Babu).

Correlation between the structure (substrate properties) of the materials and residual stress determined by X-ray diffraction were shown in Figures 4.111- 4.115 (with no error bars

shown on brass substrate, as the errors were small [Table 4.10]). The residual stress decreased with increasing coefficient of thermal expansion (Figure 4.111), slightly increased with increasing substrate melting point (Figure 4.112), decreased with increase in specific heat capacity (Figure 4.113), slightly increased with increasing specific heat capacity (Figure 4.114). Conversely, residual stress after heat treatment increased with increasing coefficient of thermal expansion (Figure 4.115).

The relationship between the wear loss and substrate properties are shown in Figures 4.116-4.119 (with no error bar shown, as the errors were small [Table 4.10]). No discernable relationship could be seen between wear loss and coefficient of thermal expansion (Figure 4.116). With increasing substrate melting point, the wear loss increases with a possible maximum at $\sim 1100^{\circ}\text{C}$ (Figure 4.117). No relationship exists between the wear loss and microhardness (Figure 4.118). Whilst, the wear loss decreased with increasing specific heat capacity (Figure 4.119), the wear loss on aluminum was very low.

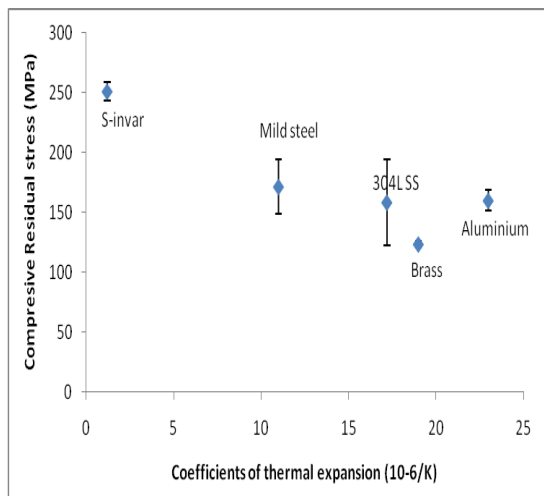


Figure 4.111. Correlation between the coefficients of thermal expansion and residual stresses of grit-blasted substrates

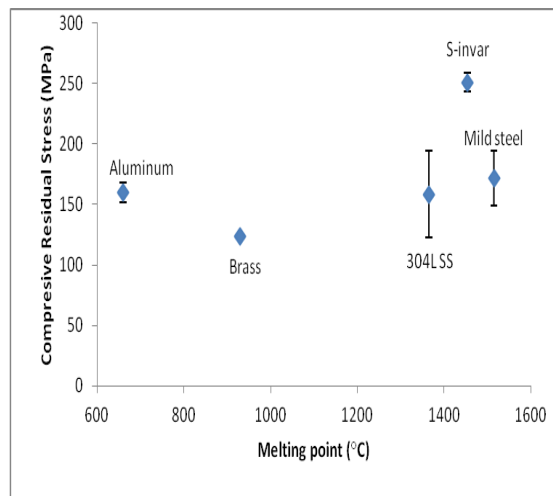


Figure 4.112. Correlation between the melting point and residual stresses of the grit-blasted substrate samples.

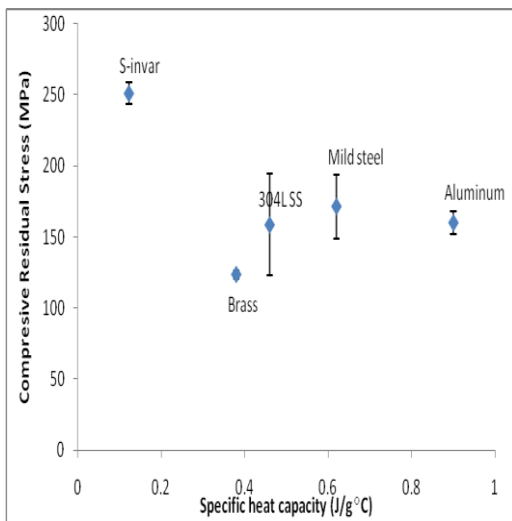


Figure 4.113. Correlation between the specific heat capacity and residual stresses of the grit-blasted substrate samples.

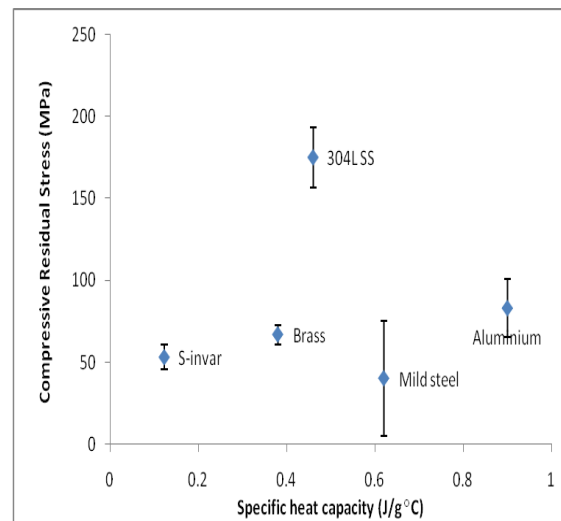


Figure 4.114. Correlation between the specific heat capacity and residual stresses of the annealed grit-blasted substrate samples.

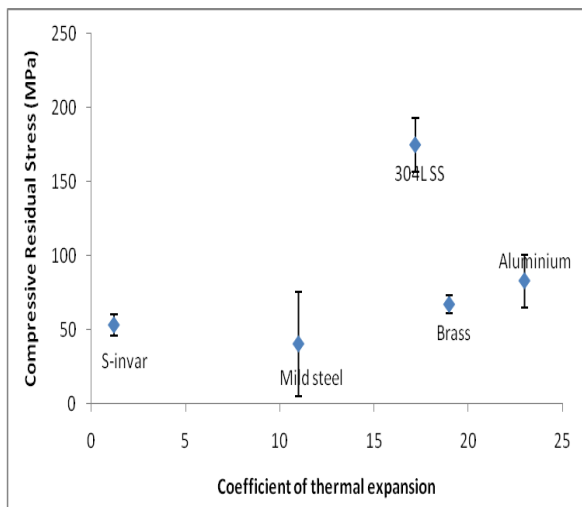


Figure 4.115. Correlation between the coefficient of thermal expansion and residual stresses of the annealed grit-blasted substrate samples.

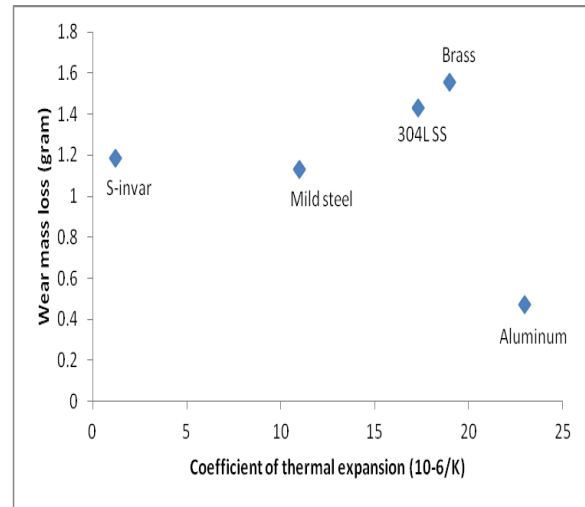


Figure 4.116. Correlation between the substrate coefficients of thermal expansion and wear loss, showing no discernable relationship.

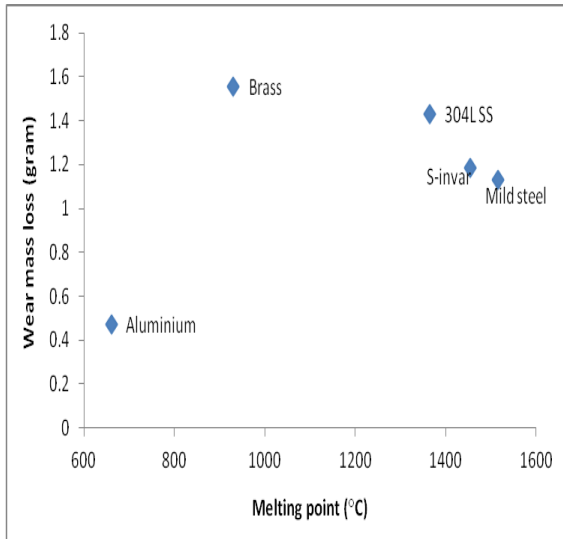


Figure 4.117. Correlation between the melting temperature and wear mass loss, showing a possible maximum at ~1100°C.

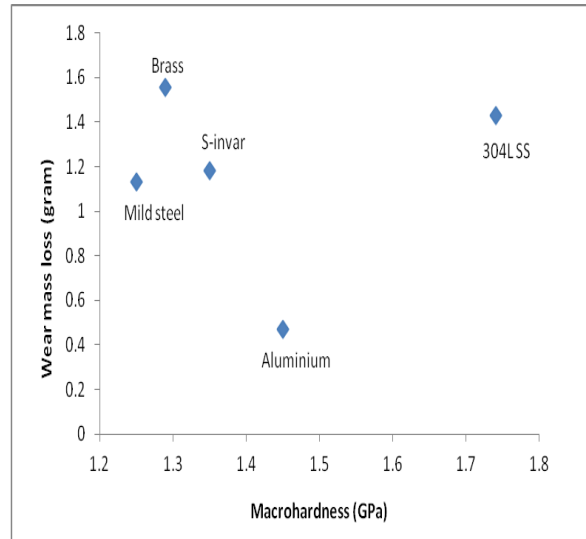


Figure 4.118. Correlation between the substrate macrohardness and wear loss.

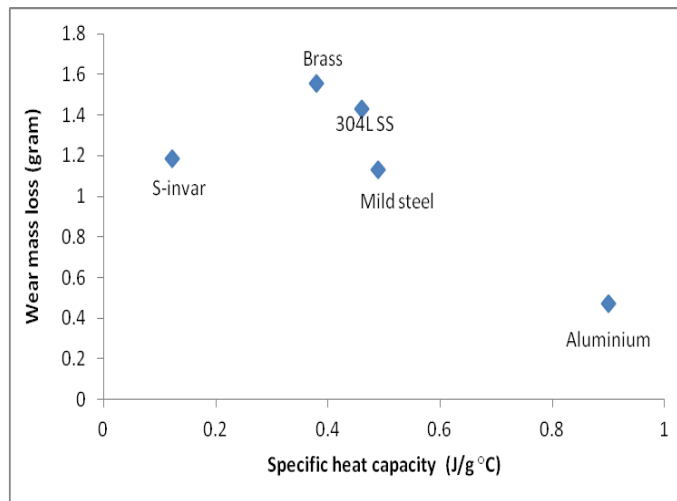


Figure 4.119. Correlation between the substrate specific heat capacity and wear loss of the substrates.

There was a correlation between the wear loss and the coating residual stress determined by neutron diffraction, as shown in Figure 4.120. Except for the heat treated mild steel sample, the samples with the lowest residual stress experienced the highest wear loss. Thus, the least

residual stress and highest wear was for super-invar, and the highest residual stress and lowest wear was for aluminium.

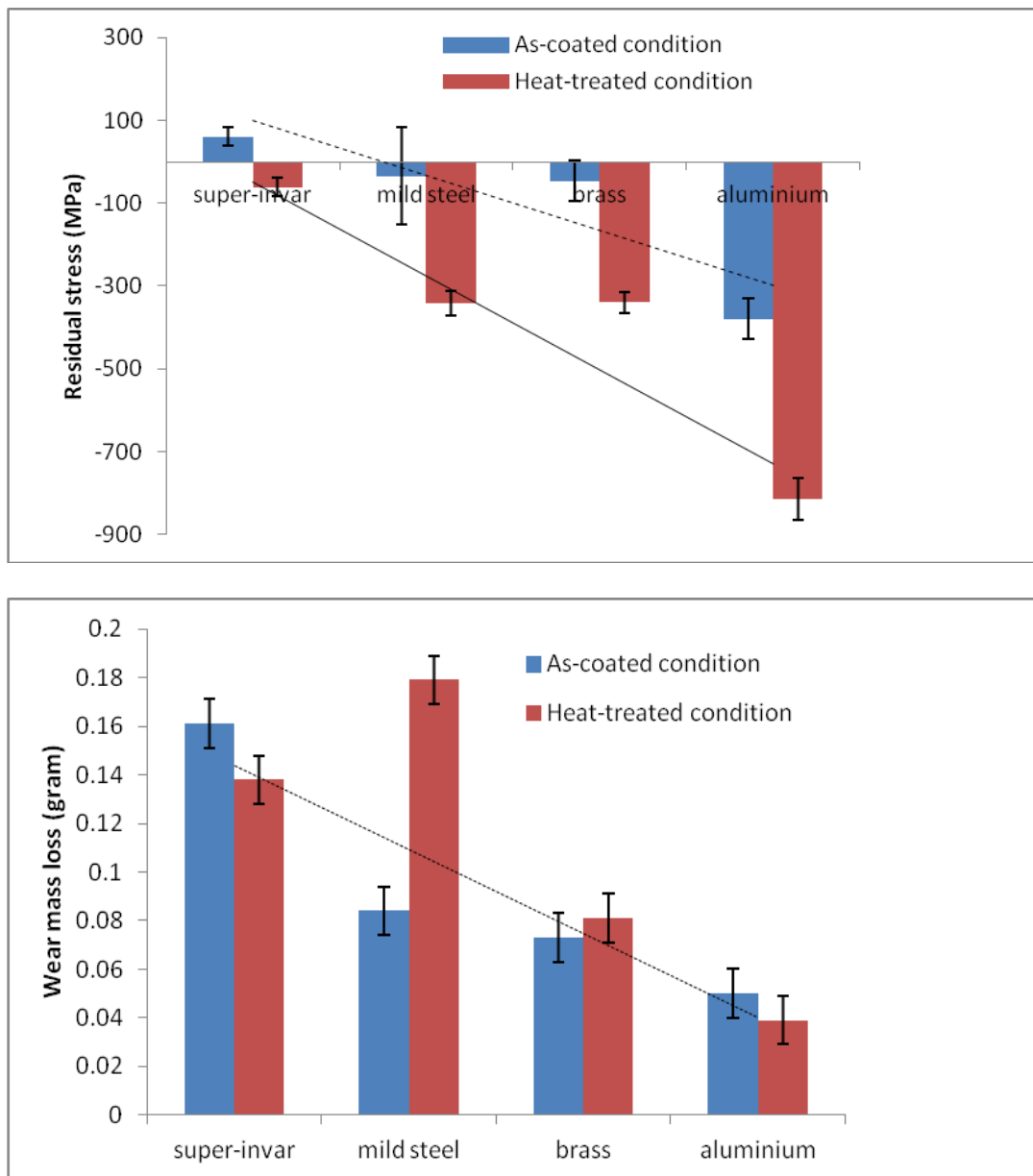


Figure 4.120. Correlation between residual stress (upper graph) and wear loss (bottom graph) of the as-sprayed and heat treated samples.

CHAPTER 5: DISCUSSION

5.1. Batch A (Commercial samples)

5.1.1. Effect of substrates on the microstructure of thermally sprayed WC-17wt% Co coating

The phases, grain size and morphology of WC-Co powder affected the mechanical properties of the coatings. The highest hardness was achieved for the aluminium as-coated substrate that contained the phases WC, Co and W_2C . The lowest coating hardness was observed for super-invar, which contained the phases WC, W_3C and Co. The coating on 304L stainless steel substrate also contained W_3C , but its effect did not appear to be as great as in super-invar. It appeared that W_3C was detrimental to hardness, whereas W_2C was not. Di Maio *et al.* [2005Mai] measured the microhardness of W_2C as $2980 \pm 100 \text{ kg.mm}^{-2}$ and W_3C as $2650 \pm 100 \text{ kg.mm}^{-2}$, but were not determined in the current work. Stewart *et al.* [2000Ste] found that W_2C formed on splat quenching and was caused by dissolution of WC in the Co matrix. Bouaricha *et al.* [2004Bou] reported that microhardness would be closely related to a coating's porosity level and degradation of the carbide phase during spraying. Several secondary phases appeared in the as-sprayed coatings, despite their absence in the starting material [2000Ste, 2006Cel].

It was expected that the hardness would decrease with increasing grain size in line with the Hall-Petch relationship, but this was not conclusive, with the small amount of data and large scatter (Figure 4.13). However, hardness decreased with increasing porosity, as expected (Figure 4.14). The microhardness increased with increasing coefficient of thermal expansion (Figure 4.15). Thus, coating hardness depends on microstructural features, such as the level of porosity and residual stress resulting from the coating technique. The porosities were below 0.7%, similar to the work of Zhao *et al.* [2004Zha]. The variations in porosity values across the different coatings might result from fuel gas flow differences during coating preparation, as observed by Arturas [2005Art], since the substrate material were different. The effect of flame conditions on the microstructure of the nanostructured WC-12Co coating was investigated by Wang *et al.* [2004Wan2] who found that the microstructure was significantly influenced by the ratio of the oxygen to fuel flow. Under conditions of lower oxygen/fuel ratios, the nanostructured coating presented a relatively dense microstructure and

severe decarburization of WC phase occurring during spraying. With increased oxygen flow/fuel flow ratios, the bonding of WC particles in the coating became less and the decarburization of WC-Co reduced, owing to limited heating to the powder.

The processing parameters could have had an effect [2005Art, 2006Dan] on the coatings of this study, since different parameter yield different coating properties. The surface roughnesses were expected to be good due to grit blasting the substrate before coating. However, microhardness increases with increasing surface roughness (Figure 4.16). With increasing melting temperature, the surface roughness decreased (Figure 4.17). Similarly, surface roughness increases with increasing coefficient of thermal expansion (Figure 4.18).

The differences observed in the coating results, such as size of WC grains, roughness, hardness, and new phases, occurred despite using same powder as a feedstock. These differences were deduced to be due to: the influence of substrate on coating; the properties of each substrate, which played a crucial role in the cooling rate of the samples after the coating deposition. The processing parameter of the coating techniques and substrates might have influenced the occurrence of the secondary carbide phases appear in the as-sprayed coating [2005Art].

In summary, the structure of WC-Co coatings sprayed by HVOF on different substrates gave different properties, despite using the same powder (WC-17 wt% Co) as feedstock. The occurrence of small amounts of W_2C and W_3C phases after coating could not be explained due to the substrate melting temperature as the decarburization occurred at both the lowest and the highest substrate melting temperatures. However, since the approach with this research was to characterize coatings on different substrates resulting from the standard individual HVOF coating procedure, the coating procedure was not strictly monitored or optimised.

5.1.2. X-ray diffraction measurement of residual stress in WC-Co thermally sprayed coatings onto metal substrates

From the literature it is known that the stress states of bulk WC-Co material were is compressive in the WC component, with the Co binder phase being in tension [2003Coa]. This is due to the lower coefficient of expansion of the Co binder than WC. The experimental results of the residual stresses in as-sprayed coatings for WC plane were quite different from each other (Figure 4.23), despite the same powder being used as the feedstock. There was a large variation in the residual stresses, albeit with large errors, and these did not appear to be related to coating hardness. These variations in the residual stresses might have been due to the following mechanisms:

- (1) differences in coefficient of thermal expansion,
- (2) decomposition of WC,
- (3) specific heat capacity of the respective substrate,
- (4) kinetic impact of the particle on the substrate during the HVOF process, caused by the heat transport from the coating to the substrate; as all play a crucial role in cooling and solidification of the coating after deposition (Table 3.2),
- (5) process parameters, and
- (6) surface morphology.

Wenzelburger *et al.* [2006Wez] reported that differences in residual stresses of coated systems can be attributed to four mechanisms:

- (1) melting behaviour of the spray particles in the hot gas jet,
- (2) impulse transfer of the impinging particles to the component surface,
- (3) heating of the component due to heat transfer from the particles and from the gas jet, and
- (4) the differences in thermal expansion of the coating material and the substrate.

Even without coating, laboratory X-ray measurements of WC-Co, particularly with Co or Cr radiation, will indicate surface stress, which is due to relaxation of the bulk thermal microstress, as shown by Krawitz *et al.* [1985Kra]. They demonstrated that using X-ray diffraction to measure the bulk thermal microstress is flawed, due to the geometric rotation and limited penetration depth. Thus, to compensate, the different contributions to the stresses need to be identified. For example, the unstressed values of the free WC is needed as well as

the coating, meaning that the d -zero of the loose powder or coating flakes must be measured. Another mechanism is to measure the stress while sequentially removing the substrate. The residual stress of the loose WC-17Co powder used for this research was determined as -3.8 ± 18.6 MPa. This was a very small value, and well within the range of ± 18 MPa expected for powder, found by Prevey [1996Pre]. However, the values of the residual stresses present in the coatings were very low. This could be due to flaws in the coating [1985Kra], localised microcracking within the coatings, surface roughness, as well as surface stress relaxation.

The as-sprayed coatings' residual stresses could be either tensile or compressive, depending on the difference between the coefficient of thermal expansion of the substrate material and comparison to that of coatings. The as-sprayed coating on super-invar produce a residual stress that was tensile and the rest were compressive, despite same powder and application process. This might be due to the following reasons:

- (1) lower thermal coefficients expansion of super-invar substrate (Table 4.1) to WC coatings;
- (2) microcracking due to residual stresses developed in the coating (Figure 4.9). These could act as stress concentrators that have lead to stress relaxation due to cracking,
- (3) high porosity and secondary phases (e.g. W_3C) were found on the as-sprayed coating on super-invar (Table 4.1 and Figure 4.2. The exact amount of W_3C on the surface was not known. Pejryd *et al.* [1995Pej] used modified layer-removal techniques to determine the through-thickness residual stress distribution present in the coatings. Coatings of WC-Co/Cr and WC-Co were deposited by HVOF process on a Ti-6Al-4V substrate. The residual stresses in the WC-Co/Cr coating were tensile, and compressive in the substrate near the surface. Conversely, the results of the WC-Co coatings were opposite to the system WC-Co/Cr, showing compressive stresses in the coating and tensile stresses in the substrate, despite similar processing and coating compositions.

Moderate compressive stresses found in as-sprayed coatings on brass, 304L stainless steel and aluminium substrates showed a greater effect of the peening mechanism of stress formation than thermal quenching. The peening effect (work hardening) resulted from bounced-off alumina particle. The addition of alumina to the substrate helps improving the coating deposition (Figure 4.21). Because alumina only plays a role during peening, roughen the substrate surface in preparation of the deposition and increased the adhesion of the coating on the substrate. Amirhaghi *et al.* [2001Ami] reported that both the thermal and the

intrinsic (from the coating process) stresses can contribute to the total residual stress in the coating. Intrinsic stresses can arise from impurities.

Many factors and parameters can affect the properties of the coatings, and make it increasingly difficult to directly compare results of coatings from other sources. Factors such as feedstock powder, spraying conditions, equipment, process parameters and substrates can all lead to large changes in the microstructure of the coating. Stewart *et al.* [1998Ste] found tensile residual stresses of 219 ± 12 MPa for a WC-17Co coating deposited on a mild steel substrate.

From the current work, a coating with low compressive residual stress (approximately 150MPa) would not cause a problem, such as spallation, because the stress would not be close to the yield strength of the coating. Conversely, the coating with a tensile stress coated super-invar, experienced microcracking and spallation failures that would be detrimental in service.

The coating microhardness increased with increasing coefficients of thermal expansion (Figure 4.15), despite secondary phases (W_2C and W_3C) being found on as-sprayed coating on aluminum and super-invar. Here, the different phase hardnesses (WC: $2350 \pm 100 \text{ kgmm}^{-2}$ [1985Vin], W_3C : $2650 \pm 100 \text{ kgmm}^{-2}$ and W_2C : $2980 \pm 100 \text{ kgmm}^{-2}$ [2005Mai]) did not appear to have an effect, and this was probably due to the small amounts of W_2C and W_3C . The residual stresses for super-invar, with a coefficient of thermal expansion 1.2 was tensile, but with increasing coefficients of thermal expansion, the nature changed to compressive, and subsequently increased (Figure 4.22). With increasing the specific heat substrate capacity, nature of residual stress changed to compressive and subsequently increased (Figure 4.23). (However, there were only four data points.)

The experimental results using a reflection of $\{112\}_{WC}$ showed that the residual stresses were quite different (Table 4.4). The compressive nature had a beneficial effect on the coating's adhesion and mechanical properties [2008San]. The reason for the compressive stress in the coated samples were the same as discussed for the reflection $\{202\}_{WC}$. There was a large variation in the residual stresses with large errors, and these did not appear to be related to the coating hardness, nor to the difference between the coating and substrate hardness or surface roughness.

No relationship could be seen with melting point and residual stress (Figure 4.24). The residual stress increased with increasing coefficient of thermal expansion (Figure 4.25). With increasing specific heat capacity, the residual stress increased (Figure 4.26). However, there are only four data points, so a relationship was difficult to discern.

The calculated penetration depth of Co-K α radiation was 3-4 μ m in WC. Therefore, X-ray diffraction analysed a near surface layer. The results could be an advantage for predicting near-surface residual stress changes in WC-cermets due to frictional and sliding wear, where the wear mechanisms, such as ploughing, abrasion etc. are related to very near-surface changes [Ola2012].

In summary, the residual stresses for reflection $\{202\}_{WC}$ were compressive on as-sprayed coatings on brass, 304L stainless steel and aluminium, whilst tensile stress was found on the coated super-invar despite the same powder being used as feedstock. The differences in the stress results, although small, were due to the role played by the coefficient of thermal expansion of each substrate during cooling. Microcracks were found in the coating on super-invar, which had a tensile residual stress, while the samples with compressive residual stress had no micro-cracks. A strong link exists between the residual stresses results and microstructure (in terms of nature of residual stress), as the microcracks found in the coated super-invar causes stress relaxation that yield tensile stress. The residual stress of the reflection $\{112\}_{WC}$ were compressive in comparison to reflection of $\{202\}_{WC}$ due to the differences in irradiated position used for the measurement.

5.1.3. Effect of substrate on the 3-body abrasion wear of HVOF WC-17wt%Co coatings

The investigation of the abrasive wear properties of the four coated substrates gave different wear resistances (Figure 4.28 and 4.29), despite using the same WC-Co feedstock powder. Despite having the highest hardness, the coated aluminium samples had the highest wear rate (Figure 4.29), and the highest level of Co binder removal (Figure 4.30). Removal of the binder phase provided stress relief to the carbides causing the carbide grains to crack as the stresses inside the grains are relieved. Cracking of the exposed carbide grains may also have occurred due to the micro-fatigue action of the abrasive against the carbide. These types of wear mechanisms, found on all the worn surfaces, are common in the abrasion of HVOF coatings [2006Mur]. The poor performance of the coated aluminium may also be attributed to the W_2C phase present in this coating (Figure 4.2), which was due to decarburization occurring during spraying [1992Ner, 1998Ver]. Engqvist *et al.* [1999Eng] reported that the hardness of the W_2C phase is 3000HV, which is higher than WC (HV=1300-2300). Therefore, the W_2C would increase the overall coating hardness, explaining why this coating had the highest hardness value. However, W_2C is brittle [2006Obe] and fractures easily during abrasion, which would reduce abrasion resistance. Therefore, the combination of high binder removal and eta phase contributed to the high wear rates observed for the coated aluminium, despite having the highest hardness.

The coated brass and super-invar samples were in the mid-range of mass losses for all the samples (Figure 4.28), and considering the small standard deviations (0.001) in mass loss, could be considered as having equal wear resistances. The coated super-invar had the highest porosity, lowest hardness, W_3C (HV = 2650±100 [2005Mai]) and micro-cracks (not present in the other coatings) which should have led to this coating experiencing the highest wear rate. The coated brass samples had the lowest porosity (Table 4.1), second highest hardness (Table 4.2), no eta phase or micro-cracks, and were therefore expected to have a lower wear rate than the coated super-invar samples.

The lowest wear rates, which indicate a better abrasion resistance, were shown by the coated 304L stainless steel samples. However, these coatings had only the third highest hardness and the second highest porosity (Table 4.1). The worn coated 304L stainless steel samples (Figure 4.33) appeared to have had a high degree of melting during deposition. This is known to lead to a better bond strength between substrate and coating [2000Ste], as well as better bonding

between the carbide grains and binder. This is probably the reason why there was very little binder removal, few cracked carbide grains and in general, smoother wear scars observed for this coating.

The paradox between the wear rates and coating properties such as hardness, eta phase and micro-cracking indicate that other factors played a role in the wear behaviour of these coatings, despite using the same feedstock powder and the same coating deposition parameters. The results indicated that coating hardness is dependent on substrate, therefore hardness, and consequently the wear response of a coating cannot be generalized for a specific coating, irrespective of substrate. It was expected that the coating hardness would decrease with increasing WC grain size (Figure 4.13) however the change in hardness is minor hence the carbide grain size does not contribute significantly to the differences observed in the wear rates. Hardness decreased with increasing porosity as expected (Figure 4.14). The variations in porosity across the different coatings might be as a result of fuel gas flow during coating deposition, as observed by Arturas [2005Art], since the substrates were different materials. However, the overall measured porosity levels were low, and with the exception of the super-invar sample, and similar for all coatings. Thus, the role of porosity in the observed wear response was considered minor. The differences in the hardness values of the coatings may be attributed to the role played by the substrate properties (Table 3.2) during cooling and solidification of the coating after deposition which influenced the residual stresses produced. The coating hardness was observed to increase with increasing coefficient of thermal expansion of the substrate (Figure 4.15).

The processing parameters during deposition are also known to affect coating hardness [2005Art, 2006Wez], although these were kept constant in the current study for all the coatings. During deposition, each powder particle is heated in the combustion chamber of the HVOF gun and then projected towards the substrate. On impact with the substrate, the liquid deforms into a lamella, which cools down and solidifies. The temperature of the combustion chamber could be as high as 3000°C, and then the temperature decreases depending on the difference between this temperature and the coating's melting range. Using forced cooling, the temperature of the substrate of a WC-Co coating was approximated to be 500°C by Stoke *et al.* [1999Sto]. The cooling of both substrate and coating after spraying leads to the formation of residual stresses in the individual lamellar structures.

In the current study, the contribution of residual stresses and strains on the wear performance of the different substrate-coating combinations was considered. The origin of residual stresses in coatings has been investigated by several authors [1998Sch, 1999Ste], who showed that the material and the deposition process may produce residual stresses which can cause a large mismatch between thermal, structural and mechanical properties of the layers and the substrates. For thermal spray coatings, quenching stresses due to rapid cooling of the coating, thermal mismatch stresses between the substrate and the coating and phase transformations during deposition have been identified as sources of residual stresses [1990Kur, 1998Mat]. Residual stress in the material can be tensile or compressive, and the nature of the overall residual stress in coated systems may be determined by criteria identified by Stokes and Looney [1999Sto] on the basis of the cooling stresses associated with the relative values of coefficients of thermal expansion between coating and substrate. The authors determined that a tensile stress would develop in the coating when $\alpha_c > \alpha_s$, while a compressive stress would develop when $\alpha_c < \alpha_s$, where α_c and α_s represent the values of coefficients of thermal expansion for the coating and substrate respectively. However, residual stress results (Table 4.3) is in agreement with this criteria identify by stokes and Looney [1999Sto].

In the current work (Figure 4.20), compressive stresses were found on the coatings deposited onto the brass, 304L stainless steel and aluminium substrates, whilst tensile stresses were found on the coated super-invar. These variations in the residual stresses were also considered to be similar to factors reported in Section 5.1.2, which are considered to play a crucial role in cooling and solidification of the coating after deposition [2006Wez].

The tensile stress in the super-invar coating likely led to the micro-cracks in the coating deposited onto that substrate. The same was found by Stokes and Looney [1999Sto], who realised that compressive stresses may lead to buckling or delamination of the coating. However, this was not observed on the coatings deposited onto the brass, 304L stainless steel and aluminium substrates which showed compressive stresses. The coated aluminium, which had the highest compressive stress, had the highest wear rate. As stated earlier, the preferential removal of the Co binder phase the carbide grains to crack, which then relaxed the residual stresses, as shown by re-measurement. The high stress levels (Figure 4.24) were considered to be the reason for the high degree of carbide grain cracking in the worn surface, which subsequently gave high wear rates. The coated brass samples showed compressive stresses and the coated super-invar had tensile stresses, yet the wear rates of the coatings on

these two coated substrates were similar. The coated 304L stainless steel, which had the lowest compressive stress, had the best wear resistance. Thus, the role of residual stresses on abrasion resistance is crucial.

Some understanding of the wear response of the different coatings may be gained from considering the interaction between the SiO₂ abrasive and the coating microstructures. The SiO₂ abrasive particle size ranged from 300 to 600 µm, while the average WC grain size of the coatings was in the range of 0.12 to 0.19 µm. On this basis, all the coatings responded homogeneously during wear, even though the Co binder was preferentially removed. The hardness of the SiO₂ abrasive is 800HV [1992Hut], while the hardness of the coatings ranged from 807 to 1042HV. The ratio of the hardness of the abrasive particles (H_a) to the hardness of the coatings (H_m) i.e. ($H_{\text{abrasive}} / H_{\text{material}}$) was in the range of 0.77-0.99. These calculated ratios are less than 1.2, which signifies the boundary condition between soft and hard abrasion defined by Hutchings [1992Hut], and would therefore place the abrasive wear of all the coatings in the soft abrasion category. This classification agrees with the extent of damage observed on the worn surfaces, where the soft Co phase was preferentially removed, while the hard WC particle remained largely intact. The SiO₂ abrasives (800HV [1992Hut]) were unable to indent and crack the WC particles (range of 807 to 1042HV) due to the differences in the hardness values. The applied stress (F/A) during abrasion was calculated to be 0.06MPa, but the actual pressure was expected to be higher than this, as the real contact area between individual abrasive particles and the coating surface was lower than the surface area of 420mm² used to calculate the nominal stress. The calculated yield strength of the coatings in Table 4.5 far exceeded the applied pressure, and indicated that all four coatings should have good abrasion resistance.

Strong correlations were observed between the yield strength, residual stress and wear rate of the coatings (Table 4.5). The higher yield strength samples had higher residual stresses, showing that the residual stress was proportional to the yield strength. The wear resistance of a coating increased with increasing residual stress and the yield strength. However, the discrepancy of the as-coated super-invar was due to partial stress relaxation, caused by the microcracking the coating.

In summary, the abrasive wear resistance of WC-17wt%Co thermal sprayed coatings deposited onto four different substrates yielded very different wear resistance characteristics,

despite being produced from the same feedstock powder and using the same deposition parameters. The highest mass loss was recorded for the coating on the aluminium substrate, while the coated 304 stainless steel showed the lowest mass loss. The coatings on brass and super invar experienced similar mass losses. The main wear mechanisms were preferential removal of the Co binder phase, as well as cracking and rounding of the carbide grains. The differences in wear behaviour may be related to residual stresses, where the highest compressive residual stress led to the highest wear rate. The coatings deposited onto brass had compressive stresses, while those on super-invar had tensile stresses, albeit low. However, the two coatings had similar wear rates, but the fine grain size in super-invar most likely compensated for its low tensile stress in terms of wear rates. Thus, the residual stresses only partially contributed to the differences in wear resistance, and the whole condition needs to be considered, although further study is required to provide conclusive evidence of the role of residual stresses on the abrasion resistance of these coatings.

5.2. Batch B (Substrate procured from Goodfellow in UK)

5.2.1. Microstructural characteristics of HVOF sprayed WC-Co coatings on metal substrates

The morphology of a dry and sintered powder (Figure 4.1) was relatively simple. The powder showed a dense structure with WC clusters cemented by cobalt, which were both identified from XRD and EDX. The cross-sections through the coatings (Figure 4.34-4.39) showed typical thermal sprayed microstructures. The noticeable features were the lamellar structure (due to individual splats forming layered structure), pores, and distinct differences in the WC particle sizes within the cobalt matrix. Rounded WC particles were also noticed on the coated brass sample. This was due to the high temperature reached inside the flame during the thermal spray process. In addition, localised microcracking was found. These surface cracks might have occurred as a result of both thermal expansion mismatch between the substrate and coating, as well as thermal stress generated during cooling and solidification of coating layers. The porosity was less than 0.8%. The difference in porosities within the different coatings was expected, since control of the process conditions was not optimized.

The WC particles after spraying showed decreased grain sizes (Table 4.6) from the starting powder grain size ($1.2 \pm 0.3 \mu\text{m}$). This might be attributed to the combination of three effects: localised microcracks found in the micrographs resulting from the thermal mismatch between the coefficient of thermal expansion of the coating and the substrate, which may have weakened the bond between WC particle and the binder. The rounding of the WC particles during spraying resulted from dissolution into liquid phase.

Comparison of the XRD spectra for the WC-17Co coatings with the feedstock powder (Figure 4.40) showed that no phase transformation occurred during spraying on 304L stainless steel, brass, aluminium and super-invar. However, a small amount of $\text{Co}_6\text{W}_6\text{C}$ (eta phase) was found in the as-sprayed coating on mild steel, and had been reported in coatings deposited by HVOF [2004Sto, 1996Ner, 2006Kha]. No metallic Co was found on as-sprayed coating on mild steel after deposition, suggesting that the tungsten and carbon diffused into the cobalt binder and formed eta phases [1998Vil], or XRD was not sensitive to cobalt [1996Li]. The occurrence of eta phase was probably as a consequence of the carbide or

tungsten dissolution and/or diffusion into matrix which led to a super saturation of the matrix. Therefore, it is believed that the degree of phase transformation could depend on the substrates' properties, which were different from each other. This decomposition is thought to be a major problem in the wear resistance of a coating, as it results in eta phase being part of the binder which is brittle [2003Sud]. In addition, there was an increased background of the WC-Co coatings in comparison to the feedstock powder (at a diffraction angle of 42° to 45°). This was due to the reduction in grain size or the effect of residual stresses in the coating, as a result of the high temperature associated with HVOF process.

Hardness is a vital mechanical property of the coatings that need to be measured to ensure reliability in the specific application [1994Tuc]. The coated layer provides wear resistance, while the substrate supports any impact to which the component (coating and substrate) is subjected. Hardness results (Table 4.6 and Figure 4.41) showed major differences between the coatings and substrates. This confirms the properties of WC-Co coatings, whilst the higher hardnesses of the coatings than the substrates as expected might be due to the following reasons:

- (a) contribution of grit-blasting (i.e. alumina) which was used in roughened substrate, and
- (b) cohesive strength of the individual splats as a result of the high impact velocity of the coating particles.

The highest hardness was achieved for the coated 304L stainless steel that had WC, and Co with low porosity. The coating on the mild steel contained $\text{Co}_6\text{W}_6\text{C}$ and WC, but the influence of the eta phase did not appear as large, perhaps due to lower porosity. The $\text{Co}_6\text{W}_6\text{C}$ phase was not detrimental to hardness, but only small peak of $\text{Co}_6\text{W}_6\text{C}$ was found. The lowest coating hardness was for the brass sample, which showed WC and Co, and might be due to the high porosity, despite the low mean grain size and beneficial homogeneous size distribution. The as-sprayed coating on aluminium also contained WC and Co, but its hardness was much higher due to the lower porosity, mean grain size and good homogeneous size distribution. The hardness decreased with increasing grain size (Figure 4.42) as the Hall-Petch relationship [1951Hal]. Hardness did decrease with increasing porosity, as expected (Figure 4.43). Moreover, differences in the hardness values of the coatings on the different substrates might be due to minor diffusion of elements from substrates to the coatings during deposition. Correlation also exists in the order of hardnesses between substrate and as-sprayed coating on 304L stainless steel, aluminium, and super-invar, but not on the mild

steel, due to the microcracking and level porosity in the coating (Figure 4.44). However, the mild steel substrate with a low hardness performed as well as those of relatively higher hardness. This anomalous behaviour suggested that apart from substrate hardness and effect of grit-blasting, there was another significant factor responsible for the mechanical properties of a coating. Related to this anomalous behaviour, the increased WC peak intensity of the coating showed that residual stresses were present. It is interesting that as-sprayed coatings rendered stresses that were both tensile or compressive for different samples (Figure 4.52). As-sprayed coatings on super-invar, mild steel, brass and 304L stainless steel produced residual stresses that were tensile. The coatings had localised microcracking, due to residual stresses developed within. The microcracking partially relieved thermal stresses in the coatings, thus leading to tensile stresses. Therefore, microcracking in the coatings demonstrated that the spraying parameters needed to be properly optimized. Montay *et al.* [2004Mon] found the evaluation of residual stresses to be crucial for investigations regarding coating/substrate adhesion, since the in-plane normal stresses may lead to cracking, spalling, or buckling in the coating layer. The residual stress found in the as-sprayed coating on mild steel was lower than the as-sprayed coating on the brass substrate, which might have contributed positively to the improvement in its hardness value. The higher tensile stress found on the as-sprayed coating on super-invar ($1.2 \times 10^{-6}/\text{K}$) might have been due to its low coefficient of thermal expansion compared to the WC-Co coating ($5.4 \times 10^{-6}/\text{K}$). Moderate compressive stresses in the as-sprayed coating on the aluminium substrate, despite little microcracking, showed the beneficial effect of peening on stress formation over thermal quenching.

The negative slope observed in Figure 4.47 corresponds to a compressive residual stress in the WC-17Co coating. The positive slope observed in Figures 4.48-4.51 corresponds to a tensile stress in the WC-17Co coating. Homogeneous stress in the WC-17Co coating is indicated by the linear behaviour of these data.

The residual stresses for the WC-Co coatings on different substrates (Figure 4.52) were quite different from each other, despite same powder being used as a feedstock. This was due to differences in substrate properties (Table 3.2) which played an important role in cooling, solidification and formation of the lamellae. Ricardo *et.al.* [2012Ric] found that for lower substrate temperatures, the morphology of lamellae was irregular splash-shaped. However, over the transition temperature of the substrate (melting point), the morphology of the

lamellar was rather short cylinders with higher contact area and stronger adhesion to the substrate. Residual stresses results of Batch A samples (Section 4.1.2) suggested that the differences in residual stresses of as-sprayed coatings could be attributed to decomposition of WC, and specific heat capacity of the respective substrate (Figure 4.23), kinetic impact on the substrate during HVOF process, caused by the heat transport from the coating to the substrate, as well as surface morphology.

X-ray diffraction measurements have a lower penetration in the WC-Co coatings. The results showed moderate residual stress on the as-sprayed coating on mild steel, whereas the stress on the substrate was very small. The predicted stress value (derived from the stress balance condition) and experimental value was estimated at -36 ± 118 MPa and 28 ± 334 MPa respectively.

However, differences between coating characterization and stress results of batch A (commercial substrates) and Batch B (substrates procured from Goodfellow) were due to differences in thickness, which induced different cooling rates and interactions with the incoming droplets.

In summary, the microstructural characteristics of HVOF sprayed WC-Co coatings deposited on five different substrates were different, despite, being produced from same feedstock powder and using the same deposition parameters. The as-sprayed coating on 304L stainless steel had the highest macrohardness and lowest porosity. XRD on the coating showed mainly WC, with Co and $\text{Co}_6\text{W}_6\text{C}$ as minor phases. The residual stresses of as-sprayed coatings on 304L stainless steel, mild steel, brass and super-invar were tensile, due to microcracking found in the coating (releasing the stress), whilst a compressive stress was found in the as-sprayed aluminium, despite little microcracking. This shows the effectiveness of peening on the stress formation over thermal quenching.

5.2.2. Systematic investigation of residual strains associated with WC-Co coatings thermal sprayed onto metal substrates

The depth resolved strain variation in the as-received brass substrate sample displayed a significant oscillatory variation with depth, reminiscent of the cold working production. This complicated determination of the unstrained lattice parameter reference which was required for the strain conversions. This was addressed by calculating the lattice parameter that would render the normal stress component to be zero, i.e. assuming a bi-axial stress condition throughout. The value calculated with this approach gave a result similar to that of the lattice parameter averaged for both measurement directions as function of depth through the sample thickness. Even though the lattice parameter through thickness for the invar parent material was more constant, a similar approach was followed with the strain determination for the super invar samples. The unstrained lattice parameter for the WC phase was determined from coating flakes chipped from the coated samples.

The strain results shown include all data points measured without smoothing. Significant systematic variations were observed in the X-ray synchrotron results of the brass, super-invar and 304L stainless steel samples. This was attributed to the small gauge volumes analysed that were susceptible to grain size, systematic errors and orientation effects [2004Ste]. The gauge volume is a trade-off between the need for spatial resolution within the expected strain field and the time available for data collection [2012Ros]. In the neutron diffraction data, the strains were averaged over larger gauge volumes, rendering smoother data lines, at the cost of lower positional resolution, especially close to the surfaces where steep strain gradients were observed in both the grit-blasted and as-coated samples.

The grit-blasted samples indicated substantial surface and subsurface modification in both substrate materials. Upon the rebound of the shot, together with the restraining influence of the deeper unaffected material, elastic recovery induced residual stresses parallel to the surface, while the metal beneath had reaction-induced tensile stress. The normal components acquire large tensile strains, with the in-plane components being compressive to depths of 0.5 mm for the synchrotron results, and approximately 0.8mm for the neutron results. The compressive nature of in-plane component after grit blasting compared to the parent material originated from the localized plastic deformation inherent to the grit-blasting effect, giving work hardening. The depth of this deformation depends on the blasting intensity. As a

comparison, in steel the depth deformation due to shot peening at intensity level 6A, only extends 0.2 mm [2008Zha]. Thus, the grit blasting surface preparation was more severe than the traditional shot peening that is routinely applied to sample surfaces prone to stress corrosion cracking or fatigue. The compressive residual stress resulting from grit blasting is directly dependent on the blasting pressure, grit size, and distance from the substrate surface [1997Mel, 2009Cha]. The blasting intensity can be determined with the curvature method. The intensity of the grit blasting used in the sample preparation of this study was not quantified, since the standard industrial HVOF procedure was applied. All the samples of this study were done sequentially with the same set-up, keeping conditions the same.

The magnitudes and depth dependence of the as-coated brass and super-invar samples (Figures 4.53-4.56) had strain magnitudes and depth dependences similar to those observed on the equivalent grit-blasted samples. The strains in the WC coating determined from the Synchrotron results (Figures 4.53 and 4.55) gave comparatively small residual strain values for both the in-plane and normal strain components. The strains displayed a gradient dropping off from the surface to the coating-substrate interface region. Both WC peaks used in the analysis, $(101)_{wc}$ and $(112)_{wc}$, gave similar results, although only results for the $(101)_{wc}$ reflection are reported. The low magnitudes for the strain values were ascribed to the high stiffness of the WC hardmetal. (modulus of elasticity of 722 GPa) were compared to brass (122 GPa).

Significant compressive stresses were observed at the near-surface regions of the grit-blasted and coated samples. The magnitudes of the synchrotron results were significantly larger than those for neutron plot (Figures 4.54 and 4.56) due to the better depth resolution attained with the significantly smaller gauge volume. The neutron results were averaged over larger gauge volumes. The systematic approach followed revealed that the primary origin for the substantial increases in residual stress in the near surface regions was the grit blasting surface treatment, with minimal apparent changes in the results between the grit-blasted and as-coated samples.

The depth resolved results for both in-plane and normal components of strain for coated 304L stainless steel determined from the synchrotron Figure 4.57. The stress in the as-received parent material remained constant throughout the sample thickness within the systematic scatter observed. The grit-blasted substrate had substantially altered residual strains at the

surface in both strain components. In the WC coating, both components of strain were unusually small, with a large discontinuity at the interface. The magnitude and depth dependence of the overall strain field in the as-coated substrate was similar to that of the grit-blasted substrate.

In the coated systems for brass, super-invar and 304L stainless steel (Figures 4.58-4.62), the in-plane stresses in the WC phase showed depth dependence initially increasing in magnitude to a peak at approximately mid coating thickness, then decreasing as the interface was approached. The maximum tensile stress did not exceed 250 MPa. A similar depth-dependence was observed by Stoica *et al.* [2004Sto2] from synchrotron investigations of WC-Co deposited on steel substrates using the $\sin^2\psi$ technique at two different beam energies (15 and 25 keV), and the penetration depth was estimated as 5 μm . Their results gave compressive residual stresses in the range -270MPa to -332MPa for the as-coated conditions. Overall, the trends determined for the stresses in the WC coatings were similar.

The results obtained from the substrates indicate that the HVOF process was not influenced by the differences in CTEs of the substrate materials. Furthermore, notwithstanding the impact nature of the HVOF process, little significant additional stress contributions from the kinetic impact energy of the splats were evident. Thus, minimal thermal energy transfer took place between the coating splats and the substrates, without producing any thermal stress. The lower stresses in the coatings were possibly due to the localized microcracking associated with the molten spray splats being quickly quenched to the substrate temperature. The underlying substrate constrained the thermal contraction of the splats, resulting in tensile stresses in the splats that exceeded the breaking strengths of the material, leading to repeated relaxation through microstructural cracks (remembering the brittle nature of the cermet). Since the grit blast stress condition was not altered in coated brass sample, it is an indication that the substrate was not heated to any significant extent. The normal stress relief annealing temperature of brass is 375°C (selected as 40% of the substrate melting point).

There was a good agreement between the neutron and synchrotron results for the residual stresses in the substrates (i.e. parent material). This was due to the substrates of Batch B samples having better quality, and the suitable parameters employed for the diffraction measurements. Batch A samples had lower quality, having coarser grain structure and more

texture (preferred orientation). However, the microcracking found in the coatings of both batches could be due to deposition parameters which were not optimized.

Direct quantification of the contributions due to grit-blasting and the coating process were attained by considering the plastic strain profiles (eigenstrains) rather than the residual stresses [2008Zha].

It is important to evaluate not only the surface and maximum subsurface values of the compressive residual stresses, but also the depth of the plastically deformed layer. Since depth resolved strain information exists, assessment of the strain results enables non-destructive assessment and quantification of the respective contributions. Residual stress characterization along the sample depth into regions dominated by contributions from different deformation processes allowed for the grit-blast and coating near surface permanent strains to be extracted from the residual strain profiles. The strain profile below the treated surface was a combination of elastic bending and the remaining residual compression near the blasted surface caused by the permanent stretching from the grit impact. Grit-blast and coating associated induced plastic strain profiles were determined by subtracting the residual stress profile from the straight line fitted to the elastic bending profile observed below the surface-treated layer.

The plastic strain (eigenstrain) profiles for the respective grit-blasted substrates with the superposed coated sample results are given in Figures 4.63-4.65. The small differences between the plastic strain after grit blasting and the as-coated condition indicate the higher effect of the peening mechanism than thermal stresses in the as-coated samples.

Thermal treatment could alter the stress state, arising from the differences in the CTEs between the coating and the substrates. Luyckx *et al.* [2007Luy] annealed above 600°C to induce recrystallisation of the amorphous Co binder phase, forming $\text{Co}_6\text{W}_6\text{C}$ and $\text{Co}_2\text{W}_4\text{C}$ eta carbides. The residual stresses in the coating became progressively more compressive with increased annealing temperature, which improved abrasive wear resistance.

Order of magnitude correlation was observed between the average residual stress determined in the coating by X-ray diffraction (XRD) and that measured at the near surface region with X-ray synchrotron (SR), but they were quite different (Table 4.7). This is due to differences

in gauge volume or collimator (between the measuring techniques) used for the measurements, as well as their penetrating depths. Comparison of the residual stress in grit-blasted substrates measured by XRD showed lower compressive values to SR. The differences are attributed to the depth of measurement: XRD measuring to depths limited to 2 micrometers, whilst the values reported for SR are averaged over all data points through depth. This could also be related to reverse yielding of the material regions close to the surface. The residual stress in as-coated coatings measured by XRD and SR had similar residual stresses but different values, due to the differences in their spatial resolution.

In summary, the residual stress results of the synchrotron and neutron techniques employed in the non-destructive characterization study of HVOF coated substrates gave qualitatively similar results in accordance to the respective gauge volumes employed. The systematic approach clearly showed that the WC-Co thermal sprayed coating process itself of brass, 304L stainless steel and super-Invar did not really contribute significantly to the residual strains in the substrates. The large strain / stress misfit between the coating and the substrates originated primarily from the grit-blasted surface preparation of the substrates and extended 0.5 mm into the substrates. The residual stresses in the WC coatings had a parabolic dependence with depth, initially rising from a low value on the surface to a maximum tensile stress at around the mid coating thickness, not exceeding 400MPa, decreasing to the coating-substrate interface. It thought that the generally low stresses in the coatings originated from localized relaxation due to microcracking.

5.2.3. Residual stress in thin WC-Co coated systems studied by high-precision neutron diffraction

The residual stresses in the as-sprayed WC phase coatings (Table 4.8) determined under the different conditions were compressive, but quite different on the brass, aluminum and mild steel substrates. There was good agreement between the direct (experimental) and indirect measurement method (Utilizing stress balance principle from the substrate stress profile via Stoney approach [1996Cly]). The compressive stress might have occurred due to the following reasons:

- (a) Higher coefficient of thermal expansion of the substrates than coating,
- (b) Greater effect of the peening mechanism of stress over thermal quenching due to the high particle velocity of JP5000 spraying.

It would be expected that surface preparation (grit-blasting) plays an important parts on the coating adhesion, as well as coating quality (durability). The substrate has to be properly prepared in order to remove contaminants, moisture, corrosion products, to achieve maximum coating adhesion. Jianhong *et al.* [2008Jia] worked on the influence of grit-blasting and thermal spray coating on the performance near the surface on the substrates. The results showed that both the grit-blasting process and thermal spraying process harden the substrate and microhardness on or near the surface.

The as-sprayed coating on the mild steel substrate had a tensile residual stress of low magnitude, and the rest were compressive, despite the same powder and application process. This behaviour might be due to the following reasons:

- (a) Microcracking due to residual stresses developing in the coating.
- (b) New phases (C_6W_6C) that have been produced in the previous amorphous area (in Figure 4.40).

After heat-treatment, the stresses were almost ten times higher than the as-sprayed coatings. These larger compressive values demonstrated the effect of temperature and the coefficient of thermal expansion of the coating and substrate materials. Similarly, the rate of

cooling/heating during post-treatment can significantly influence the residual stress or strain profile, which was not considered in this research work [1990Kur, 1990Gil, 1991Kur2].

Results of the stress profiles measured in the mild steel substrate sample are shown in Figure 4.66. Figure 4.66b shows a change in slope of the stress profile, while that in Figure 4.66a was small and almost invisible. The differential stress distributions (differences between coated samples and substrate-only samples) are given in Figure 4.67 for both conditions investigated. For the as-sprayed sample, stress in the substrate was very small and the predicted stress value in the coating derived from stress balance condition was estimated at -36 ± 118 MPa for mild steel, and -47 ± 48 MPa for the brass. Relatively large errors resulted from the lever rule applied and error propagation, so that ratio between the error in coating (~ 118 MPa) and an individual error in substrate (~ 10 MPa) are related by a factor $t_{subs}/t_{coat}/\sqrt{N_{subs}}$, where N_{subs} is the number of measurement points taken in the substrate [2012Ven]. Thus, with the given thickness ratio, significant accuracy improvement can be achieved by measuring more points or/and with better accuracy. Although uncertainty of ~ 100 MPa might be seen to be large, for the annealed sample it can be considered as acceptable with stress value in coating -340 ± 80 MPa on mild steel. This unambiguously demonstrates that a substantially larger compressive residual stress developed after thermal treatment. With heat-treatment, the initial stress distribution with characteristic peening stress in the substrate disappears. The newly-formed stress was thermal and originated from the fact that CTE of mild steel and brass is larger than CTE of the WC coating which generated compressive stresses in the coating when the system was cooled from the stress-relieve annealing temperature.

The stress profiles measured in the as-sprayed grit-blasted sample and its stress-relief annealed counterpart of aluminum were expected (Figure 4.68). For the as-prepared condition the near surface, stress was dominated by the shot blasting surface preparation that induced approximately -75 MPa at the surface, decreasing with depth, to have no further influence deeper than 0.7 mm. A non-linear trend was observed in the back part region of the sample. In the annealed aluminium sample, the compressive stress due to the cold work shot-blasting contribution, as well as the non-linearity of the stress profile through thickness, had been removed.

In Figure 4.69a, the aluminum substrate of the as-coated sample did not show significant change in stress at the coated surface side, but had a clear alteration on the back surface region, possibly resulting from stress relaxation due to heat input associated with the HVOF coating process. The annealing treatment (Figure 4.69b) did not give a significant change in the stress in the substrate material, but increased the compressive stress in the coating. The general approach followed in determining the contribution purely due to the coating process alone is to subtract the stress of the grit-blasted samples from their counterpart coated samples. However, due to the non-linearity in the as-prepared grit-blasted aluminum sample and the change in results in the back region of its as-coated counterpart, this procedure could not be applied. An alternative approach was followed by modelling the profile in the as-coated sample as comprising a linear contribution due to the coating with a typical peening (grit-blasting) characteristic superposed at the coated surface side. The stresses calculated in the WC coatings by imposing a stress balance were determined to be -378 ± 50 MPa and -814 MPa for the as-sprayed and stress relieved conditions.

For super-invar, two approaches were tested in order to measure residual stress in 200 μm thick WC coatings using neutron diffraction. It was shown that in materials with high absorption of neutrons (for example, Ni in the super-invar), the direct measurement of the thin WC coatings were not an optimal strategy because of large losses on neutron beam. In these materials, the indirect derivation of the stress in coating through the stress/momentum balance condition, when stress profile is accurately measured through thickness, is the best option.

It is thought that the greater advantage of neutron diffraction over X-ray measurement was due to its ability to determine the values for d -zero (unstressed material) from the coating flakes (unlike X-ray diffraction where no d -zero values were measured). These coating flakes would have been free of macrostress between the coating and substrate, although d -zero material would only contain microstresses. Krawitz *et al.* [2013Kra] demonstrated that neutrons enable the study of thermal residual microstresses in cemented carbides, due to their much greater penetration, because they are unchanged particles. The bulk microstress or coating macrostress present in the 200 micron coating was not determined in this research work. It is thought that the bulk thermal residual microstresses in WC based systems change substantially under the action of tensile and compressive load, and contribute significantly to the high toughness of the coating.

Many factors and parameters, such as thermal history and deposition parameters, make it increasingly difficult to directly compare results of coatings from other sources [2012Ola]. Stokes and Looney [2004Sto] determined the residual stresses in WC-Co coatings by an analytical method similar to that of Clyne *et al.* [1996Cly], and reported tensile stresses of 82 MPa and 15 MPa for coatings of thicknesses of 200 and 600 μm respectively. Stoica *et al.* [2004Sto2] determined the residual stresses of WC-12Co coatings deposited by HVOF, employing Synchrotron XRD at 15 and 25 KeV. They found that the values of residual stresses before wear tests were -270 MPa, with the maximum being at -332 MPa. Ahmed *et al.* [2007Ahm] investigated the influence of vacuum heat treatment on the residual stress of thermal spray cermet coatings using neutron diffraction. They observed the average values of the stress in the as-sprayed and heat-treated coating layers to be -553 MPa and -492 MPa respectively. The changes in the stress gradient after the heat-treatment, was related to the microstructural changes, caused by diffusion zones at the coating - substrate interface. The residual stresses of this investigation were much lower than those of Ahmed *et al.* [2007Ahm], which could be due to differences in feedstock powder, annealing temperature, process, substrates and surface roughness. There was a concern that the stresses were too small to have an effect on the abrasion resistance, although Figure 4.120 shows that the abrasion resistance decreased with increasing residual stress. It is thought that the low residual stresses measured in the as-sprayed coatings could be due to microcracking, and the influence of the substrate on the coating and porosity. Porosity has been shown to affect the tensile bond strength of the coating [2010Bab].

In general, the difference between the residual stress values observed and those in the literature depend not only on the technique and deposition parameters, but also on the method employed for deposition, which can as well have different phases, resulting in residual stresses as the volume changes due to thermal expansion [1995Pej].

A strong correlation between residual elastic strain (stress) and the thermal expansion of the substrate material was observed (Figure 4.70). The highest strain was observed in aluminium substrate samples ($\text{CTE} = 23 \times 10^{-6} \text{ 1/K}$), while the smallest strain was in the super-Invar samples ($\text{CTE} = 23 \times 10^{-6} \text{ 1/K}$). This suggests a thermal origin of the residual stress in the coating/substrate system for both as-sprayed and annealed samples. The fact that residual stress/strain was larger in the annealed series was most likely due to quenching (solidification of the molten particles) contributing tensile stresses into the total balance, producing less

compressive stresses for the as-sprayed condition. Other factors (e.g. difference in heat dissipation or interplay of several phases and their transformation during HVOF spraying in comparison with annealing process) can also lead to a shift in the stress balance. In-addition, the reduction of the broadness the XRD peaks in Figures 4.79 to 4.83 compared to the as-sprayed samples indicated that much of the plastic damage was relieved, and so the much higher stresses, due to differential shrinkage (due to the different coefficients of expansion) on cooling was established.

In summary, the detailed residual stress profiles allowed a direct comparison of the various regions of interest in the thermal spray coating system, i.e. coating, coating-substrate interface, as well as the substrate. The measured results in the thin coatings showed favourable agreement with a stress balance (Stoney) approach [1996Cly] using the through thickness stress profiles in the substrate materials. It was shown that in coating materials with high absorption of neutrons (Fe, Ni), the direct measurement of the thin WC coatings was problematic because large losses from neutron beam.

5.2.4. Effect of heat treatment on the microstructure and abrasive wear of thermal sprayed WC-Co coatings

The characterization of the as-sprayed coatings was fully discussed in Section 5.2. Cross-sections of the microstructures of the as-sprayed coatings showed typical lamellar structures, varying porosities, rounded WC particles and distinct differences in WC carbide grain sizes. After the annealing, the coating cross-sections (Figures 4.71-4.78) showed a wide distribution of equiaxed WC grain sizes, a noticeable lamellar structure and a reduction of the porosities. The EDX results indicated that both as-sprayed and heat treated coatings were composed of W, C and Co which constituted the WC grains and cobalt binder phase. In addition, localised microcracking was found in the cross-sections of the annealed samples. These microcracks might have occurred as a result of thermal mismatch between the substrates and coatings, and from the thermal stresses generated during cooling and solidification of coating. (The cracks may also due to the relaxation of the stresses as well as sample preparation prior to microscopic evaluation.) Surprisingly, nickel was found in the annealed as-sprayed coating on super-invar substrate after the heat treatment. The nickel of small amount is thought to have originated from the super-invar substrate ($\text{Fe}_{66}\text{Ni}_{34}$), and confirmed that diffusion took place between the coating and substrate.

Comparison of the WC grain sizes (Table 4.9) of the annealed and initial as-sprayed coated samples shows a reduction after annealing. This could be due to the partial dissolution of WC, as well as localised microcracking in the coatings. Therefore, reduction of the WC grain sizes after heat treatment might improve the wear resistance due to the Hall-Petch relationship [1951Hal]. It has been shown that heat treatment of these coatings significantly improved the erosion resistance under the high velocity impact conditions [2004Mat].

Porosity is an important feature that influences the coating properties. It is believed that porosity is undesirable, as it leads to poor coating cohesion/adhesion, premature coating cracking, and delamination or spalling [2005Cra]. The annealed coated samples had less porosity (less than 1%) than the as-sprayed samples. Crawler [2005Cra] reported that one of the sources of porosity was shadowing due to the angle of impingement of the spray stream. It is associated with the amount of unmelted particles that become trapped in the coating. Reduction in porosities after heat treatment could be due to effect of temperature on the coating microstructures.

XRD analyses (Figures 4.79-4.83) showed no new phases were produced after annealing, although the Co peaks became more clear and all the WC peaks became sharper on the coated 304L stainless steel, super-invar, brass and aluminum substrate samples. This could be due to either diffusion equilibrating the different cell sizes, and the reduction in stress. In addition, a noticeable reduction in the XRD intensity with a shift of 0.1° in the diffraction angle was found after heat treatment. This shift of the Bragg angles was due to the elastic changes of lattice spacing, from the relief of the residual stresses on annealing. On the other hand, complete transformation of amorphous phases to crystalline eta phases ($\text{Co}_6\text{W}_6\text{C}$) were found on the coated mild steel substrate, as well as a decrease in the intensities of WC after heat treatment. This could be due to the dissolution of WC in cobalt, and increased formation of eta carbide [2006Kha]. Chang *et al.* [2012Cha] reported that rapid splat cooling encouraged the formation of the eta phase. Annealing at 600°C - 700°C led to recrystallisation of the original amorphous phase into $\text{Co}_6\text{W}_6\text{C}$ and metallic cobalt.

Hardness can be used to determine some mechanical properties of a material. Decreased macrohardnesses of the substrates were found after the heat treatment (Figure 4.84). There were small reductions between 0.66% - 3% on super-invar, 304L stainless steel and mild steel substrates, whilst higher reductions of 33% and 48% were found on brass and aluminum substrates after heat treatment. These differences are likely due to stress relief of the substrate. The greater hardness reduction in the aluminum and brass substrates were due to their lower melting points, which caused larger stress relaxation after being heat treated at 375°C , compared to the other substrate.

Comparing the macrohardnesses of as-sprayed and annealed WC-17Co coatings (Figure 4.84), an increase of 10% was found on the coated mild steel after heat treatment which is attributed to the increased formation of the hard eta phases after annealing (Figure 4.82). Conversely, a reduction was found on the remaining coated substrate samples. Hardness reduction of about 30-32% was found on the annealed coatings on aluminum and 304L stainless steel after heat treatment. This could be due to the effect of stress relaxation in the coating. A reduction of about 1% on coated super-invar and 7% on coated brass substrate after heat treatment indicated low stress relaxation occurred in the coating. Also, a reduction in the porosity, small grain size on annealing could contribute to the reduction in their macrohardnesses. It was proposed that up to approximately 600°C , the decrease in the

hardness of WC-Co alloy was due mostly to the softening of the individual phases (WC and binder), while above 600°C, the softening of the WC-Co alloys is mostly due to easier slip transfer across grain boundaries [1998Mil]. However, the mechanism mentioned above could play an important role in the hardness results of the coated substrate samples.

The experimental residual stresses on the grit-blasted samples (Figure 4.85 and Table 4.10) were quite different from each other, despite using the same alumina for grit-blasting of the substrates. There were large larger errors. The differences between the residual stresses of the grit-blasted materials might be due to the following reasons:

- (1) Influence of substrate roughness after blasting with alumina grit,
- (2) Differences in work hardening coefficient of various metal substrate after grit-blasting [2005Osa], and
- (3) Work hardening effect on the substrates, since, grit-blasting was carried by a pressurised air stream which hurled the grit against the surface of the workpiece (Figure 4.68 and 4.69).

All the grit-blasted samples had compressive residual stresses, which agreed with Chander *et al.* [2009Cha]. Wisdom dictates that the coefficient of thermal expansion and specific heat capacity does not influence the grit-blasting, since the process is being carried out under cold working condition. Nevertheless, correlation exists between the stress and substrate properties. The compressive residual stress of the grit blasted samples decreased with increasing coefficient of thermal expansion (Figure 4.111). With increasing melting point of substrate, the compressive residual stresses were decreased (Figure 4.112). The residual stress at specific heat capacity of 0.123 J/g°C (super-invar) was extremely high, but with increasing specific heat capacity, the residual stress value increased (Figure 4.113).

Comparison of the grit-blasted and annealed grit-blasted samples (Figure 4.85) showed a greater reduction in the cold working process after heat treatment. This is due to the stress relief followed heat treatment. There was higher stress relaxation in the samples with larger substrate coefficients of thermal expansion, compared to those samples with low coefficients of thermal expansion.

The nature of residual stress on the as-sprayed coatings was both tensile and compressive. Low tensile stresses were found on the as-sprayed coatings on 304L stainless steel, mild steel,

brass and super-invar substrates, whilst a moderate compressive stress was found on the coated aluminum substrate. The full discussion on the as-sprayed coatings is given in Section 5.2. After heat treatment, the nature of the residual stresses in the as-sprayed coatings changed to compressive. This could be due to the higher effect of the peening mechanism of stress formation over the thermal quenching stress; the effect of the coefficient of thermal expansion of the sample (larger coefficients giving larger expands); and the various stress relaxation mechanisms that could operate during annealing [1998Ste, 2002God]. Moreover, the moderate compressive stress in the coated substrate samples following heat treatments, could be due to partial relaxation of the stresses in the coatings owing to low material substrate strengths at that temperature, as well as development of the stresses on cooling where the substrate contracted more than the coating, putting the latter into compression [1998Ste]. The initial trend or correlation that existed between specific heat capacity and coefficients of thermal expansion did not exist after heat treatment (Figures 4.114 and 4.115). The high surface stresses in the as-sprayed samples were reduced by annealing, but this might not be practical in application. The observed surface residual stresses of ~100 MPa in the as-sprayed samples could have important effects on the structural integrity, in both static or dynamic friction environments.

The substrate wear is shown in Figure 4.86 and the wear rates in Figure 4.90. The results showed that the brass substrate had the highest mass loss, with a peak pull-out observed before 10 minutes, followed by 304L stainless steel substrate. The aluminum substrate gave the best wear resistance, which was surprising, but this would have been caused by the precipitates (although they were too small to be identified on the micrographs), while super-invar and mild steel substrate were in the middle. Conversely the substrate hardness does not correlate with the mass loss, and the microstructures have to be considered too.

The relationship between the microstructure of the materials and their abrasive wear resistance was studied by Berns [1995Ber] and Scholl *et al.* [1997Sch], but was inconclusive (Although the material were not the same with the one discussed here). With increasing coefficients of thermal expansion, wear showed no discernable relationship (Figure 4.116). Correlation between melting point and wear loss of the substrate showed a possible maximum at ~1100°C (Figure 4.117). No relationship could be recognised between macrohardness and wear loss (Figure 4.118), hence, the initial hardness cannot be used as a universal indicator of abrasive wear resistance [1998Gar].

The effect of grit-blasting on the wear resistance of the substrates sample was studied, and the results are presented in Figures 4.87 and 4.90. The grit-blasted brass sample consistently had the highest average mass loss, while grit blasted 304L stainless steel, mild steel and super-invar substrate samples showed similar trends of parabolic wear rate in the middle. The grit-blasted aluminum substrate had the lowest mass loss after 30 minutes. These results do not follow the known trends of increasing material hardness being associated with an increased in wear resistance of the material. There was a large improvement in the wear resistance (about 45-50 %) after grit-blasting. This improvement is likely due to the work hardening effect on the substrate after grit blasting with alumina which increases the surface hardness thereby increasing the resistance to wear.

The abrasion resistance of the coatings on the different substrates was studied with the mass loss results shown in Figure 4.88 and the wear rates in Figure 4.90. The mass loss for coated super-invar had a peak of 0.9g between 5-10 minutes of wear testing. This could be due to surface roughness of the coating. Overall, the as-sprayed coatings had better wear resistances compared to the grit-blasted substrates. The highest mass loss recorded for the coated super-invar substrate. The coated mild steel substrate and brass substrates had similar mass losses within experimental error. The same was found for the coated aluminum and 304L stainless steel substrates which had the lowest mass losses. The coatings results showed improved wear resistance after WC-Co thermal spraying. It is expected that the microcracks could affect the wear resistance, however the results showed that microcracking found in the coatings were seen as beneficial in promoting abrasion wear resistance of the coatings [1998Ste], this could be due to low tensile stress in the coatings.

Baik *et al.* [2007Bai] reported that non WC (η phase) was detrimental to wear resistance, whilst Qiao *et al.* [2001Qia] found the sliding wear rate of as-sprayed coatings increased with increasing decomposition products. Thus, decomposition resulted in a lowering of wear resistance. However, the current work has shown (Figure 4.82) that low amount of η phase found only on coated mild steel had a favorable effect on the particle/matrix cohesion, and was therefore helpful for the abrasion resistance of WC-Co coatings, even if the corresponding phases have brittle behaviour. This is similar to the work of Lia *et al.* [2000Lia]. The high wear rate for the super-invar coating might be correlated with the localised porosity, despite higher hardness with low mean grain size. The coated mild steel and brass substrates were in the middle of the range of the wear rates. The coated mild steel

had $\text{Co}_6\text{W}_6\text{C}$ and WC, but since the sample had a higher mean grain size, despite low porosity, this could have increased the abrasive wear rate. The coated brass sample had only WC and Co phases, but had higher porosity which could have increased the wear. Lower wear rate was shown by coated 304L stainless steel with the highest hardness, low porosity and high mean grain sizes. The coated aluminum sample gave the best (lowest) wear resistance. This could be due to the following reasons:

- (1) The mainly WC proportion, low porosity, despite high mean grain sizes.
- (2) The large alteration that was found in the residual stress measured on grit-blasted sample via neutron measurements (Figures 4.68 and 4.69) could create a strong anchor between the coating-substrate, and improved wear resistance.
- (3) The hard surface on substrate (aluminium) suggested that the substrate must be absorbing the impact energy after thermally sprayed.
- (4) The larger compressive stress found in the coated aluminium (Table 4.8) could also improved the wear resistance, as well as the highest residual elastic strain (Figure 4.70).

Residual stresses also have an influence on the resistance to abrasive wear because they interact with the mechanical system of the surface. In this respect, different residual stress value in the coatings might play a role in the differences in the wear rate of the coatings despite same feedstock powder.

In the residual stress measurements done using synchrotron and neutrons on as-sprayed brass, 304L stainless steel and super-invar samples (Figures 4.53-4.61), large misfits between the coatings and substrates were found and were attributed to the grit-blasting surface preparation of the substrate prior to deposition. The differences in strain misfit (strain profile) between substrate and coating, as well as the residual stresses in the carbide influenced the adhesion between the two materials, and consequently influenced the coatings' integrity and wear performance. The surface roughness created by grit-blasting will play an important role in the mechanical interlock and increases the bond strength between the coating and the substrate [2008Jia]. This is in agreement with the good wear resistance found on the coated aluminium substrate.

The results of the annealed coated samples are presented in Figure 4.89, and the wear rates in Figure 4.90. A similar trend of increasing mass loss with time was seen in the annealed coated samples. The annealed coatings on mild steel consistently showed the highest average

mass loss, despite having the highest hardness. Annealed coatings on brass and 304L stainless steel showed similar trends, despite differences in the hardnesses. These results did not agree with increased hardness being associated with decreased wear rate [1998Gar]. The wear rate of annealed coated sample were lower than the as-sprayed coating for 304L stainless steel, aluminum and super-invar samples, whilst higher for as-sprayed coatings on mild steel and brass substrate after heat treatment. The increase in the wear rate of mild steel, despite the residual stresses being compressive, could be due to formation of more eta phase after heat treatment (Figure 4.82). It appeared that higher eta phase was detrimental to the wear resistance, but not hardness after heat treatment. The slight increase in wear rate on coated brass substrates could have been due to the effect of residual stress after heat treatment. The slight increase in wear resistance of coated brass after annealing at 375°C was substantial, since no new phases were seen to occur after heat treatment at this temperature. This increase could be due to the following:

- (1) Lowest compressive residual stress found in the coating via neutron measurement, and
- (2) Gross-through thickness cracking found in the coating.

The changes of the nature of residual stresses from tensile to compressive on the surface of the coatings determined by X-ray diffraction (Figure 4.85) might have improved (decreased) the wear resistance for the coated 304L stainless steel, aluminum, and super-invar.

Khameneh *et al.* [2006Kha] reported that the mass loss for heat treated coatings was higher than as-sprayed coatings, whilst Kim *et al.* [2007Kim] found that heat treatment improved the wear resistance of the coatings. The current work has shown that the wear rate for heat treated samples was either higher or lower, due to the integrity of coating, state of residual stress present in the coatings, phases in the coatings especially presence of eta. The material properties such as hardness and porosity also played a role as well as the interaction between the material and the SiO₂ abrasive since wear is not an intrinsic properties.

Further understanding of the wear response of the different as-received substrates, grit-blasted substrates, as-sprayed and heat treated coatings may be gained from considering the interaction between the coating microstructure and the SiO₂ abrasive. The hardness of the SiO₂ abrasive was 800HV [1992Hut], while hardness of the substrate ranged from 120-180HV. The ratio of the hardness of the abrasive (H_a) to the hardness of the as-received substrates (H_m) i.e. (H_a/H_m) was in the range 4.44 to 6.67. These calculated ratios were more

than 1:2, which signifies the boundary condition between soft and hard abrasion according to Hutchings [1992Hut], and therefore placed the abrasive wear on the substrates in the hard abrasion category. This is in agreement with the extent of plastic deformation observed on the worn surfaces. The harder SiO₂ abrasives are able to cut into the softer substrate surfaces and cause severe damage. Some of the SiO₂ particle fragment became embedded in the substrate due to their high hardness (Figures 4.91-4.95) and the continuous pressure applied by the abrasive wheel during testing. The hardness of the grit-blasted substrates ranged from 160-190HV [2008Jia]. The (H_a/H_m) ratio was in the range 4.21-5.00, and therefore also placed the abrasive wear of all the grit-blasted substrate samples in the hard abrasion category. This is in agreement with the plastic deformation observed on the worn surfaces (Figures 4.96-4.100). There was a reduction in the (H_a/H_m) ratio of grit-blasted substrate compared to the respective substrate. This can be related to the work hardening rates of the different materials as well as the stresses (both residual and abrasion induced strain).

The as-sprayed coatings (Figures 4.101-4.105), performed better than the as-received substrates and the grit-blasted substrates during wear testing, as expected. The hardness of the coatings ranged from 660 to 911HV. The H_a/H_m ratio was in the range 0.88-1.2, thus placing the abrasive wear in the soft abrasion category, where the SiO₂ abrasive was unable to indent the WC particles due to the latter's higher hardness. Both soft and hard abrasion categories were found on the annealed coated samples (Figures 4.106-4.110), which could be due to the effect of temperature on thermal expansion of the coatings and substrates, as well as stress relaxation. Hard abrasion was not observed on the SEM micrographs of the worn annealed coatings on the 304L stainless steel ($H_a/H_m = 1.26$) (Figure 4.101), brass ($H_a/H_m = 1.30$) (Figure 4.104), and aluminium ($H_a/H_m = 1.39$) (Figure 4.106), because the H_a/H_m ratios were very close to the boundary of soft abrasive.

The wear performances of the as-sprayed and heat-treated samples are compared in Table 4.10. The coating wear resistance (which was inversely proportional to the wear rate) was directly proportional to the stress state of the coating, as determined by neutron diffraction (Table 4.8). The most resistant sample was that with the aluminium substrate, and the least resistant sample was super-invar, for both as-sprayed and the heat-treated counterparts. Although this seems surprising, the reason for the good wear resistance in the aluminium substrate samples was partly due to the precipitates.

The fracture toughness can influence the wear performance of coatings, and it would have been advantageous to measure it. However, the coatings were relatively thin (200µm thick), and efforts to produce indentation cracking on the coating cross-sections, for generating Palmqvist cracks was not successful, similar to Kumori *et al.* [2010Kum].

In summary, the effect of annealing on the microstructure and residual stress of WC-17Co HVOF coatings was studied. The coatings had lower porosity, reduction of pores and localized microcracking after heat treatment. However, the coating microstructural features were widely different, despite same powder used as feedstock. Lower porosity in the coating after heat treatment is a fundamental requirement to achieving good abrasion resistance of the coatings. There were changes in the residual stress states, from tensile to compressive, due to partial relaxation between the coating and substrate. The different wear rates of the as-received substrates, grit-blasted substrates and as-received and annealed WC-Co coatings were investigated. About 45 - 50% reduction in the wear rate of grit-blasted samples over the substrates was found, thus confirming the improved wear resistance which grit-blasting rendered. About 80 - 95% reduction in the wear rates of the coating compared to the substrate was found, confirming the protective wear resistance which WC-Co coatings provided to soft substrate materials. The abrasive wear rate of the WC-Co coatings after the heat treatment were influenced by a variety of factors including coating integrity, phases present, material properties and the residual stress state of the coating, showing how complex the materials are.

CHAPTER 6

6.0. Conclusions and recommendation

6.1. Conclusions

This thesis covered the investigation of the techniques for determining the residual stresses in WC-17Co thermal sprayed coatings and studying the effect of residual stress on its abrasion resistance on different substrates in two batches of samples). Batch A samples were commercial samples of thickness 9 mm, whilst Batch B samples had 6 mm thickness, and were procured from Goodfellow, UK, with mild steel samples (SABS 1431 grade 300WA) in addition. The main difference between A and B was the latter was finer grained, with minimal texture effects, for easier comparison with the diffraction experiments. The choice of the substrate was to give a range of different coefficients of thermal expansion. Based on the results obtained from this research, the following conclusions were drawn.

- (1) Typical HVOF thermal sprayed microstructures of WC-Co coatings were found (on both Batches A and B), whilst the different substrates gave different properties, despite using the same powder (WC-17 wt% Co) as feedstock. This was due to differences in their substrate properties which affected cooling after deposition of the coating.
- (2) The residual stresses measured by X-ray diffraction were either compressive or tensile on as-sprayed coatings. The differences in the stress results, although small, were due to the coefficients of thermal expansion of each substrate.
- (3) The abrasive wear resistance of WC-17wt%Co thermal sprayed coatings deposited onto four different substrates (Batch A) and the separate wear resistances measured for the as-received substrates, grit-blasted substrates, as-received and annealed WC-Co coatings (Batch B) yielded very different wear resistance characteristics. The differences in wear resistance values is attributed to a range of interacting factors such as microstructural and mechanical properties and the interaction with the SiO₂ abrasive. For Batch B there was an approximate 45 – 50% reduction in the wear rate of the grit-blasted substrates compared to the as-received substrates. There was about 80 – 95% reduction in the wear rate of the coating compared to the substrates, confirming the well known application of using hardmetal coatings to protect soft substrates. The wear resistance was found to be directly proportional to the residual stresses, and the aluminium alloy had the best wear resistance, partly due the precipitates.

- (4) The residual stress results of the synchrotron and neutron techniques gave qualitatively similar results, in accordance to the respective gauge volumes. The systematic approach followed (which identified the different contributions) showed that the WC-Co coating contributed slightly to the residual strains in the substrates, and the effect of the grit-blasting was greater. The large strain / stress misfit between the coating and the substrates originated primarily from the grit-blasted surface preparation of the substrates, which extended 0.5 mm into the substrates. The residual stresses in the WC coatings had a parabolic dependence with depth, initially rising from a low value on the surface to a maximum tensile stress at around the mid coating thickness, not exceeding 400MPa, decreasing to the coating-substrate interface. It thought that the generally low stress values in the coatings originated from localized relaxation due to microcracking.
- (5) The detailed residual stress profiles determined by neutron diffraction allowed a direct comparison of the various regions of interest in the thermal spray coating system, i.e. coating, coating/substrate interface, as well as the substrate. The measured results in the thin coatings showed favourable agreement with a stress balance (Stoney) approach [1996Cly] using the through thickness stress profiles in the substrate materials. It was shown that in materials with high absorption of neutrons (e.g. Ni in super-invar), the direct measurement of the thin WC coatings were difficult, and not advised, because of large losses of the neutron beam.
- (6) The coatings had lower porosity, reduction of pores and localized microcracking after heat treatment. However, the coating microstructures were very different due to their substrate properties. Lower porosity in the coating after heat treatment is necessary for good abrasion resistance. There were changes in the residual stress state, from tensile to compressive, due to partial relaxation between the coating and substrate after the heat treatment. The abrasive wear rate of the WC-Co coatings after the heat treatment were either be higher or lower, depending on the coating integrity, phases present and residual stress state of the coating.

The differences between coating and stress results of Batch A (commercial substrate) and Batch B (substrate procured from Good fellow) were due to differences in manufacturer and composition, as well as their substrate thickness which induced different cooling rates and interactions with the incoming droplets.

6.2 Recommendations

Despite these encouraging findings, further modification to the coating is necessary to maximize the compressive residual stresses and improve mechanical properties of the coating. On this basis, the following suggestions are considered necessary for future study.

- (1) TEM studies of the coating microstructure may be necessary in order to understand the crystal structure orientation relationship between the coating and the substrate.
- (2) The parameter of grit-blasting need to be optimised.
- (3) Simulation work on residual stress analysis may be needed.
- (4) The effect of different annealing temperatures and techniques on the coatings needs to be investigated, and optimised.
- (5) The effect of cooling rates of the coatings should be investigated.

REFERENCES

- [1951Hal] E.O. Hall, The Deformation and Ageing of Mild Steel, Proceedings of the Physical Society, B64 (1951) 747-753.
- [1952Ogi] R.E. Ogilvey, M.Sc. Thesis, Massachusetts Institute of Technology, 1952.
- [1953Ful] R.L. Fullman, Measurement of Particle Sizes in Opaque Bodies, Transactions AIME, 197 (1953) 447-432.
- [1955Gur] J. Gurland and P. Bardzil, Relation of Strength, Composition and Grain Size of Sintered WC-Co Alloys, Transactions AIME, 203 (1955) 331-315.
- [1958Kro] E. Kroner, Berechnung der elastischen Konstanten des Vielkristalls aus den Konstanten den Einkristallis, Zeitschrift für Physic, A Hadrons and Nuclei, 151 (1958) 504-518.
- [1959Koi] D.P. Koistinen and R.E. Marburger, A Simplified Procedure for Calculating Peak Position in X-Ray Residual Stress Measurements on Hardened Steel, Transactions ASM, 51 (1959) 537-550.
- [1963Gur] J. Gurland, The Fracture Strength of Sintered Tungsten Carbide Cobalt Alloys in Relation to Composition and Particle Spacing, Transactions AIME, 227 (1963) 1146-1150.
- [1965Gur] J. Gurland and C.T. Liu, Transactions of the American Society for Metal, 58 (1965) 66-73.
- [1966San] R.L. Sands and C.R. Shakespeare, Powder Metall-Particle and Application, Newnes, London, 1966.
- [1970Gur] J. Gurland, Microstructural Aspects of the Strength and Hardness of Cemented Tungsten Carbide, in "Materials Metal Cutting", The Iron and Steel Institute, UK, (1970) 152-156.
- [1971Uhl] H.H. Uhlig, Corrosion and Corrosion Control on Introduction to Corrosion Science and Engineering, Second edition, 1971.
- [1974App] R.F. Apps, The Influence of Surface Preparation on the Bond Strength of Flame Sprayed Aluminium Coatings into Mild steel, Journal of Vacuum Science Technology, 11 (1974) 741-746.
- [1974Blo1] R.I. Blombery, C.M. Perrot and P.M. Robinson, Abrasive Wear of Tungsten Carbide-Cobalt Composites I. Wear Mechanisms, Journal of Material Science Engineering, 13 (1974) 93-100.

- [1974Blo2] R.I. Blombery and C.M. Perrott, Wear of WC-Co Composites during Abrasion on Silicon Carbide, *Journal of the Australian Institute of Metals*, 19 (1974) 266-269.
- [1974Hub] J.H. Hubbell, W.H. McMaster, N.K. Del Grede and J.H. Mallett, X-ray cross sections and attenuation coefficients, J.A. Ibers, W.C. Hamilton (Eds) *International Tables for X-ray Crystallography*, Kynoch Press, Birmingham, England, 1974.
- [1975Bac] G.E. Bacon, *Neutron Diffraction*, 3rd Edn., Oxford University Press, Oxford.
- [1975Tay] T.A. Taylor, Phase Stability of Chrome-Carbide Ni-Cr Coatings in Low Oxygen Environments, *Journal of Thermal Spray Technology*, 12 (3) (1975) 790-794.
- [1978Lar] J. Larsen-Basse and E.T. Koyanagi, Abrasion of WC-Co Alloys by Quartz, *Trans. ASME*, 78 (1978) 4.
- [1978Say] R. Sayles and T.R. Thomas, Surface Topography as a Nonstationary Random Process, *Nature (London)*, 271 (1978) 431-434.
- [1979Cah] J.R. Cahoon, W.H. Broughton, and A.R. Kutzak, The Determination of Yield Strength from Hardness Measurements, *Metallurgical Transactions A*, 2(7) (1971) 1979-1983.
- [1979Exn] H.E. Exner, Physical and Chemical Nature of Cemented Carbide, *International Metals Review*, 24 (1979) 149-173.
- [1979Lar] J. Larsen-Basse and E.T. Koyanagi, Abrasion of WC-Co Alloys by Quart, *Journal of Lubricant Technology*, 101 (1979) 208-211.
- [1981McP] R. McPherson, The Relationship between the Mechanism of Formation Microstructure and Properties of Plasma-Sprayed Coatings, *Thin Solid Films*, 83 (1981) 297-310.
- [1981Sar] V.K. Sarin, *Cemented Carbide Cutting Tools*, *Advances in Powder Technology* Ed., D.Y. Chin, ASM International, Materials Park, Ohio, USA. 1981, 253-287.
- [1982Mur] T. Mura, *Micro-mechanics of Defects in Solids*, Martinus Nickoff, Publishers, Hague, Neitherlands, 1982.
- [1982Tho] T.R. Thomas (Ed.) *Rough Surfaces*, Longman, London, 1982.
- [1982Zuk] J.A. Zukas, T. Nicholas, H.F. Swift, L.B. Greszezuk and D.R. Curran, *Impact Dynamics*, John Wiley and sons Inc., New York, USA. (1982).
- [1983Bro] J.A. Browning, US Patent, 4416421, 1983.

- [1984Wya] J.C. Wyant, C.L. Koliopoulos, B. Bhushan and O.E. George, An Optical Profilometer for Surface Characterization of Magnetic Media, ASLE Trans., 27 (1984) 101-113.
- [1985All] A.J. Allen, M.T. Hutchings, C.G. Windsor and C. Andreani, Neutron Diffraction Methods for The Study of Residual Stress Fields, Advances in Physics, 34 (1985) 445-473.
- [1985Ara] Y. Arata, A. Ohmori and E. Gofuku, WC-Co High Energy Thermal Spray Coatings Structures and Mechanical Properties, Trans. JWRI, 14 (2) (1985) 267-273.
- [1985Bhu] B. Bhushan, J.C. Wyant and C.L. Koliopoulos, Measurement of Surface Topography of Magnetic Tapes by Mirau Interferometry, Appl. Opt., 24 (1985) 1489-1497.
- [1985Kra] A.D. Krawitz, The Use of X-ray Stress Analysis for WC-base Cermets, Materials Science Engineering, 75 (1985) 29-36.
- [1985Lar] J. Larsen-Basse, Proceedings of International Conference on Wear of Materials, Vancouver, Canada, 14th-18th April, (1985) 39-44.
- [1985Vin1] M.E. Vinaya, F. Kassabji, J. Guyonnet and P. Fauchais, Journal Vacuum Science Technology, A3 (1985) 2483-2489.
- [1985Vin] M.E. Vinayo, F. Kassabji, J. Guyonnet and P. Fauchis, Plasma Sprayed WC-Co Coating: Influence of Spray Conditions (Atmospheric and Low Pressure Plasma Spraying) on the Structure, Porosity, and Hardness, Journal Vacuum Science Technology, A 3(6) (1985) 2483-2489.
- [1986Coh] J.B. Cohen, The Measurement of Stresses in Composites, Powder Diffraction, 1 (1986) 15-21.
- [1986Die] G.E. Dieter, Mechanical Metallurgy, 3rd Edn., McGraw-Hill, (1986) 327-332.
- [1986Han] C. Hansen, Diverse Book Abrasion and Erosion; Grundlagen, Betriebliche Erfahrungen, Verminderung, Carl Hansen Verlag, Munchen, (1986) 830.
- [1986Has] M. Hasatani and J. Kimura, Fundamental and Application of Combustion Kyoritsn Publishing Ltd., Tokyo, (1986) 37-41.
- [1986Lar] J. Larsen-Basse and N. Devnani, Binder Extrusion as a Controlling Mechanism in Abrasion of WC-Co Cemented Carbides, Institute of Physics Conference Series, No. 75: Chapter 9, (1986) 883-895.

- [1986Wya] J.C. Wyant, C.L. Koliopoulous, B. Bhushan and D. Basila, Development of a Three-Dimensional Noncontact Digital Optical Profiler, *ASME Journal of Tribology*, 108 (1986) 1-8.
- [1987Gru] H.W. Grunling, K. Schneider and L. Singheiser, Mechanical Properties of Coated System, *Material Science Engineering*, 88 (1987) 177-189.
- [1987Noy] I.C. Noyan and J.B. Cohen, *Residual Stress*, Springer Verlag, New York. (1987).
- [1987Ric] D.S. Rickerby, G. Eckold, K.T. Scott and I.M. Buckley-Golder, The Inter-relationship between Internal Stress, Processing Parameters and Microstructure of Physically Vapour Deposited and Thermally Sprayed Coatings, *Thin Solid Films*, 154 (1987) 125-141.
- [1987Wig] J. Wigren, Grit Blasting as Surface Preparation before Plasma Spraying, in *Thermal Spray: Advances in Coatings Technology*, D.L. Houck (Ed.) ASM International Materials Park, OH, USA, (1987) 99-104.
- [1988Bar] G. Barbezat, E. Muller, and B. Walser, Applying Tungsten Carbide Cobalt Coating by High Velocity Combustion Spraying, *Sulzer Technical Rev*, 4 (1988) 27-33.
- [1988Bhu] B. Bhushan, J.C. Wyant and C.L. Koliopoulos, A New Three dimensional Digital Optical Profiler, *Wear*, 122 (1988) 301-312.
- [1988Lan] S.R. Lange and B. Bhushan, Use of Two- and Three- Dimensional Noncontact Surface Profiler for Tribology Application, *Surface Topography*, 1 (1988) 277-290.
- [1988Sch] W. Schedler, *Hard Metals for Practical Users*, VDI-Verlag, Dusseldorf, (1988) 5-29.
- [1988Viv] B. Vivien, Selecting Process Values for In-Service Reliability, *Process Engineering*, 100 (6) (1988) 33-36.
- [1988Wig] J. Wigren, Technical note: Grit Blasting as Surface Preparation before Plasma Spraying Coating Technology, 34 (1) (1988) 101-108.
- [1989Dor] M.R. Dorfman, B.A. Kushner, J. Nerz and A.J. Rotolico, A Technical Assessment of High Velocity Oxygen-fuel versus High Energy Plasma Tungsten Carbide-Cobalt Coatings for Wear Resistance, in *Proc. 12th Int. Thermal Spray Conf.*, London, I.A. Bucklow (Ed.), 4th-9th June, (1989) 108-12.

- [1989Fau] P. Fauchais, A. Grimaud, A. Vardelle and M. Vardelle, The Plasma Spraying, *Ann. Phys. Fr.*, 14 (1989) 261-310.
- [1989Kra] A.D. Krawitz, D.G. Reichel and R.L. Hitterman, Residual Stress Distribution in WC-Ni Composites, *Material Science Engineering*, A119 (1989) 127-134.
- [1989Kul] P. Kulu, The Abrasive Erosion Resistance of Powder Coatings, *Journal of Tribology*, 8(4) (1989) 12-25.
- [1989Met] Metco/Perkin Elmer, Diamond Jet System and Gun Manual (1989).
- [1989Ram] V. Ramnath and N. Jayaraman, Characterization and Wear Performance of Plasma Sprayed WC-Co Coatings, *Material Science Technology*, 5 (1989) 382-388.
- [1989Sta] Stan Grainger (Ed.), *Engineering Coatings-Design and Application*, Abington Publishing, Woodhead Publishing Ltd., Cambridge, England, 1989.
- [1989Von] H. Von Weingrubber and M. Abou-Aly *Handbunch Technische Oberflächen-Typologie, Messung and Gebrauchsverhalten*, Friedr. Vieweg and Sohn, Braunschweig/Wiesbaden, (1989) 448.
- [1990Els] R. Elsing, O. Knotek and U. Balting, Calculation of Residual Thermal Stresses in Plasma-Sprayed Coatings, *Surface Coating Technology*, 43-44 (1990) 416-425.
- [1990Gil] S.C. Gill and T.W. Clyne, Stress Distributions and Material Response in Thermal Spraying of Metallic and Ceramic Deposits, *Metallurgical Transactions B*, 21B (1990) 377-385.
- [1990Ito] H. Ito, R. Nakamura, M. Shiroyama and T. Sasaki, ASM International, *Thermal Spray Research and Applications*, Proceedings of the Third National Thermal Spray Conference, Long Beach, CA, USA, 20th-25th May, (1990) 233-238.
- [1990Kow] K.A. Kowalsky, D.R. Marantz, M.F. Smith and W.F. Oberkamp, HVOF-particle Flame Diagnostics and Coating Characteristics; Proceedings of the Third National Thermal Spray Conference, Long Beach, CA., 20th-25th May, (1990) 546-587.
- [1990Kra] A.D. Krawitz and T.M. Holden, The Measurement of Residual Stresses using Neutron Diffraction, *MRS Bull. XV*, (1990) 57-64.
- [1990Kur] S. Kuroda, T. Fukushima, and S. Kitahara, Generation Mechanisms of Residual Stresses in Plasma-Sprayed Coatings, *Journal of Vacuum*, 41 (1990) 1297-1299.

- [1990Len] W.J. Lenling, M.F. Smith and J.A. Henfling, Proceedings of the Third National Thermal Spray Conference, Long Beach, CA, USA, (1990) 227-232, 20th-25th May.
- [1990Maj] S. Majumdar and A.D. Kwawitz, Residual Thermal Stresses and Strains in a WC-Base Cemented Carbide Composite, Material Science Engineering, A123 (1990) L1-L3.
- [1990Mas] T.B. Massalski (Ed.), Binary Alloy Phase Diagram Phase Diagrams, ASM International, Materials Park, Ohio, USA, (1990).
- [1990Ner] J. Nerz, B. Kushhner and A. Rotolico, Effects of Deposition Methods on the Physical Properties of Tungsten Carbide 12wt% Cobalt Thermal Spray Coatings, in Protective Coatings: processing and characterization, R.M. Yazici (Ed.), Warrendale, PA, TMS, (1990) 135-143.
- [1990Seo] K. Seol, Ph.D. Thesis, University of Missouri-Columbia, 1990.
- [1990Tak] S. Takeuchi, M. Ito and K. Takeda, Modelling of Residual Stress in Plasma-Sprayed Coatings: Effect of Substrate Temperature, Surface Coating Technology, 43-44 (1990) 426-435.
- [1990Var] D.J. Varacalle, G.R. Smolik, G.C. Wilson, G. Irons and A. Walter, An Evaluation of Tungsten Carbide Coatings Fabricated with the Plasma Spray Process, the Minerals, Metals and Material Society, (1990) 121-134.
- [1990Way] S.F. Wayne, J.G. Baldoni, S.T. Buljan, Abrasion and Erosion of WC-Co with Controlled Microstructures, Tribology Transactions, 33 (1990) 611-617.
- [1991Bhu] B. Bhushan and B.K. Gupta, Handbook of Tribology, McGraw-Hill, New York, USA (1991).
- [1991Kur1] S. Kuroda and T.W. Clyne, The Quenching Stress in Thermally Sprayed Coatings, Thin Solid Films, 200 (1991) 49 -66.
- [1991Kur2] S. Kuroda and T.W. Clyne, Proceedings of the Second Plasma-Technik-Symposium, Plasma-Technik AG, (Eds.) S. Blum-Sandmeier, H. Eschnauer, P. Huber, A.R. Nicoll (Eds.), Switzerland, 3 (1991) 273-283.
- [1991Nag] S.V. Nagender and P.R. Rao, Phase Diagram of Binary Tungsten Alloys, The Institute of Metals, Electronic Publishing Center, New Delhi, India, 1991.
- [1991Ner1] J. Nerz, B. Kushner and A. Rotolico, Characterisation of Tungsten Carbide Coatings as a function of Powder Manufacturing and Deposition Technologies, High Performance Ceramic Films and Coatings, (1991) 27-36.

- [1991Ner2] J.E. Nerz, B.A. Kushners and A.J. Rotolico, Microstructural Evaluations of Tungsten Carbide-Cobalt Coatings, Proceedings of the 4th National Thermal Spraying Conference, Pittsburgh, PA, USA, 4th-10th May, (1991) 115-120.
- [1992Bak] H. Baker and H. Okamoto (Eds.), ASM Handbook Volume 3: Alloy Phase Diagrams, ASM International Materials Park. OH,USA, 2 (1992) 115.
- [1992Hut] I.M. Hutchings, Tribology: Friction and Wear of Engineering Materials, Edward Arnold, 1992.
- [1992Ner] J. Nerz, B. Kushner and A. Rotolico, Microstructural Evaluation of Tungsten Carbide-cobalt Coatings, Journal of Thermal Spray Technology, 1 (20) (1992) 147-152.
- [1993Kes] M.K. Keshavan and K.T. Kembalyan, Wear Characterisation and Practical Applications of Thermal Spray Coatings in Drilling Applications in Proceedings of the 1993 National Thermal Spray Conference, C.C. Bernt and S. Sampath (Eds.), 635-641, ASM International, Materials Park, OH, USA, 7th-11th June 1993.
- [1993Tom] T. Tomita, Y. Takatani, Y. Kobayashi, Y. Hadara and H. Nakahira, Durability of WC/Co Sprayed Coatings in Molten Pure Zinc, ISIJ International, 33 (9) (1993) 982-988.
- [1993Pro] X. Provot, H. Burlet, M. Vardavoulis, M. Jeandin, C. Richard, J. Lu and D. Manesse, Comparative Studies of Microstructure, Residual Stress Distributions and Wear Properties for APS WC-Co Coatings of Ti6Al4V, Proceedings of the 1993 National Thermal Spray Conference, Anaheim, Canada, 7-11, June 1993.
- [1993Ver] A.T.J. Verbeek, Plasma Sprayed Thermal Barrier Coatings: Production, Characterization and Testing, Eindhoven University, 1993.
- [1994Gil] S.C. Gill and T.W. Clyne, Investigation of Residual Stress Generation During Thermal Spraying by Continuous Curvature Measurement, Thin Solid Films 250 (1994) 172-180.
- [1994Gre] D.J. Greving, E.F. Rybicki and J.R. Shadley, Through-Thickness Residual Stress Evaluation for Several Industrial Thermal Spray Coatings Using a Modified Layer-Removal Method, Journal of Thermal Spray Technology, 3(4) (1994) 379-388.
- [1994Kho] K.A. Khor and N.L Loh, Hot Isostatics Pressing of Plasma Sprayed Ni-Base Alloys, Journal of Thermal Spraying, 3(1) (1994) 57-62.

- [1994Kim] H.J. Kim, Y.G. Kweon and R.W. Chang, Wear and Erosion Behaviour of Plasma Sprayed WC-Co Coatings, *Journal of Thermal Spray Technology*, 3(2) (1994) 169-178.
- [1994Res] H. Reshetnyak and J. Kubarsepp, Mechanical Properties of Hardmetals and their Erosive Wear Resistance, *Wear*, 177 (1994) 185-193.
- [1994Tuc] R.C. Tucker Jr., *Handbook of Deposition Technologies for Films and Coatings*, William Andrew publication, Noyes, 1994.
- [1994Whi] D.J. Whitehouse, *Handbook of Surface Metrology*, Institute of Physics, Bristol, 1994.
- [1995Ber] H. Berns, Microstructural Properties of Wear-Resistant Alloys, *Wear*, 181-183 (1995) 271-279.
- [1995Bhu] B. Bhushan (Ed.), *Handbook of Micro/Nanotribology*, CRC Press, Boca Raton, FL, USA, 1995.
- [1995Ito] A. Itoh and T.W. Clyne, Initiation and Propagation of Interfacial Cracks During Spontaneous Debonding of Thermally Sprayed Coatings: Proceedings of the Eight National Thermal Spray Conference, 425-432, Texas, USA, 11th-15th September 1995.
- [1995Kur] S. Kuroda, T. Dendo and S. Kitahara, Quenching Stress in Plasma-Sprayed Coatings and its Correlation with the Deposit Microstructure, *Journal of Thermal Spray Technology*, 4(1) (1995) 75-84.
- [1995Lav] S. Ho and E.J. Lavernia, Thermal Residual Stresses in Metal Matrix Composites, *Applied Composite Materials*, 2 (1995) 1-30.
- [1995Paw] L. Pawlowski, *The Science and Engineering of Thermal Spray Coatings*, John Wiley and Sons Inc., London (1995).
- [1995Pej] L. Pejryd, J. Wigren, D.J. Greving, J.R. Shadley and E.F. Rybicki, Residual Stresses as a Factor in the Selection of Tungsten Carbide Coating for a Jet Engine Application, *Journal of Thermal Spray Technology*, 4(3) (1995) 268-274.
- [1995Poo] C.Y. Poon and B. Bhushan, Comparison of Surface roughness measurements by Styles Profiler, AFM and Non-Contact Optical Profiler, *Wear*, 190 (1995) 76-88.
- [1995Ste] D.A. Stewart, P.H. Shipway and D.G. McCartney, Abrasive Wear Behaviour of Conventional and Nanocomposites HVOF-Sprayed WC-Co Coatings, *Wear*, 225 (1995) 789-785.

- [1995Var] D.J. Varacalle Jr., R.S. Hartley, L.B. Lundberg, J. Walker and W.L. Riggs II, 8th National Thermal Spray Conference –Advance in Thermal Spray Science and Technology, ASM International, 359-363, Houston, Texas, USA, 11th-15th September 1995.
- [1995Ver] C. Verdon, Microstructure and Erosion Resistance of WC-M Coatings deposited by HVOF Thermal Spraying, Switzerland, 1995.
- [1995Vuo] P. Vuoristo, K. Niemi, T. Mantyla, L.-M. Berger and M. Nebelung, Comparison of Different Hard Metal like Coatings Sprayed by Plasma and Detonation Gun Processes, Proceedings 8th National Thermal Spray Conference, 309-315, Houston, Texas USA, 11th-15th September 1995.
- [1996Ber] L.M. Berger, P. Vuoristo, T. Mantyla, W Kunert, W. Lengauer and P. Ettmayer, Microstructure and Properties of WC-Co-Cr Coatings, Thermal spray: Practical Solutions for Engineering Problems, C.C. Berndt (Ed.), ASM International, Materials Park, OH,USA, (1996) 97-106.
- [1996Cly] T.W. Clyne and S.C. Gill, Residual Stresses in Thermally Sprayed Coatings and their effect on Interfacial Adhesion, Journal of Thermal Spray Technology, 5(4) (1996) 401-418.
- [1996Gri] B.J. Griffiths, D.T. Gawne and G. Dong, The Erosion of Steel Surfaces by Grit-Blasting as a preparation for Plasma Spraying, Wear, 194 (1) (1996) 95-102.
- [1996Gui] J.M. Guilemay, J. Nutting and J.M. de Paco, Characterization of Three WC-12Co Powders and Coatings obtained by High Velocity Oxyl-fuel Spraying, Association of Italiana di Metallurgica, Milan, (1996) 395-398.
- [1996Gur] J. Gurland, and J.D. Knox, From Sintered Tungsten to Cemented Tungsten Carbide, A Historical Review of Two Related Technologies, 3 (1996) 219-228.
- [1996Jen] R. Jenkins and R.L. Snyder, Introduction to X-Ray Powder Diffractometry, Wiley, New York, 1996.
- [1996Kal] P. Kallas, Indentation Energy and Abrasive Wear of Metals, Wear, 198 (1996) 77-85.
- [1996Kha] M.S.A. Khan and T.W. Clyne, Microstructure and Abrasion Resistance of Plasma Sprayed Cermet Coatings, in Thermal Spray: Practical solutions for Engineering Problems, C.C. Berndt (Ed.), ASM International, Materials Park, Ohio, USA (1996) 113-122.

- [1996Kor] K. Korpiola and P. Vuoristo, Effect of HVOF Gas Velocity and Fuel to Oxygen Ratio on the Wear Properties of Tungsten Carbide Coating, Thermal Spray: Practical Solutions for Engineering Problems, C.C. Berndt, Ed., ASM International, (1996) 177-184.
- [1996Li] C.J. Li, A. Ohmori and Y. Harada, Effect of Powder Structure of Thermally Sprayed WC-Co Coatings. Journal of Materials Science, 31 (1996) 785-794.
- [1996Mar] D. Mari and A.D. Krawitz, J.W. Richardson and W. Benoit, Material Science Engineering, A209 (1996) 197-205.
- [1996Ner] J. Nerz and B. Kushner, A. Rotolico, Microstructural Evaluation of Tungsten Carbide-Cobalt Coatings, Journal of Thermal Spray Technology, 5 (1) (1996) 67-69.
- [1996Per] A.J. Perry, J.A. Sue and P.J. Martin, Practical Measurement of the Residual Stress in Coatings, Surface Coating Technology, 81 (1996) 17-28.
- [1996Pre] P.S. Prevey, Current Applications of X-Ray Diffraction Residual Stress Measurement, Developments in Materials Characterization Technologies, Eds. G. Vander Voort and J.Friel, ASM International Materials Park, OH, (1996) 103-110.
- [1996Sie] S. Siegmann and C.A. Brown, Investigations on the Substrate Surface Morphology for Thermal Sprayed Coating, 17th International SAMPE European Conference: Success of Materials by Combination, Basel, Switzerland, 28th-30th May 1996. ISBN/ISSN: 3-5920477-3-2, 149-158.
- [1996Sta] E.A. Starke, Jr and J.T. Staley, Application of Modern Aluminium Alloys to Aircraft, Prog. Aerospace Science, 32 (1996) 131-172.
- [1996Wei] C.M. Weisbrook and A.D. Krawitz, Thermal Residual Stress Distribution in WC-Ni Composites, Material Science Engineering, A209 (1996) 318-328.
- [1997Ahm] R. Ahmed and M. Hadfield, Experimental Measurement of the Residual Stress Field within Thermally Sprayed Rolling Elements. Wear, 209 (1997) 84-95.
- [1997Gho] P.K. Ghosh, and N. Ram, Characteristics of Heat Treated Tungsten Carbide embedded Nickel Base Hard Surfacing on Structural Steel Produced by Gas Thermal Spray Process, International Journal of Joining Materials, 9(3) (1997) 114-121.
- [1997Khe] J. Khedkar, A.S. Khanna and K.M. Gupta, Tribological Behaviour of Plasma and Laser Coated Steels, Wear, 205 (1997) 220-27.

- [1997Mel] M. Mellali, A. Grimaud, A.C. Leger, P. Fauchais and J. Lu, Alumina Grit Blasting Parameters for Surface Preparation in the Plasma Spraying Operation, *Thermal Spray Technology*, 6(2) (1997) 217-227.
- [1997Mil] V. Yu, S. Milman, S. Chugunova, V. Goncharuck and S. Luyckx, Low and High Temperature Hardness of WC-6wt%Co Alloys I.T. Northrop, *International Journal of Refractory Metals and Hard Materials*, 15 (1997) 97-100.
- [1997Res] H. Reshetnyak and J. Kubarsepp, Structure Sensitivity of Wear Resistance of Hardmetals, *International Journal of Refractory Metals and Hard Materials*, 15 (1997) 89-98.
- [1997Sch] M. Scholl, R. Clayton and Y. Jia, Deterioration Behaviour of Thermomechanical Refiner Plates, *Wear*, 203-204 (1997) 65-76.
- [1997Spo] S. Spooner and X.L. Wang, Diffraction Peak Displacement in Residual Stress Samples due to Partial Burial of the Sampling Volume, *Journal of Applied Crystallography*, 30 (1997) 449-455.
- [1997Usm] S. Usmani, S. Sampath, D.L. Houck and D. Lee, Effect of Carbide Grain Size on the Sliding and Abrasive Wear Behaviour of Thermally Sprayed WC-Co Coatings, *Tribology Transactions*, 40 (3) (1997) 470-478.
- [1997Woo] R.J.K. Wood, B.G. Meller and M.L. Binfield, Sand Erosion Performance of Detonation Gun Applied Tungsten Carbide/Cobalt Coating, *Wear*, 211 (1997) 70-83.
- [1998Aka] K.Ai. Akasawa, Wear Properties of WC-Co Coatings with Plasma and High Velocity Oxy-Fuel Spraying, *Proceedings of 15th ITSC, Nice, France, 25th-29th May, (1998)* 281-286.
- [1998Cha] A. Chandak, R. Sivakumar and G. Balasubramanian, Tribological Solutions for Engineering Industries by HVOF-Topgun Spraying in Thermal Spray: Meeting the Challenges of the 21st Century, *Proceedings of the 15th International Thermal Spray Conference, ASM International, C. Coddet, Ed., 531-543, Nice, France 25th-29th May 1998.*
- [1998Gar] I.I. Garba, Correlation Between Abrasive Wear Resistance and Changes in Structure and Residual Stresses of Steel, *Tribology Letters*, 5 (1998) 223-229.
- [1998Kre] H. Kreye, P. Heinrich and G. Loewe, Jet Kote Spraying with Different Fuel Gas. Arata Y. *Proceedings of the International Symposium on Advanced*

- Thermal Spraying Technology and Allied Coatings, Osaka, Japan, High Temperature Society (1998) 73-78.
- [1998Kur1] S. Kuroda, Y. Tashiro, H. Yumoto, S. Taira and H. Fukanuma, C. Coddet (Ed.), Proceedings of the 15th International Thermal Spray Conference ASM International, 569-574, Nice, France, 25th-29th May 1998.
- [1998Kur2] S. Kuroda, Christian Coddet (Ed.), proceedings of the 15th International Thermal Spray Conference, ASM International, 539-550, Nice, France, 25th-29th May 1998.
- [1998Lug] E. Lugscheider, C. Herbst and L. Zhao, Parameter Studies on High Velocity Oxy-Fuel Spraying of MCrAlY Coatings, Surface Coating Technology, 108-109 (1998) 16-23.
- [1998Lui] C.D. Luiz, HVOF Process, Its Characteristics, Advantage and Use, Presented at 5th International Conference on Advance in Surface Engineering and 2nd International Seminar on Surface Engineering, Mogi das Cruzes, 11th-13th November 1998.
- [1998Mat] J. Matejicek, S. Sampath and H. Herman, C. Coddet (Ed.), Proceedings of the 15th International Thermal Spray Conference, ASM International, 419-424, Nice, France, 25th-29th May 1998.
- [1998Mil] Yu.V. Milman, S. Luyckx and I.T. Northrop, Influence of Temperature, Grain Size, and Cobalt content on the Hardness of WC-Co Alloys, International Journal of Refractory Metals and Hard Materials, 17 (1999) 39-44.
- [1998Ste] A. Stewart, P.H. Shipway and D.G. McCartney, Influence of Heat Treatment on the Abrasive Wear Behaviour of HVOF Sprayed WC-Co Coatings, Surface Coating Technology, 105 (1998) 13-24.
- [1998Ver] C. Verdon, A. Karimi and J-L. Martin, A study of High Velocity Oxy-fuel Thermally Sprayed Tungsten Carbide based Coatings. Part 1: Microstructures. Material Science Engineering A, 46(1-2) (1998) 11-24.
- [1998Vil] H.L. de Villiers-Lovelock, J. Kinds and P.M. Young, Characterization of WC-12Co Thermal Spray Powders and HPHVOF Wear Resistance Coatings, Journal of Powder Metallurgy, 41(4) (1998) 292-299.
- [1998Vil] H.L. de Villiers-Lovelock, Powder Processing Structure Relationships in WC-Co Thermal Spray Coatings: A Review of the Published Literature, Journal Thermal Spray Technology, 7(3) (1998) 357-372.

- [1999Bed] J. Beddoes and J.G. Parr, Introduction to Stainless Steel, ASM International, Material Park, OH, 83 (1999).
- [1999Eng] H. Engqvist, S. Ederyd, N. Axen and S. Hogmark, Grooving Wear of Single-Crystal Tungsten Carbide. *Wear*, 230(2) (1999) 165-174.
- [1999Jac] L. Jacobs, M.M. Hyland and M. de Bonte, Study of the Influence of Microstructural Properties on the Sliding Wear Behaviour of WC-Co, *Journal of Thermal Spray Technology*, 8 (1999) 125-132.
- [1999Pin] J. Pina, A. Dias and J.L. Lebrun, Mechanical Stiffness of Thermally Sprayed Coatings and Elastics Constants for Stress Evaluation by X-Ray Diffraction, *Materials Science Engineering*, A267 (1999) 130-144.
- [1999Ste] D.A. Stewart, P.H. Shipway and D.G. McCartney, Abrasive wear behaviour, of convectional and nanocomposite HVOF-Sprayed WC-Co Coatings, *Wear*, 225-229 (1999) 789-798.
- [1999Sto] J. Stokes and L. Looney, HVOF System Definition to Maximise the Thickness of Formed Components, *Proceedings of Advances in Materials and Processing Technologies*, Vol. 2, 775-784, Dublin, Ireland, 19th-20th May (1999).
- [2000Fri] A. Fritsch, R. Gardow and A. Killinger, Development of Highly Wear Resistant Coatings for Deflector Blades in Paper Industry, *Thermal Spray Surface Engineering via Applied Research (Proceedings of ITSC 2000)*, ASM International, C.C. Berndt, Ed., 1051-1055, Montreal, Canada, 8th-11th May 2000.
- [2000Lia] H. Liao, B. Normand and C. Coddet, Influence of Coating Microstructure on the Abrasive Wear Resistance of WC/Co Cermet Coatings, *Surface Coatings Technology*, 124 (2000) 235-242.
- [2000Sta] M.H. Staia, E. Ramos, A. Carrasquero, A. Roman, J. Lesage, D. Chicet and G. Mesmacque, Effect of Substrate Roughness Induced by Grit Blasting upon Adhesion of WC-17%Co Thermal Sprayed Coatings, *Thin Solid Films*, 377-378 (2000) 657-664.
- [2000Ste] D.A. Stewart, P.H. Shipway and D.G. McCartney, Microstructure Evolution in Thermally Sprayed WC-Co Coatings: Comparison between Nanocomposite and Conventional Starting Powders, *Acta Materialia*, 48 (2000) 1593-1604.
- [2000Sto] J. Stokes and L. Looney, Properties of WC-Co Components Produced Using the HVOF Thermal Spray Process, *Proceedings of the 1st International*

- Thermal Spray Conference, C.C. Berndt (Ed.), ASTM International, 263-271, Montreal, Canada, 8th-11th May 2000.
- [2000Vil] H.L. De Villiers Lovelock, The Effect of Vanadium Carbide Additions on the Microstructure and Wear Resistance of WC-Co HP/HVOF, M.Sc. Dissertation, University of the Witwatersrand. 2000.
- [2001Ami] S. Amirhaghi, H.S. Reehal, R.J.K. Wood and D.W. Wheeler, Diamond Coating on Tungsten Carbide and their Erosive Wear Properties, Surface Coating Technology, 135 (2001) 126-138.
- [2001Gui] J.M. Guilemany, J.M. Miguel, S. Vizcaino and F. Climent, Role of Three-Body Abrasion Wear in the Sliding Wear Behaviour of WC-Co Coatings Obtained by Thermal Spraying, Surface Coating Technology, 140 (2001) 141-146.
- [2001Mur] J.K.N. Murthy, D.S. Rao and B. Venkataramam, Effect of Grinding on the Erosion Behaviour of WC-Co-Cr Coating Deposited by HVOF and Detonation Gun Spray Processes, Wear, 249 (2001) 592-600.
- [2001Nas] M.N. Nascimento, R.C. Souza, I.M. Miguel, W.L. Pigatin and H.J.C. Voorwald, Effects of Tungsten Carbide Thermal Spray Coatings by HP/HVOF and Hard Chromium Electroplating on AISI 4340 High Strength Steel, Surface Coating Technology, 138 (2001) 113-24.
- [2001Qia] Y. Qiao, Y.R. Liu and T.E. Fischer, Sliding and Abrasive Wear Resistance of Thermal Sprayed WC-Co Coatings, Journal Thermal Spray Technology 10 (2001) 1596-1604.
- [2001Ska] G. Skandan, R. Yao and B.H. Kear, Multimodal Powders, A new class of Feedstock Material for Thermal Spraying of Hard Coatings, Scripta Materialia, 44 (2001) 1699-1702.
- [2001Str] E. Strock, P. Ruggiero and D. Reynolds, The Effect of Off-Angle Spraying on the Structure and Properties of HVOF WC/CoCr Coatings in Thermal Spray 2001: New Millenium (Proceedings of ITSC 2001), ASM International, C.C. Berndt, K.A. Khor and E.F. Lugscheider (Ed.), 671-676, Singapore, 28th-30th May 2001.
- [2001Wit] P.J. Wither and H.K.D.H. Bhadeshia, Residual Stress Part 1: Measurement Technique, Material Science Technology, 17 (2001) 355-366.

- [2002God] C. Godoy, E.A. Souza, M.M. Lima and J.C.A. Batista, Correlation between Residual Stresses and Adhesion of Plasma Sprayed Coating: Effects of a Post-Annealing Treatment, *Thin Solid Films*, 420-421 (2002) 438-445.
- [2002Kuk] P. Kuku and S. Zimakov, Wear Resistance of Thermal Sprayed Coatings on the Base of Recycled Hardmetal, *Surface and Coating Technology*, 130 (2000) 46-51.
- [2002Kul] P. Kulu, Selection of Powder Coatings for Extreme Erosion Wear Conditions, *Advanced Engineering Materials*, 4(6) (2002) 392-397.
- [2002Net] D.A. Nethercot and L. Gardner, Exploiting the Special Features of Stainless Steel in Structural Design, *Proceedings of the Third Conference on Advances in Steel Structures*, Hong Kong, China, 1 (2002) 43-55.
- [2002Pih] T. Pihl, Powder Coatings for Abrasive Wear, Ph.D. Thesis, Texas Technology University, TTU Press, (2002) 124.
- [2003Bob] B. He. Bob, Fundamental of X-ray Powder Diffraction, *Powder Diffraction Journal*, 18(2) (2003) 106-113.
- [2003Coa] D.L. Coats and A.D. Krawitz, Effect of Particle Size on Thermal Residual Stress in WC-Co Composite, *Materials and Engineering*, A359 (2003) 338-342.
- [2003Dal] D. Dalman, S. Benmedhakene, H. Kebir, C. Richard, A. Laksimi, and J.M. Roleandt, Investigation of Failure Mechanisms in WC-Co Coated Materials, *Surface and coatings Technology*, 173(2) (2003) 130-143.
- [2003Kir] H. Kirl, H. Ludewig and L. Mausner, Super-Invar as a Target for a Pulsed High-Intensity Proton Beam, *Proceedings of the Particle Accelerator Conference*, (2003) 1628-1630.
- [2003Pin] J. Pina, A. Dias and J.L. Lebrun, Study by X-ray Diffraction and Mechanical Analysis of the Residual Stress Generation during Thermal Spraying, *Material Science and Engineering*, A347 (2003) 21-31.
- [2003Sud] T. Sudprasert, P.H. Shipway and D.G. McCartney, Sliding Wear Behaviour of HVOF Sprayed WC-Co Coatings deposited with both Gas-Fuelled and Liquid Fuelled System, *Wear*, 255 (2003) 943-949.
- [2003Wit] P. Withers, M.E. Fitzpatrick and A. Lodini (Eds.), *Analysis of Residual Stress by Diffraction using Neutron and Synchrotron Radiation*, Taylor and Francis (London), 2003.

- [2003Yan] Q. Yang, T. Senda and A. Ohmori, Effect of Carbide Grain Size on Microstructure and Sliding Wear Behaviour of HVOF Sprayed WC-12%Co Coatings, *Wear*, 254 (2003) 23-34.
- [2004Bou] S. Bouaricha and B. Marple, Phase Structure-Mechanical Property Relationships in HVOF-Sprayed WC-12Co Coatings, *Proceedings of the International Thermal Spray Conference*, Osaka, Japan, 10th-12th May 2004, ISBN 3-87155-792-7.
- [2004Dav] J.R. Davids, *Handbook of Thermal Spray Technology*, ASM International, Ohio, USA. 2004.
- [2004Kel] T. Keller, N. Margadant, T. Pirling, M.J.R. Escibano and W. Wagner, Residual Stress Determination in Thermally Sprayed Metallic Deposits by Neutron Diffraction, *Materials Science and Engineering A*, 373 (2004) 33-34.
- [2004Kha] Sh. Khameneh Asl, M. Heydarzadeh Sohi and S.M.M. Hadavi, The Effect of Heat Treatment on Residual Stresses in HVOF Sprayed WC-Co Coating, *Materials Science Forum*, 465-466 (2004) 427-432.
- [2004Li] C.J. Li, Y.Y. Wang, G.J. Yang, A. Ohmori and K.A. Khor, Effect of Solid Carbide Particle Size on Deposition Behaviour, Microstructure and Wear Performance of HVOF Cermet Coatings. *Materials Science and Technology*, 20(9) (2004) 1087-1096.
- [2004Mon] G. Montay, A. Cherouat, A. Nussair and J. Lu, Residual Stresses in Coating Technology, *Journal of Material Science Technology*, 20(1) (2004) 81-84.
- [2004Osm] Osman Anderoglu, *Residual Stress Measurement Using X-Ray Diffraction*, M.Sc. Dissertation, A & M University Texas USA, 2004.
- [2004Ste] A. Steuwer, J.R. Santisteban, M. Turski, P.J. Withers and T. Buslaps, High-Resolution Strain Mapping in Bulk Samples using Full-Profile Analysis of Energy-Dispersive Synchrotron X-ray Diffraction Data, *Journal of Applied Crystallography*, 37 (2004) 883-889.
- [2004Sto] J. Stoke and L. Looney, Residual Stress in HVOF Thermally Sprayed Thick Deposits, *Surface Coating Technology*, 18 (2004) 177-178.
- [2004Sto2] V. Stoica, R. Ahmed, M. Golshan and S. Tobe, Sliding Wear Evaluation of Hot Isostatically Press Thermal Spray Cermet Coatings, *Journal Thermal Spray Technology*, 13(1) (2004) 93-107.
- [2004Wan] J. Wang, K. Li, D. Shu, X. He, B. Sun, Q. Guo, M. Nishio and H. Ogawa, Effects of Structure and Processing Technique on Properties of Thermal Spray

- WC-Co and NiCrAl-WC-Co Coatings, *Material Science Engineering*, A371 (2004) 187-192.
- [2004Wan2] Y. Wang, C. Li, M.A. Jian and G. Yang, Effect of Flame Conditions on Abrasive Wear Performance of HVOF Sprayed Nanostructure WC-12Co Coatings, *Trans. Nonferrous Metallurgical Society China*, 14(2) (2004) 72-76.
- [2004Yu] D.Y.W. Yu and F. Spaepen, The Yield Strength of Thin Films on Kapton, *Journal Applied Physics*, 95(6) (2004) 2991-2997.
- [2004Zha] L. Zhao, M. Maurer, F. Fischer, R. Dicks and E. Lugscheider, Influence of Spray Parameters on the Particle In-flight Properties and the Properties of HVOF Coating of WC-CoCr, *Wear*, 257 (2004) 41-46.
- [2005Art] B. Arturas, Influence of Temperature on Tungsten Carbide Coating Sprayed by Different Spray Systems, *Material Science*, 2(11) (2005) 105-109.
- [2005Cra] D.E. Crawmer, Coating Structures, Properties, and Materials, *Handbook of Thermal Spray Technology*, J.R. Davis (Ed.), ASM International, 2005.
- [2005Hut] M.T. Hutchings, P.J. Wither, T.M. Holden and T. Lorentzen, Introduction to the Characterization of Residual Stress by Neutron Diffraction, Taylor and Francis Group LLC, UK, 2005, ISBN 0-203-40281-2.
- [2005Kul] P. Kulu, R. Tarbe and A. Vallikivi, Abrasion Wear of Powder Materials and Coatings, *Material Science*, 11(3) 230-234.
- [2005Mai] D. Di Maio and S.G. Roberts, Substrate and Elastic Recovery Effects in Hardness Measurement of CVD WC based Coatings, *Philosophical Magazine* 85(1) (2005) 33-43.
- [2005Mac] C.N. Macho, Preparation, Characterization and Testing of WC-VC-Co HP/HVOF Thermal Spray Coatings, Ph.D. Thesis, University of the Witwatersrand, 2005.
- [2005Osa] S. Osawa, T. Itsukaichi and R. Ahmed, Influence of Substrate Properties on the Impact Resistance of WC Cermet Coatings, *Journal of Thermal Spray Technology*, 14(4) (2005) 495-501.
- [2005Voo] H.J.C. Voorwald, R.C. Souza, W.L. Pigatin and M.O.H. Cioffi, Evaluation of WC-17Co and WC-10Co-4Cr Thermal Spray Coatings by HVOF on the Fatigue and Corrosion Strength of AISI 4340 Steel, *Surface Coating Technology*, 190 (2005) 155-164.
- [2006Cel] E. Celik, O. Culha, B. Uyulgan, N.F. Ak Azem, I. Ozdemir and A. Turk, Assessment of Microstructural and Mechanical Properties of HVOF Sprayed

- WC-based Cermet Coatings for a Roller Cylinder, *Surface and Coatings Technology*, 200 (2006) 4320-4328.
- [2006Kha] Sh. Khameneh Asl, M. Heydarzadeh Sohi, K. Hokamoto and M. Uemura, Effect of Heat Treatment on Wear Behaviour of HVOF Thermally Sprayed WC-Co Coatings, *Wear*, 260 (2006) 1203-1208.
- [2006Mur] J.K.N. Murthy and B. Venkataraman, Abrasive Wear Behaviour of WC-CoCr and $\text{Cr}_3\text{C}_2\text{-20(NiCr)}$ deposited by HVOF and Detonation Spray Processes. *Surface Coating Technology*, 200 (2006) 2642-2652.
- [2006Obe] J.B. Oberste, B. Marple and C. Moreau, Suspension Plasma Spraying of Nanostructured WC-12Co Coatings. *Journal Thermal Spray Technology*, 15(4) (2006) 676-681.
- [2006Wez] M. Wenzelburger, D. Lopez and R. Gadow, Methods and Application of Residual Stress Analysis on Thermally Sprayed Coatings and Layer Composites, *Surface and Coatings Technology*, 201 (2006) 1995-2001.
- [2007Ahm] R. Ahmed, H. Yu, L. Edwards and J.R. Santisteban, Influence of Vacuum Heat Treatment on the Residual Stress of Thermal Spray Cermet Coatings, *Proceedings of the World Congress on Engineering*, Vol. II, London, UK., 2nd-4th July 2007.
- [2007Bai] K.H. Baik, J.H. Kim and B.G. Seong, Improvements in Hardness and Wear Resistance of Thermally Sprayed WC-Co Nanocomposite Coatings, *Materials Science and Engineering A*, 449-451 (2007) 846-849.
- [2007Kim] J.H. Kim, K.H. Baik, B.G. Seong and S.Y. Hwang, Effects of Post-Spraying Heat Treatment on wear Resistance of WC-Co Nanocomposite Coatings, *Materials Science and Engineering A*, 449-451 (2007) 876-879.
- [2007Kra] P.V. Krakhmalev, Abrasion of Ultrafine WC-Co by Fine Abrasive Particles, *Transactions of Nonferrous Metals Society of China*, 17 (2007) 1287-1293.
- [2007Luy] S. Luyckx and C.N. Machio, Characterization of WC-VC-Co Thermal Spray Powders and Coating, *International Journal of Refractory Metals and Hard Materials*, 25 (2007) 11-15.
- [2008Jia] H. Jianhong, D. Bruce and T. Wolfe, Peening Effect of Thermal Spray Coating Process, *Journal of Thermal Spray Technology*, (2008) 214-220.
- [2008San] Y.Y. Santana, P.O. Renault, M. Sebastiani, J.G. Barbera, J. Lesage, E. Bemporad, E. Le Bourhis, E.S. Puchi-Cabrera and M.H. Staia.

- Characterization and Residual Stresses of WC-Co Thermally Sprayed Coatings, *Surface and Coatings Technology*, 202 (2008) 4560-4565.
- [2008Zha] S.-Y. Zhang, A.M. Venter, W.J.J. Vorster and A.M. Korsunsky, High-Energy Synchrotron X-ray analysis of Residual Plastic Strains induced in Short-Peened Steel Plate, *Journal Strain Analysis*, 43 (2008) 229-241.
- [2009Cha] K.P. Chander, M. Vashista, K. Sabirudding, S.Paul and P.P. Bandyopadhyay, Effects of Grit Blasting on Surface Properties of Steel Substrates, *Materials and Design*, 30 (2009) 2895-2902.
- [2009Kam] S. Kamnis and S. Gu, Numerical Modelling of In-flight Particle Dynamics of Non-Spherical Powder, *Surface and Coatings Technology*, 203 (2009) 3485-3490.
- [2009Mah] R.A. Mahesh, R. Jayaganthan and S. Prakash, Microstructural Characteristics and Mechanical Properties of HVOF Sprayed NiCrAl Coating on Superalloys, *Journal of Alloys and Compounds*, 468 (2009) 392-405.
- [2009Mar] D. Mari, B. Clausen, M.A.M. Bourke and K. Buss, Measurement of Residual Thermal Stress in WC-Co by Neutron Diffraction, *International Journal of Refractory Metals and Hard Materials*, 27 (2009) 282-287.
- [2009Mat] S. Mathew, B. James and M. Hyland, The Role of Microstructure in the Mechanism of High Velocity Erosion of Cr₃C₂-NiCr Thermal Coating: Part 2, Heat Treated Coatings, *Surface and Coatings Technology*, 203 (2009) 1094-1100.
- [2010Ast] ASTM G65-04, Standard Test Method for Measuring Abrasion using the Dry/Rubber Wheel Apparatus, *Annual Book of ASTM Standards Philadelphia*. (03) (02) 2010.
- [2010Bab] P.S. Babu, B. Basu and G. Sundararajan, Abrasive Wear Behaviour of Detonation Sprayed WC-12Co Coatings: Influence of Decarburization and Abrasive Characteristic, *Wear*, 268 (2010) 1387-1399.
- [2010Kum] K. Kumari, K. Anand, M. Bellacci and M. Giannozzi, Effect of Microstructure on Abrasive Wear Behaviour of Thermally Sprayed WC-10Co-4Cr Coatings, *Wear*, 268 (2010) 1309-1319.
- [2010Mab] L. Mabotja, Final Year Research Project Report, University of the Witwatersrand, 2010.

- [2010Nta] M. Ntakadzeni, Final Research Project Report, University of the Witwatersrand, 2010.
- [2010Rob] R.J.K. Wood, Tribology of Thermal Sprayed WC-Co Coatings, International Journal of Refractory Metals and Hard Materials, 28 (2010) 82-94.
- [2010Sah] T. Sahraoui, S. Gruessasma, M.A. Jeridane and M. Hadji, HVOF Sprayed WC-Co Coatings: Microstructure Mechanical Properties and Friction Moment Prediction, Material and Design, 31 (2010) 1431-1437.
- [2011Azi] M.J. Azizpour, S. Norouzi, H.M. Majd, D. Sajedipour, R.M. Sadr, M.D. Mehr, S.A. Shoabi and R. Mohammadi, Development Trend in Investigating of Residual Stresses in WC-Co Coating by Thermal Spraying, World Academy of Science Engineering and Technology, 74 (2011) 499-502.
- [2011Ric] M. Richert and B. Leszczynska-Madej, Effect of the Annealing on the Microstructure of HVOF Deposited Coatings, Journal of Achievements in Materials and Manufacturing Engineering, 46(1) (2011) 95-102.
- [2012Cha] Li Chang-Jiu and Y. Guan-Jun, Relationships Between Feedstock Structure, Particle Parameter, Coating Deposition, Microstructure and Properties for Thermally Sprayed Conventional and Nanostructured WC-Co, International Journal of Refractory Metals and Hard Materials, (2012) in press.
- [2012Ola] O.P. Oladijo, A.M. Venter, L.A. Cornish and N. Sacks, X-ray diffraction Measurement of Residual Stresses in WC-Co Thermally Sprayed Coatings onto Metal Substrates, Surface Coating Technology, 206 (2012) 4725-4729.
- [2012Ric] C.A. Ricardo, M.B. Carmen, J.P. Fernando, A. Helene and F. Pierre, The Influence of Dry Particle Coating Parameters on Thermal Coatings Properties, Advance Plasma Spray Applications, 2 (2012) 39-60.
- [2012Ros] N.S. Rossini, M. Dassisti, K.Y. Benyounis and A.G. Olabi, Methods of Measurement Residual Stresses in Components, Materials and Design, 35 (2012) 572-588.
- [2012Ven] A.M. Venter, T. Pirling, T. Buslaps, O.P. Oladijo, A. Steuwer, T.P. Ntsoane, L.A. Cornish and N. Sacks, Systematic Investigation of Residual Strains Associated with WC-Co Coatings Thermal Sprayed onto Metal Substrates, Surface Coatings Technology, 206 (2012) 4011-4020.
- [2013Kra] A.D. Krawitz and E.F. Drake, Compressive Hard Materials: Volume I Cemented Carbides Residual Stress, in press.

- [URLCoe] Coefficients of Linear Thermal Expansion, URL: www.Engineeringtoolbox.com/Linear-Expansion-Coefficients-d-95.html (Accessed: 2011/11/09).
- [URLMel] Melting Temperatures of Metals, URL: www.Auto-ware.com/Techref/Meltpoint.htm.(Accessed: 2010/11/07).
- [URLRes] Residual Stress Determination, URL: [http:// Sites.Google. Com /Site/ Temfemguy /Research/Residual – Stress – in - alloy Forging](http://Sites.Google.Com/Site/Temfemguy/Research/Residual-Stress-in-alloy-Forging) (Accessed: 2011/11/09).

APPENDIX A

RAW DATA OF AVERAGE MASS LOSS IN ABRASION TESTS LOAD = 25N

BATCH A SAMPLES

Table B1. Dry abrasion wear loss of WC-17Co coatings on different substrates.

Time (minutes)	Brass (g)	304L stainless steel (g)	Super-invar (g)	Aluminum (g)
0	0	0	0	0
5	0.027	0.029	0.028	0.032
10	0.042	0.045	0.041	0.053
15	0.056	0.056	0.057	0.067
20	0.072	0.065	0.069	0.079
25	0.083	0.076	0.082	0.09
30	0.093	0.085	0.092	0.1

BATCH B SAMPLES

Table B2. Dry abrasion wear loss of the parent material (metal substrate).

Time (minutes)	Mild steel (g)	Brass (g)	Aluminium (g)	Super-invar (g)	304L stainless steel (g)
0	0	0	0	0	0
5	0.630	0.936	0.305	0.544	0.703
10	0.830	1.777	0.367	0.827	0.993
15	0.960	1.314	0.401	0.960	1.170
20	1.060	1.424	0.428	1.054	1.295
25	1.062	1.494	0.450	1.129	1.367
30	1.129	1.558	0.471	1.183	1.430

Table B3. Dry abrasion wear loss of the grit-blasted samples.

Time (minutes)	Aluminum (g)	304L stainless steel (g)	Brass (g)	Mild steel (g)	Super-invar (g)
0	0	0	0	0	0
5	0.147	0.270	0.363	0.293	0.198
10	0.182	0.344	0.475	0.419	0.264
15	0.214	0.413	0.554	0.480	0.356
20	0.239	0.485	0.600	0.536	0.429
25	0.266	0.567	0.613	0.577	0.510
30	0.278	0.602	0.653	0.617	0.569

Table B4. Dry abrasion wear loss of WC-17Co coating on different substrates.

Time (minutes)	Mild steel (g)	Brass (g)	Aluminum (g)	Super-invar (g)	304L stainless steel (g)
0	0	0	0	0	0
5	0.025	0.022	0.017	0.064	0.029
10	0.038	0.034	0.027	0.086	0.040
15	0.049	0.045	0.035	0.107	0.046
20	0.061	0.056	0.043	0.127	0.052
25	0.072	0.066	0.051	0.144	0.059
30	0.084	0.073	0.057	0.161	0.066

Table B5. Dry abrasion wear loss of annealed WC-17Co coating on different substrates.

Time (minutes)	Mild steel (g)	Brass (g)	Aluminium (g)	Super-invar (g)	304L stainless steel (g)
0	0	0	0	0	0
5	0.052	0.023	0.015	0.061	0.013
10	0.091	0.038	0.022	0.081	0.021
15	0.118	0.050	0.026	0.100	0.025
20	0.143	0.060	0.030	0.114	0.029
25	0.166	0.072	0.034	0.127	0.032
30	0.179	0.081	0.039	0.138	0.035

APPENDIX B

JOURNAL PAPERS PUBLISHED DURING THE COURSE OF THIS Ph.D

- **O.P. Oladijo**, A.M. Venter, L.A. Cornish, and N. Sacks, X-ray Diffraction Measurement of Residual Stress in WC-Co Thermally Sprayed Coating onto Metal Substrates, *Surface Coating Technology*, 206(23) (2012) 4725-4729.
- A.M. Venter, T. Pirlin, T. Buslap, **O.P. Oladijo**, L.A. Cornish, N. Sacks, Systematic Investigation of Residual Strains Associated with WC-Co Coatings Thermal Sprayed onto Metal Substrate, *Surface Coating Technology*, 206(19-20) (2012) 4011-4020.
- **O.P. Oladijo**, N. Sacks, L.A. Cornish, A.M. Venter, Effect of Substrate on the 3 body Abrasion Wear of HVOF WC-17 wt% Co Coatings, *International Journal of Refractory Metals and Hard Materials*, 35 (2012) 288-294.
- A.M. Venter V. Luzin, **O.P. Oladijo**, L.A. Cornish and N.sacks, Study of Interactive Stresses in Thin WC-Co Coating of Thick Mild Steel Substrate using High Precision Neutron Diffraction, *MECA/SECA IV*, 7th-9th September 2011, University of Hamburg, Hamburg, Germany. Manuscript accepted for publication by Materials Science Forum.
- Andrew M. Venter, **O. Philip Oladijo**, Lesley A. Cornish and Natasha Sacks, Characterization of the Residual Stress in HVOF WC-Co Coatings and Substrates. Manuscript accepted for publication by Material Science Forum.

CONFERENCE PAPERS PUBLISHED

- **O.P. Oladijo**, L.A. Cornish, A.M. Venter, and N. Sacks, Characterisation of WC-Co Thermal Spray Coatings on Different Substrates, *Proceedings of the Microscopy Society of Southern Africa Conference*, Volume 39, p. 51, 8th – 11th December 2009, Durban. ISSN 0250-0418 : ISBN 0-620-35056-3.
- **O.P. Oladijo**, A.M. Venter, L.A. Cornish, N. Sacks and S. Shrivastava, Effect of Substrates on the Microstructure of Thermally Sprayed WC-4.88wt%Co Coatings, *Powder Metallurgy International Conference*, Florence, Italy, October 10th-14th 2010, Vol. 3, paper 66, pp. 1-8.
- **O.P. Oladijo**, L.A. Cornish, A.M. Venter, and N. Sacks, Abrasion of WC-4.88wt%Co Thermal Spray Coatings on Different Substrate, *Proceedings of the*

Microscopy Society of Southern Africa Conference, Volume 40, p. 62, Bela-Bela, South Africa, 26th-29th October 2010. ISSN 0250-0418 : ISBN 0-620-35056-3.

- **O.P. Oladijo**, L.A. Cornish, A.M. Venter and N. Sacks, Influence of Residual Stresses of the WC-Co Thermal Sprayed Coatings on Metal Substrate, Proceedings of the Microscopy Society of Southern Africa Conference, Volume 41, p. 35, Pretoria, South Africa, 4th-9th December 2011. ISSN 0250-0418 : ISBN 0-620-35056-3.
- **O.P. Oladijo**, L.A. Cornish, A.M. Venter and N. Sacks, Effect of Heat Treatment on the Microstructure and Residual Stress in the WC-17Co Coated System, Proceedings of the Microscopy Society of Southern Africa Conference, Volume 42, p. 100, Cape Town, 4th – 7th December 2012. ISSN 0250-0418 : ISBN 0-620-35056-3.
- Vladimir Luzin, Andrew M. Venter, **O. Philip Oladijo**, Lesley Cornish, Natasha Sacks, Residual Stress in WC-Co Coated Systems Studied by High Resolution Neutron Diffraction. 5th Asian Thermal Spray Conference, 26th-28th November 2012, Ibaraki, Japan. Selected contributions to be published in Journal of Thermal Spray Technology.
- **O.P. Oladijo**, A.M. Venter, L.A. Cornish, N. Sacks and N. Tshepo, Evaluation of HVOF Coatings on Different Substrates, accepted for Coating Science International Conference, Amsterdam, Netherlands, 24th-28th June 2013. To be published in Journal of Progress Organic Coatings.
- A.M. Venter, **O.P. Oladijo**, V. Luzin, L.A. Cornish, N. Sacks, Performance Characterisation of Metallic Substrates Coated by HVOF WC-Co, accepted for International Metallurgical Coating Conference, San Diego, USA, 2013. To be published in the Journal of Surface Coating Technology.

PRESENTATIONS

- Presentation for the Carbide and Cermet Focus Area at the Annual CoE-SM workshop, 1st February 2010.
- **O.P. Oladijo**, A.M. Venter, L.A. Cornish, N. Sacks, Studying the Abrasion of WC-Co Thermal Spray Coatings on Different Substrate, abstract for presentation at the Powder Metallurgy Association of South Africa Symposium, 27th October 2010.
- **O.P. Oladijo**, A.M. Venter, L.A. Cornish, N. Sacks, Characterization and Residual Stresses of WC-Co Thermally Sprayed Coatings on Metal Substrate, abstract for

presentation at the Powder Metallurgy Association of South Africa Symposium, 27th October 2011.

- **O.P. Oladijo**, L.A. Cornish, A.M. Venter, N. Sacks, Residual Stress Determination in the Thermally Sprayed WC-Co by Neutron Diffraction, abstract for presentation at the Wits 4th Cross-Faculty Symposium, 22nd October 2012.
- **O.P. Oladijo**, L.A. Cornish, N. Sacks, A.M. Venter, Effect of the Annealing on the Microstructure of HVOF Deposited WC-17Co Coatings, abstract for presentation at the Powder Metallurgy Association of South Africa Symposium, 31st October 2012.

JOURNAL PAPERS IN PREPARATION

- **O.P. Oladijo**, A.M. Venter, L.A. Cornish, N. Sacks, Microstructural Characteristic of HVOF Sprayed WC-Co Coatings on Metal Substrate, to be submitted to Material Science Engineering A.
- **O.P. Oladijo**, L.A. Cornish, N. Sacks, A.M. Venter, Contributions of the Coating Processes in the Wear Resistance of WC-17Co Coating, to be submitted to Wear.
- **O.P. Oladijo**, A.M. Venter, L.A. Cornish, and N. Sacks, Correlation between Residual Stress and Abrasive Wear Resistance in WC-17Co Thermally Sprayed Coating onto Metal Substrates, to be submitted to Surface Coating Technology.



X-ray diffraction measurement of residual stress in WC-Co thermally sprayed coatings onto metal substrates

O.P. Oladijo^{a,b,*}, A.M. Venter^{a,b}, L.A. Cornish^a, N. Sacks^a

^a School of Chemical & Metallurgical Engineering and DST/NRF Centre of Excellence in Strong Materials, University of the Witwatersrand, Private Bag 3, WITS, 2050, South Africa

^b Research & Development Division, NECSA Limited, Pretoria, South Africa

ARTICLE INFO

Article history:

Received 15 November 2011

Accepted in revised form 23 January 2012

Available online 1 February 2012

Keywords:

Residual stress

HVOF

WC-Co coating

ABSTRACT

Investigation of the residual stresses and microstructural properties associated with HVOF thermal spray coating of WC-17 wt% Co of same thickness on three substrates with coefficients of thermal expansion different to that of WC. The residual stresses were measured by X-ray diffraction $\sin^2\psi$ techniques using $\text{CoK}\alpha$ radiation. The results indicated residual stresses that have different natures for the as-sprayed coatings despite using the same powder as feedstock. The magnitudes of the stresses in the as-sprayed condition are low.

© 2012 Elsevier B.V. All rights reserved.

1. Introduction

Thermally sprayed WC-Co coatings are widely used in industry as they offer an effective and economic method to protect base material against environmental load and confer wear resistance without compromising other attributes of the component [1]. The control of the residual stress is a primary issue in coating technology. Residual stresses are those stresses that remain after deformation with all external forces removed. The origin of the residual stresses in coating has been thoroughly investigated [2,3]. Both material and deposition process may produce a residual stress, which may be particularly critical in applications where a large mismatch exists between thermal, structural and mechanical properties of the layers and substrates. In the case of thermal spray coatings, quenching stresses due to rapid cooling of the coating, thermal mis-match stresses between the substrate and the coating, phase transformations during deposition have been identified as sources. Veebeek [4] proposed three stages for the formation of ultimate residual stress in the plasma spray process: The first stage concerns solidification of single particle due to the temperature difference between the substrate and the particles. The second stage involves the heating up of the substrate during the coating process, caused by the heat transport from the coating to the substrate. The third stage concerns the stresses caused by the cooling down of the substrate and the coating together after the coating process has been completed. Residual stress in material can either be tensile or compressive depending on the direction of the forces. The nature of the overall residual stress in coated systems may be determined by criteria identified by Stokes and Looney [5]. A major

contributor is cooling stresses associated with the relative values of their coefficients of thermal expansion, α , relative to that of the substrate material. As the temperature decreases after deposition the following options are feasible;

- $\alpha_c > \alpha_s$: a tensile stress is generated in the coating. This may lead to adhesion loss or cracking of the coating.
- $\alpha_c = \alpha_s$: no cooling stress will develop.
- $\alpha_c < \alpha_s$: the resulting cooling stress is compressive. If excessive, even this generally beneficial condition may lead to problem conditions such as buckling that can lead to delamination.

Thus, residual stress plays a vital role in materials as it can either enhance or degrade performance. Non-destructive stress determination is essential since it offers the possibility of stress examination as a final quality check before service, or allows stress monitoring development during the component's lifetime [6]. Specific to coatings, X-ray diffraction is a valuable technique to measure residual strain [7]. It can be applied for material that is crystalline, has relatively fine grain structure (μm grain size) and with minimal preferred orientation to produce diffraction pattern from any orientation of the sample surface. The sample may be metallic or ceramic. With this technique, diffraction peaks of suitable intensity and free of interference from overlapping Bragg peaks are selected in the high back-reflection region [6].

Investigation of residual stresses in as-sprayed WC-Co thermal spray coatings employing different techniques have not yet fully unravelled the stress nature. Wang et al. [8] using $\text{CuK}\alpha$ and Pina et al. [9] using Cr radiation evaluated the residual stresses of a HVOF WC-12Co coating by employing the $\sin^2\psi$ method and reported that residual stress of the coating was tensile. The objective of this work

* Corresponding author.

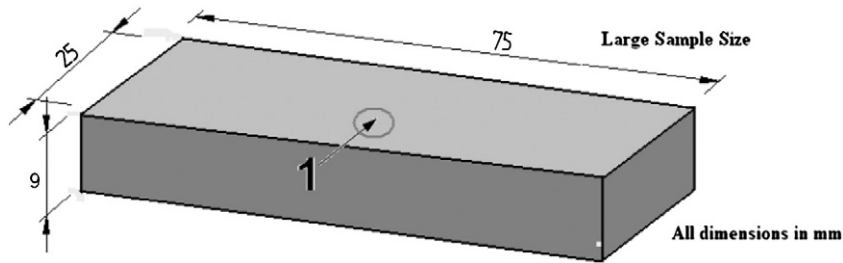


Fig. 1. Sample geometry and measurement positions for the strain analyses. The 200 μm thick WC-Co coatings have been deposited on the 25 x 75 mm² top surface. Strain measurements were taken at position 1. SEM and microstructural investigations were done on samples cut from the 10 x 25 mm² surface.

was to further explore the use of X-ray diffraction to determine the residual strain in WC-17 wt% Co HVOF coating on different substrates, and to extend it to investigate the influences of hardness and coefficients of thermal expansion on the nature of stress.

2. Experimental procedure

Brass, aluminium, and super-invar of specimen were selected as substrates that render the situation where the CTE are different to different extents to the coating. The sample size and measurement position are shown in Fig. 1.

Before deposition, the substrates were grit-blasted with alumina particles to clean and roughen the surface. Commercially available WC-17wt%Co of size -45 + 15 micron was used as feedstock. It was prepared by spray drying and sintered. The coating of 200 μm was deposited by the HVOF techniques using a TAFA JP5000 gun [10]. The parameters were the same on all coated samples and were as follow: 4 in. gun barrel; 380 mm spray distance; 0.0227 m³/h fuel (kerosene) flow rate; and 56.6 m³/h oxygen flow rate, thus similar to the parameter used elsewhere [10,11]. The cross-sectional microstructure of the coatings was studied using scanning electron microscopy (SEM) and energy dispersive analysis (EDS). The crystalline structure of the coating was characterized by X-ray diffractometer (XRD). The observations were done on the cross sections of the coated samples. The determined parameters are shown in Table 1. Grain size distribution from SEM images at 5000x magnification rendered values given in Table 1, i.e. all in μm in size.

The residual stresses on the as-sprayed coating surface were determined by X-ray diffraction using Co-K α radiation having wavelength (energies) of 1.78897 Å (7 keV). Stresses measured by X-ray diffraction were focussed only on the WC phase of the composite coating. The Co radiation penetrates approximately 4 μm thus providing investigation of the near surface region of the coatings (as done by other authors [12]). The residual stress measurements comprised accurate determination of the shift of the WC (202) Bragg peak observed at $2\theta = 143.69^\circ$ since this high angle peak was free of interference from other peak. The strain measurement geometry is shown schematically in Fig. 2. The lattice strain was obtained from the shift of the define Bragg peak position. The residual stress measurement was performed in ψ geometry using $\sin^2\psi$ for both positive and negative ψ tilt angles. With the $\sin^2\psi$ techniques the strain-free lattice parameter is obtained from the $\psi = 0$ value. The anode settings were 40 kV and 40 mA.

Table 1
Material characteristics of the different substrates [10].

Substrate	Specific heat capacity (J/g°C)	Melting Point (°C)	α [$10^6/\text{C}$]	HV Coating (GPa)	Porosity %
Brass	0.380	930	19	10.04 \pm 0.01	0.5149 \pm 0.001
aluminum	0.900	660	23	10.22 \pm 0.02	0.4581 \pm 0.002
Super-invar	0.123	1454	1.2	7.91 \pm 0.01	0.7529 \pm 0.001

α = Coefficient of linear thermal expansion.

For conversion of strain to stress the Elastic constants used for the {202} reflection of WC were $S_1 = -3.247 \times 10^{-7} \text{ MPa}^{-1}$, $1/2S_2 = 1.948 \times 10^{-6} \text{ MPa}^{-1}$, and Poisson's ratio of 0.20. These values were calculated based on Neerfield-Hill's module [7]. Data were analysed using Leptos software, version 6 as part of the Bruker AXS suite of software for residual stress analysis. A video (Laser) camera system enables alignment of the sample measurement position to the centre of the goniometer to 20 μm . The instrumental set-up included a graphite monochromator and 0.8 mm diameter collimator on the instrument primary side. Diffraction collection was done using a two-dimensional High Star (Bruker AXS) detector. Measurements were taken with the samples oriented in six different azimuth angles; 0° , 180° , 90° , 270° , 45° , 225° to determine the full stress tensor using the iso inclination geometry.

2.1. Fundamental equations for stress measurement with XRD²

The fundamental principle of 2D measurement is based on relationship between stress tensor and diffraction cone distortion. The merit of the 2D is that, point on diffraction rings are used to analyse the result with less data collection time. The fundamental equation for strain and stress measurement by diffraction, using 2D detectors is given by

$$f_{11}\epsilon_{11} + f_{12}\epsilon_{12} + f_{22}\epsilon_{22} + f_{13}\epsilon_{13} + f_{23}\epsilon_{23} + f_{33}\epsilon_{33} = \ln\left(\frac{\sin\theta_0}{\sin\theta}\right) \quad (1)$$

where, f_{ij} connotes the strain coefficient, while $\ln\left(\frac{\sin\theta_0}{\sin\theta}\right)$ determines the diffraction cone distortion at the particular (γ , 2θ) position. The material for this investigation is isotropic. Therefore, two independent elastic constants, Young's modulus, E and Poisson ratio, ν or macroscopic elastic constants were taken into consideration, as related by $1/2S_2 = (1 + \nu)/E$ and $S_1 = -\nu/E$. Then, the equation for stress measurement, using 2D detector is given by [13]:

$$P_{11}\sigma_{11} + P_{12}\sigma_{12} + P_{13}\sigma_{13} + P_{22}\sigma_{22} + P_{23}\sigma_{23} + P_{33}\sigma_{33} = \ln\left(\frac{\sin\theta_0}{\sin\theta}\right) \quad (2)$$

$$\text{where, } P_{ij} = \begin{cases} (1/E)[(1 + \nu)f_{ij} - \nu] = \frac{1}{2}S_2f_{ij} + S_1 & \text{if } i = j \\ (1/E)(1 + \nu)f_{ij} = \frac{1}{2}S_2f_{ij} & \text{if } i \neq j \end{cases}$$

Yu et al. [14] stated that for biaxial stress state, i.e. the only in-plane stress components, the above equation will become:

$$P_{11}\sigma_{11} + P_{12}\sigma_{12} + P_{22}\sigma_{22} + \frac{1 - 2\nu}{E}\sigma_{ph} = \ln\left(\frac{\lambda}{2d_0'\sin\theta}\right) \quad (3)$$

The biaxial stress state corresponds to the straight line of the $d - \sin^2\psi$ plate.

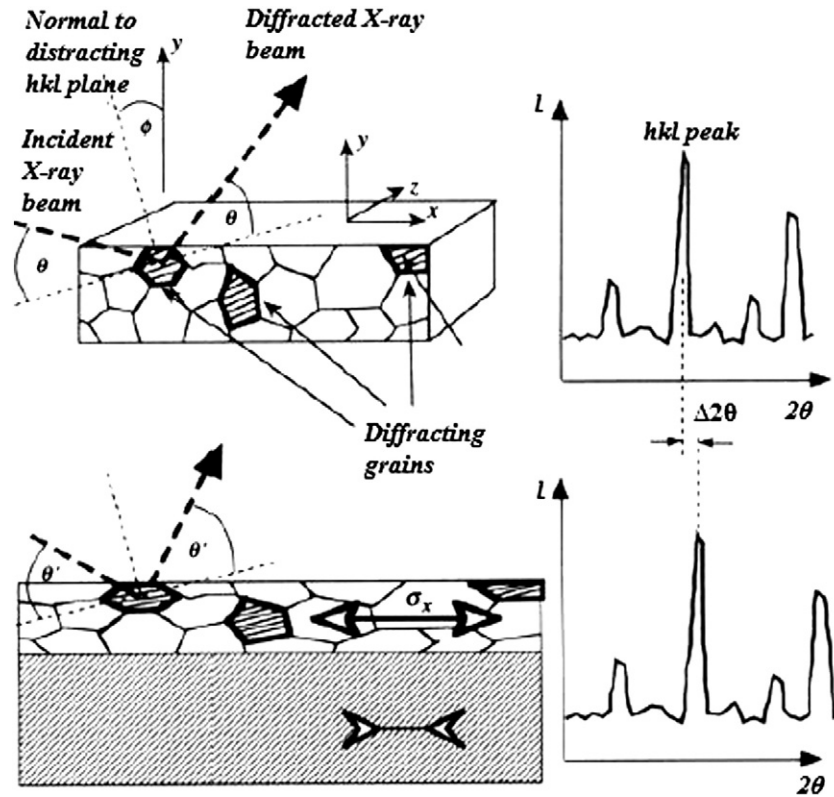


Fig. 2. Schematic diagram of the XRD strain measurement $\sin^2\psi$ technique for measurement of the residual stress [3].

2.2. The mean penetration depth

The mean penetration depth was calculated by [7]:

$$\tau = \frac{\sin\theta \cos\psi}{2\mu} \quad (4)$$

Where τ is the mean penetration depth, μ is the linear absorption coefficient, ψ is the tilt angle and θ is the Bragg peak position in degrees with the linear absorption coefficients determined according to [15].

3. Results

SEM images of the coating cross section after metallographic preparation are shown in Fig. 3. The coatings show a typical microstructure of a WC-Co alloy: the light phase consists of WC grains and dark phase is the cobalt binder while the black portions are pores. Micro-cracking was found on as-sprayed super-invar.

XRD pattern of the as-sprayed coating were shown in Fig. 4. The XRD results of the as-sprayed coating on aluminium showed WC and metallic Co with only small amount of W_2C . The as-sprayed brass sample showed WC with no Co. The as-sprayed coating on super-invar revealed the presence of WC, W_3C and Co peak. The representative of d vs $\sin^2\psi$ is shown in Fig. 5. The d - $\sin^2\psi$ of the sample shows a negative slope for as-sprayed coating on aluminium and brass except coated super-invar which shows positive slope. The residual stresses determined under the assumption of planar stress conditions are given in Table 2 and Fig. 6. The residual stresses have been determined to be compressive in the as-sprayed coatings on aluminium and brass whilst tensile on the coated super-invar. Notwithstanding the nature of the stress values, they are relatively low valued.

4. Discussion

The typical thermal sprayed coating morphology characterized by the presence of lamella boundaries, pores and equiaxial WC grains of different size embedded in the Co matrix were observed (Fig. 3). EDX confirmed that the coatings were composed of W, Co, and C. Although the macrographs of coatings are similar, their performance properties determined by mechanical testing (Vicker's hardness of 5 kg load) results are significantly different as shown in Table 1. These results indicate that microstructural analysis in WC-Co coatings do not reveal information for differentiating coating performance.

The stress state of the WC-Co bulk material was determined to be compressive in the WC component with the Co binder phase being in tension [16]. This is due to the lower thermal coefficients expansion of the Co binder compared to WC. The experimental results of the residual stresses found on as-sprayed coatings were quite different from each other despite same powder used as the feedstock. There was a large variation in the residual stresses with large errors and these did not appear to be related to coating hardness. These variation in residual stresses might be due to the following mechanism: (1) differences in coefficient of thermal expansion; (2) decomposition of WC; (3) specific heat capacity of the respectively substrate; (4) kinetic impact of the particle on the substrate during the HVOF process, caused by the heat transport from the coating to the substrate; as all play a crucial role in cooling and solidification of the coating after deposition (Table 2). In-addition, process parameters and surface morphology may also contribute. Wenzelburger et al. [17] reported that differences in residual stresses of coated systems can be attributed to four mechanisms: melting behaviour of the spray particles in the hot gas jet, impulse transfer of the impinging particles to the component surface, heating of the component due to heat transfer from the particles and from the gas jet, and the differences in thermal expansion of the coating material and the substrate.

It is interesting to note that the as-sprayed coatings render values that are both tensile and compressive dependent on the substrate

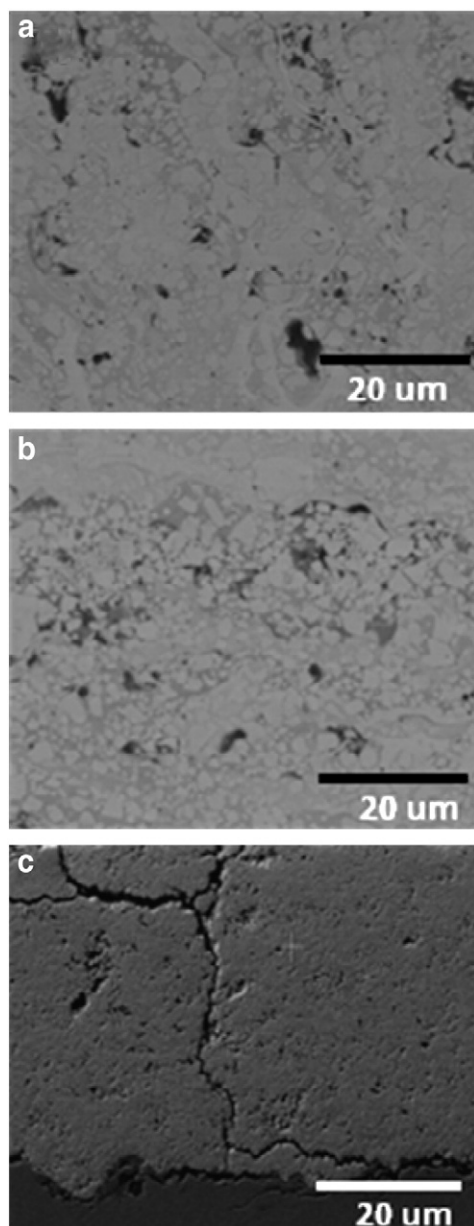


Fig. 3. SEM/BSE images showing WC-Co coating on (a) brass, (b) aluminium, and (c) super-invar. The light phase consists of WC grains and dark phase is the cobalt binder while the black portions are pores.

material coefficient of thermal expansion. The as-sprayed coating on super-invar produce residual stress that are opposite in sign (tensile) despite same powder and application process. This might be due to the following reasons; (1) lower thermal coefficients expansion of super-invar substrate (Table 1) to WC coatings; (2) microcracking found on its microstructure due to residual stresses develop in the coating vicinity. This could act as stress concentrators in the microstructure of coating, and which could cause failure of the formed material under high load, inducing tensile residual stresses; (3) high porosity and secondary phase (i.e. W_3C) found on as sprayed coating on super-invar. The exact amount of W_3C content on the surface is not known. Pejryd et al. [18] reported in his research work using modified layer-removal techniques to determine the through-thickness residual stress distribution present in the coating system. Coating composition of WC-Co/Cr and WC-Co was deposited by HVOF process on Ti-6Al-4V substrate and found that the residual stresses of WC-Co/Cr coating system was tensile in coating and compressive in the substrate near the surface, while the results of the WC-

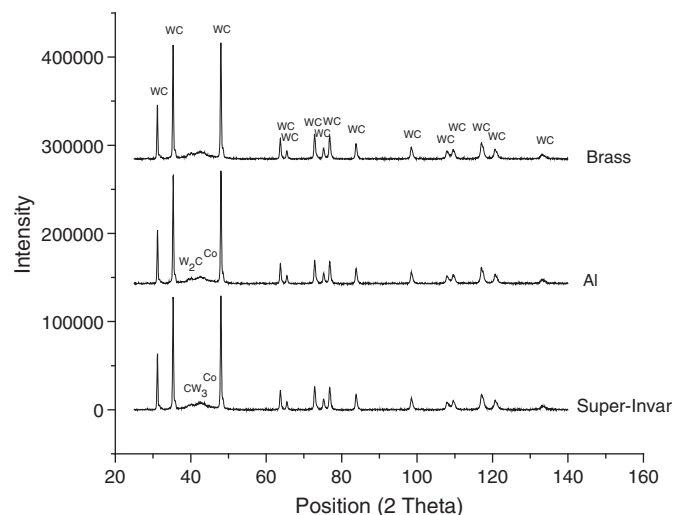


Fig. 4. XRD pattern of the as-sprayed coating.

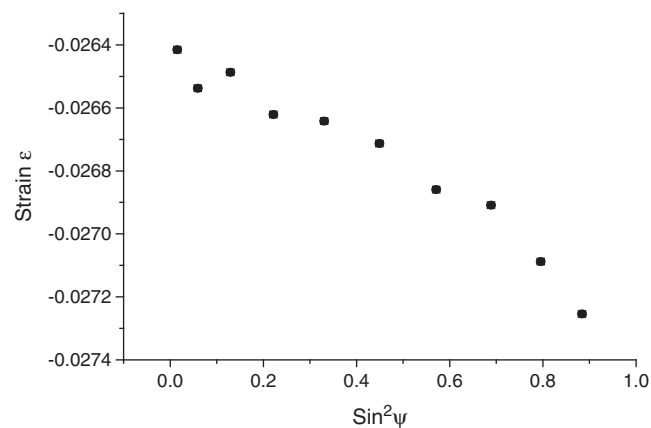


Fig. 5. The plot of d vs $\sin^2\psi$ for as-sprayed coating on brass substrate.

Co coating was opposite to the system WC-Co/Cr showing compressive in coating and tensile in the substrate, despite similar application and coating composition. Moderate compressive stresses in as-sprayed coatings on brass and aluminium substrate reflects dominances of peening mechanism of stress formation over thermal quenching. This peening effect is due to grit-blast of substrate by alumina before deposition of coating. Amirhaghi et al. [19] reported that both thermal and intrinsic stresses can contribute to the total residual stress in the coating. Intrinsic stress can arise from impurities.

There is large amount of factors and parameters which can affect the properties of the coatings. These factors make it increasingly difficult to directly compare results of coating from other source. Factors such as feedstock powder, spraying conditions, equipment, process parameters and substrates can all lead to dramatic changes in the microstructure of the coating. Stewart et al. [20], working with WC-17Co coating deposited on steel substrate, reported a tensile residual stresses of 219 MPa and standard error in the mean of 12 MPa. Ahmed et

Table 2
Determined residual stresses value in WC coating deposited on different substrate.

Coated Substrates	Co-K α (MPa)
Brass	-53.5 ± 28.0
aluminum	-129 ± 26.2
Super-invar	74 ± 30.6

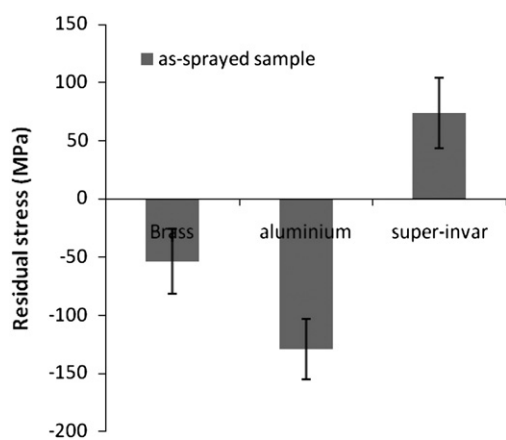


Fig. 6. Residual stresses result of WC-Co coating on different substrate.

al. [21] working with a WC-12Co deposited on stainless steel sample, reported tensile residual stresses of 259 MPa and 37 MPa. Wang et al. [8] and Pina et al. [9] also reported a value of 165 and 112 MPa respectively. Pejryd et al. [18] reported the residual stress for a WC-Co coating on A-1 and F-1 samples to be -234 MPa and -822 MPa. Stoica et al. [22] determined the residual stresses of WC-12Co coatings deposited by HVOF employing synchrotron XRD at 15 and 25 KeV and found that the value of residual stress before wear tests are confined in an interval of about -270 MPa with maximum at -332 MPa. Santana et al. [23] determined the residual stresses of an as-ground WC-12Co coating of two different thicknesses, by mean of two different methods, X-ray diffraction and hole drilling techniques. It has been determined that the surface residual stresses measured by X-ray diffraction are of compressive in nature, which could be due to grinding process. The result of the hole drilling test indicated that the through thickness residual stress distribution are not uniform and are characterized by the presence of tensile peak stresses. Such stresses were observed to decrease towards the coating-substrate interface where the compressive component of the stress state becomes greater than the tensile stresses.

However, based on this investigations, a coating with lower magnitude of compressive residual stress (approximately -150 MPa) would not leads to problem condition such as spallation, because the stress would likely be farther from corresponding yield strength. Coatings with tensile strength experience microcracking and spallation (coated super-invar) failure that might rendered their performance irrelevant during service.

The coating microhardness increases with increasing coefficients of thermal expansion despite the secondary phases found on as-sprayed coating on aluminum and super-invar. Di Maio et al. [24] measure the microhardness of W_3C and W_2C as $2650 \pm 100 \text{ kgmm}^{-2}$ and $2980 \pm 100 \text{ kgmm}^{-2}$ respectively but not determined in this research work. The residual stresses at coefficients of thermal expansion 1.2 (super-invar) was tensile, but with increasing coefficients of thermal expansion the state changes to compressive and subsequently increases. However, there are only three data points since

the choice of substrate materials were based on our industrial purpose.

The calculated penetrating depth of Co-K α radiation is 3–4 μm in WC. Therefore, X-ray diffraction analysed a near surface layer. This information can be an advantage for predicting near-surface residual stress change in WC-cermet due to frictional and sliding wear, where wear mechanisms such as ploughing, abrasion etc. are related to very near surface changes.

5. Conclusions

The residual stresses show compressive stresses on as-sprayed coating on brass and aluminium, whilst tensile stress was found on coated super-invar despite same powder was used as feedstock. The differences in stress results though small in magnitude are due to the role play by each substrate properties in the cooling and solidification processes. A strong link exists between the residual stresses results and SEM micrographs.

Acknowledgements

The authors wish to acknowledge the financial and technical support of Nuclear Energy Corporation of South Africa, the DST/NRF Centre of Excellence in Strong Materials and the University of the Witwatersrand.

References

- [1] D.A. Stewart, P.H. Shipway, D.G. McCartney, *Wear* 225–229 (1999) 789.
- [2] S. Kuroda, T. Fukushima, S. Kitahara, *Thin Solid Film* 164 (1988) 157.
- [3] T.W. Clyne, S.C. Gill, *J. Therm. Spray. Technol.* 5 (4) (1996) 401.
- [4] A.T.J. Verbeek, *Production, Characterisation and Testing*, Eindhoven University, 1993.
- [5] J. Stokes, L. Looney, *Proceedings of the 1st International Thermal Spray Conference*, ASTM International, 2000, p. 263.
- [6] S.P. Prevey, *Am. Soc. Met.* 10 (1986) 380.
- [7] I.C. Noyan, J.B. Cohen, *Residual Stress Measurement by Diffraction and Interpretation*, Springer, New York, 1987.
- [8] J. Wang, K. Li, D. Shu, H. Xin, B. Sun, Q. Guo, M. Nishio, H. Ogawa, *Mater. Sci. Eng.* A371 (2004) 187.
- [9] J. Pina, A. Diass, J.L. Lebrun, *Mater. Sci. Eng.* A347 (2003) 21.
- [10] O.P. Oladijo, A.M. Venter, L.A. Cornish, N. Sacks, S. Shrivastava, *PM2010 Powder Metallurgy World Congress Proceedings*, 3 (66), 2010, p. 1, European Powder Metallurgy Association, Florence, Italy.
- [11] S. Luyckx, C.N. Machio, *Int. J. Ref. Met. Hard Mater.* 25 (2007) 11.
- [12] J.K.N. Murthy, D.S. Rao, B. Venkataraman, *Wear* 249 (2001) 592.
- [13] Bob B. He, *Powder Diffraction* 18 (2) (2003) 71.
- [14] D.Y.W. Yu, F. Spaepen, *J. Appl. Phys.* 95 (6) (2004) 2991.
- [15] J.H. Hubbell, W.H. McMaster, N.K. Del Grede, J.H. Mallett, in: J.A. Ibers, W.C. Hamilton (Eds.), *International Tables for X-ray Crystallography*, Kynoch Press, Birmingham, England, 1974.
- [16] D.L. Coats, A.D. Krawitz, *Mater. Eng.* A359 (2003) 338.
- [17] M. Wezelburger, D. Lopez, R. Gadow, *Surf. Coat. Technol.* 201 (2006) 1995.
- [18] L. Pejryd, J. Wigren, D.J. Greving, J.R. Shadley, E.F. Rybicki, *J. Therm. Spray. Technol.* 4 (3) (1995) 268.
- [19] S. Amirhaghi, H.S. Reehal, R.J.K. Wood, D.W. Wheeler, *Surf. Coat. Technol.* 135 (2001) 126.
- [20] D.A. Stewart, P.H. Shipway, D.G. McCartney, *Surf. Coat. Technol.* 105 (1998) 13.
- [21] R. Ahmed, M. Hadfield, *Wear* 209 (1997) 84.
- [22] V. Stoica, R. Ahmed, M. Golshan, S. Tobe, *J. Therm. Spray. Technol.* 13 (1) (2004) 93.
- [23] J.G.La. Barbera, J. Lesage, E. Bemporad, E. Le Bourhis, E.S. Puchi-Cabrera, M.H. Staia, *Surf. Coat. Technol.* 202 (2008) 4560.
- [24] D. Di Maio, S.G. Roberts, *Philos. Mag.* 85 (1) (2005) 33.



Systematic investigation of residual strains associated with WC–Co coatings thermal sprayed onto metal substrates

Andrew M. Venter^{a,b,*}, Thilo Pirling^c, Thomas Buslaps^d, O. Philip Oladijo^b, Axel Steuer^e,
Tshepo P. Ntsoane^a, Lesley A. Cornish^b, Natasha Sacks^b

^a Research and Development Division, Necsa Limited, Pretoria, South Africa

^b DST/NRF Centre of Excellence in Strong Materials, University of the Witwatersrand, South Africa

^c Institut Laue-Langevin, Grenoble, France

^d European Synchrotron Radiation Facility, Grenoble, France

^e ESS Stora Algotan 4, Lund, Sweden and NMMU, Gardner Avenue, Port Elizabeth, South Africa

ARTICLE INFO

Article history:

Received 21 October 2011

Accepted in revised form 27 March 2012

Available online 4 April 2012

Keywords:

Residual strains

WC–Co coatings

Neutron diffraction

Synchrotron X-rays

High-velocity oxygen-fuel

Eigenstrain

ABSTRACT

Using penetrating high-energy synchrotron X-ray radiation and thermal neutrons, the residual strains and stresses associated with the high-velocity oxygen-fuel (HVOF) thermal spray coating of WC–Co on two different substrate materials with significantly different coefficients of thermal expansion (CTE) to that of the coating material, have been investigated in a systematic approach. This approach enabled quantification of the residual strain and stress contributions that emanate from the different processing steps associated with the coating process. An eigenstrain approach enabled direct comparison of the contributions of the different processing steps to the plastic strains. It is shown that the dominant contribution originates from the grit-blast surface preparation step. Contributions purely from the coating process are not distinguishable from that of the grit blasting process within the measurement accuracy. For the as-coated samples no obvious contributions ascribable to the differences in the CTEs of the substrates, or impact related effects are observed.

© 2012 Elsevier B.V. All rights reserved.

1. Introduction

Tungsten-carbide based *cermet* coatings with metallic cobalt binders, e.g. WC–Co, are frequently used when wear resistance, high surface hardness and low coefficient of friction similar to sintered carbide materials are required. In the industry, WC–Co coatings are typically deposited on components by plasma or flame spray processes [1,2]. Of these, the high-velocity oxygen-fuel (HVOF) spraying process has inherent advantages in that the thermal spray process is dominated by kinetic energy rather than thermal energy. Oxygen and fuel are mixed and burnt in a combustion chamber at high flow rates (up to 1000 l/min) and with pressures up to 12 bar in order to produce a high-speed supersonic gas jet. Powder particles in the size range 5–65 µm are injected into the gas jet where they are heated and accelerated at 600–650 m/s towards the substrate. On impact with the substrate, particles flatten plastically against the work piece surface strongly bonding to the substrate to form a laminar coating composed of many layers called splats. The HVOF gun is rastered across the substrate to build up the required coating thickness in a number of passes. Notwithstanding the high temperatures associated

with the process, the overall thermal energy absorbed in the component is small, being the energy of each individual small droplet deposited. In the WC–Co system, in the torch part of the spray gun, the tungsten carbide melts and reacts with the Co metal binder to form ternary carbides, and also decarburization of the WC to form metallic W or secondary carbides such as W₂C. In addition, thermal strains generated as the coating cools in contact with the cooler substrate give rise to residual stresses parallel and transverse to the surface. Of the various spraying processes, the HVOF method has been found to deposit coatings with significantly lower levels of carbide decomposition and phase transformations [3]. Recent studies of HVOF processes indicate that significant peening stresses arise due to the impact high-velocity particles [4,5].

Depth resolved investigations of residual stresses in WC–Co thermal spray coatings employing different techniques have not yet fully unraveled the residual stress nature. Most techniques utilize destructive or material removal approaches which inadvertently lead to changes in the residual stress conditions [6]. Residual stress analysis of bulk WC and other cemented carbides by neutron diffraction has become routinely used owing to the deep penetration depths of the thermal neutrons which are generally about 1000 times greater than X-rays [7–9]. This enables determination of volumetric stress states and bulk averages. It is generally observed that the stress is compressive in the WC phase and tensile in the Co phase. This originates from the thermal stresses when the material is sintered between 1650 and

* Corresponding author at: Research and Development Division, Necsa Limited, Pretoria, South Africa. Tel.: +27 12 305 5038; fax: +27 12 305 5851.

E-mail address: Andrew.Venter@necsa.co.za (A.M. Venter).

1720 K and cooled to room temperature due to the differences in CTEs of WC and Co. At room temperature, WC has a stress of about –500 MPa and Co about 2500 MPa [7].

In coated substrate systems, residual stresses are a superposition of contributions from the sample production history (cold work related to forging, rolling, extrusion), surface preparation (roughening through grit blasting) and the coating deposition process. Inherent to the nature of the HVOF coating deposition process, residual stresses due to the coatings arise from the impact, cooling, solidification and solid-state cooling of the splats, first onto the substrate and subsequently onto existing splats as the coating is built up layer by layer.

There have been numerous methods applied to determine the residual stresses in cermet coatings [references contained in 11,12]. Most techniques require surface finishing treatment (grinding, electro-polish, etc.) that inherently alters the as-deposited residual stress condition and material removal (electrolytic polishing) for depth resolved information. Investigations of cermets [11] by incremental-hole drilling and laboratory X-ray diffraction layer removal techniques, reported a systematic increase in compressive stress with depth up to the coating substrate interface, ascribed to the inherent peening action of the HVOF coating process [6]. In addition it is expected that due to the thermal nature of the HVOF coating procedure, it would lead to interactive thermal stresses between the coating and substrate.

This study investigates the potential role that differences in the coefficients of thermal expansion (CTE) between different substrate materials and WC–Co coatings could have to mutually improve the functional properties of the substrate-coating combination. Favorable properties could potentially lead to possible substitutes for bulk sintered carbides in some wear applications. The integrity of these sprayed deposits is strongly influenced by the residual stress profiles in the deposit as well as the substrate. Amongst others, the residual strain/stress conditions are important contributors influencing the wear performance [10]. A systematic characterization of the residual stresses emanating from the various process steps involved in the HVOF process is reported here. The study included the parent material (as-received reference state) prior to and after the grit-blasted surface roughening preparation, as well as the final as-coated samples. This perspective primarily focused on influences introduced into the substrate materials, and where possible, supplemented by results on the coatings. The substrates were taken to be thick enough to absorb effects associated with the coating procedure without deformation. To exploit the thermal nature of the HVOF coating procedure, substrate materials were specifically chosen to have coefficients of thermal expansion (CTE) different to that of the coating material, in order to explore their role on the thermal residual stress responses in both the coatings and substrates, owing to the extent of the mismatch. WC has a CTE of $4.6\text{--}5.0 \times 10^{-6} \text{ K}^{-1}$ over the temperature range 20 to 1000 °C. Substrates were chosen to have CTEs respectively larger than WC, i.e. brass with CTE $19.0\text{--}20.5 \times 10^{-6} \text{ K}^{-1}$ over the temperature range 20 to 100 °C, and lower than WC, i.e. invar (controlled expansion alloy) with CTE $1.7\text{--}2.0 \times 10^{-6} \text{ K}^{-1}$ over the temperature range 20 to 90 °C. In general, if the thermal expansion coefficient of the substrate is larger than that of the coating material a compressive residual stress is expected in the coating, with the inverse expected for a substrate

material with expansion coefficient lower than that of the coating material.

Diffraction based techniques are noninvasive and when using penetrating radiation, no surface preparation is required and depth resolved information is attainable.

2. Experimental

2.1. Samples

WC–Co coatings (WC Co 83/17; powder size $-45 + 15 \mu\text{m}$; Flame Spray Technologies FST K-674.23) were deposited by the HVOF technique using an industrial 6-axis robotic HP/HVOF Tafa JP 5000® gun [13] to produce thicknesses of 200 μm on the two different substrate materials. Substrate materials, brass and super-invar, were procured from Goodfellow as plates respectively $150 \times 150 \times 6 \text{ mm}^3$ and $100 \times 100 \times 6.35 \text{ mm}^3$ in size with temper states half hard (brass) and annealed (super-invar). It is essential to have samples that are fine grained with minimal industrial processing, to have minimized recrystallization and cold working effects, that would complicate the diffraction analyses where small gage volumes are employed. Details of the plate samples are given in Table 1.

Samples were extracted from the plates as shown in Fig. 1 by water jet cutting to have representative samples from each of the HVOF processing steps, i.e. parent material (as-received reference), grit-blasted (surface roughening) and HVOF as-coated. As part of the HVOF sample preparation procedure directly prior to coating, the substrates were grit-blasted on one side to clean and roughen the surfaces. The grit blasting and coating were done on as large as possible plates to render homogenous deposition. After the HVOF process smaller samples, approximately $25 \times 25 \text{ mm}^2$ in size, were cut from the larger samples for the microstructural and diffraction investigations. Coating deposition parameters are given in [10,13]. For this study 3 samples each for the two materials were investigated, i.e. parent material (reference, as-received), grit-blasted and as-coated.

The neutron diffraction investigations were done on the $25 \times 25 \text{ mm}^2$ samples whereas the synchrotron investigations were done on a thinned wedge, shown in Fig. 1, cut from the neutron samples by electrical discharge machining (wire cutting under water using a 0.3 mm diameter wire). This sample shape offered different beam pathlength selections, especially through the coating, to enable on-line empirical selection of the beam sample pathlengths that would render sufficient diffracted intensity from the WC phase, but still presenting a pathlength of more than 2 mm. Retaining as thick as possible samples for these investigations, i.e. at least one order of magnitude thicker than the coating thickness, was essential to ensure that the in-plane (parallel to the coated surface) and normal components of residual strain were not adversely relaxed.

2.2. Investigative techniques

Material characterization results are discussed in [13] with parameters relevant to the reporting of the residual stress investigation in this

Table 1
Material characteristics [7].

Substrate material	CTE [$10^{-6}/\text{K}$]	Hv coating [GPa]	Chemical phase content (XRD results)		Porosity [%]	WC grain size [μm]	Melting point [°C]
			Substrate	Coating			
Alpha brass (Cu63/Zn37)	19	10.04 ± 0.01	Cu_5Zn_3 , $\text{Co}_3\text{W}_3\text{C}$, Zn	WC, W, Amorphous Co	0.46 ± 0.01	0.13 ± 0.01	930
Super-invar (Fe64/Ni3)	1	7.91 ± 0.01	FeNi, C	CW_3 , Co	0.75 ± 0.01	0.13 ± 0.02	1454

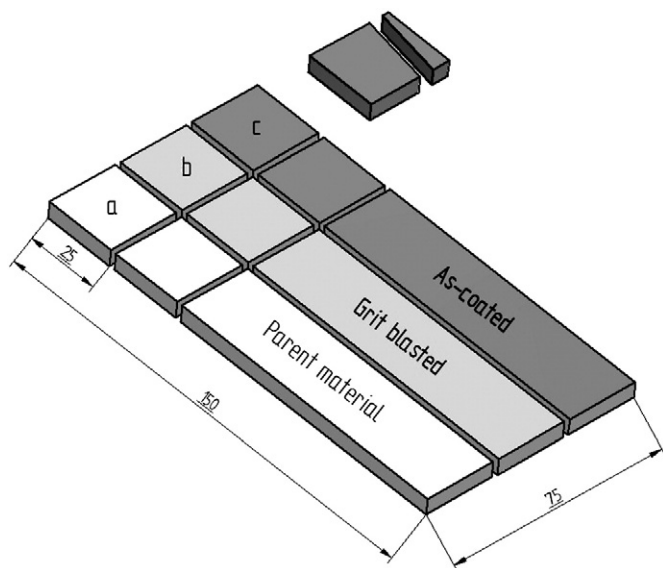


Fig. 1. Schematic diagram showing the locations where samples were extracted from the as-procured plates, designated as parent material (reference state throughout this study), grit-blasted substrate and as-coated sample.

document summarized in Table 1. Characterization of the coatings included:

- Porosity, grain size, macrohardness and microstructure examined on the coating top surface and on cross sections;
- Elemental and chemical phase composition using scanning electron microscope (SEM) and X-ray diffraction (XRD);

- Residual strain and stress analyses using both synchrotron radiation (SR) and neutron diffraction (ND).

The laboratory XRD crystalline phase investigations confirmed that: no phase changes had occurred in either of the substrate materials owing to the cold-working action associated with the grit-blasting surface preparation; the coating phase in both samples is WC with no other carbide phases present that may have resulted from the thermal nature of the coating procedure; and the Co binder phase is predominantly present as an amorphous phase as no crystalline phase could be detected. Optical images of the WC–Co coating cross sections, Fig. 2, indicate a dense structure consisting of nano-sized granular grains with porosity less than 1%, though occasional microcracks are present within the coatings in directions parallel to the coatings.

By exploiting the penetration depths of high energy synchrotron radiation (SR) and thermal neutrons (ND), depth resolved strain information was possible. The approaches reported here utilized 80–200 keV white beam synchrotron X-rays from the ID15A instrument at the ESRF employed in energy dispersive mode, as well as 1.74 Å monochromatic thermal neutrons on the SALSA neutron strain scanner of the ILL.

Notwithstanding the brilliance and high energy of the synchrotron X-ray beam employed, beam depth penetration is limited to a few millimeters in WC. This beam attenuation is proportional to the atomic number of the material being investigated [14]. For this reason the thinned wedge sample shapes were used to investigate the coatings. To ensure consistency in results, all synchrotron investigations were done on sample shapes and sizes that rendered identical measurement geometries and beam-sample pathlengths. It was empirically determined that 2.3 mm of WC–Co (dimension parallel to the in-plane direction; primary beam direction parallel to the in-plane direction) rendered data of sufficient accuracy for strain

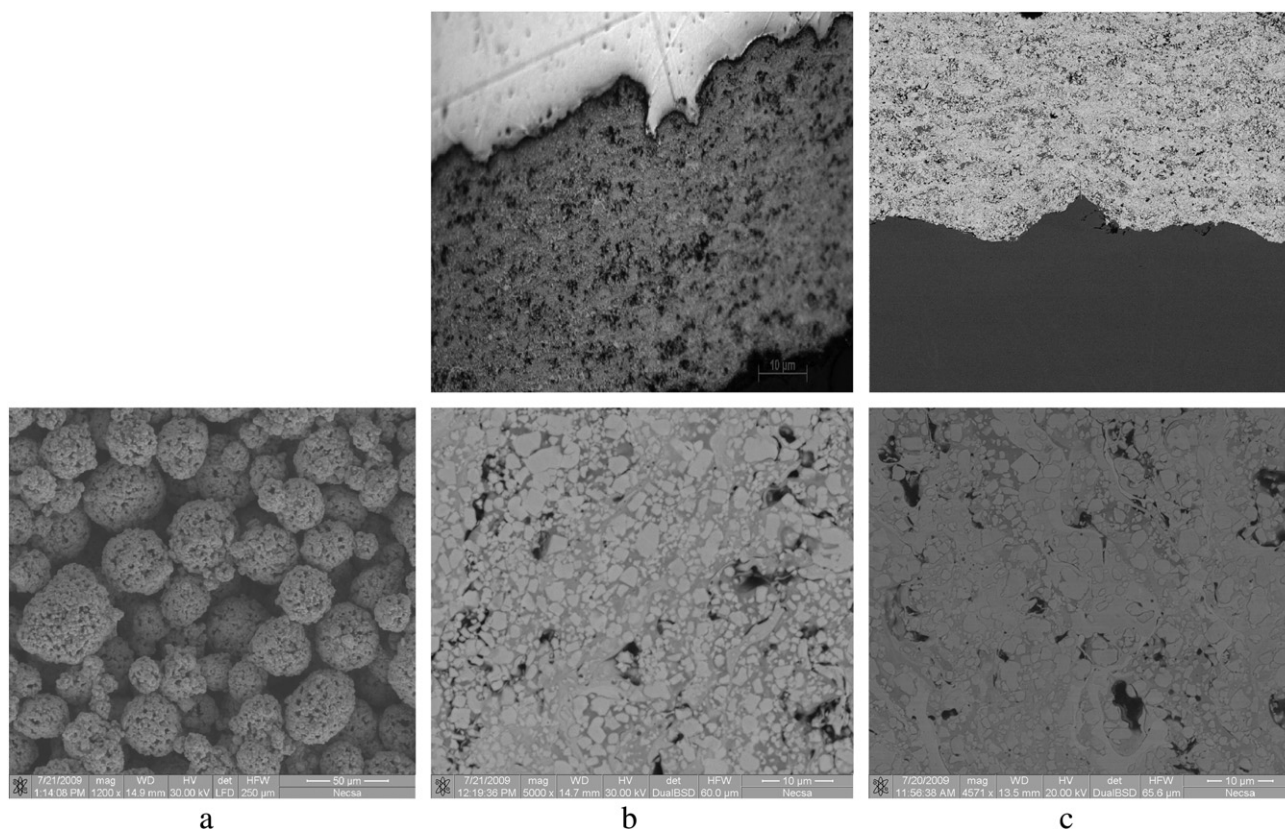


Fig. 2. Optical micrographs (top pictures) of the cross sections and SEM images of the WC–Co starting powder (a) and coatings on the brass (b) and super-invar (c) substrates. The coatings display the usual banded microstructure typical of thermally sprayed coatings. EDS analyses of the SEM images of WC–Co powder (50 μm scale on bottom right) of the coated samples (10 μm scale on bottom right) identify the dark areas as Co, medium light areas as WC and light areas as W₂C. The medium colored areas on the optical images are the substrate.

determination, though prolonged data acquisition times had to be taken. Line scan profiles of the in-plane and normal components of strain in the coatings were taken simultaneously with SR, Fig. 3, using the WC-(101) and (112) peaks that presented the highest diffracted intensities. All other peaks were weak or had significant overlap with fluorescence peaks from the high energy of the X-ray beam. Measurement times per position were 1200 s in the WC and 60 s for the substrate materials. With the transmission geometry employed, depth resolved information was achieved by stepwise vertical positioning of the sample with reference to the $0.03 \times 0.06 \text{ mm}^2$ (through surface depth \times in-plane width) incident beam cross section. The instrument was equipped with two detectors, respectively offset 10° from the primary beam in the horizontal and vertical planes, that render the in-plane and surface normal components of strain. The irradiated volume in the sample was a rectangular cross section (defined above) and spanning the entire thickness of the sample, i.e. 2.3 mm. Instrument calibration was periodically performed with an iron powder sample.

The neutron investigations were done on SALSA, equipped with oscillating 0.6 mm radial collimators defining the gage volume (Fig. 3). A nominal beam width of 0.6 mm could be established in the sample depth. An inherent advantage of the radial collimators is that surface aberration effects are minimized [9]. A beam size (depth \times in-plane dimensions) of $0.6 \times 15 \text{ mm}^2$ was employed at the geometrical center of the $25 \times 25 \times 6 \text{ mm}^3$ sample sizes. With SALSA being a constant wavelength instrument equipped with a single detector, the neutron measurements were done on the (311) and (200) reflections for the brass and invar materials respectively by employing 20 minutes measurement times per depth position. With the neutron investigations, measurements were done for both transmission (in-plane strain component) and reflection (normal strain component) geometries as shown in Fig. 3b. This was achieved by 90° horizontal rotation of the sample with reference to the scattering geometry. Notwithstanding prolonged data acquisition from the WC (101) peak, no intensity distinguishable above background could be extracted.

It was necessary to accurately determine the position of the sample surface on the designated coated surface side of all samples. This was achieved by scanning the sample surface through the incident beam (synchrotron X-ray and neutron), i.e. entry scan [9]. The surface location was determined when the overall integrated intensity dropped to 50% of the value obtained from a fully submerged gage volume. It was assumed that, under this condition, half the beam spot is submerged within the sample. It is estimated that the sample surfaces were determined within $\pm 0.03 \text{ mm}$ for the synchrotron measurements and $\pm 0.1 \text{ mm}$ for the neutron measurements.

3. Results and discussion

Depth resolved residual strain results for the brass samples, Figs. 4 and 5 respectively for the synchrotron and neutron investigations, and correspondingly for the invar samples, Figs. 6 and 7, are presented. The lattice strain was determined from the lattice plane spacings d_{hkl} of specific crystallographic (hkl) reflections measured as a function of depth and sample orientation (in-plane or normal components)

$$\varepsilon = \frac{d_{hkl} - d_{hkl}^0}{d_{hkl}^0}$$

Where d_{hkl}^0 values are the strain free lattice plane spacing of the real sample.

Since only single peak analysis was possible with the neutron diffraction investigations, all data processing was done on the same Bragg peaks throughout for direct correlation of the results irrespective of techniques used. Data were taken at all measurement positions with fully submerged gage volumes. No surface aberration effects were observed.

The depth resolved strain variation in the as-received brass parent material (reference state) sample displays a significant oscillatory variation with depth reminiscent of the cold working production thereof. This complicates determination of the unstrained lattice parameter reference required for the strain conversions. This was addressed by calculating the lattice parameter that would render the normal stress component zero, i.e. assuming a bi-axial stress condition throughout. The value calculated with this approach gave a result similar to that of the lattice parameter averaged for both measurement directions as function of depth through the sample thickness. Notwithstanding the lattice parameter through thickness for the invar parent material being more constant, a similar approach was followed with the strain determination in the invar samples. The unstrained lattice parameter for the WC phase was determined from coating flakes that were chipped from the coated samples.

The strain results shown include all data points measured without smoothing. Significant systematic variations (scatter) are observed in the SR results of both material systems. This is attributed to the small gage volumes employed that are susceptible to grain size, systematic errors and orientation effects [15]. In the ND data, the strains are averaged over larger gage volumes rendering smoother data lines, at the cost of lower positional resolution, especially close to the surfaces

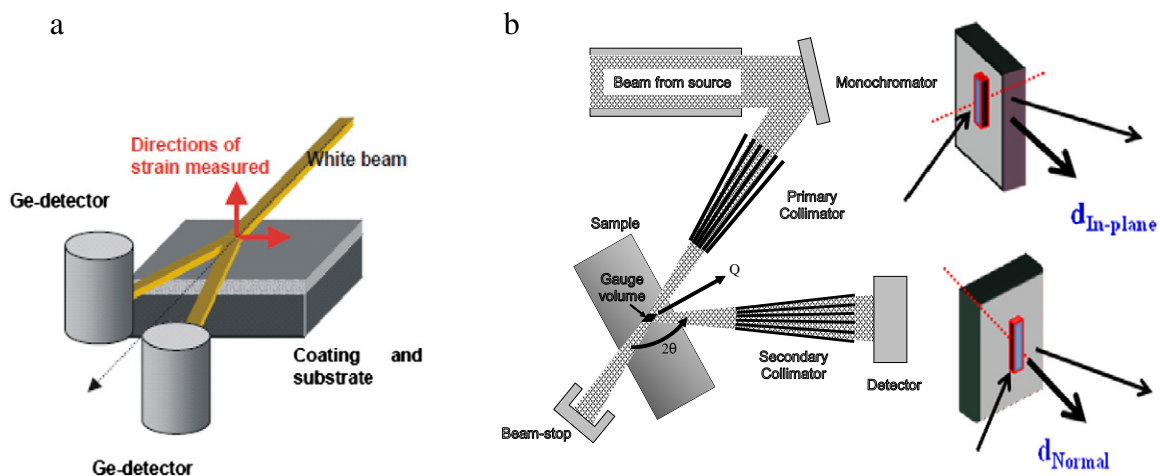


Fig. 3. Measurement geometries employed with the SR (a) and ND (b) investigations. The use of two detectors with the SR investigations allows simultaneous measurement of the in-plane and normal strain components. Note that the rectangular sample shape merely indicates the measurement geometry. Samples used in this study were the thinned wedges as discussed in the text and shown in Fig. 1. For the ND investigations the samples had to be reoriented to facilitate measurement of the different strain directions as shown in (b). The schematics show the radial collimation geometry that minimizes surface aberration contributions [9].

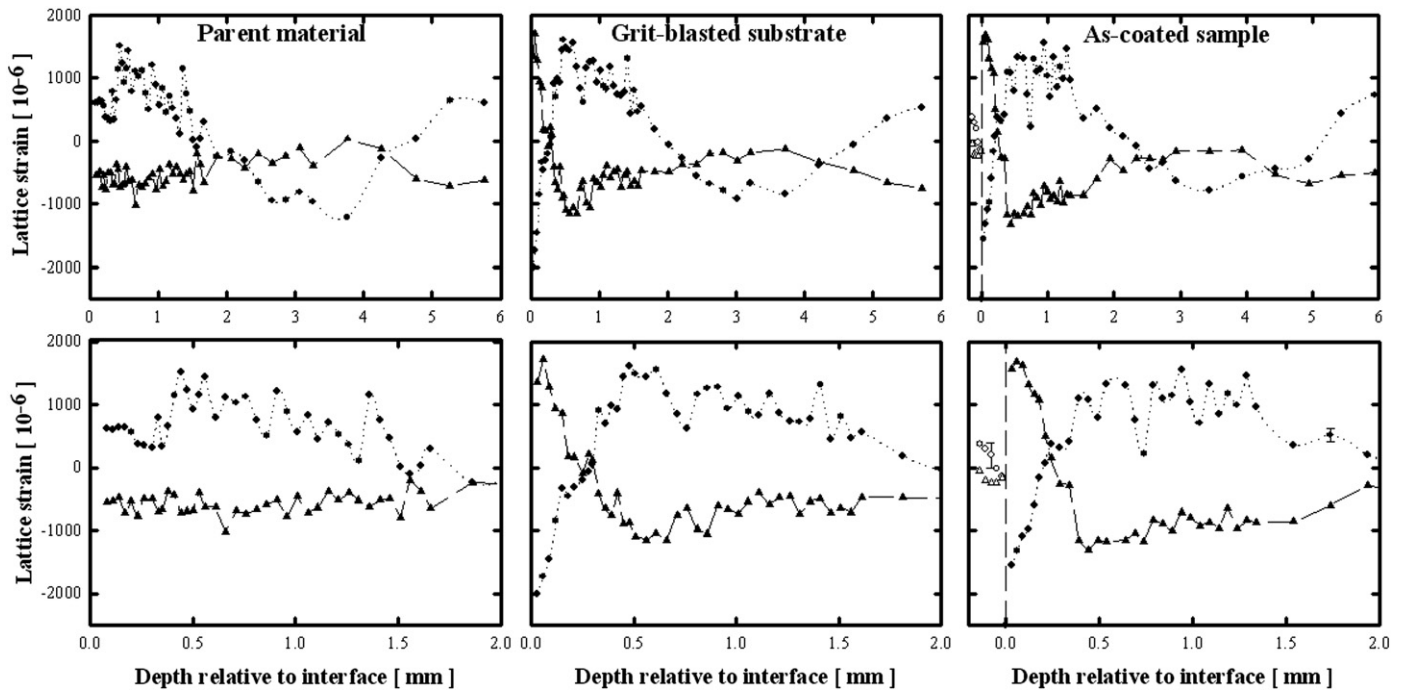


Fig. 4. Residual strain depth dependence determined from the lattice plane spacing of the (311) Cu and (101) WC Bragg peaks measured with synchrotron X-ray diffraction on the thinned wedge brass sample set. Results are for the parent material reference state (left set), the grit-blast substrate (center set) and HVOF as-coated sample (right set). The substrate coating interface is at 0 mm. The bottom sets of figures show an enlarged view of the results at the near surface region. The error bars indicate the systematic error associated with the measurements. The lines through the symbols are guides to the eye. Legend: ●, substrate in-plane component; ▲, substrate normal component; ○, WC in-plane component; △, WC normal component.

where steep strain gradients are observed in the grit-blasted and as-coated samples.

The grit-blasted samples indicated substantial surface and subsurface modification in both substrate materials. Upon the rebound of the shot, together with the restraining influence of the deeper unaffected

material, elastic recovery induces residual stresses parallel to the surface, while the metal beneath has reaction induced tensile stress. The normal components acquire large tensile strains with the in-plane components being compressive up to depths of 0.5 mm from the synchrotron results and approximately 0.8 mm from the neutron results. This compressive

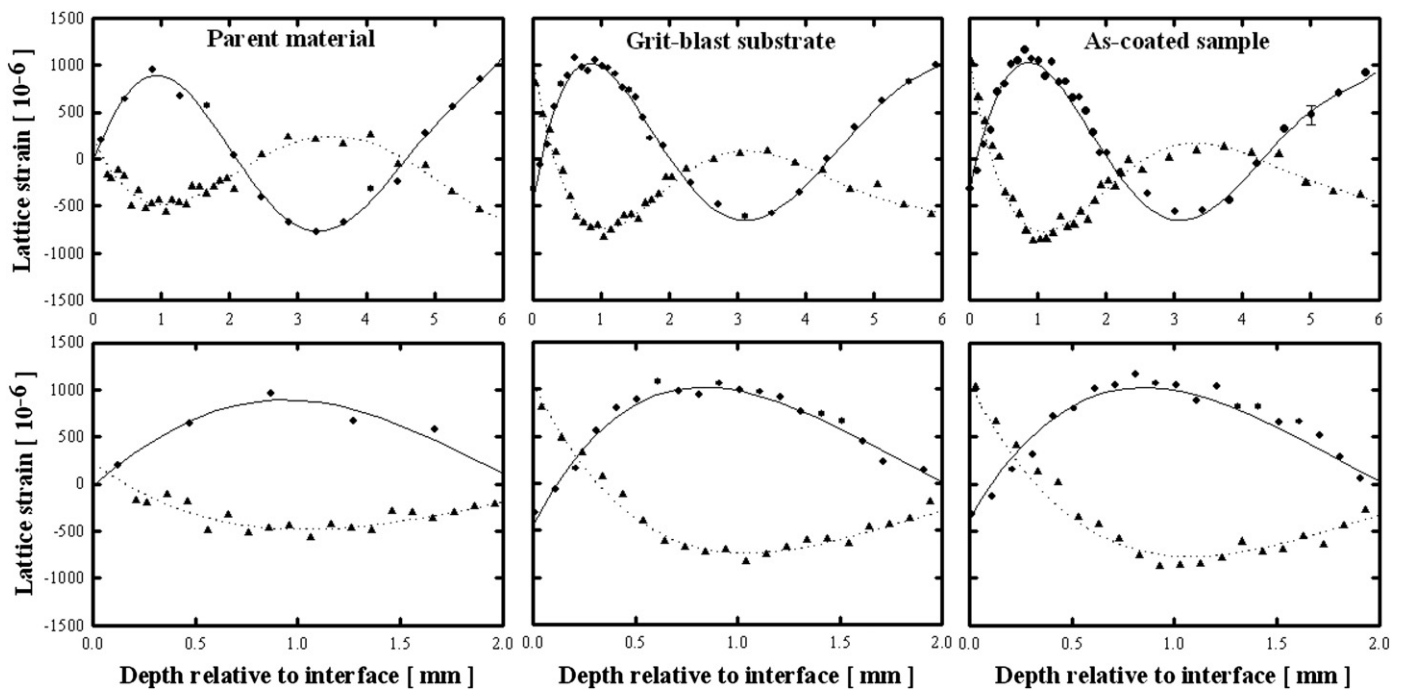


Fig. 5. Residual strain depth dependence determined from the lattice plane spacing of the (311) Cu Bragg peak measured with neutron diffraction on 25 × 25 mm² brass sample set. Results are for the parent material reference state (left set), the grit-blast substrate (center set) and HVOF as-coated sample (right set). The bottom sets of figures show an enlarged view of the results at the near surface region. The lines through the symbols represent polynomial curve fits to enable stress calculations at corresponding depth values. The error bars indicate the systematic error associated with the measurements. Legend: ●, substrate in-plane component; ▲, substrate normal component.

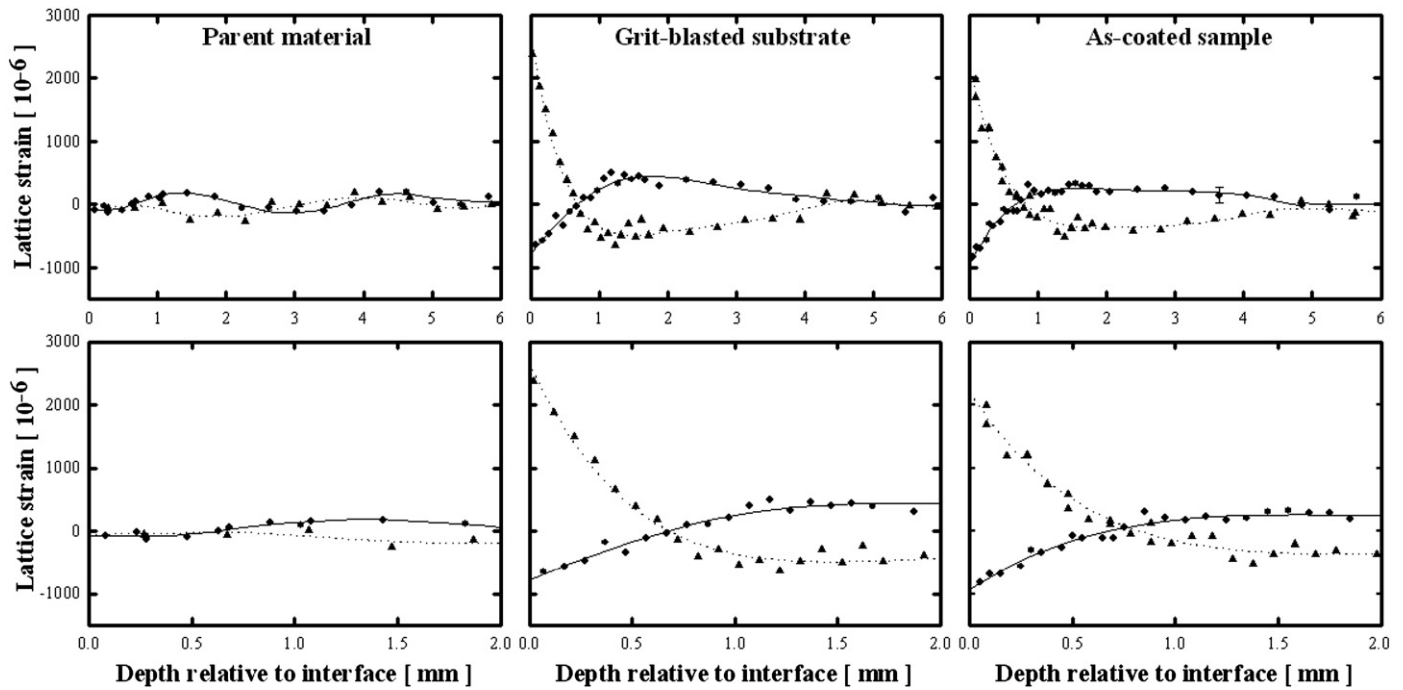


Fig. 6. Residual strain depth dependence determined from the lattice plane spacing of the (200) Ni and (101) WC Bragg peaks measured with synchrotron X-ray diffraction on the thinned wedge invar sample set. Results are for the parent material reference state (left set), the grit-blast substrate (center set) and HVOF as-coated sample (right set). The substrate coating interface is at 0 mm. The bottom sets of figures show an enlarged view of the results at near surface region. The error bars indicate the systematic error associated with the measurements. The lines through the symbols are guides to the eye. Legend: ●, substrate in-plane component; ▲, substrate normal component; ○, WC in-plane component; △, WC normal component.

nature of the in-plane component after grit blasting compared to the parent material originates from the localized plastic deformation inherent to the grit-blasting effect (work hardening). The significant depth this deformation extends to is reminiscent of the blasting intensity. As a comparison, in steel the depth deformation due to shot peening at

intensity level 6A, only extends 0.2 mm [16]. Thus the grit blasting surface preparation is more severe than traditional shot peening that is routinely applied to condition sample surfaces that are prone to stress corrosion cracking or fatigue. The compressive residual stress resulting from grit-blasting is directly dependent on the blasting pressure, grit size and

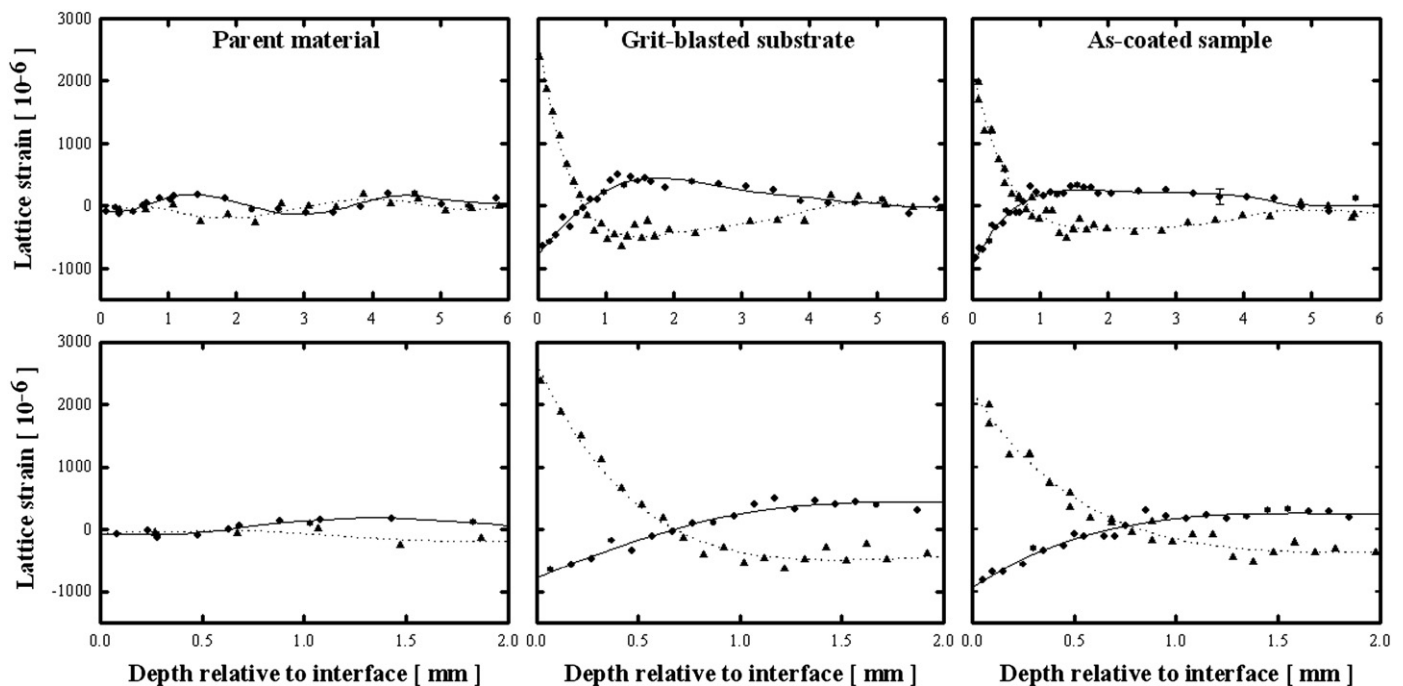


Fig. 7. Residual strain depth dependence determined from the lattice plane spacing of the (200) Ni Bragg peak measured with neutron diffraction on $25 \times 25 \text{ mm}^2$ invar sample set. Results are for the parent material reference state (left set), the grit-blast substrate (center set) and HVOF as-coated sample (right set). The bottom sets of figures show an enlarged view of the results at the near surface region. The lines through the symbols represent polynomial curve fits to enable stress calculations at corresponding depth values. The error bars indicate the systematic error associated with the measurements. Legend: ●, substrate in-plane component; ▲, substrate normal component.

distance from the substrate surface [17,18]. The blasting intensity can be determined with the curvature method. The intensity of the grit blasting used in the sample preparation of this study was not quantified since the standard industrial HVOF procedure was applied. All the samples of this study were done sequentially with the same setup.

The magnitudes and depth dependence of the as-coated samples display strain magnitudes and depth dependences similar to that observed for the equivalent grit-blasted samples. The strains in the WC coating determined from the SR results indicate comparatively small residual strain values for both the in-plane and normal strain components. The strains display a gradient dropping off from the surface to the coating–substrate interface region. Both WC peaks used in the analysis, WC (101) and WC (112) show similar results, although only results for the WC (101) reflection are reported. The low magnitudes for the strain values are ascribed to the high stiffness of the WC hardmetal that has a modulus of elasticity of 722 GPa compared to 122 GPa for brass.

The in-plane residual stresses existing in the samples are displayed in Figs. 8–11. Since the synchrotron investigations were taken simultaneously with the same sample setup, direct conversion of the strains to stresses for each depth position could be done from the in-plane and normal components of strain. The neutron diffraction measurements necessitated different reorientations of the samples and were measurements thus not taken at coincident depth positions. To enable stress determinations, 6th order polynomial curves rendered good fits to the strain (lattice parameter) profiles with the fits shown in Figs. 5 and 7 respectively. Stresses were subsequently determined from the fitted curves rendering the smooth curves shown in Figs. 9 and 11.

For a bi-axial stress condition, a reasonable assumption for coatings thinner than 2 mm, is that the stress normal to the surface σ_{\perp} is zero, with the in-plane stress ($\sigma_{//}$) then determined from

$$\sigma_{//} = \frac{1}{\frac{1}{2}S_2(hkl)} \left(\frac{d_{//} - d_{\perp}}{d_{\perp}} \right)$$

where $S_2(hkl)$ is the corresponding diffraction elastic constant for the material and reflection, $d_{//}$ is the in-plane component of the lattice plane spacing and d_{\perp} is the normal component of the lattice plane spacing at the corresponding depth measurement position. Table 2 summarizes the elastic constants used in the determination of the stress values.

Significant compressive stresses are observed at the near surface regions of the grit-blasted and coated samples. The magnitudes revealed by the synchrotron results are larger than those of the neutron results owing to the better depth resolution attainable with the smaller gage volume, whereas the neutron results are averaged over larger gage volumes. The systematic approach followed with this investigation reveals that the primary origin for the substantial increases in residual stress in the near surface regions is due to the grit-blast surface treatment, with minimal apparent changes in the results between the grit blasted and as-coated samples. In both the coated systems, the in-plane stresses in the WC phase show depth dependence initially increasing in magnitude to have a maximum approximately mid coating thickness from where it falls off as the interface is approached. The maximum tensile stress does not exceed 250 MPa in either of the substrates irrespective of their CTEs. Included on the coating results are the in-plane residual stresses determined from X-ray diffraction using Co radiation (6 keV) rendering penetration depths of 2 μm [19]. A similar depth dependence was observed [20] in the WC phase with synchrotron investigations of WC–Co deposited on steel substrates using the $\sin^2\psi$ technique at two different beam energies (15 and 25 keV) with estimated penetration depth 5 μm . Compressive residual stresses in the range -270 MPa to -332 MPa were reported for the as-coated condition, which though become spread over the range 250 MPa to -1800 MPa after post wear sliding tests. The low value of the stresses in the coatings is possibly ascribed to the occurrence of localized microcracking associated when the molten spray splats being quickly quenched to the substrate temperature. The underlying substrate constrains the thermal contraction of the splats, resulting in tensile stresses in the splats that due to the brittle nature of

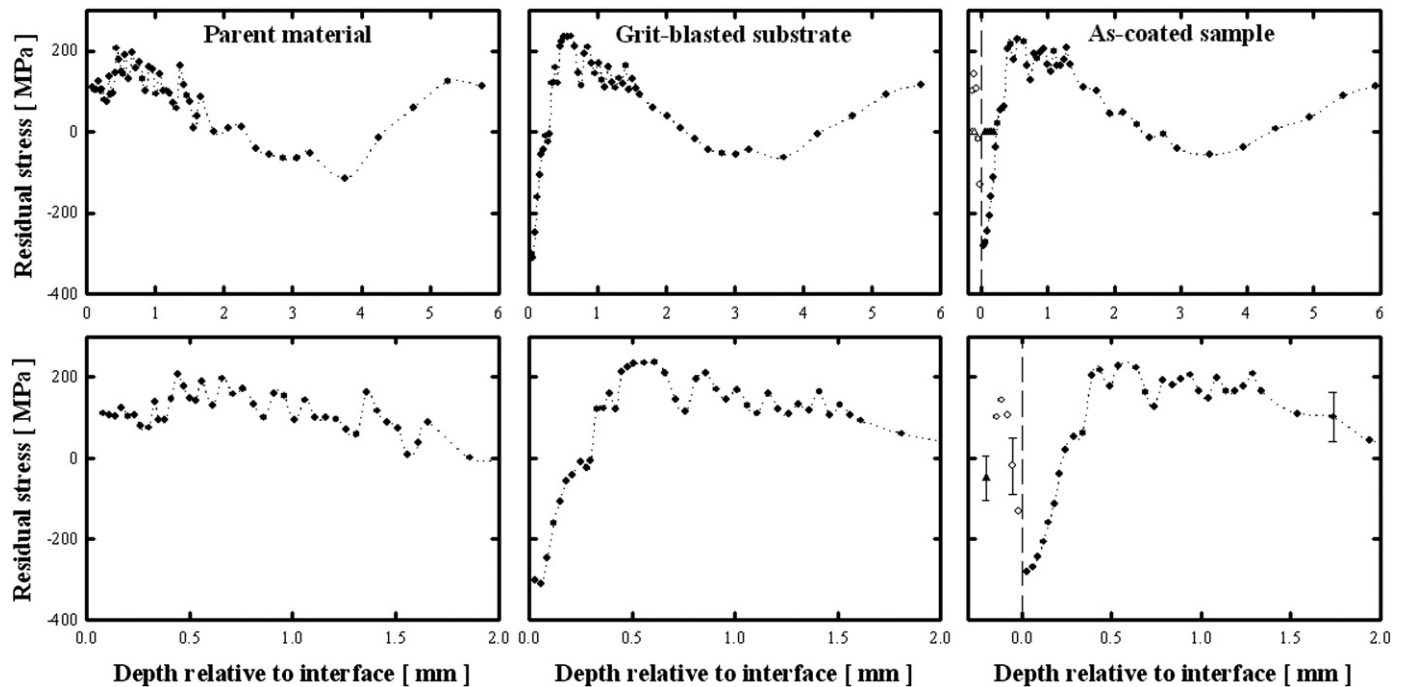


Fig. 8. In-plane residual stress depth dependence determined from the lattice strain results of the (311) Cu and (101) WC Bragg peaks measured with synchrotron X-ray diffraction on the thinned wedge brass sample set. Results are for the parent material reference state (left set), the grit-blast substrate (center set) and HVOF as-coated sample (right set). The near surface residual stress of the WC determined with laboratory X-rays (Co radiation) is also indicated [19]. The substrate coating interface is at 0 mm. The bottom sets of figures show an enlarged view of the results at the near surface region. The error bars indicate the systematic error associated with the measurements. The lines through the symbols are guides to the eye. Legend: ●, substrate in-plane stress; ○, WC in-plane stress; ▲, WC near surface stress (laboratory X-rays).

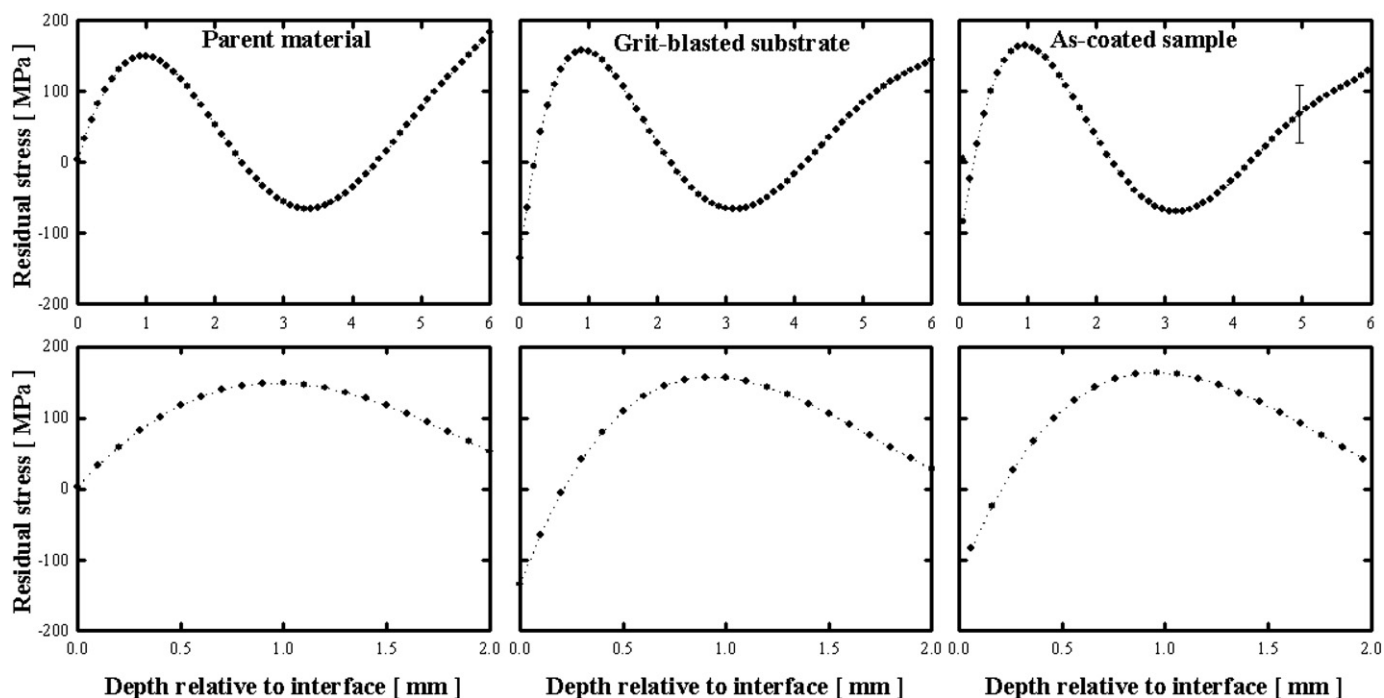


Fig. 9. In-plane residual stress depth dependence determined from the fitted lattice strain results of the (311) Cu Bragg peak measured with neutron diffraction on the $25 \times 25 \text{ mm}^2$ brass sample set. Results are for the parent material reference state (left set), the grit-blast substrate (center set) and HVOF as-coated sample (right set). The bottom sets of figures show an enlarged view of the results at the near surface region. The error bars indicate the systematic error associated with the measurements. The lines through the symbols are guides to the eye.

the cermets, exceed the breaking strengths of the material, leading to repeated relaxation through microstructural cracks.

Direct quantification of the contributions due to grit blasting and the coating process can be attained by considering the plastic strain profiles (eigenstrains) rather than the residual stresses [16]. It is

important to evaluate not only the surface and maximum subsurface values of the compressive residual stresses, but also the depth of the plastically deformed layer. Since depth resolved strain information exists from this investigation, assessment of the strain results enables non-destructive assessment of the respective contributions. Decomposition

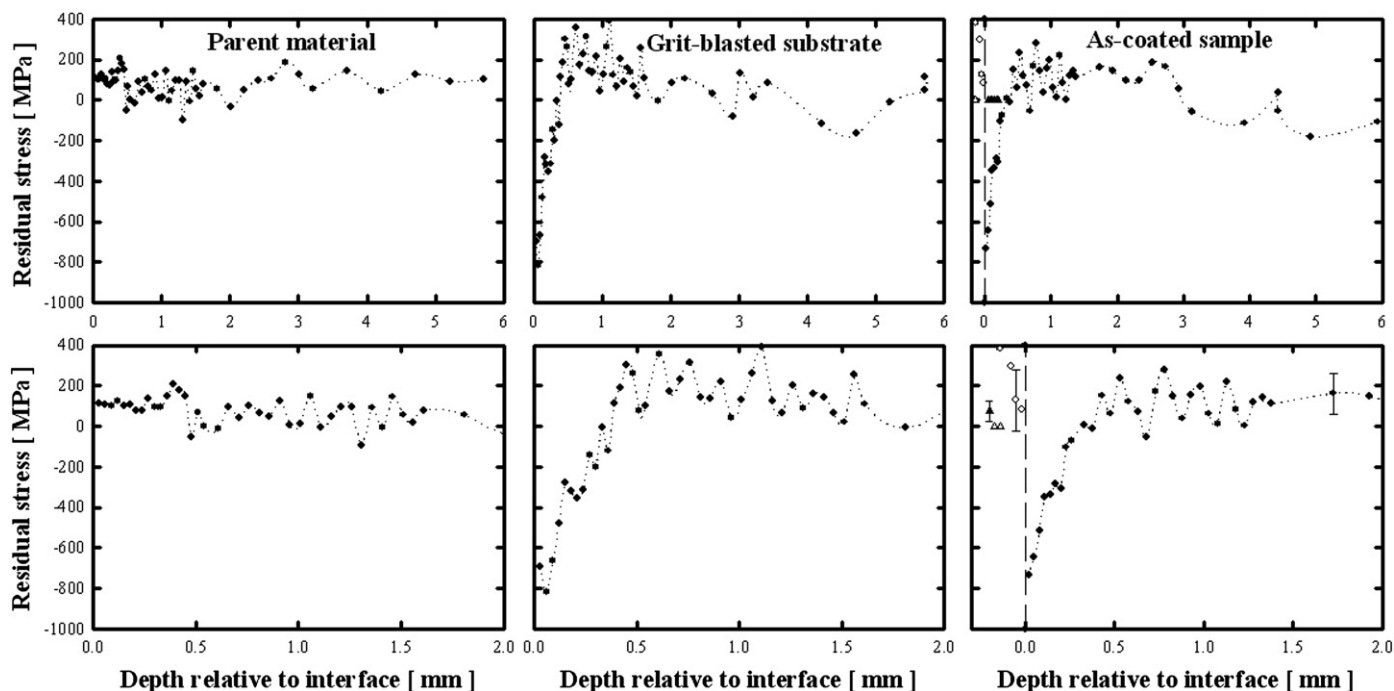


Fig. 10. In-plane residual stress depth dependence determined from the lattice strain results of the (200) Ni and (101) WC Bragg peaks measured with synchrotron X-ray diffraction on the thinned wedge invar sample set. Results are for the parent material reference state (left set), the grit-blast substrate (center set) and HVOF as-coated sample (right set). The near surface residual stress of the WC determined with laboratory X-rays (Co radiation) is also indicated [19]. The substrate coating interface is at 0 mm. The bottom sets of figures show an enlarged view of the results at the near surface region. The error bars indicate the systematic error associated with the measurements. The lines through the symbols are guides to the eye. Legend: ●, substrate in-plane stress; ○, WC in-plane stress; ▲, WC near surface stress (laboratory X-rays).

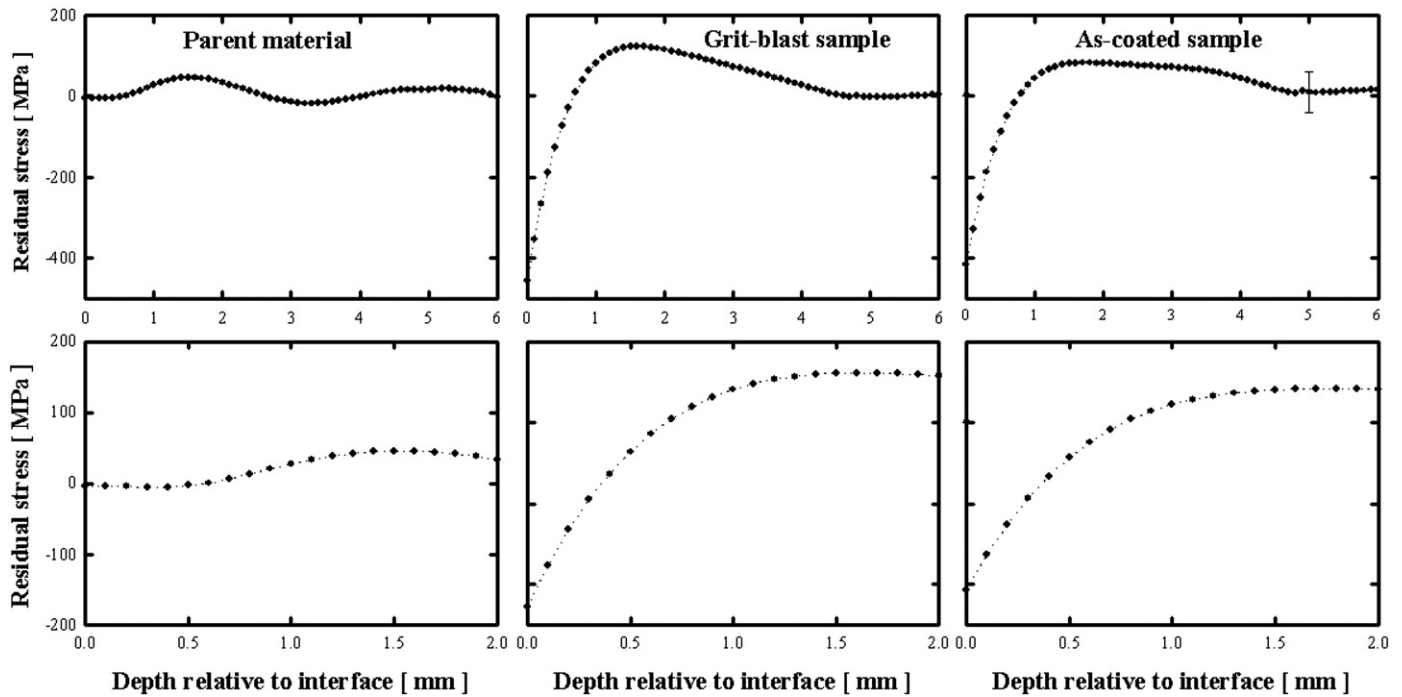


Fig. 11. In-plane residual stress depth dependence determined from the fitted lattice strain results of the (200) Ni Bragg peak measured with neutron diffraction on the $25 \times 25 \text{ mm}^2$ invar sample set. Results are for the parent material reference state (left set), the grit-blast substrate (center set) and HVOF as-coated sample (right set). The bottom sets of figures show an enlarged view of the results at the near surface region. The error bars indicate the systematic error associated with the measurements. The lines through the symbols are guides to the eye.

of the residual stress characteristics along the sample depth into regions dominated by contributions from different deformation processes, i.e. plastic and elastic, allows for the grit-blast and coating near surface permanent strains to be extracted from the residual strain profiles. The strain profile below the treated surface is the combination of elastic bending with the remaining residual compression arises near the blasted surface in response to permanent stretching induced by grit impact. Estimation of the grit-blast and coating associated induced plastic strain profiles has been determined by subtracting the residual stress profile from the linear elastic response in the interior of the sample. This was done as a linear extrapolation of the elastic bending profile, measured below the plastic layer, to the surface. Figs. 12 and 13 show the plastic strain (eigenstrain) profiles (difference curves) for the respective grit-blasted substrates onto which the results from analyses of the coated samples are superimposed. With minimal difference between the plastic strain dependences after the grit-blasting and as-coated conditions, the results show the dominance of the peening mechanism of stress formation over thermal stresses in the as-coated samples. Furthermore, notwithstanding the impact nature of the HVOF process, no significant additional stress contributions reminiscent of the kinetic impact energy of the splats is evident. It is concluded that minimal thermal energy transfer takes place between the coating splats and the substrates, thus not capable of activating the thermal stress mechanism. Since the grit blast stress condition is not altered in the coated brass sample, it is an indication that the substrate was not heated

to any significant extent, i.e. lower than the stress relieve annealing temperature of brass which is 375°C . The results obtained from the substrates indicate that the HVOF process in the as-coated samples is not influenced by the differences in CTEs of the substrate materials.

Thermal treatment may alter the stress state as this could mobilize the differences in CTEs between the coating and the substrates. A recent publication [10] found that annealing above 600°C induced recrystallization of the amorphous Co binder phase with the formation of eta carbides $\text{Co}_6\text{W}_6\text{C}$ and $\text{Co}_2\text{W}_4\text{C}$, and that the residual stresses in the coating became progressively more compressive with increased annealing temperature that improved abrasive wear resistance.

4. Conclusions

The residual stress results of the two techniques employed in the non-destructive characterization study of HVOF coated substrates give qualitatively similar results in accordance to the respective gage volumes employed. The systematic approach followed clearly shows that the WC–Co thermal sprayed coating process of both brass and super-invar alone does not contribute significantly, as a single contributing factor, to the residual strains in the substrates. This study shows the large strain/stress misfit between the coating and the substrates emanates primarily from the grit-blast surface preparation of the substrates that extends up to at 0.5 mm into the substrates. The residual stresses in the WC coatings have a parabolic dependence with depth, initially rising from a low value

Table 2
Elastic constants used in the determination of the stress values.

Material	Reflection used	Lattice parameter [Å]	S_1 [TPa^{-1}]	$1/2S_2$ [TPa^{-1}]	Young's modulus [GPa]	Poisson ratio
Brass (Cu63/Zn37)	Cu (311)	1.144	−2.902	11.106	122	0.354
Invar (Fe64/Ni3)	Ni (200)	1.796	−1.910	7.539	178	0.339
WC	WC (101)	1.879	−0.321	1.707	722	0.232
	WC (112)	1.023	−0.318	1.686	666	0.234

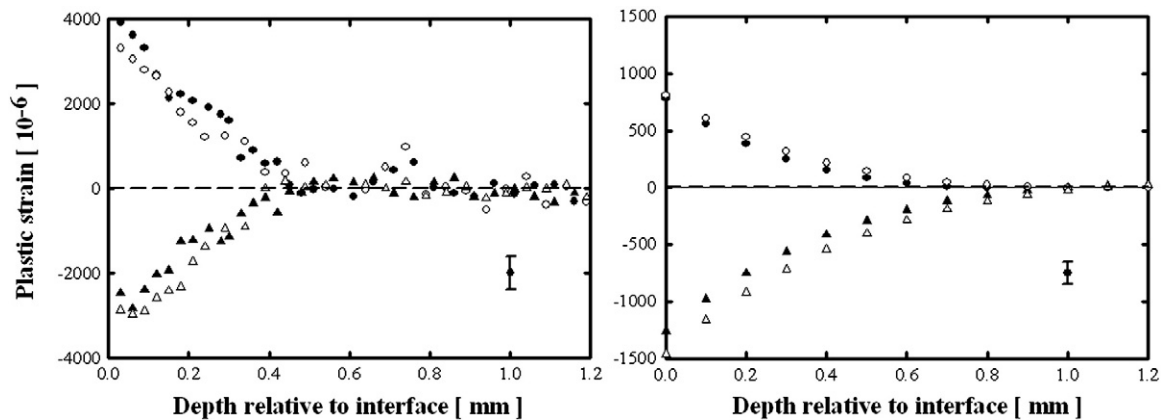


Fig. 12. Plastic strain profiles (eigenstrains) for brass as determined from strain results of X-ray synchrotron (left) and neutron diffraction (right). Legend: ●, grit blast in-plane component; ▲, grit blast normal component; ○, as-coated in-plane component; △, as-coated normal component.

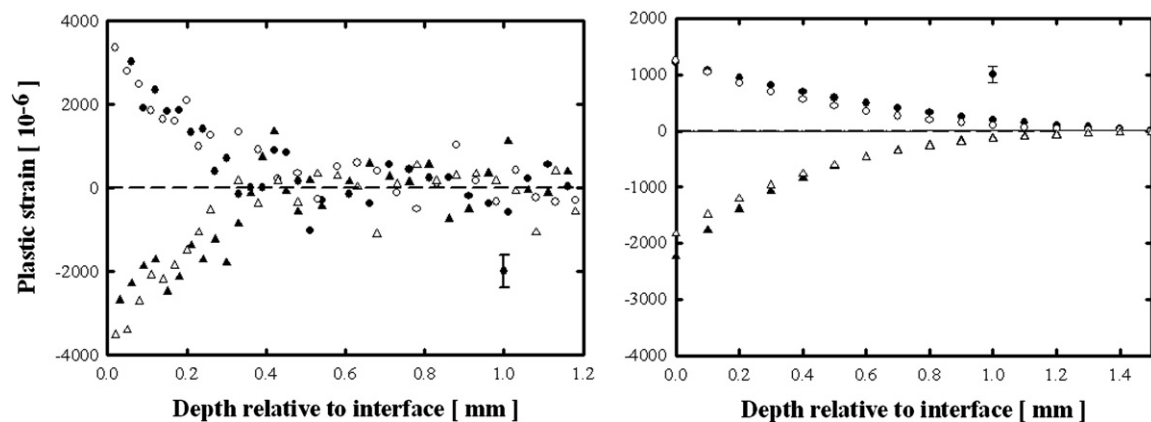


Fig. 13. Plastic strain profiles (eigenstrains) for invar as determined from strain results of X-ray synchrotron (left) and neutron diffraction (right). Legend: ●, grit blast in-plane component; ▲, grit blast normal component; ○, as-coated in-plane component; △, as-coated normal component.

on the surface to a maximum tensile stress at mid coating thickness not exceeding 250 MPa, whereafter it falls off to a low value at the coating-substrate interface. It is postulated that the generally low stress values in the coating originate from localized relaxation due to the microcracking.

Acknowledgments

The authors acknowledge support from Necsa Limited, DST/NRF Centre of Excellence in Strong Materials, University of the Witwatersrand, as well as the ILL and ESRF for the beam time awarded on the SALSA and ID15A instruments respectively, and the support provided during the investigations.

References

- [1] J. Stokes, L. Looney, *Surf. Coat. Technol.* 148 (2001) 18.
- [2] M.R. Dorfman, B.A. Kushner, J. Nerz, A.J. Rotolico, *Proceedings of the 12th International Conference on Thermal Spraying*, the Welding Institute, Abington, Cambridge, CB1 6AL, 1989, p. 291.
- [3] A. Karimi, C. Verdon, G. Barbezat, *Surf. Coat. Technol.* 57 (1993) 81.
- [4] P. Bansal, P.H. Shipway, S.B. Leen, *Acta Mater.* 55 (2007) 5089.
- [5] R. Gadow, M.J. Riegert-Escribano, M. Buchmann, *J. Therm. Spray Technol.* 14 (1) (2005) 100.
- [6] M. Wenzelburger, M. Escribano, R. Gadow, *Surf. Coat. Technol.* 180–181 (2004) 429.
- [7] D. Mari, A.D. Krawitz, J.W. Richardson, W. Benoit, *Mater. Sci. Eng.* 197 (1996) (and references therein).
- [8] D. Maria, B. Clausen, M.A.M. Bourke, K. Buss, *Int. J. Refract. Met. Hard Mater.* 27 (2009) 282.
- [9] T. Keller, N. Margadant, T. Pirling, M.J. Riegert-Escribano, W. Werner, *Mater. Sci. Eng. A* 373 (2004) 33.
- [10] S. Luyckx, C.N. Machio, *Int. J. Refract. Met. Hard Mater.* 25 (2007) 11.
- [11] Y.Y. Santana, P.O. Renault, M. Sebastiani, J.G. La Barbera, J. Lesage, E. Bemporad, E. Le Bourhis, E.S. Puchi-Cabrera, M.H. Staia, *Surf. Coat. Technol.* 202 (2008) 4560.
- [12] D.A. Stewart, P.H. Shipway, D.G. McCartney, *Surf. Coat. Technol.* 105 (1998) 12.
- [13] O.P. Oladijo, A.M. Venter, L.A. Cornish, N. Sacks, S. Shrivastava, *PM2010 Powder Metallurgy World Congress Proceedings*, Florence, Italy, 3(66), 2010, p. 1.
- [14] P. Withers, in: M.E. Fitzpatrick, A. Lodini (Eds.), *Analysis of Residual Stress by Diffraction Using Neutron and Synchrotron Radiation*, Taylor and Francis, London, 2003, p. 170.
- [15] A. Steuwer, J.R. Santisteban, M. Turski, P.J. Withers, T. Buslaps, *J. Appl. Crystallogr.* 37 (2004) 883.
- [16] S.-Y. Zhang, A.M. Venter, W.J.J. Vorster, A.M. Korsunsky, *J. Strain Anal.* 43 (2008) 229.
- [17] M. Mellali, A. Grimand, A.C. Leger, P. Fauchais, J. Lu, *Therm. Spray Technol.* 6 (2) (1997) 217.
- [18] K.P. Chander, M. Vashista, K. Sabiruddin, S. Paul, P.P. Bandyopadhyay, *Mater. Des.* 30 (2009) 2895.
- [19] O.P. Oladijo, A.M. Venter, L.A. Cornish, N. Sacks, *Surf. Coat. Technol.* (in press), doi: 10.1016/j.surfcoat.2012.01.044.
- [20] V. Stoica, R. Ahmed, M. Goishan, S. Tobe, *J. Therm. Spray Technol.* 13 (1) (2004) 93.



Effect of substrate on the 3 body abrasion wear of HVOF WC-17 wt.% Co coatings

O.P. Oladijo^{a,b}, N. Sacks^{a,b,*}, L.A. Cornish^{a,b}, A.M. Venter^{b,c}

^a School of Chemical & Metallurgical Engineering, University of the Witwatersrand Private Bag 3, WITS, 2050, South Africa

^b DST/NRF Centre of Excellence in Strong Materials, South Africa

^c Research & Development Division, NECSA Limited, Pretoria, South Africa

ARTICLE INFO

Article history:

Received 23 February 2012

Accepted 25 June 2012

Keywords:

HVOF
Cemented carbide
Abrasion
Coating

ABSTRACT

WC-17 wt.% Co coatings were deposited using high velocity oxy-fuel (HVOF) spraying onto four different substrate materials, namely aluminium, brass, 304 stainless steel and super-invar. These substrates have different coefficients of thermal expansion which have been shown to influence the final coating microstructural properties. The abrasive wear properties of the coatings were characterised using an ASTM-G65 three body abrasive wear machine with silica sand as the abrasive. The highest mass loss was recorded for the coating on the aluminium substrate whilst the coated 304 stainless steel showed the lowest mass loss. The coatings on brass and super invar experienced similar mass losses. SEM studies of the worn surfaces showed preferential removal of the Co binder phase as well as cracking and rounding of the carbide grains. The differences in wear behaviour may be attributed to the presence of residual stresses where the highest compressive residual stress led to the highest wear rate. The coatings deposited onto brass showed compressive stresses whilst those deposited onto super-invar had tensile stresses, yet these two coatings had similar wear rates. Thus further study is required to provide conclusive evidence of the role of residual stresses on the abrasion resistance of these coatings.

© 2012 Elsevier Ltd. All rights reserved.

1. Introduction

Increasingly demanding engineering applications have led to increased requirements for coatings and substrates so that they retain their mechanical strength and integrity during operation and to ensure longer component lifetimes [1]. In wear resistance applications, the coatings generally provide the resistance to wear, whilst the substrate material provides support for any impact to which the component may be subjected. The high velocity oxyfuel (HVOF) spraying process is a thermal spray deposition process used to deposit dense tungsten carbide coatings with excellent wear properties. This is primarily due to the low decomposition rate of WC during spraying, which in turn is a result of the high velocities and relatively low temperatures employed during deposition [2]. Generally, WC-Co coatings in the order of 200 to 400 μm thick are used in commercial applications without compromising the substrate material properties [3]. The abrasive wear of WC-Co coatings has been studied by many authors, generally under sliding wear conditions [1,4–6]. However, not all aspects of the abrasive wear behaviour of these coatings have been fully investigated, in particular when deposited onto different substrates. The objective of this work is to evaluate the abrasive wear resistance of WC-17 wt.% Co thermal spray coatings deposited onto four different substrates in order to assess

the effect of substrate on the coating's wear behaviour. The wear mechanisms were investigated and related to coating microstructure.

2. Experimental procedure

A commercially available, spray dried and sintered, WC-17 wt.% Co powder with a mean particle size of $45 \pm 15 \mu\text{m}$ was used as the feedstock powder. Fig. 1 is a scanning electron microscope (SEM) image of the powder showing a spherical morphology with EDS confirming the presence of W, Co and C. Coatings were sprayed using a TAFA JP5000 gun system to produce a coating thickness of approximately 200 μm . The spray parameters were similar to those used by reference [7] and were kept constant for all coatings. The parameters were as follows: 4 in. gun barrel; 380 mm spray distance; 0.0227 m³/h fuel (kerosene) flow rate; 56.6 m³/h oxygen flow rate. All coatings were deposited onto $75 \times 25 \times 9 \text{ mm}$ substrates which had been grit blasted with alumina under identical conditions prior to coating. Four types of substrates were used, namely aluminium, 304L stainless steel, super invar and brass. The coated samples were ground and polished to a 0.5 μm surface finish.

Microstructural characterisation of the coatings is reported elsewhere [8,9] with the results listed in Table 1 for ease of reference. For the microstructural analysis, cross-sections were examined by optical microscopy (OP) and scanning electron microscopy (SEM) equipped with EDS. The crystalline structure of the coatings was characterised by X-ray diffraction (XRD) using Cu-K α radiation at 40 kV and 20 mA. The grain size of the coatings was determined from polished cross-sectional SEM micrographs

* Corresponding author at: School of Chemical & Metallurgical Engineering, University of the Witwatersrand Private Bag 3, WITS, 2050, South Africa.

E-mail address: Natasha.Sacks@wits.ac.za (N. Sacks).

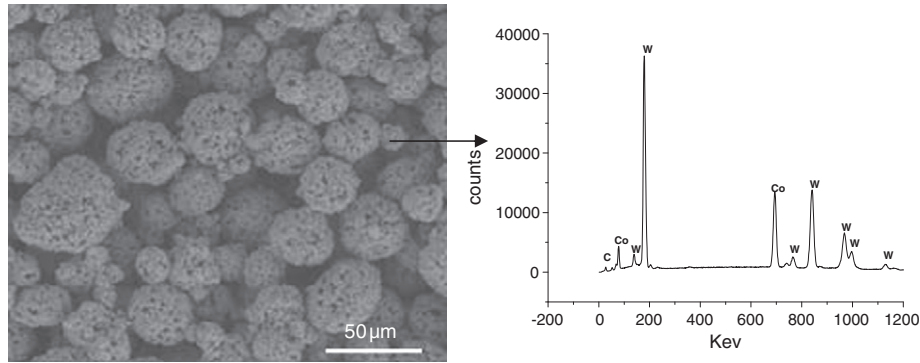


Fig. 1. SEM/BSE image showing morphology of the feedstock powder with EDS analysis.

and using linear analysis. Microhardness measurements were conducted on the cross sections of the samples using a Vickers indenter and a load of 5 kg at a dwell time of 10 s. The reported hardness is the average of five measurements. Residual stress analysis was done using an X-ray stress analyzer with Co-K α radiation filtered by V using the $\sin^2\theta$ method. The anode power was 40 kV and 40 mA. The WC (112) diffraction plane was scanned at 0.001° per step whilst the interplanar spacing value was plotted as the function of $\sin^2\theta$, and the stress determined from the slope of the curve. A detailed description of the residual stress method and analysis can be found in reference [9] with the results listed in Table 2 for ease of reference.

Three body abrasive wear tests were performed on an ASTM-G65 dry sand rubber wheel apparatus. Fig. 2 shows a schematic diagram of the test set-up [10]. Silica sand procured from Rolfe's silica with a particle size distribution between 300 and 600 μm was used as the abrasive material at a flow rate of 4.3 g/s. The morphology of the silica abrasive is presented in Fig. 3 which shows the angular nature of the particles. An applied load of 25 N and rotational wheel speed of 140 revs/min were employed. Each sample was abraded for 30 min with the mass loss being recorded at 5 min intervals. For each coated substrate, three specimens were used and the average mass loss per 5 min interval was used to determine the wear rate. The wear scars were examined using SEM.

3. Results

Optical and scanning electron microscopy showed similar microstructures of the coatings deposited onto the different substrates as shown in Figs. 4 and 5. The coatings showed a lamellar microstructure

which is due to individual splats forming a layered structure. The porosity levels are clearly evident in the optical micrographs shown in Fig. 5 whilst a number of large pores are visible in the SEM images in Fig. 4. In general the calculated porosity levels are low (Table 1) for

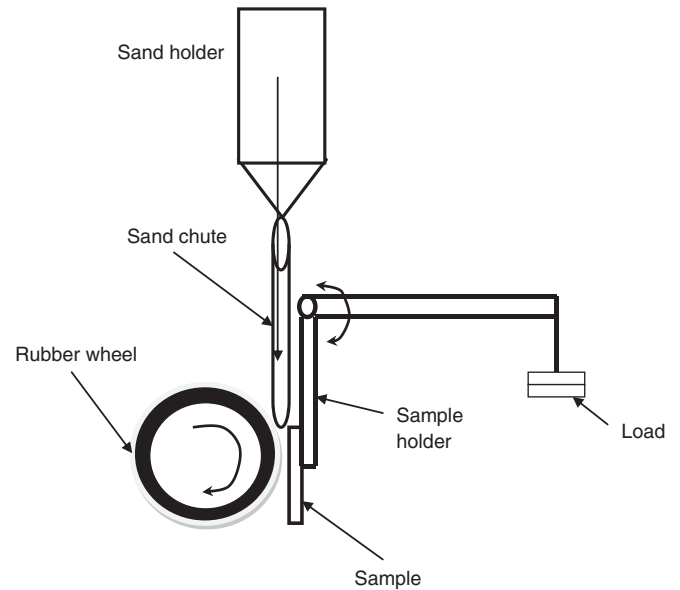


Fig. 2. Schematic diagram of the ASTM-G65 wear test machine [10].

Table 1
Coating properties [8,9].

Substrate	Coating porosity (%)	WC grain size (μm)	Residual stress (MPa)	Coating HV ₅ (GPa)
Aluminium	0.5149 ± 0.001	0.150 ± 0.01	-129 ± 26.2	10.22 ± 0.02
Brass	0.4581 ± 0.002	0.127 ± 0.01	-53.5 ± 28.0	10.04 ± 0.01
304L SS	0.5596 ± 0.001	0.185 ± 0.02	Not measured	9.41 ± 0.01
Super invar	0.7529 ± 0.001	0.133 ± 0.02	74 ± 30.6	7.91 ± 0.01

Table 2
Material properties [8,9].

Materials	Specific heat capacity (J/g °C)	CTE ($10^{-6}/\text{k}$)	Melting point (°C)
Brass	0.380	19	930
Aluminium	0.900	23	660
Super invar	0.123	1.2	1454
304L stainless steel	0.460	17.3	1365
WC	0.171	6.0	2870

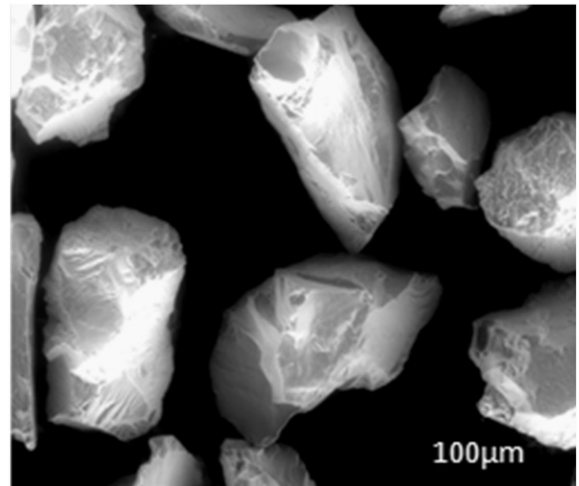


Fig. 3. Morphology of silica abrasive.

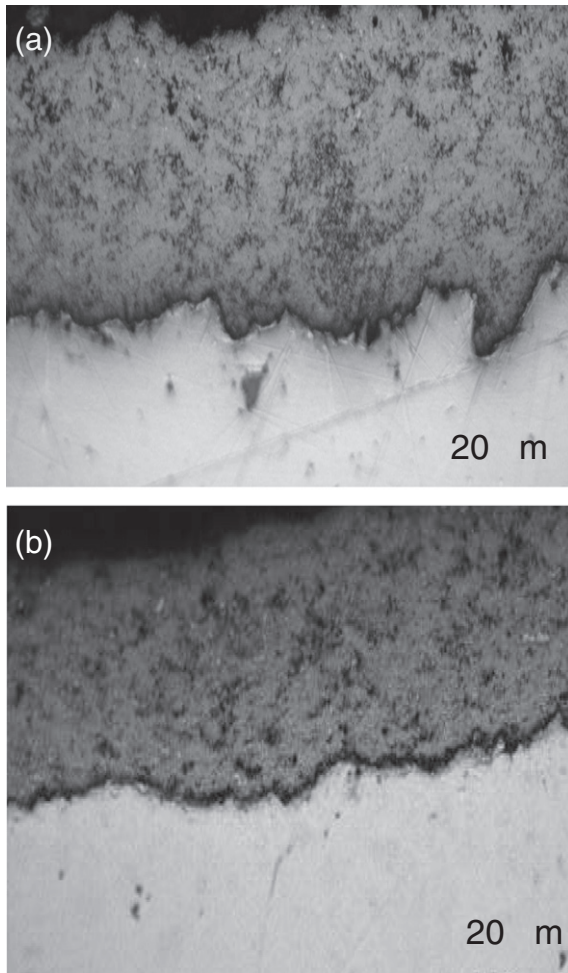


Fig. 4. Optical micrographs of the WC-17 wt.% Co coating on (a) aluminium and (b) brass.

all coatings except that deposited onto the super-invar; which is in agreement with the optical micrographs in Fig. 5. The WC grains were mainly equiaxed in shape and embedded in the Co matrix. EDS scans revealed that all the coatings were composed of W, Co and C. The coating deposited onto the 304L stainless steel substrate also indicated the presence of aluminium at the interface which originates from the alumina grit-blast preparation of the substrates prior to coating deposition. No evidence of diffusion was found at the interfaces between substrate and coating. The coatings on the super-invar substrate showed micro-cracks in some regions as shown in Fig. 6. These cracks are thought to be caused by the residual stresses which develop during deposition [9] and would weaken the bonding strength between coating and substrate and are expected to influence the wear properties. The mean WC grain sizes of the coatings are given in Table 1 and were in general similar and small. It might be expected that less porosity would be associated with the smaller grain size, but this was not the case.

Fig. 7 shows the X-ray diffraction spectra of the powder and coated surfaces. The feedstock powder comprised only of WC and Co. Prominent WC peaks were found on all coatings, whilst Co was only detected on the coated aluminium and super-invar substrates. EDS scans revealed that Co is present on all four coated substrates. Its omission from the XRD spectra indicates that the amount of pure Co is too low to be detected which suggests that the cobalt binder in these two coatings may be saturated by tungsten and carbon. Traces of eta phase in the form of W_2C on the aluminium and W_3C on the super-invar were detected. Stewart et al. [11] reported that W_2C formed on splat quenching and was caused by dissolution of WC in the Co matrix.

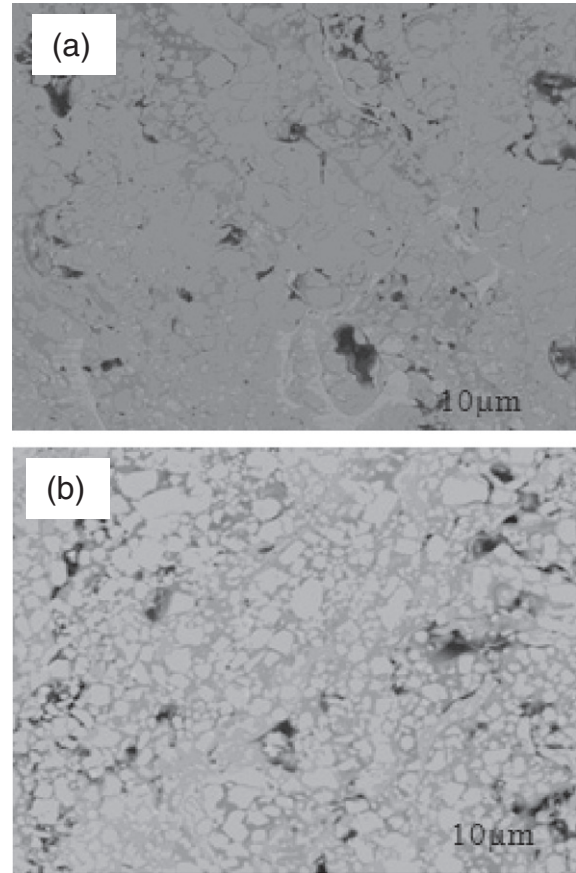


Fig. 5. SEM/BSE images of the coating on (a) brass and (b) 304L stainless steel. The light phase is WC and the dark phase is Co.

The hardness of the substrates and coatings is shown in Fig. 8. The highest hardness was achieved for the coated aluminium which is partially due to the presence of the hard eta phase. The lowest coating hardness was found for super-invar. Although eta phase was also found on this coating the micro-cracks revealed during microscopic examination led to a reduction in hardness. The hardness of the coated brass is slightly lower than that of the aluminium, whilst the coated 304L stainless steel had the third lowest hardness.

The results of average cumulative mass loss for each coated substrate during the 30 min test duration are shown in Fig. 9, with the wear rates for each coated substrate after 30 min shown in Fig. 10. The general trend of increasing mass loss as time progresses is seen

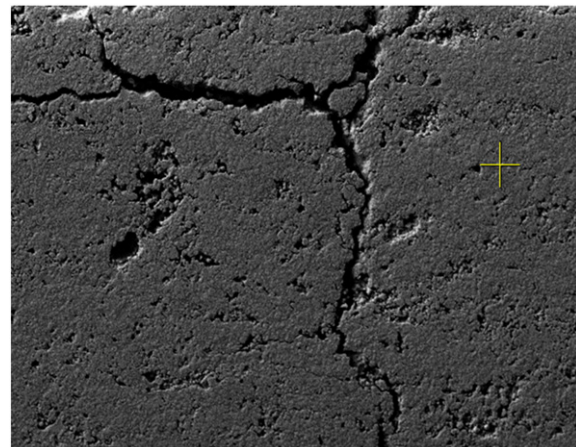


Fig. 6. Micro-cracks observed on the coated super-invar.

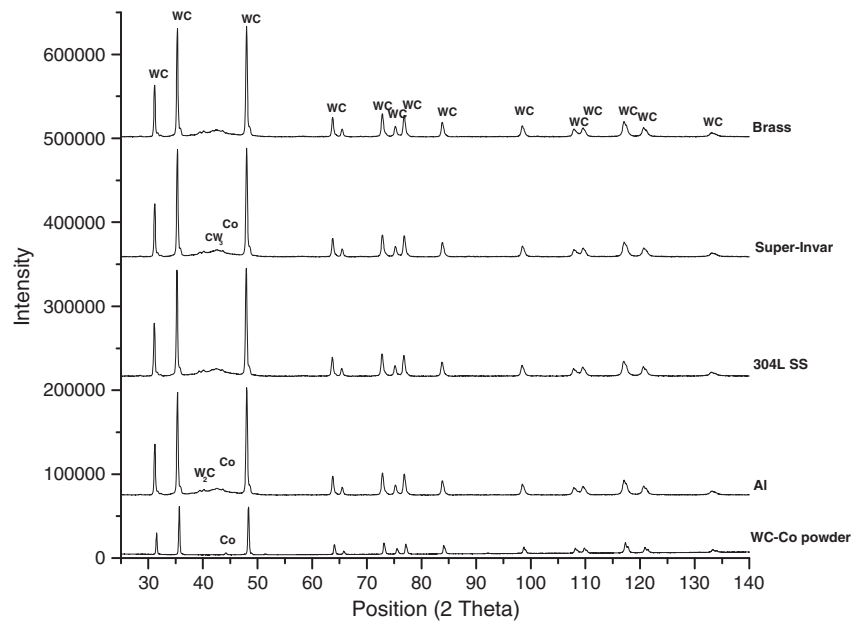


Fig. 7. XRD pattern of the WC powder and as-sprayed coating.

for all coated substrates. The coated aluminium consistently shows the highest average mass loss, despite having the highest hardness. The coated brass and super-invar samples show similar mass loss trends. The coated 304 stainless steel begins to show the lowest mass loss after 20 min, even though it has the second lowest hardness value. These results do not follow the general trend of increasing hardness being associated with a decrease in wear rate. This implies that additional factors are determining the wear response of the coated substrates.

To understand the wear behaviour, the wear scars were examined using SEM. Fig. 11 shows plan view SEM images of the worn surfaces. Similar wear features were observed on all four worn coated substrates. However, the degree of damage differed among the substrates. The worn coated aluminium images revealed extensive cracking of the carbide grains, as well as fragmenting of the carbides into smaller pieces. Fewer cracked and fragmented carbides were observed on the coated super-invar and brass substrates, with extremely few seen on the coated 304L stainless steel substrates. The worn surfaces of all the coated substrates were also characterised by Co binder removal in selected areas leaving the carbide grains unsupported. The coated 304L stainless steel showed limited binder removal whilst the coated aluminium reflected the highest level of binder removal. Rounding of the carbide grain edges was observed on all four worn coated substrates. In random

areas, individual and multi-grain pull-out, as well as surface micro-crack paths was noticed. A few deep wear grooves were visible, indicating the direction of abrasive wear.

4. Discussion

The investigation of the abrasive wear properties of the four coated substrates gave different wear resistances despite using the same WC-Co feedstock powder. It was observed that despite having the highest hardness, the coated aluminium samples had the highest wear rate. SEM studies showed that this coated substrate had the highest level of Co binder removal. Removal of the binder phase provides relief to the matrix causing the carbide grains to crack as the stresses inside the grains are relieved. Cracking of the exposed carbide grains may also occur due to micro-fatigue action of the abrasive against the grains during testing. These types of wear mechanisms, found on all the worn surfaces, are common in the abrasion of HVOF coatings [12]. The poor performance of the coated aluminium may also be attributed to the W_2C phase present in this coating. The presence of this phase is said to be due to decarburization occurring at high temperature during spraying [13,14]. Engqvist et al. [15] reported that the hardness of the W_2C phase is 3000 HV which is higher than WC (HV = 1300–2300). Therefore this phase would increase the overall coating hardness and explains why this coating had the highest hardness value. However W_2C is reported to be brittle [16] and fractures easily during abrasion. Therefore

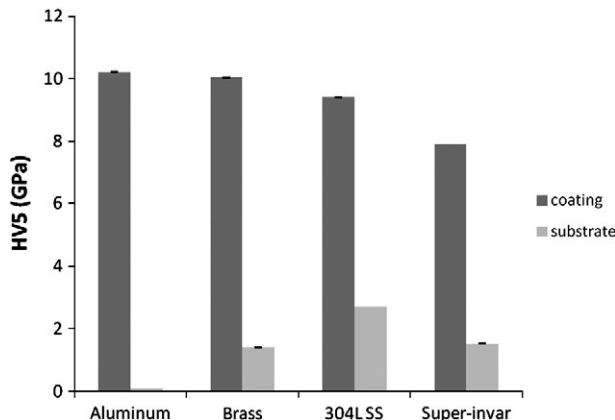


Fig. 8. Hardness of the WC-Co coatings and the different substrates.

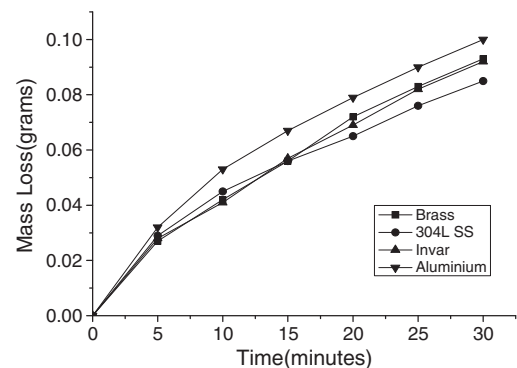


Fig. 9. Average cumulative mass loss for each substrate coating.

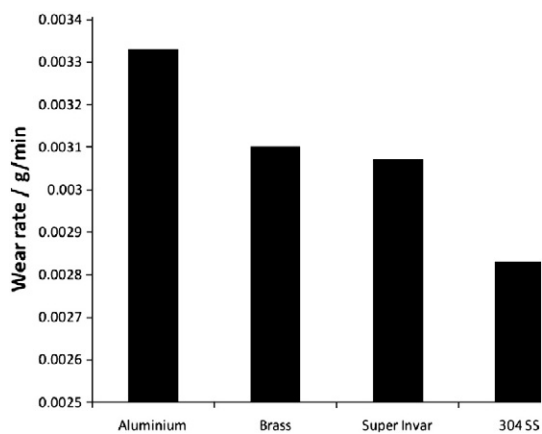


Fig. 10. Wear rate of coated substrates after 30 min of testing.

the combination of high binder removal and eta phase contributed to the high wear rates observed for the coated aluminium despite having the highest hardness.

The coated brass and super-invar samples were in the mid-range of mass loss, and considering the small standard deviations in mass loss, could be considered as having equal wear resistances. The coated super-invar had the highest porosity, lowest hardness, W_3C ($HV = 2650 \pm 100$ [17]) and micro-cracks (not present in the other coatings) which should have led to this coating experiencing the highest wear rates; but did not. The coated brass samples had the lowest porosity, second highest hardness, and no eta phase or micro-cracks and were therefore expected to have a lower wear rate than the coated super-invar substrates. The lowest wear rates, which signify a better abrasion resistance, were shown by the coated 304L stainless steel samples. Yet these coatings had only the third highest hardness and the second highest porosity. In SEM studies of the worn coated 304L stainless steels it appeared that a high degree of melting is occurring during deposition. This is known to lead to a better bond strength between substrate and coating, as well as better bonding between the carbide grains and binder [11]. This is probably the reason why very little binder removal, few cracked carbide grains and in general, smoother wear scars were observed for this coating.

The paradox between the wear rates and coating microstructural properties such as hardness, eta phase and micro-cracking indicates that other factors play a role in the wear behaviour of these coatings despite using the same feedstock powder and the same coating deposition parameters. The results indicated that coating hardness is dependent on substrate, therefore hardness and consequently the wear response of a coating cannot be generalised for a specific coating irrespective of substrate. It was expected that the coating hardness would decrease with increasing WC grain size, but this was not conclusive with the small amount of data and high scatter. However, hardness decreased with increasing porosity as expected. The differences in the hardness values of the coatings may be attributed to the role played by the substrate properties (Table 2) during cooling and solidification of the coating after deposition which influence the residual stresses produced. The coating hardness was observed to increase with increasing coefficient of thermal expansion of the substrate. The processing parameters during deposition are also known to affect coating hardness [18,19] although these were kept constant in the current study for all the coatings. During deposition each powder particle is heated in the combustion chamber of the HVOF gun and then projected towards the substrate. On impact with the substrate, it deforms into a lamella which cools down and solidifies. The combustion temperature could be as high as 3000 °C and then the temperature decreases depending on the difference between this and the coating's melting range. Using forced cooling, the temperature of the substrate of a WC-Co coating was approximated to be 500 °C by Stoke et al. [20]. The cooling of both substrate and coating after spraying

leads to the formation of residual stresses in the individual lamellar structures. The variations in porosity across the different coatings might be as a result of fuel gas flow during coating deposition, as observed by Arturas [18] since the substrates were different materials. However the overall measured porosity levels are low and with the exception of super-invar, are similar for all coatings. Thus the role of porosity in the observed wear response is considered minor.

Some understanding of the wear response of the different coatings may be gained from considering the interaction between the SiO_2 abrasive and the coating microstructure. The SiO_2 abrasive particle size ranged from 300 to 600 μm , whilst the average WC grain size of the coatings is in the range of 0.12 to 0.19 μm . On this basis all the coatings responded homogeneously during wear, even though the Co binder is preferentially removed. The hardness of the SiO_2 abrasive is 800 HV [21] whilst the hardness of the coatings ranged from 807 to 1042 HV. The ratio of the hardness of the abrasive particles to the hardness of the coatings (H_a/H_m) is in the range of 0.77–0.99. These calculated ratios are less than 1.2 which signifies the boundary condition between soft and hard abrasion as defined by Hutchings [21] and would therefore place the abrasive wear of all the coatings in the soft abrasion category. This classification confers with the extent of damage observed on the worn surfaces, where the soft Co phase is preferentially removed whilst the hard WC grains remain largely intact. The SiO_2 abrasives are unable to indent and crack the WC grains due to their differences in hardness values. The applied stress during abrasion was calculated to be 0.06 MPa but the actual pressure is expected to be higher than this as the real contact area between individual abrasive particles and the coating surface is lower than the surface area of 420 mm² used to calculate the nominal stress. The yield strength of each coating was calculated using Cahoon et al.'s [22] formula with n assumed to be 0.15 and the values are listed in Table 3. The yield strength of the coatings far exceeds the applied pressure and indicates that all four coatings have a good abrasion resistance.

In the current study the contribution of residual stresses and strains on the wear performance of the different substrate–coating combinations has been considered. The origin of residual stresses in coatings has been investigated by several authors [2,3] and it has been shown that the material and the deposition process may produce residual stresses which can cause a large mismatch between thermal, structural and mechanical properties of the layers and substrates. Specific to thermal spray coatings, quenching stresses due to rapid cooling of the coating, thermal mismatch stresses between the substrate and the coating and phase transformations during deposition have been identified as sources of residual stresses. Residual stress in the material can be tensile or compressive and the nature of the overall residual stress in coated systems may be determined by criteria identified by Stokes and Looney [20] on the basis of the cooling stresses associated with the relative values of coefficients of thermal expansion between coating and substrate. The authors determined that a tensile stress would develop in the coating when $\alpha_c > \alpha_s$ whilst a compressive stress would develop when $\alpha_c < \alpha_s$ where α_c and α_s represent the values of coefficients of thermal expansion for the coating and substrate respectively.

In work published by the current authors (Table 2), compressive stresses were found on the coatings deposited onto the brass and aluminium substrates, whilst tensile stresses were found on the coated super-invar [9]. These variations in the residual stresses were considered to be due to the following factors which are considered to play a crucial role in cooling and solidification of the coating after deposition: (1) differences in coefficient of thermal expansion; (2) decomposition of WC; (3) specific heat capacity of the respective substrate; (4) kinetic impact of the particle on the substrate during the HVOF process caused by the heat transport from the coating to the substrate. The tensile stress observed in the super-invar coating likely led to the micro-cracks observed in the coating deposited onto this substrate. The same was found by Stokes and Looney [20], who also stated that compressive stresses may lead to buckling or

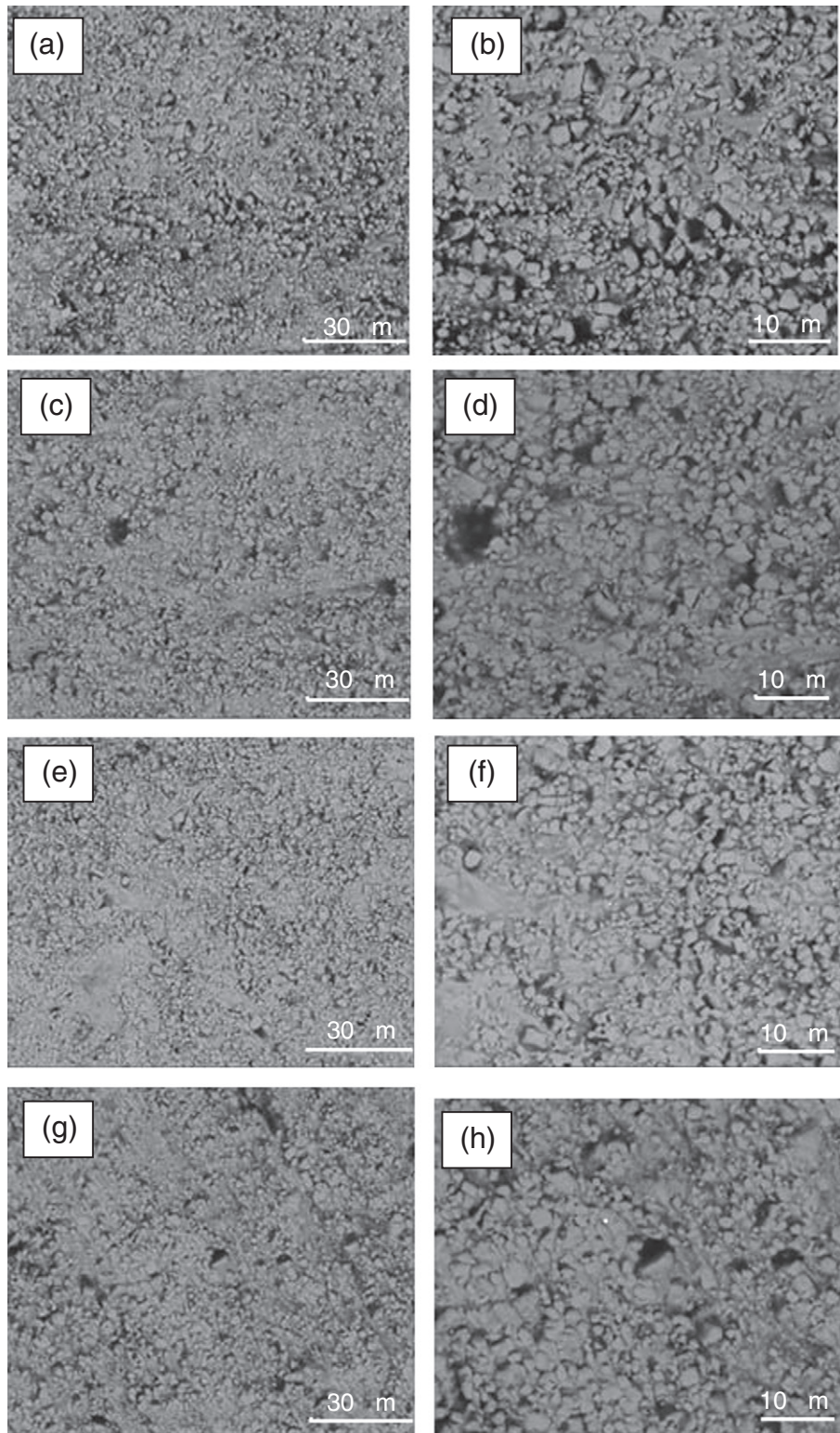


Fig. 11. SEM/BSE micrographs of the worn coating surfaces on (a) and (b) aluminium (c) and (d) brass (e) and (f) super-invar (g) and (h) 304L stainless steel.

Table 3

Yield strength of the coatings.

Substrate	Brass	Aluminium	Super-invar	304L Stainless steel
Coating yield strength (GPa)	2.37	2.41	1.87	2.22

delamination of the coating. However this was not observed on the coatings deposited onto the brass and aluminium substrates which showed compressive stresses. The coated aluminium which had the highest compressive stress had the highest wear rate. As stated earlier the preferential removal of the Co binder phase causes relaxation of these residual stresses which facilitates carbide grain cracking. The high stress levels observed in this coating are considered to be

the reason for the high degree of carbide grain cracking observed in the worn surface of this coating which subsequently led to the high wear rates measured. The coated brass samples showed compressive stresses and the coated super-invar had tensile stresses, yet the wear rates of the coatings on these two substrates were similar. Thus the role of residual stresses on abrasion resistance needs further study before any conclusive remarks can be made. Analysis of strain mismatch between coating and substrate to understand the adhesion properties is underway and some initial results on the brass and super-invar materials can be found in reference [23] using synchrotron measurement. A large strain misfit between the coating and the substrates was found and this was attributed to the grit-blasting surface preparation of the substrates prior to deposition. The different substrates showed different strain behaviour with the measured strain values in the coatings being low in magnitude. These differences in strain misfit between substrate and coating as well as the residual stresses in the carbide coating will influence the adhesion properties between the coating and substrate and consequently influence the coating's integrity and wear performance.

6. Conclusions

The abrasive wear resistance of WC-17 wt.% Co thermal sprayed coatings deposited onto four different substrates yielded very different wear resistance characteristics despite being produced from the same feedstock powder using the same deposition parameters. The highest mass loss was recorded for the coating on the aluminium substrate whilst the coated 304 stainless steel showed the lowest mass loss. The coatings on brass and super invar experienced similar mass losses. SEM studies of the worn surfaces showed preferential removal of the Co binder phase as well as cracking and rounding of the carbide grains. The differences in wear behaviour may be attributed to the presence of residual stresses where the highest compressive residual stress led to the highest wear rate. The coatings deposited onto brass showed compressive stresses whilst those deposited onto super-invar had tensile stresses, yet these two coatings had similar wear rates. Thus further study is required to provide conclusive evidence of the role of residual stresses on the abrasion resistance of these coatings.

Acknowledgements

The authors wish to acknowledge the financial and technical support received from the Department of Science and Technology in South Africa, the National Research Foundation in South Africa, the Nuclear Energy Corporation of South Africa (NECSA), and the University of the Witwatersrand. The authors also wish to thank Tshepo Ntsoane

and Ryno van der Merwe from NECSA for assistance with XRD and SEM analysis.

References

- [1] Wood RJK. Tribology of thermal sprayed WC-Co coatings. *Int J Refract Met Hard Mater* 2010;28:82–94.
- [2] Schwetke R, Kreye H. Microstructure and properties of tungsten carbide coatings sprayed with various HVOF spray systems. *Proc 15th Int Thermal Spray Conference*, Nice, France; 1998.
- [3] Stewart DA, Shipway PH, McCartney DG. Abrasive behaviour of conventional and nanocomposite HVOF-sprayed WC-Co coatings. *Wear* 1999;225–229:789–98.
- [4] Guilemany JM, Miguel JM, Vizcaino S, Climent F. Role of three-body abrasion in the sliding wear behaviour of WC-Co coatings obtained by thermal spraying. *Surf Coat Technol* 2001;140:141–6.
- [5] Wang YY, Li CJ, Ma J, Yang GJ. Effect of flame conditions on abrasive wear performance of HVOF sprayed nanostructured WC-12Co coatings. *Trans Nonferrous Met Soc China* 2004;14:72–6.
- [6] Sudaprasert T, Shipway PH, McCartney DG. Sliding wear behaviour of HVOF sprayed WC-Co coatings deposited with both gas-fuelled and liquid-fuelled systems. *Wear* 2003;255:943–9.
- [7] Luyckx S, Machio CN. Characterization of WC-VC-Co thermal spray powders and coatings. *Int J Refract Met Hard Mater* 2007;25:11–5.
- [8] Oladijo OP, Venter AM, Cornish LA, Sacks N. PM2010 Powder Metallurgy World Congress Proceedings, Florence, Italy, 3(66); 2010. p. 1–8.
- [9] Oladijo OP, Venter AM, Cornish LA, Sacks N. X-ray diffraction measurement of residual stresses in WC-Co thermally sprayed coatings onto metal substrates. *Surf Coat Technol* 2012;206(23):4725–9.
- [10] Mabotja M. Research project report. University of the Witwatersrand; 2010.
- [11] Stewart DA, Shipway PH, McCartney DG. Microstructural evolution in thermally sprayed WC-Co coatings: comparison between nanocomposite and conventional starting powders. *Acta Mater* 2000;48:1593–604.
- [12] Murthy JKN, Venkataraman B. Abrasive wear behaviour of WC-CoCr and Cr₃C₂-20(NiCr) deposited by HVOF and detonation spray processes. *Surf Coat Technol* 2006;200:2642–52.
- [13] Nerz J, Kushner B, Rotolico A. Microstructural evaluation of tungsten carbide-cobalt coatings. *J Therm Spray Technol* 1992;1(2):147–52.
- [14] Verdon C, Karimi A, Martin J-L. A study of high velocity oxy-fuel thermally sprayed tungsten carbide based coatings. Part 1: Microstructures. *Mater Sci Eng A* 1998;46(1–2):11–24.
- [15] Engqvist H, Ederyd S, Axen N, Hogmark S. Grooving wear of single-crystal tungsten carbide. *Wear* 1999;230(2):165–74.
- [16] Oberste Berghaus J, Marple B, Moreau C. Suspension plasma spraying of nanostructured WC-12Co coatings. *J Therm Spray Technol* 2006;15(4):676–81.
- [17] Di Maio D, Roberts SG. Substrate and elastic recovery effects in hardness measurement of CVD WC based coatings. *Philos Mag* 2005;85(1):33–43.
- [18] Arturas B. Influence of temperature on tungsten carbide coating sprayed by different spray systems. *Mater Sci* 2005;2(11):105–9.
- [19] Martin W, Daniel L, Rainer G. Methods and application of residual stress analysis on thermally sprayed coatings and layer composites. *Surf Coat Technol* 2006;201:1995–2001.
- [20] Stoke J, Looney L. HVOF system definition to maximise the thickness of formed components. Dublin, Ireland: *Proc Advances in Materials & Processing Technologies*; August 1999.
- [21] Hutchings IM. Tribology: Friction and Wear of Engineering Materials. Edward Arnold; 2002.
- [22] Cahoon JR, Broughton WH, Kutzak AR. The determination of yield strength from hardness measurements. *Metall Trans A* 1971;2(7):1979–83.
- [23] Venter AM, Pirling T, Buslaps T, Oladijo OP, Steuwer A, Ntsoane TP, et al. Systematic investigation of residual strains associated with WC-Co coatings thermal sprayed onto metal substrates. *Surf Coat Technol* 2012;206(19–20):4011–20.

Effect of Substrates on the Microstructure of Thermally Sprayed WC-4.88 wt% Co Coatings

O.P. Oladijo^{1,2,3} A.M. Venter^{2,3} L.A. Cornish^{1,2} N. Sacks^{1,2} and S. Shrivastava^{2,4}

¹*School of Chemical & Metallurgical Engineering, University of the Witwatersrand
Private Bag 3, WITS, 2050, South Africa*

²*DST/NRF Centre of Excellence in Strong Materials, University of the Witwatersrand*

³*Research & Development Division, NECSA Limited, Pretoria, South Africa*

⁴*School of Physics, University of Witwatersrand, Private Bag 3, WITS, 2050, South Africa*

Abstract

Aluminium, 304L stainless steel, super-invar and brass substrates were coated with WC-4.88wt%Co using the High Velocity Oxy-Fuel (HVOF) technique. Microstructure and phase identification studies were done using optical microscopy, scanning electron microscopy, X-ray diffraction and atomic force microscopy. X-ray residual stress and microhardness measurements were also undertaken. Porosity and grain sizes were determined. From the X-ray diffraction spectra of the sprayed coatings, differences in the phases present for each coated substrate were observed. The coatings had similar microhardnesses within experimental error. The residual stress results were different for each coating sprayed onto different substrates. These differences were interpreted as originating from the different specific heat capacities and coefficients of linear thermal expansion of the substrates.

1. Introduction

WC-Co alloys are widely used in many industrial fields owing to their advantageous characteristics including high hardness, moderate toughness, and excellent wear resistance [1-2]. Thermal spray coatings are widely applied in industrial technology for the protection of base materials against different types of environmental effects such as temperature, chemically aggressive fluids, abrasive wear and hot gas corrosion. Many authors have conducted research on the different types of deposition methods, the effect of powder morphology and spray parameters on microstructure evolution and coating properties [3-4]. The microstructure and wear performance of WC coatings can be influenced by many factors including the spray processing method [6,7], and structure of feedstock [6-9]. However, not all aspects are fully understood. WC-Co coatings also depend on the characteristics of the substrate. The High Velocity Oxy-Fuel (HVOF) spraying process has become one of the preferred techniques for depositing dense WC coatings on a variety of substrates to give excellent wear performance, owing to its high velocity of placing particles and relatively low temperatures, which result in less decomposition of the WC during spraying [5]. In wear-resistance applications, the coated layer provides the wear resistance, while the substrates support any impact to which the component (coating and substrate) is subjected. The objective of this work was to examine the effect of substrate on the microstructure of WC-Co coatings sprayed by the HVOF process. The work was also done to gain a better understanding of the decomposition process of tungsten carbide during thermal spraying and the structure of the coatings.

2. Experimental procedure

The WC-4.88 wt% Co powder used as a feedstock was prepared by sintering. The typical morphology of the powder is shown in Fig. 1. The surface of the substrate to be coated was machined, chamfered and grit blasted with aluminum before deposition. Coatings of about

200µm in thickness were deposited on four substrates, namely aluminium, 304L stainless steel, super-invar and brass samples of 12x10x9mm in size. These were prepared by using a TAFA JP5000 HVOF spraying system. Kerosene was the fuel and oxygen was used for the deposition of the coating. Specimens were cut and metallographic samples were made of the cross-sections through the coatings. Cold mounting resin was used and the final polish was 0.5µm.

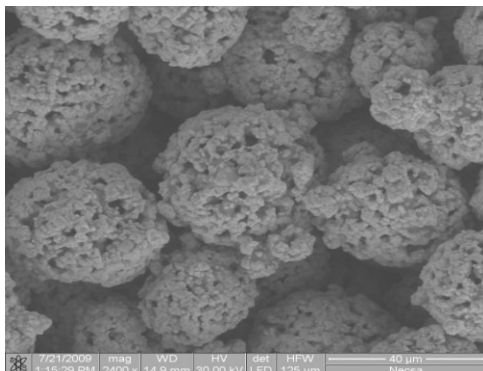


Fig. 1. SEM/BSE micrograph of WC-4.88 wt%Co powder.

For microstructure analysis, optical microscopy (AXION 25) and scanning electron microscopy (SEM) with backscattered electron imaging (BSE) was used. The porosity of the coatings was determined using Archimedes' principle. The grain size of the coatings was determined from the polished cross-sectional micrographs obtained from the scanning microscope and using linear analysis. An atomic force microscope (AFM) with a tip radius <10nm was employed to measure the surface roughness of the coatings cross section using a surface area of 25.4µm². Microhardness measurements were conducted on the cross sections of the samples using a Vicker's indenter and a load of 5kg at a dwell time of 10s. The result was obtained from an average of five readings. X-ray diffraction (XRD) was conducted for the powders and coatings with Cu-Kα radiation at 40kV and 20mA on a Philips 1710 Diffractometer. Residual stress measurement taken on coating surface was done on an X-ray stress analyzer with Co-Kα radiation filtered by V using the sin²θ method. The anode power was 40kV and 40mA. The WC (112) diffraction plane was scanned at 0.001° per step while the interplanar spacing value was plotted as the function of sin²θ, and the stress was determined from the slope of the curve.

3. Results

3.1 X-ray diffraction

Fig. 2 shows the X-ray diffraction spectra of the powder and coated surfaces. The starting powder comprised only WC and Co, but different phases were found for the different coated samples. All the coatings had a broad peak at $2\theta \approx 44^\circ$. The XRD results of the coated aluminium sample showed WC and metallic Co with only a small amount of W₂C. The coating on 304L stainless steel revealed the presence of WC only with no Co. Detection of cobalt (Co) can be slightly compromised as XRD can be sensitive to the detection of cobalt [10]. For super-invar, the XRD spectrum was significantly different from the others and was of a poorer quality, with broad peaks. There were large Co peaks as well as large W₃C peaks. The brass sample showed WC, no Co and the possibility of some free W by the slight peak at $2\theta \approx 44^\circ$. Two different carbides were found; W₂C in aluminium sample, and W₃C on the super-invar.

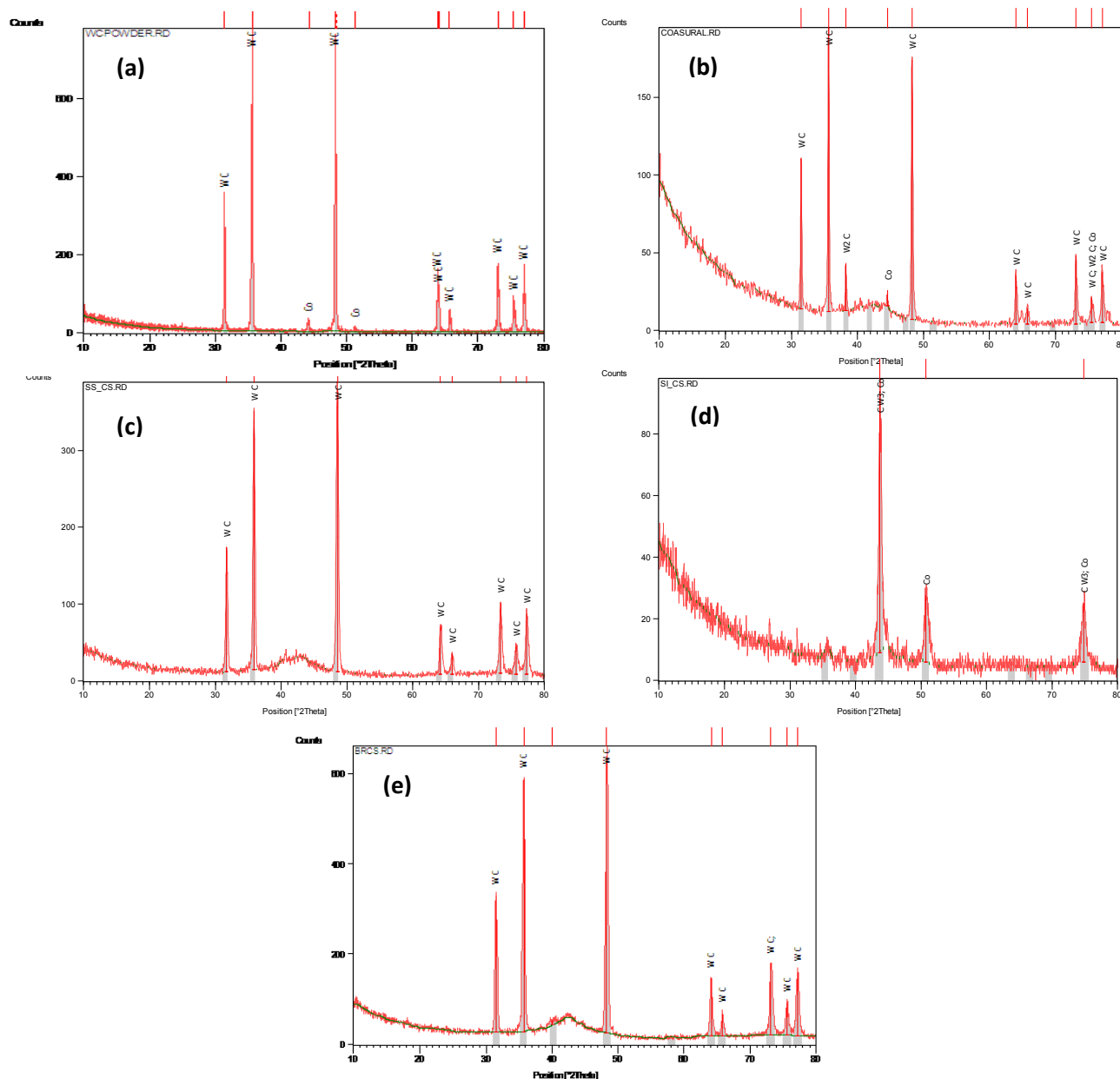


Fig. 2 XRD spectra of (a) WC-4.88% wt% Co powder and (b) coated aluminum sample, (c) coated 304L stainless steel sample, (d) coated super-invar sample and (e) coated brass sample

3.2 Microstructure characterization

Optical and scanning electron microscopy showed similar microstructures of the coatings deposited on the different substrates. The optical micrograph in Fig. 3 shows how the coating fitted the irregular surface, which would create a good mechanical bond. The porosity can also be seen. The SEM/BSE micrographs of the WC-4.88 wt% Co coatings are shown in Fig. 4. At a higher magnification, the coatings showed pores and equiaxed WC grains of different sizes in a Co matrix. EDX analysis showed that all the coatings were composed of W, Co and C, except for the 304L stainless steel sample which had Al in addition. The presence of aluminium at the interface is thought to originate from the alumina grit blast preparation of the substrate before deposition of the coating. The phase contrasts are in agreement with X-ray diffraction results.

The porosities observed in the microstructures were very low, except for super-invar which had a slightly higher porosity.

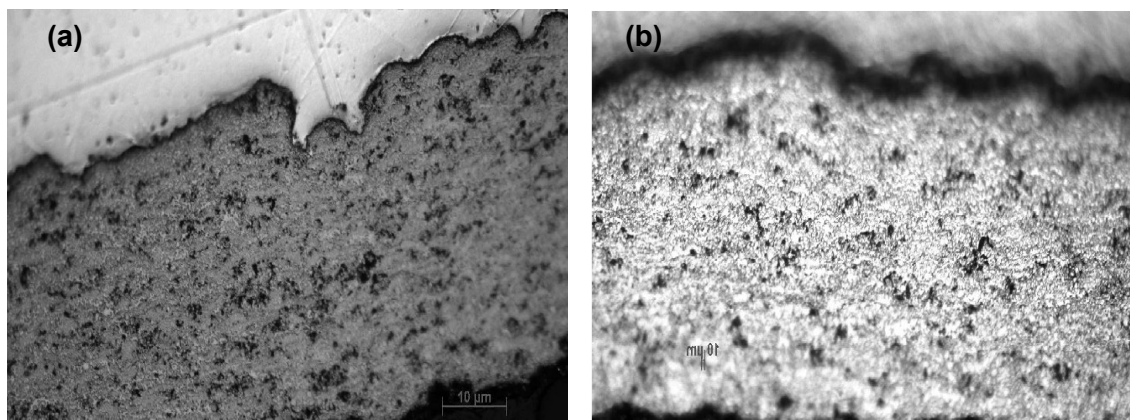


Fig. 3. Optical micrographs of WC-4.88 wt% Co coatings (bottom) on different substrates: (a) aluminium and (b) brass

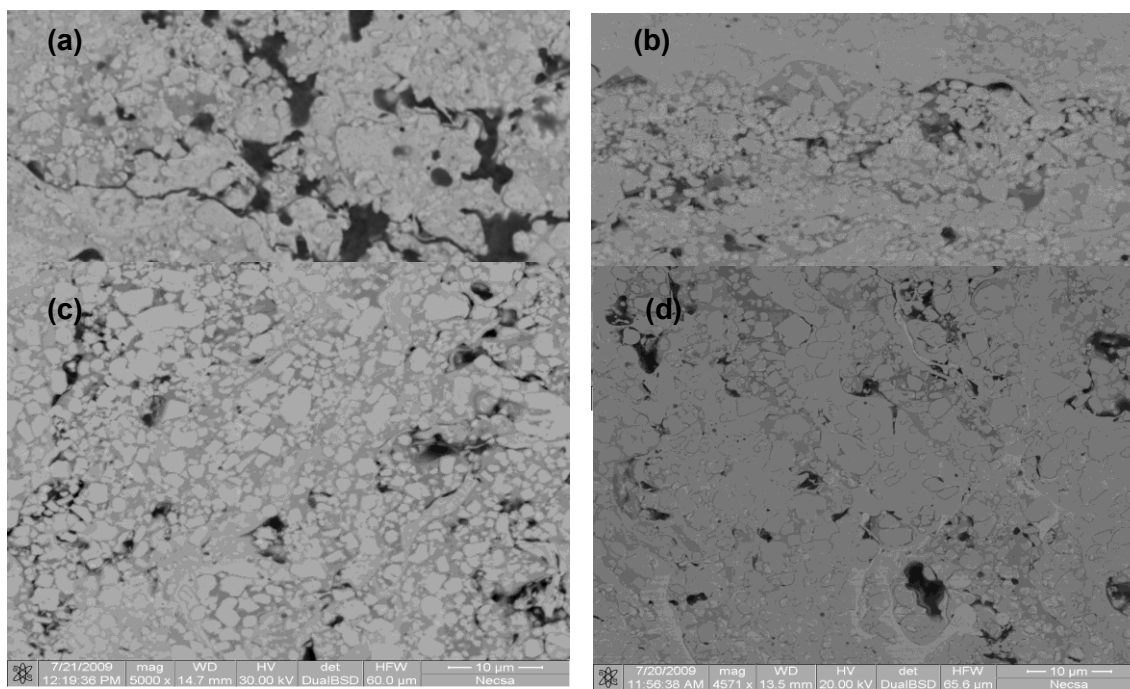


Fig. 4. SEM/ BSE images of WC-4.88 wt% Co coatings on different substrates: (a) aluminium, (b) 304L stainless steel, (c) super-invar and (d) brass.

3.3 Grain size and porosity

The grain size and morphology of WC-Co powder affect the mechanical properties of the coatings. Initial WC grain size is 0.37 μm. The mean WC grain sizes in the coatings are given in Table 1.

Table 1. Porosity, mean grain size and substrate physical properties.

Substrate	Porosity (%)	WC grain size(μm)	Melting Point ($^{\circ}\text{C}$)	Specific heat capacity ($\text{J/g}^{\circ}\text{C}$)	$\alpha(10^6/\text{C at } 20^{\circ}\text{C})$
Aluminium	0.5149 ± 0.001	0.150 ± 0.01	660	0.900	23
Brass	0.4581 ± 0.002	0.127 ± 0.01	930	0.380	19
304L SS	0.5596 ± 0.001	0.185 ± 0.02	1365	0.460	17.3
Super-invar	0.7529 ± 0.001	0.133 ± 0.02	1454	0.123	1.2

α =coefficient of linear thermal expansion

The mean grain sizes were in general similar and small. It might be expected that less porosity would be associated with smaller grain size, but this was not the case. The grain size distribution in Fig. 5 shows a good homogeneous distribution for stainless steel and brass, whereas more irregular grain sizes were seen in aluminium and super-invar. Table 1 shows that the porosity of the super-invar coating was a little higher than the rest of the samples, which is in agreement with metallography. The brass sample had slightly lower porosity.

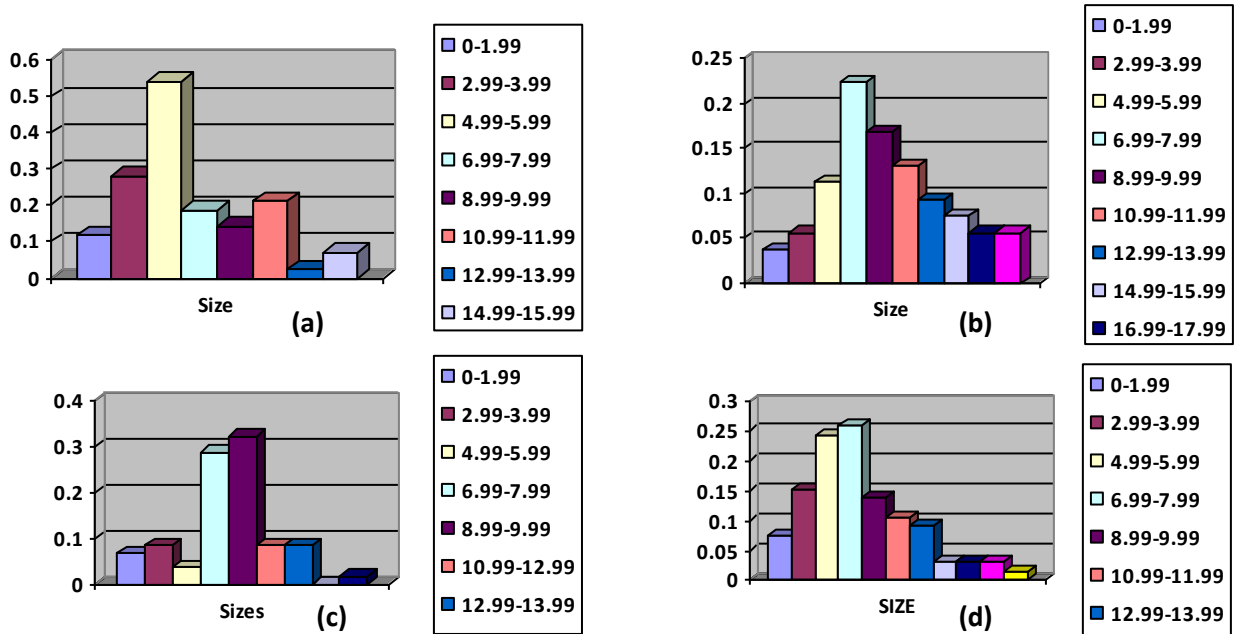


Fig. 5 Grain size distribution of the coatings on different substrates: (a) aluminium, (b) 304L stainless steel, (c) super-invar and (d) brass.

3.4 Surface Roughness

The three-dimensional surface roughness measured on the coatings by atomic force microscopy is shown in Fig. 6, and the results are given in Table 2. The aluminium and brass samples had similar roughness values.

Table 2. Properties of the coatings.

Substrate	Surface roughness Rq (nm)	Residual stress of WC (MPa)	HV coating (GPa)	HV substrate (GPa)
Aluminium	35	-149.8±50.2	10.22±0.02	0.09±0.01
Brass	32	-47.5±43.1	10.04±0.01	1.40±0.01
304L SS	10	-162.2±36.5	9.41±0.01	2.71±0.01
Super-Invar	24	-17.6±44.6	7.91±0.01	1.53±0.01

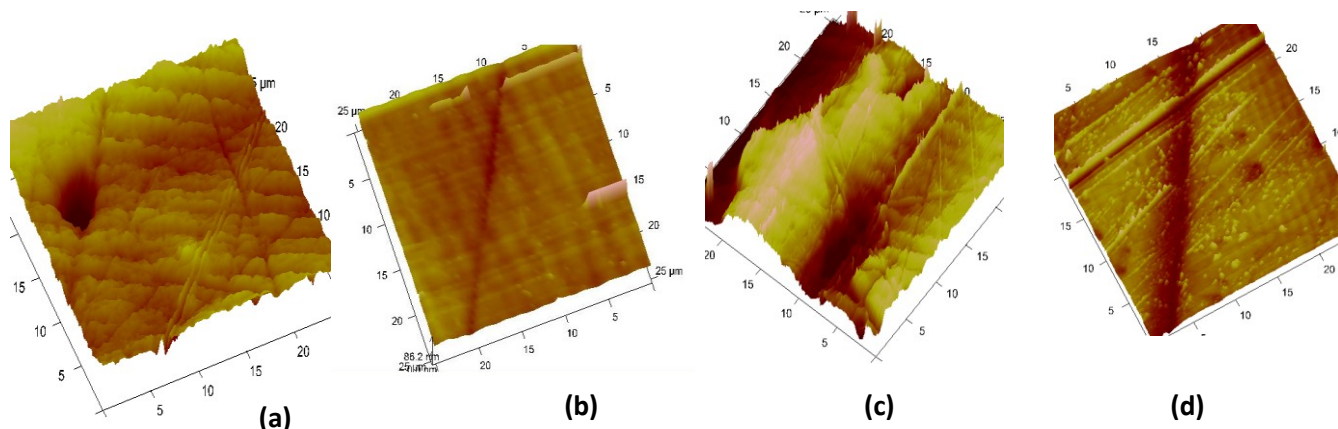


Fig. 6. AFM surface profiles of WC-4.88 wt% Co coatings on different substrates: (a) aluminium, (b) 304L stainless steel, (c) super-invar, and (d) brass.

3.5 Residual stress

The residual stresses in the WC phase at the surface of the coatings are shown in Table 2. The stresses were compressive in nature which has a beneficial effect on the coating's adhesion and mechanical properties [11]. The compressive nature might be due to the grinding process after coating affecting the first two microns, because the same WC-Co powder was used as feedstock on all the substrates.

3.6 Coating hardness

The microhardness values of both coatings and substrate are shown in Table 2 and Fig.7. The results indicate a higher microhardness in the coating compared to the substrates. The value for the coated aluminium sample was slightly higher than the other coated samples due to the occurrence of W_2C .

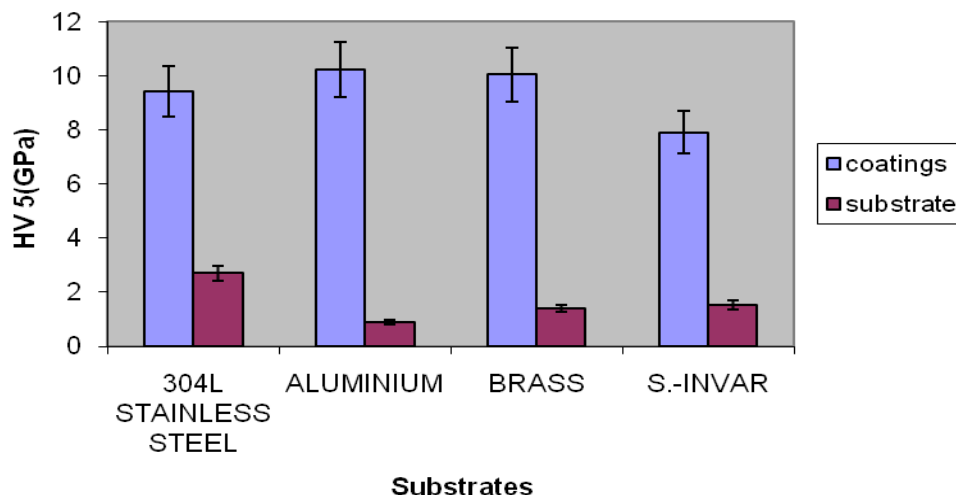


Fig. 7. Microhardness values of WC-Co coatings and the different substrates.

4. Discussion

It was observed that the highest hardness was achieved for the aluminium coated substrate that had WC, Co and W_2C . The lowest coating hardness was for super-invar, which showed WC W_3C and Co. The steel substrate also contained W_3C but its effect does not appear as great as for super-invar. W_3C is detrimental to hardness whereas W_2C is not. Di Maio et al. [12] measure the micro hardness of W_2C and W_3C as $2980 \pm 100 \text{ kg mm}^{-2}$ and $2650 \pm 100 \text{ kg mm}^{-2}$ respectively but not determined in this research work. Stewart et al. [13] found that W_2C formed on splat quenching and was caused by dissolution of WC in the Co matrix. Bouaricha et al. [14] reported that microhardness would be closely related to a coatings porosity level and degradation of the carbide phase during spraying. Several secondary phases appear in the as-sprayed coating despite the absence of any phases in the starting material [13,15]. There was no relationship between the degree of decarburization and the melting point of the substrate.

It is expected that the hardness would decrease with increasing grain size, but this was not conclusive with the small amount of data and high scatter. However, hardness decreased with increasing porosity as expected. The microhardness increased with increasing coefficient of thermal expansion. Thus, hardness depends on microstructural features such as the level of porosity and residual stresses resulting from the coating technique. The porosities were below 0.7%, similar to the work of Zhao et al. [16]. The variations in porosity across the different coatings might be as a result of fuel gas flow during coating preparation, as observed by Arturas [17] since the substrates were different materials. The experimental results show that the residual stresses were quite different. There was a large variation in the residual stresses with large errors, and these did not appear to be related to the coating hardness, nor to the difference between the coating and substrate hardness or surface roughness.

No relationship could be seen with melting point and residual stress. Similarly, no relationship was seen between coefficient of thermal expansion and residual stress, perhaps because the scatter was too high. With increasing specific heat capacity, there is a plateau of residual stress around -150MPa, which was reached between 0.4-0.5 heat capacity. However, there are only four data points. The processing parameters could also have an effect [17,18]. The surface roughnesses are expected to be good due to grit blasting the substrate before coating. No relationship could be seen between coating micro hardness and surface roughness.

The differences observed in the coating results such as size of WC grains, roughness, hardness, and new phases occur despite using same powder as a feedstock is due to: Influence of substrate on coating, the properties of each substrates which plays a crucial role in cooling

effect of the samples after deposition of coating. Thus enhance the properties of the coatings. Its contribution in adhesion of the coating is observed. Coating techniques and substrate influence might influences the occurrence of the secondary phases appear in the as-sprayed coating

5. Conclusion

The structure of WC-Co coatings sprayed by HVOF on different substrates gave different properties, despite using the same powder (WC-4.88 wt%Co) as feedstock. The occurrence of W_2C and W_3C phases after coating could not be explained due to the substrate as the decarburization occurred at the lowest and the highest temperatures. However, since the coating procedures on the samples had not been optimized, there might be too many variables. The specific heat capacity of the substrate appears to have the strongest effect.

Acknowledgements

The authors wish to acknowledge the support of NECSA, DST/NRF Centre of Excellence in Strong Materials and the University of the Witwatersrand.

References

- [1] de Villiers Lovelock H.L., Richter P.W., et al, (1998). Journal of thermal spray technology,7: 97-107.
- [2] Karimi A, Verdon C.H., Martin J.L., et al, (1995). Wear, 186-187: 480-486.
- [3] Shipway, P.H. et al, (2005). Wear, 259, 820.
- [4] Dalmas, D. et al, (2003). Surface and Coatings Technology 173,130.
- [5] Schwetzke R. and Kreye H. (1998). Proceedings of the 15th international thermal spray conference, Nice, France, pp 187-192.
- [6] Li C.J., Ohmori A., Harada Y. (1996). Journal of Materials Science, 31: 785-794.
- [7] Schwetzke R., Kreye H. (1999). Journal of thermal spray technology, 8, 433-438.
- [8] Skandan G., Yao R., Rear B.H., et al. (2001) Scripta Materialia, 44: 1699-1702.
- [9] Kreye H., Heinrich P. and Loewe G. (1998). Proceedings of the international symposium on Advanced Thermal spraying Technology and allied coatings, Osaka, Japan. High Temperature Society, 73-78.
- [10] Dalman D., et al. (2003). Surface and coating Technology 173, 130.
- [11] Santana Y.Y. et al, (2008). Surface Coating Technology, 202 4560-4565.
- [12] Di Maio D. and Roberts S.G (2005) philosophical magazine 85:1, 33-43
- [13] Stewart D.A., Shipway P.H. and Mc Cartney D.G. (2000). Acta Mater. 48:1593-604.
- [14] Bouaricha S. and Marple B. (2004). Proceedings of the International Thermal Spray Conference, ISBN 3-87155-792-7.
- [15] Celik E. et.al (2006). Surface and Coating Technology. 200:4320-8.
- [16] Zhao L. et.al (2004). Wear; 257:41-6.
- [17] Arturas B. (2005). Material Science, 11,105-109.
- [18] Martin W., Daniel L. and Rainer G., (2006). Surface and Coatings Technology 1995-2001.

Study of interactive stresses in thin WC-Co coating of thick mild steel substrate using high-precision neutron diffraction

Andrew M Venter^{1,2,a}, Vladimir Luzin^{3,b}, O Philip Oladijo^{2,c}, Lesley A Cornish^{2,d} and Natasha Sacks^{2,e}

¹Research and Development Division, Necsa Limited, Pretoria, South Africa

²DST/NRF Centre of Excellence in Strong Materials, University of the Witwatersrand, South Africa

³Bragg Institute, ANSTO, Australia

^aAndrew.Venter@necsa.co.za, ^bVil@ansto.gov.au, ^cseyiphipil@gmail.com,

^dLesley.Cornish@wits.ac.za, ^eNatasha.Sacks@wits.ac.za

Keywords: Residual stresses, WC-Co coatings, Neutron diffraction, High-velocity oxygen-fuel

Abstract. Investigations of interaction residual stresses between thin WC-Co surface coated layers on thick mild steel substrates have successfully been performed with neutron diffraction. This systematic approach was conducted on the reference grit-blasted substrates and their HVOF coated WC-Co products. Using a sub-millimeter gauge volume, precisely positioned, the stress gradient through the coated and non-coated substrates were determined and used to derive the coating stress condition prevailing in the thin coating by applying the stress balance (Stoney) approach. In addition, the average stress in each 200 μm thick coating was measured directly with very good agreement obtained between the calculated and measured stress values. Investigations were extended to determine the thermal nature of the residual stresses by studying the annealed counterpart samples as well to follow the evolution of the residual stress upon annealing.

Introduction

WC-Co cemented (WC) metal matrix (Co) composite have important mechanical properties owing to their high toughness [1], high wear resistance [2], and very large thermal residual stresses in the as-produced state [3]. Thermal sprayed coatings of these cemented carbides are widely used in industrial applications to offer protection of base materials against environmental loads including high temperature, hot gas corrosion, etc. Likewise the purpose of a coating design often is to improve the properties of the system compared to the pure base material [4]. High Velocity Oxygen Fuel (HVOF) is one of the leading thermal spray techniques [5] for the establishment of such coatings that are strongly bonded to the substrates with minimal temperature and deformation effects. Therefore their characterization is of general interest.

The aim of this study was to investigate in a systematic approach the residual stress conditions prevailing in a system of thin WC-Co coatings on mild steel substrates that has a coefficient of thermal expansion different to that of the coating. The neutron strain scanning investigations were done on the KOWARI neutron strain scanner using a sub millimeter sized gauge volume and paying special attention to gauge volume localisation accuracy and treatment of edge effects. Investigations were extended to the annealed counterpart samples to examine experimentally whether heat-treatment is beneficial for stress relaxation/alteration procedure.

Experimental

Samples for this study comprised WC-17 wt.% Co powder (28% vol. fraction), 15 micron sized, as feedstock for the HVOF coating process. Coatings about 200 μm in thickness were deposited by a TAFA JP5000 HVOF system on mild steel (SABS1431 grade 300WA) substrates. Details of the coatings deposition are discussed elsewhere [1,6].

Microstructure analysis

Influences due to annealing on the microstructures were analysed using scanning electron microscopy (SEM) equipped with energy dispersive X-ray analysis (elemental composition) and secondary electron (BSE) imaging capabilities, macrohardness measured by Vickers indenter (5kg load at a dwell time in 10s), as well as chemical phases identification by X-ray diffraction (XRD) using Cu radiation.

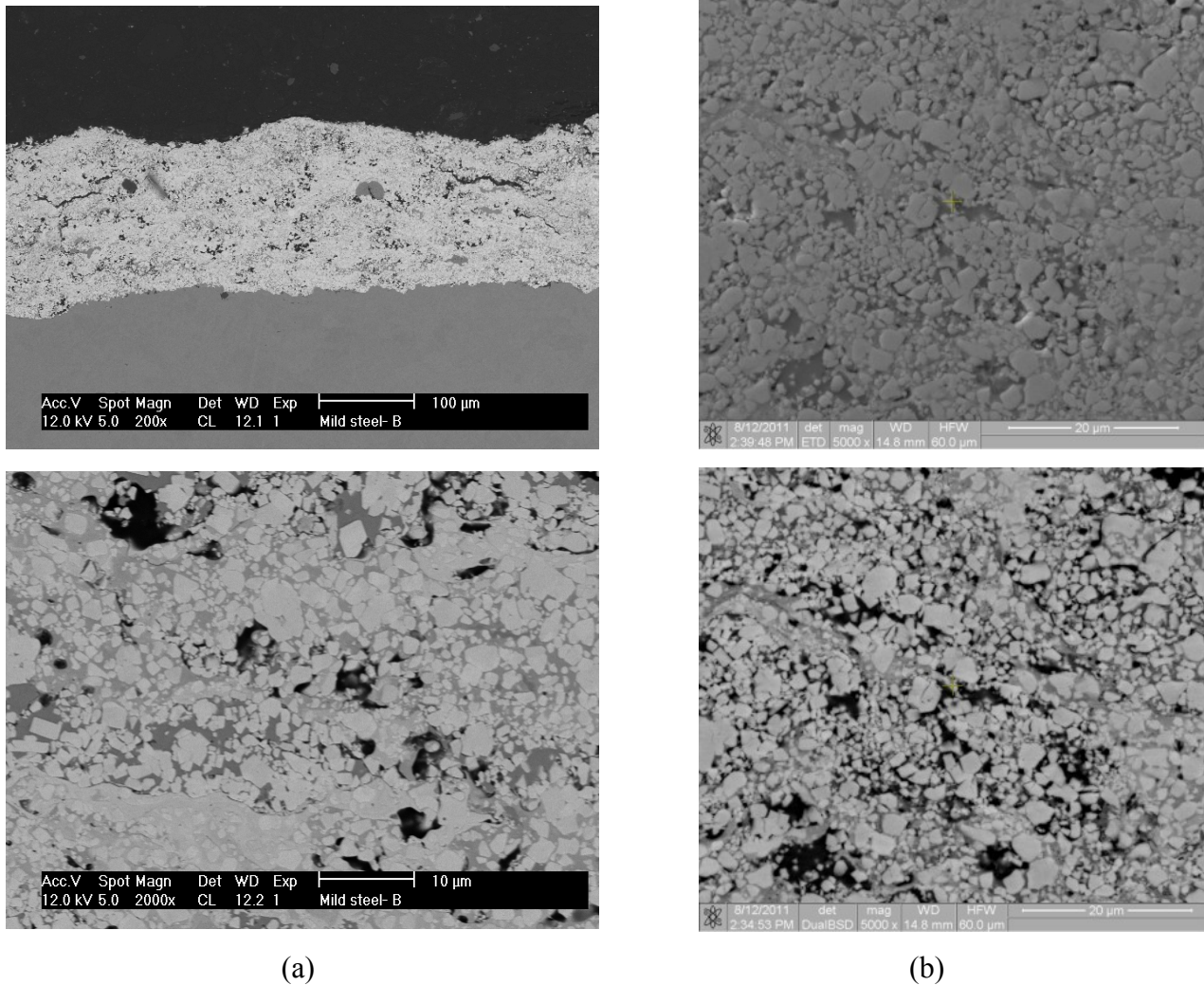


Figure 1. Results from microstructure analyses on mild steel samples: (a) SEM/EDS of coating cross section of as-coated sample; (b) SEM /EDS of sample annealed at 700 °C. The bright fields on the images are WC grains, the dark areas cobalt and the bright gray phase are eta phase of Co. On the annealed sample, Fig.1b, new crystalline and dendritic phases have been formed.

Neutron diffraction stress measurements

Owing to the extremely small coating thickness of 200 μm (in sense of neutron diffraction stress experiment) measurements were done employing a fine through thickness mesh strategy with the aim to obtain the coating stress indirectly, i.e. through stress balance in the coating/substrate system. High accuracy and large amount of data points were essential to compensate for the unfavourable ratio between the thicknesses of the coating (0.2 mm) and the substrate (e.g. 8.3 mm). In addition, an attempt has been made to measure stresses in coatings directly. The two approaches gave a good countercheck on each other.

A sub-millimetre gauge volume was chosen in order to balance different competing factors such as through-thickness spatial resolution (to be able to measure sharp stress distribution from grit blasting, possibly superimposed stress from the substrate production process, and to avoid edge effects [8,9]), statistical uncertainty (to achieve strain accuracy better than 50 μ strain) and total measurement time limited by the length of the experiment. The latter specifically limited the accuracies attainable in the WC coating owing to the relatively large neutron attenuation of steel.

The residual stresses measurements have been carried out using the neutron stress diffractometer Kowari (ANSTO, Australia). The measurements were done in individual through-thickness locations covering the entire sample thickness, forming a line profile with 0.3 mm spacing between points. In locations close to the surface (where high stress gradient was expected due to peening from grit blasting) extra points were measured. In order to optimise localisation of the gauge volume, the take-off angle $2\theta_M$ of the Si (400) monochromator was varied to maintain a close to 90° measurement geometry. Instrument settings for reflections measured in the samples are summarised in Table 1.

Table 1: Instrument settings and material constants for the reflections measured

Reflection	$2\theta_M$	λ , Å	$2\theta_B$	Gauge volume (actual), mm	Sample thickness, mm	S_1 , TPa ⁻¹	$\frac{1}{2}S_2$, TPa ⁻¹
Fe (211)	76.0°	1.67	91.3°	0.3x0.3x15	8.3	-1.26	5.72
WC (112)	64.0°	1.44	90.0°	0.3x0.3x15	0.2		1.65
WC (211)	67.0°	1.50	92.1°	0.4x0.4x15	0.2		1.82

At each location, d-spacings were measured along the principle directions, in-plane and normal to the surface. The balanced biaxial plane stress assumption was used to recalculate stresses from the measured d-spacings and the diffraction elastic constants (calculated using the self-consistent method of Kröner [7]) for the stress conversions reported in Table 1.

To separate stresses originating from the spray process from pre-existing residual stresses (e.g. from cold rolling of the substrates and/or grit blasting process), neutron stress measurements were done on the uncoated pair substrate samples. They were treated as separate samples and measured using the same procedure. The crucial part of the measurements was high positioning accuracy to enable combining multiple data sets taken from different samples and directions. Position accuracy of 0.01 mm was maintained throughout all measurements. For measurements in substrate materials that was sufficient to ensure that positioning errors are smaller than the counting statistical errors, but for stress measurements in 0.2 mm WC coating, under conditions of partial illumination, the positioning error was larger reaching value of ~100 μ strains. In this case, it was included in the analysis as a significant part of the reported total errors.

Results and discussion

Microstructural analyses

Comparison of the as-sprayed and annealed coated samples shows that new phases has been produced in the previous amorphous area and that WC grains have been partly dissolved and mixed with the cobalt matrix to produce new crystalline and dendritic phases. Heat treatment also decreased the macrohardness of the coating. Likewise, decreased grain size and increase in porosity in the annealed microstructural properties compared to as-coated are observed.

Neutron diffraction stress analysis

Results of the stress profiles measured in the mild steel substrate series are shown in Fig. 2 as a comparison between the residual stress distributions observed from the as-coated and substrate-only samples, respectively for as-coated and annealed counterpart series. The differences between each set of profiles yield the stress purely due to the elastic effect from the WC coating. It appears in Fig. 2b as a change in slope of the stress profile, while in Fig. 2a this change is small and almost invisible. Formal data analysis results of the differential stress distributions (differences between coated samples and substrate-only samples) are given in Fig. 3 for both conditions investigated. For the as-sprayed sample, stress in the substrate is very small and the predicted stress value in the coating derived from stress balance condition is estimated at -36 ± 118 MPa. Relatively large errors result from the lever rule applied and error propagation, so that ratio between the error in coating (~ 118 MPa) and an individual error in substrate (~ 10 MPa) are related by a factor $t_{subs}/t_{coat}/\sqrt{N_{subs}}$, where N_{subs} is the number of measurement points taken in the substrate. Thus, with the given thickness ratio, significant accuracy improvement can be achieved by measuring more points or/and with better accuracy. Although uncertainty of ~ 100 MPa might be seen to be large, for the annealed sample it can be considered as acceptable with stress value in coating -340 ± 80 MPa. This unambiguously demonstrates that a substantially larger compressive residual stress develops after thermal treatment.

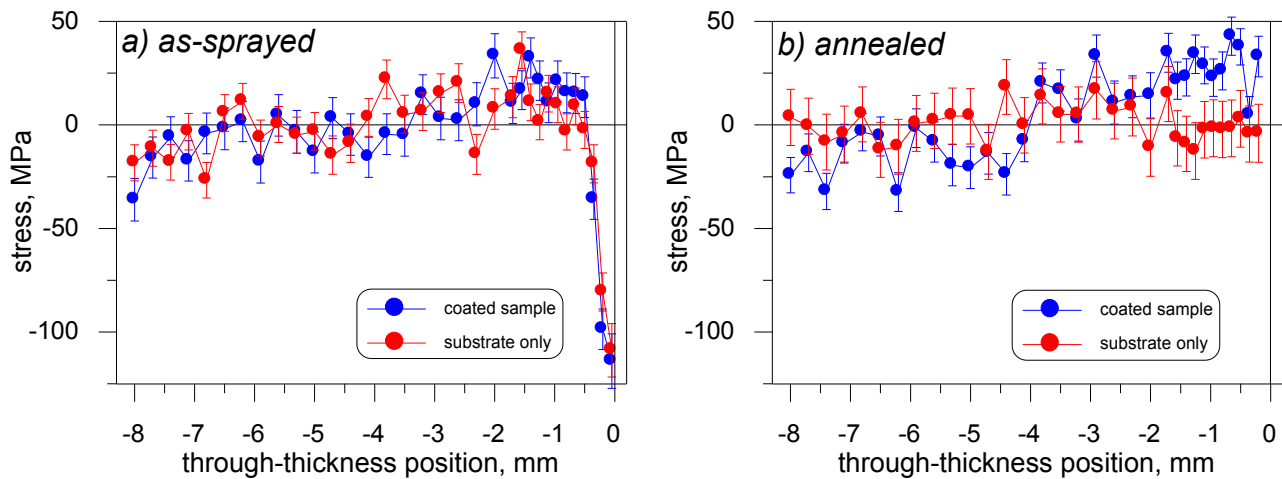


Figure 2. Experimentally measured through-thickness stress profiles for steel samples in a) as-sprayed and b) annealed conditions. Profiles measured in substrate only samples are also shown.

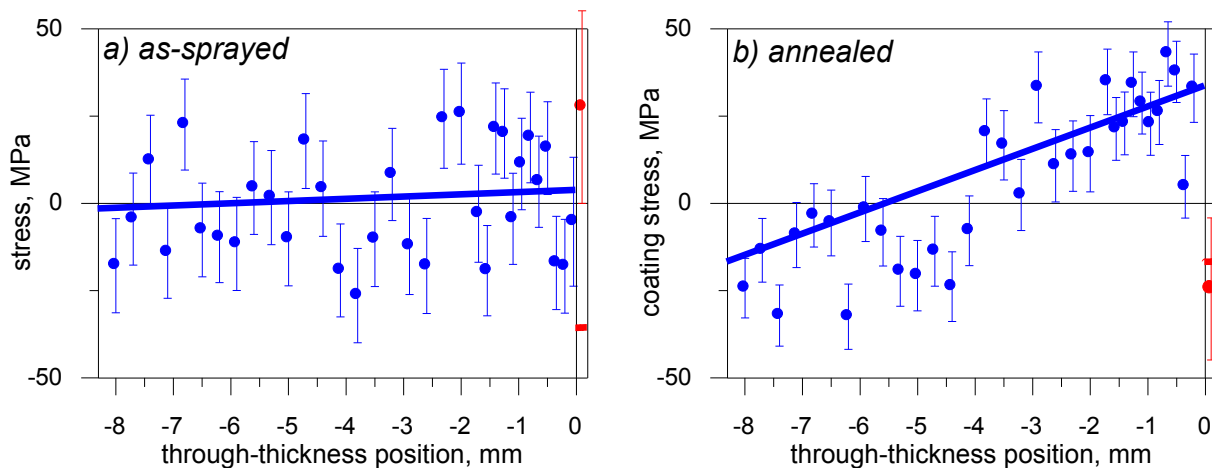


Figure 3. Experimentally determined through-thickness stress profiles for steel samples in a) as-sprayed and b) annealed conditions and model fit of the experimental data.

Table 2: Comparison of residual stresses in WC coatings determined under different thermal conditions, i.e. experimentally measured directly and predicted from stress balance using the measured through thickness stress profiles in the substrates.

Substrate/Condition	stress, MPa, experiment	stress, MPa prediction	stress, MPa average
Steel / as-sprayed	28 ± 334	-35 ± 41	-34 ± 41
Steel / annealed	-490 ± 407	-340 ± 29	-341 ± 29

For the as-sprayed WC coatings on steel substrates, the stress in the coating is moderately compressive. This demonstrates dominance of the peening mechanism of stress formation over thermal quenching stress. After heat treatment, the stresses reach almost ten times larger values.

With heat-treatment, the initial stress distribution with characteristic peening stress in the substrate disappears. The newly formed stress is thermal and originates from the fact that CTE of the metal substrate ($\alpha(\text{steel}) \sim 12 \cdot 10^{-6} \text{ K}^{-1}$) is larger than CTE of the WC coating ($\alpha(\text{WC}) \sim 2 \cdot 10^{-6} \text{ K}^{-1}$) which generates compressive stress in the coating when the system is cooled from the stress-relieve annealing temperature.

Conclusions

The coating/substrate systems in as-coated and annealed conditions were assessed using microscopy, hardness measurements x-ray diffraction analysis and residual stress neutron diffraction. Remarkably, stress in the 200 μm thick coating were measured directly, though with low accuracy, and derived indirectly, utilizing stress balance principle and by measuring the stress profiles in substrate with great care. The later approach allowed achievement of accuracies of 30-50 MPa. The peening nature of the stress in coatings in as-sprayed conditions has been confirmed and thermal origin of the residual stresses after annealing was demonstrated.

Acknowledgements

The authors acknowledge support from Necsa, DST/NRF Centre of Excellence in Strong Materials, University of the Witwatersrand, as well as the Bragg Institute for beam time awarded on the KOWARI instrument, and the support provided during the investigations.

References

- [1] O.P. Oladijo, A.M. Venter, L.A. Cornish, N. Sacks and S. Shrivastava, PM2010 Powder Metallurgy World Congress Proc. 3 (66) (2010) 1-8.
- [2] H. Liao, B. Normand, C. Coddet, Surf. Coat. Technol., 124 (2000) 235-242.
- [3] Krawitz, D.G. Reichel, R. Hitterman, Mater. Sci. Eng. A119 (1989) 127-134.
- [4] T. Keller, N. Margadant, T. Pirling, M.J. Riegert-Escribano, W. Wagner, Mater. Sci. Eng. A 373 (2004) 33-34.
- [5] J. Stokes, L. Looney, Surf. Coat. Technol., 148 (2001) 18-24.
- [6] S. Luyckx, C.N. Machio, Int. J. of Refract., Metals & Hard Materials 25 (2007) 11-15.
- [7] E. Kroner, Zeitschrift fur Physic A Hadrons and Nuclei 151 (1958) 504-518.
- [8] Spooner S and Wang X L, J. Appl. Cryst. 30 (1997) 449.
- [9] Bruno G et al. Nucl. Instr. Meth. in Phys. Res. B 246 (2010) 425.

Characterisation of the residual stresses in HVOF WC-Co coatings and substrates

Andrew M. Venter^{1,2, a}, O. Philip Oladijo^{2,3,b}, Lesley A. Cornish^{2,3,b} and Natasha Sacks^{2,3,b}

¹Research and Development Department, Necsa Limited, Pretoria, South Africa

²DST/NRF Centre of Excellence in Strong Materials, South Africa

³School of Chemical & Metallurgical Engineering, University of the Witwatersrand, South Africa

^aAndrew.Venter@necsa.co.za, ^bseyiphilip@gmail.com,

^cLesley.Cornish@wits.ac.za, ^dNatasha.Sacks@wits.ac.za

Keywords: HVOF coated substrates, WC-Co coatings, depth resolved strain/stress, eigenstrain.

Abstract. Residual strains and stresses associated with the processing steps of the industrial high-velocity oxygen-fuel (HVOF) thermal spray technique, were non-destructively characterised in both the coatings and substrates. A range of substrates, having coefficients of thermal expansion different from that of the as-coated WC-Co material, were considered to assess the potential role of the thermal misfit associated with the coating procedure. Surface and depth resolved studies of the in-plane and normal components of residual strains have been investigated by exploiting the penetrating capabilities of high energy synchrotron X-rays in conjunction with micron sized gauge volumes to enable strain gradient determination in the combined systems with high positional resolution. Results revealed large residual strain/stress mismatches at the interface region in all the substrate materials, whereas the strains/stresses in the coating material were small, seemingly independent of the substrate material. The different HVOF process contributions were qualitatively assessed in terms of an eigenstrains (plastic deformation) approach.

Introduction

Tungsten carbides (WC), traditionally classified as hardmetals, are widely used in many industries owing to their beneficial combination of functional properties. In addition to their high strength, toughness and hardness, they offer favourably high wear resistance, and can act as thermal and/or chemical barriers. Cemented carbide coatings, such as WC-Co, can provide hardness and wear resistance similar to that of solid sintered carbide components. Thus, coated cemented carbides of suitable substrate materials can potentially substitute bulk WC systems in many applications, and in doing so, alleviate the substantial over demand and competitive supply of bulk WC. In industry, substrates are routinely coated using the high-velocity oxygen-fuel (HVOF) flame spray process for thermal and chemical barriers. Such coatings are formed by the impact of molten fine powders directed at supersonic speeds onto substrate materials with a spray gun applicator. The adhesion mechanism is subsequently kinetic energy driven rather than thermal energy. The latter is limited to the contribution of each individual splat. Subsequent minimal heating of the substrates occurs.

We explore here the possible role that differences in CTE between the substrates and as-deposited coating can potentially contribute to the establishment of beneficial interactive residual stresses in the combined system that could enable utilisation of HVOF coated substrates in wear applications. The results reported here pertain to the systematic non-destructive characterization of the residual stresses associated with the HVOF process in the different substrate systems, followed from the as-received parent material to the final as-coated systems, i.e. in both the substrates and coatings, since they form an interactive system.

Experimental

Substrates have been selected with coefficients of thermal expansion (CTE) covering a range of values with respect to that of the WC-17Co powder (28% volume fraction, 15 micron particle size) as summarized in Table 1. The selected substrate materials, in order of decreasing CTEs, were 2000 series aluminium, brass, 304L stainless steel, 300WA mild steel and super invar.

Extensive characterisation investigations on the samples and coatings were done to determine the microstructural properties, hardness and chemical phase contents [1-4]. All coatings were found to be fine grained (smaller than 0.17 micrometers), had less than 1% porosity and with the coatings being primarily WC with a small amorphous content, ascribed to being metallic Co. No chemical phase changes were observed from the cold working process associated with the grit-blast surface preparation treatment on any of the substrates. It is thus concluded that the chemical contents of the as-coated coating were independent of the CTE differences between the WC-Co and the different substrates of this investigation.

Residual stress investigations of the sample sets were done with X-ray diffraction, XRD, (Co radiation giving 7 keV energy on a Bruker D8 Discover instrument equipped with an area detector) and high energy (>80 keV) synchrotron radiation, SR, (ID15A beam line at the European Synchrotron Radiation Facility, France). With these techniques, the XRD results give the residual stresses limited to a depth of 3 micrometers from the surface, with the SR results enabling depth profiling through the coating and substrates, albeit for a thinned sample geometry. Fig. 1 shows a schematic diagram of the sample selection from larger original plates and treatments routes [1]. Each substrate set comprised the as-received parent material, the grit-blast surface prepared sample and the as-coated sample. Coating thicknesses were in the order of 200 micrometers throughout, with the substrates taken to be at least 6 mm thick, so as not to be deformed by the stresses associated by the coating. Attempts to produce thicker coatings lead to delamination effects. A key material preparation step in the HVOF coating process is the grit-blast of the parent substrate material to roughen the surface for improved adhesion.

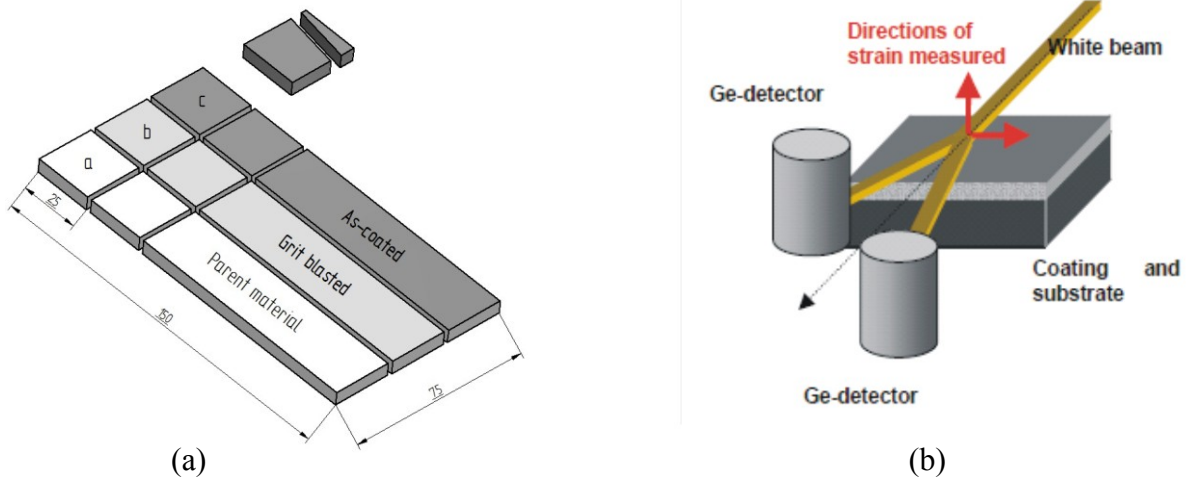


Fig. 1: Schematic of the sample selection and treatment is shown in (a). The XRD investigations were done on the samples labeled a, b and c, while the SR radiation, utilised for the depth resolved studies, were done on the thinned edge samples shown towards the top right. This latter geometry enabled in-situ beam pathlength optimization through the tough-to-penetrate WC. Measurements were done in transmission geometry through the sample thickness as shown in (b) at a beam pathlength choice of 2.5 mm. This rendered a coating geometry at least an order of magnitude thicker than the coating to limit stress relaxation during the sample cutting (electrical charge machining). For the SR investigations, the instrument was equipped with two detectors with 10° offset respectively from the primary beam in the horizontal and vertical planes, which rendered the in-plane and surface normal components of strain. [1].

Results

Gauge sizes employed were 0.8 mm diameter for the XRD and $0.03 \times 0.06 \text{ mm}^2$ (through thickness depth \times in-plane width) for the SR measurements. Instrument calibration was performed with an iron powder reference. Coincidence between the sample surface and the primary beam was established with surface entry scans [1] to an estimated accuracy of $\pm 0.03 \text{ mm}$.

Lattice strains were determined from the measured lattice plane spacings d_{hkl} with reference to the strain free lattice plane spacing d_{hkl}^0 of the as-received parent material in the case of the substrates and WC chipped flakes as reference for the coatings.

$$\varepsilon = \frac{d_{hkl} - d_{hkl}^0}{d_{hkl}^0}$$

As an example of the typical SR results attained with all the investigations on the coated systems of this study, we specifically report the strain results on the 304L stainless steel sample set as a case study in Fig. 2. The depth resolved results for both the in-plane and normal components of strain are shown. Notwithstanding each measurement point having an individual accuracy of better than 20 microstrain, the anomalous scatter between data points was attributed to the smallness of the gauge volume employed which is susceptible to grain size, systematic errors and orientation effects [5]. The scatter was retained and reported for completeness. The stress in the as-received parent material in essence remained constant throughout the sample thickness within the systematic scatter observed. The grit-blasted substrate had substantially altered residual strains at the surface in both strain components. In the WC coating, both components of strain were unusually small, taking cognizance of the large discontinuity at the interface. The magnitude and depth dependence of the overall strain field in the as-coated substrate was very similar to that of the grit-blasted substrate.

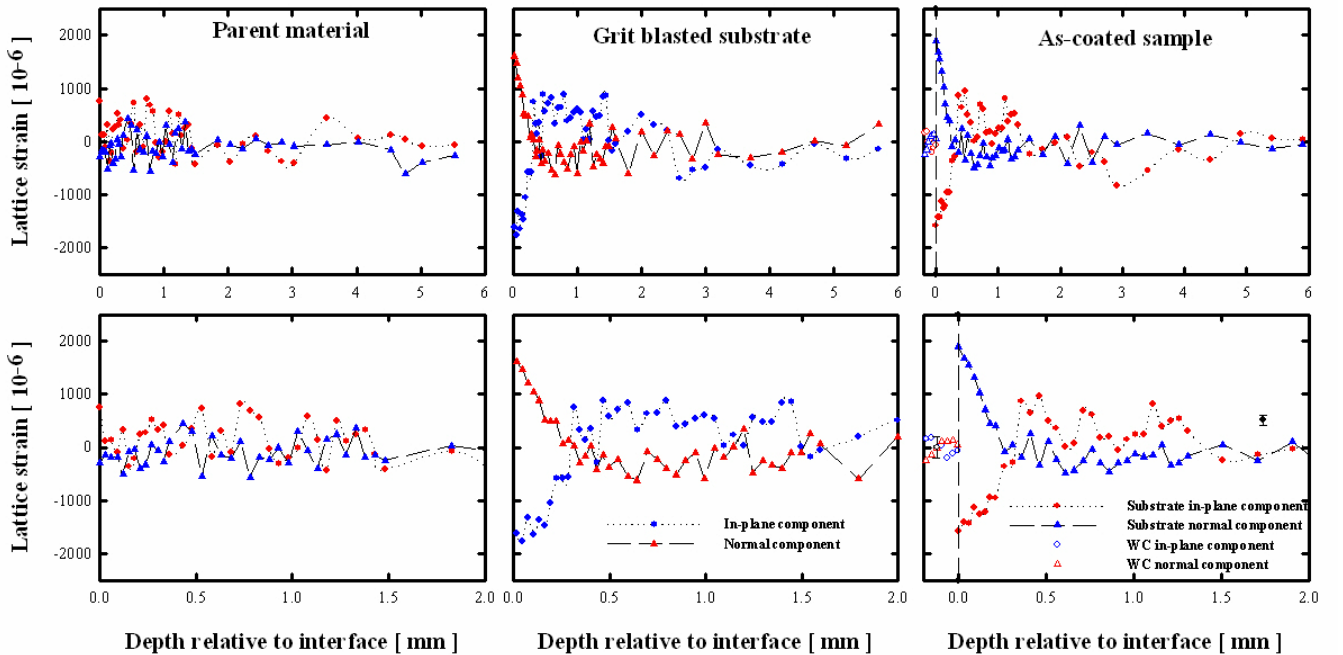


Fig. 2: Residual strain depth dependence determined from the austenite (311) reflection in the 304L stainless steel substrate and (101) WC Bragg peaks as measured by SR. Results are for the as-received parent material (left set), the grit-blast substrate (centre set) and HVOF as-coated sample (right set). The substrate coating interface is at 0 mm. The bottom set of figures show an enlarged view of the results at the near surface regions. The error bar indicates the systematic error associated with the measurements. The lines though the symbols are guides to the eye. Legend: ●, substrate in-plane component; ▲, substrate normal component; ○, WC in-plane component; △, WC normal component.

For a bi-axial stress condition, a reasonable assumption for coatings thinner than 2 mm, is that the stress normal to the surface σ_{\perp} is zero, from which the in-plane stress ($\sigma_{//}$) component can then determined from:

$$\sigma_{//} = \frac{1}{\frac{1}{2}S_2(hkl)} \left(\frac{d_{//} - d_{\perp}}{d_{\perp}} \right)$$

where $S_2(hkl)$ is the corresponding diffraction elastic constant for the material, $d_{//}$ and d_{\perp} respectively are the in-plane and normal components of the lattice plane spacing at the corresponding depth positions. Table 1 summarises the diffraction elastic constants (DEC) used in the determination of the stress values.

Fig. 3 shows the in-plane component of residual stress determined for the 304L stainless sample set. In the as-received parent material, the stresses were in essence constant throughout the sample thickness, apart from the systematic scatter. In the grit-blasted sample, large compressive stresses existed at the near surface region owing to the localized plastic deformation associated with the surface roughening step. In the as-coated sample, the stress values are not significantly different from those of the grit-blast sample. The systematic approach followed with this investigation revealed that the primary origin for the substantial compressive stress in the near surface regions in HVOF coated systems were primarily due to the grit-blast surface treatment, with minimal apparent contribution specifically from the coating step. The stress in the WC coating did show some depth dependence, although it could not be unambiguously quantified, due to the overall systematic scatter in the data. Order of magnitude correlation was observed between the average residual stress determined in the coating and that measured at the near surface region with XRD, as summarized in Table 1.

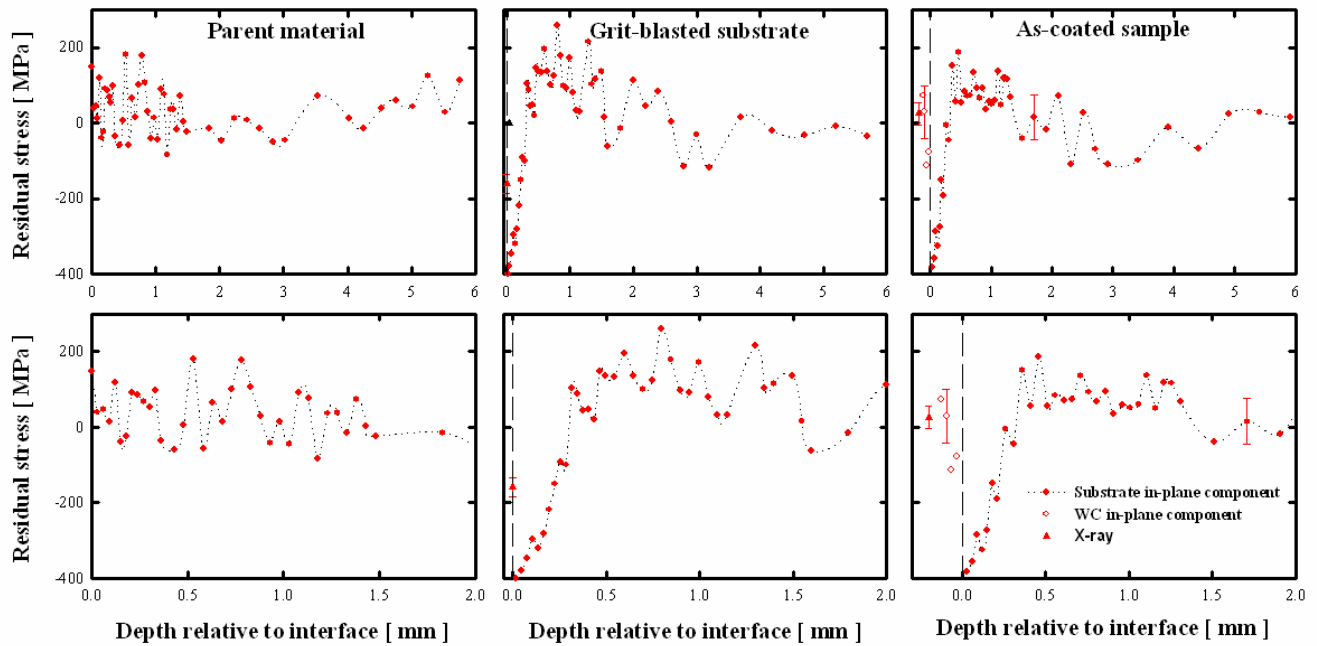


Fig. 3: In-plane residual stress depth dependence determined from the lattice strain results of the (311) austenite peak and (101) WC Bragg peaks measured with SR. Results are for the parent material reference state (left set), the grit-blast substrate (centre set) and HVOF as-coated sample (right set). The near surface residual stress of the WC determined with laboratory X-rays (Co radiation) is also indicated [1,2]. The substrate coating interface is at 0 mm. The bottom figures show enlarged views of the results at the near surface region. The error bars indicate the systematic error associated with the measurements. The lines through the symbols are guides to the eye. Legend: ●, substrate in-plane stress; ○, WC in-plane stress; ▲, WC near surface stress (laboratory X -rays).

Table 1 summarises the residual stress results for all the samples of this study as determined from XRD and SR.

The low value of the stresses in the coatings of all the substrates was ascribed to the occurrence of localized microcracking, perpendicular to the surfaces, associated with the molten spray splats being quickly quenched on impact by the cold substrate, which constrained the thermal contraction of the splats, resulting in tensile stresses in the splats, that due to the brittle nature of the cermets, exceeded the braking strength of the material, leading to relaxation through microstructural cracks [4]. Notwithstanding the resulting stress relaxation, the integrity of the coatings was not jeopardized. Cracks parallel to the surfaces would be most detrimental, as they can lead to delamination.

Table 1: Summary of materials and residual stress values determined in the substrates and HVOF coatings.

Material	CTE [10 ⁻⁶ /K]	Reflection	DEC [TPa ⁻¹]		Residual stress in grit- blast substrates [MPa]		Residual stress in as- coated coatings [MPa]	
			S ₁	½S ₂	XRD	SR	XRD	SR
WC WC-17Co	2	WC (101)	-0.321	1.707	----	----	----	----
Aluminium	23	Al (311)	-5.05	19.462	-160 ± 10	-200 ± 25	-15.7 ± 17	-160 ± 50
Brass Cu63/Zn37	19	Cu (311)	-2.902	11.106	-123 ± 10	-303 ± 25	-53.5 ± 28	-40 ± 25
304L Stainless steel Fe/Cr29/Ni16/C6	17	Fe (311)	-1.598	7.034	-159 ± 36	-458 ± 25	24.6 ± 19	22 ± 50
Mild steel SABS1431 grade 300WA	12	Fe (211)	-1.26	5.72	-172 ± 23	-441 ± 25	30.5 ± 19	60 ± 50
Super invar Fe64 / Ni 36	≤ 1	Ni (200)	-1.910	7.539	-251 ± 10	-695 ± 25	74 ± 31	288 ± 25

To quantify the different contributions associated with the two dominant processing steps, the plastic depth strain profiles (eigenstrains) [6] were considered in Fig. 4 for a number of samples of this study. The eigenstrain approach is a sensitive parameter, since the strain profiles in the samples contains the elastic strains constrained by the plastic deformation, especially near the grit-blast and coated surfaces. Inherent to our systematic approach, the eigenstrain for each process contribution was individually determinable by subtracting the measured through thickness residual elastic strain profiles in the as-received parent material from each of these samples. The curves of Fig. 4 show the plastic strain (eigenstrain) profiles associated with the different processing steps for four of the substrates.

Summary

The non-destructive and systematic approach followed with this investigation has enabled the isolation of each of the processing step contributions to the residual strains and stresses in coated substrates having a range of CTEs different the WC-Co coatings. It is concluded that the grit-blasting process primarily induced compressive stresses at the surfaces, whilst the as-coated stresses in the coatings were independent of the CTEs. The smallness of the residual stresses in the WC-Co coatings was ascribed to the formation of localized perpendicular micro cracks.

Acknowledgements

The authors acknowledge support from Necsa and the National Research Foundation (South Africa) and Department of Science and Technology (South Africa), as well as the ESRF for the beam time awarded on the ID15A and the assistance provided by T Buslaps and A Steuwer.

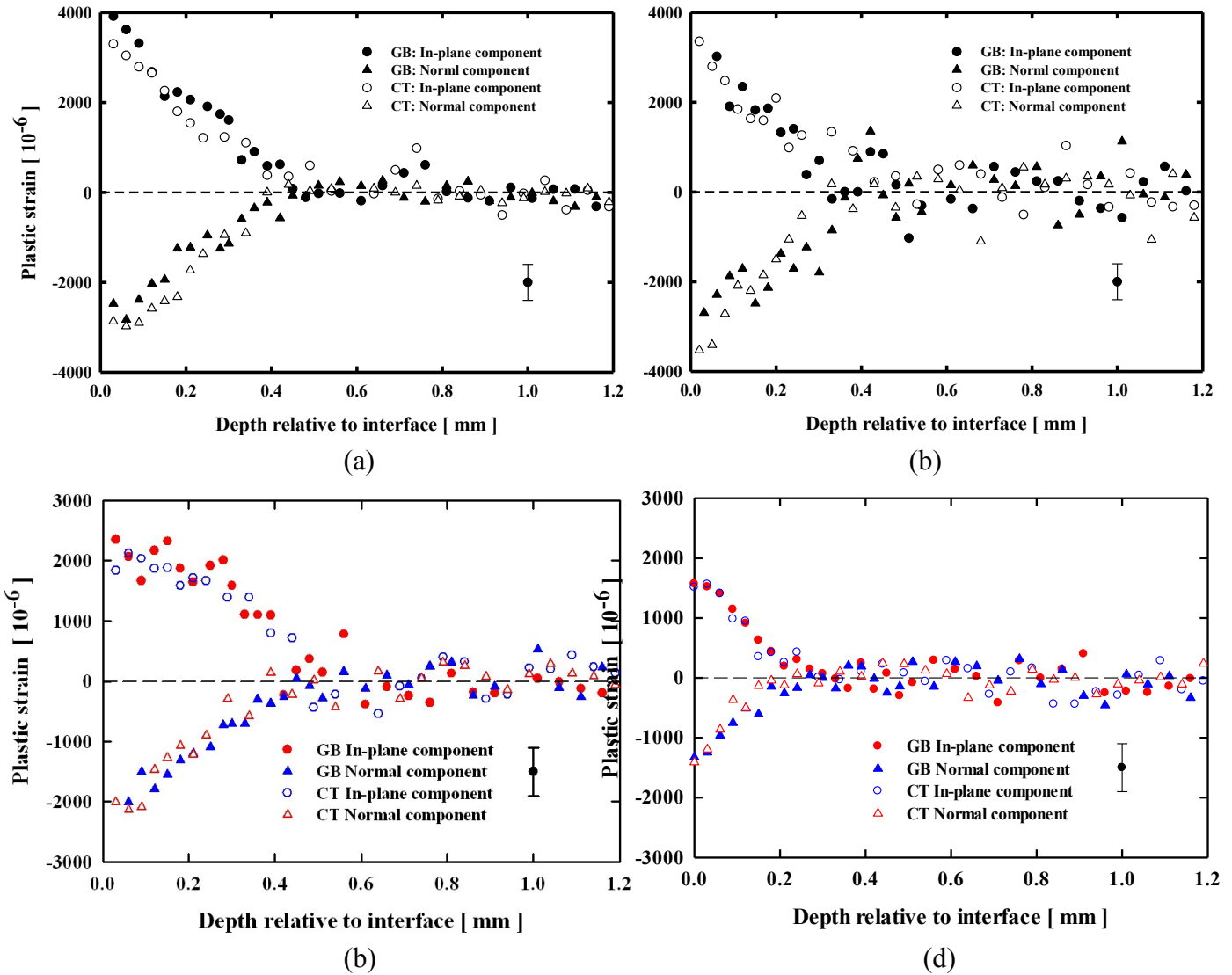


Fig. 4: Plastic strain profiles (eigenstrains) for (a) brass; (b) super invar; (c) stainless steel; (d) mild steel determined from strain results of the depth resolved X-ray synchrotron investigations. Legend: ●, grit blast in-plane component; ▲, grit blast normal component; ○, as-coated in-plane component; △, as-coated normal component.

References

- [1] Venter AM, Pirling T, Buslaps T, Oladijo OP, Steuwer A, Ntsoane TP, et al, Systematic investigation of residual strains associated with WC-Co coatings thermal sprayed onto metal substrates. *Surf. Coat. Technol.* 206 (2012) 4011–4020.
- [2] Oladijo OP, Venter AM, Cornish LA, Sacks N. *PM2010 Powder Metallurgy World Congress Proceedings*, Florence, Italy, 3(66) (2010) 1–8.
- [3] Oladijo OP, Venter AM, Cornish LA, Sacks N, X-ray diffraction measurement of residual

- stresses in WC-Co thermally sprayed coatings onto metal substrates, *Surf. Coat. Technol.* 206 (2012) 4725–4729.
- [4] Oladijo OP, Sacks N, Cornish LA, Venter AM, *Int. J. of Refractory Metals and Hard Materials* 35 (2012) 288–294
- [5] Steuwer A, Santisteban JR, Turski M, Withers PJ, Buslaps T, *J. Appl. Cryst.* 37 (2004) 883-889.
- [6] Zhang SY, Venter AM, Vorster WJJ, Korsunsky AM, *J. Strain Analysis* **43** (2008) 229-241.

Residual stress in WC-Co coated systems studied by high resolution neutron diffraction

Vladimir Luzin¹, Andrew M. Venter^{2,3}, O. Philip Oladipo^{3,4}, Lesley Cornish^{3,4}, Natasha Sacks^{3,4}

¹ Bragg Institute, Australian Nuclear Science and Technology Organisation, Lucas Heights NSW 2234, Australia

² Research and Development Division, Necsa Limited, Pretoria, South Africa

³ DST/NRF Centre of Excellence in Strong Materials, University of the Witwatersrand, South Africa

⁴ School of Chemical and Metallurgical Engineering, University of the Witwatersrand, South Africa

A series of thin (200 μm) WC-Co coatings on various thick substrates were made by HVOF spraying. Residual stress in the coated system, occurring due to discrepancy in thermal expansion of substrate and coating material and also peening and thermal relief processes, has been investigated with neutron diffraction using the KOWARI strain scanner at Australian OPAL research reactor. Residual stress profiling has been performed through thickness of the substrates and coating with high resolution in order to study evolution of the residual stress starting from the peening stress near the grit-blasted surface of substrates to stress imposed by HVOF deposition process, to stress after heat-treatment of the samples.

1 Introduction

WC-Co cemented (WC) metal matrix (Co) composite are widely used in industrial applications to protection of base materials against high temperature, hot gas corrosion, etc., due to their high mechanical properties (toughness, high wear resistance). High Velocity Oxygen Fuel (HVOF) is one of the thermal spray techniques [5] that is used for deposition of such coatings. Structural integrity of the coatings (cracking, coating-to-substrate bonding, absence of spalling and distortion effects) can be compromised by very large thermal residual stresses in the as-produced state [3]. Also, some important coating properties (e.g. wear resistance) and performance in service are stress related and require stress mitigation.

The aim of this study was to investigate systematically the residual stresses in a system of thin WC-Co coatings on substrates of different materials sprayed by HVOF. Because the difference between thermal expansion coefficient of the coating and substrate materials can be changed in wide range, the thermally induced stresses are also expected to be different. Investigation involved both as-sprayed coated samples and their annealed counterparts to examine experimentally whether heat-treatment is beneficial for stress relaxation/alteration procedure.

Studying stress WC-Co coatings with x-ray diffraction is problematic because of extremely small penetration depth of only few microns [1] and sensitivity to the surface defects (roughness, oxide films, surface cracks). The neutron diffraction with a sub millimetre spatial resolution was used to investigate residual stress in coatings and substrates through thickness because of higher penetration.

2 Experimental

2.1 Samples

Samples for this study comprised WC-17 wt.% Co powder (28% vol. fraction), 15 micron sized, as feedstock for the HVOF coating process. Coatings about 200 μm in thickness were deposited by an industrial TAFA JP5000 HVOF system on the following substrates

- Brass (Cu63/Zn37), 6.4 mm thick
- Mild steel (SABS1431 grade 300WA), 8.3 mm thick
- Invar (Fe64/Ni36), 6.5 mm thick
- Aluminium (2xxx alloy), 6.2 mm thick

Two sample sets were prepared, as-sprayed series and their counterparts after annealing. Annealing temperature of the

samples was adjusted to the substrate material: 375°C for brass, 700°C for steel, 875°C for invar and 375 for bronze and aluminium. The heat treatment was for 1 hour.

2.2 Coating characterisation

Microstructure and phase transformations due to annealing were analysed using scanning electron microscopy (SEM) equipped with energy dispersive X-ray spectrometer (EDS) and secondary electron (BSE) detector. In addition, crystallographic phase identification was carried out by X-ray diffraction (XRD) using Cu radiation. Macrohardness measured by Vickers indenter (5kg load, 10 sec dwell time).

2.3 Neutron diffraction stress measurements

If X-ray diffraction is not well suited for stress analysis in WC, the neutron diffraction stress measurements with sub-millimetre spatial resolution are also challenging because of limited flux of neutron beams. Coating thickness of 200 μm is extremely small in sense of neutron diffraction stress experiment. Two strategies were employed to resolve stress in the system: (i) a direct measurement of the stress in the WC-Co coating and (ii) an indirect approach using measurements in the substrate together with the stress balance condition in the coating/substrate system to derive stress in the coating. In the second case, high accuracy and large amount of data points (fine through-thickness mesh) were essential to compensate for the unfavourable ratio between the thicknesses of the coating (0.2 mm) and the substrate (e.g. 8.3 mm).

The residual stresses measurements have been performed on the neutron stress scanner Kowari (ANSTO, Australia). A sub-millimetre gauge volume was chosen in order to balance different competing factors such as through-thickness spatial resolution (to resolve sharp stress distribution from grit blasting statistical uncertainty (~ 50 μstrain) and reasonable total measurement time.

The measurements in substrates were done through-thickness, usually with spatial resolution 0.3 mm and with 0.3 mm spacing between mesh points. For coatings, 0.2 mm in size gauge volume was used for stress measurements, which significantly limited the attainable accuracy of stress measurements in the WC coating. To optimise localisation of the gauge volume, the neutron wavelength was adjusted to provide close to $2\theta_M = 90^\circ$ measurement geometry.

At each location, d-spacings were measured along the two principle directions, in-plane and normal to the surface. The balanced biaxial plane stress assumption was used to recalculate stresses from the measured d-spacings.

To separate spray process induced stresses from pre-existing residual stresses (especially from grit blasting process), neutron stress measurements were done on the uncoated pair substrate samples. They were treated as separate samples and measured using the same procedure.

Special attention was paid to gauge volume localisation accuracy (10 μm) and treatment of edge effects. For stress measurements in 0.2 mm WC coating, under conditions of partial illumination, the positioning error was larger (50 μm) resulting in ~ 100 $\mu\text{strains}$ and it was included in the analysis as a significant part of the reported total errors.

3 Results

3.1 Coating properties

Some of the data obtained in sample characterization are reported in the Table:

Substrate material	CTE, $10^{-6}/\text{K}$	Chemical phase content (XRD results)		WC grain size [μm]	
		As-sprayed	Annealed	As-sprayed	Annealed
α -Brass (Cu63/Zn37)	19	WC, Amorphous Co	WC, Co	1.02 ± 0.01	0.63 ± 0.01
Super-Invar (Fe64/Ni36)	1	WC, Co,	WC, Co	0.94 ± 0.01	0.64 ± 0.01
Mild steel	11	WC, Co, $\text{Co}_6\text{W}_6\text{C}$	WC, $\text{Co}_6\text{W}_6\text{C}$, $\text{Co}_3\text{W}_3\text{C}$	1.14 ± 0.01	0.53 ± 0.01
Aluminium	23	WC, Co	WC, Co	0.83 ± 0.01	0.56 ± 0.01

More data and microscopy images can also be found in [2]. The reported data demonstrate complex phase and transformation occurring during annealing process.

3.2 Residual strain/stress

As a result of the data analysis, an example of stress profile (only for Al samples) is shown in Fig. 1.

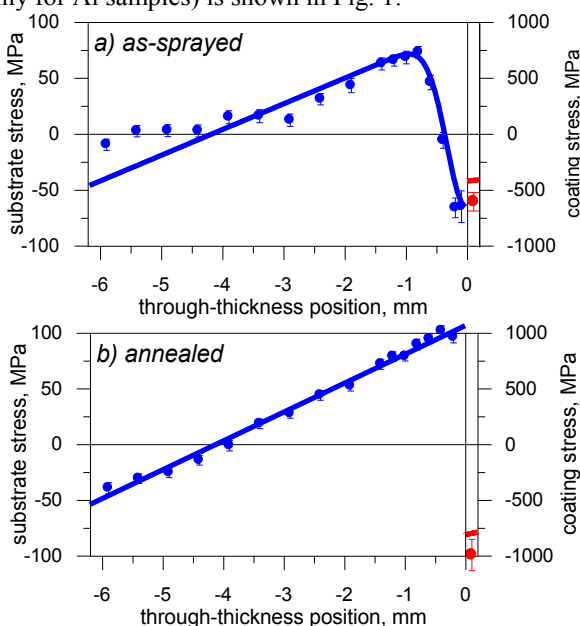


Fig. 1. Through-thickness stress profile in WC coating on aluminium substrate sample in two different conditions.

In the same figure it is demonstrated how fitting to the stress profile in the substrate the stress in the coating is conjoined (solid line) and provides estimated value for the stress in coating in the indirect approach.

In Fig. 2 coating stress values are expressed in terms of strain, so that strain can be correlated with thermal mismatch due to the difference of the thermal expansion of the coating and substrate. Negative sign of strain corresponds to coating compression.

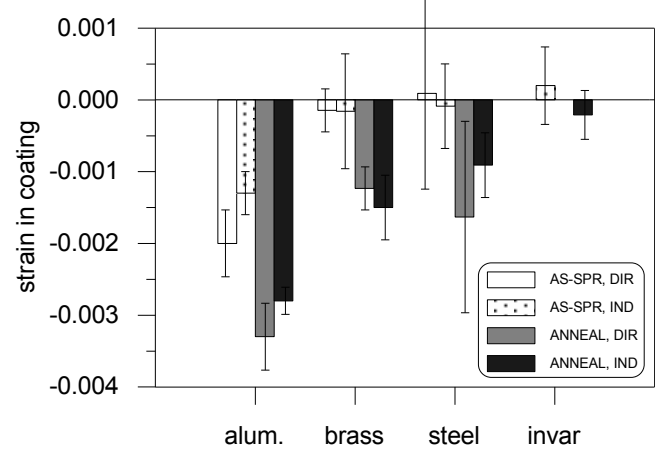


Fig. 2. Strain in samples of different substrate material.

4 Conclusions

Two approaches were tested in order to measure residual stress in 200 μm thick WC coatings on substrates of different materials, 6-8 mm thick, using neutron diffraction. It was shown that in coating materials with high absorption of neutrons (Fe, Ni) the direct measurement of the thin WC coatings is not an optimal strategy because of big losses on neutron beam. (In Ni alloy it was impossible.) In these materials the indirect derivation of the stress in coating through stress/momentum balance condition, when stress profile is accurately measured through thickness, is the best option. For weakly attenuating materials (Al, Cu, Zn) the direct and indirect measurements are almost equally good and provide similar quality results.

A strong correlation between residual elastic strain (stress) and the thermal expansion of the substrate material is observed: the highest strain is observed in aluminium substrate samples ($\text{CTE} = 23 \times 10^{-6} \text{ 1/K}$), while the smallest strain is in the Super-Invar samples ($\text{CTE} = 23 \times 10^{-6} \text{ 1/K}$). This observation suggests the thermal origin of the residual stress in the coating/substrate system and this conclusion is valid for both series of sample, as-sprayed and annealed. The fact that residual stress/strain is larger in the annealed series is most likely due to quenching (solidification of the molten particle) contributing tensile stress into total balance produces less compressive stress for as-sprayed condition. Other factors (e.g. difference in heat dissipation or interplay of several phases and their transformation during HVOF spraying in comparison with annealing process) can also lead to a shift in the stress balance.

5 References

- [1] A. D. Krawitz, Materials Science and Engineering, 75 (1985) 29-36.
- [2] O. P. Oladijo, A. M. Venter, L. A. Cornish, N. Sacks, Surface & Coatings Technology, 206 (2012) 4725-4729.

CHARACTERIZATION OF WC-Co THERMAL SPRAY COATINGS ON DIFFERENT SUBSTRATES

O.P. Oladipo,^{1,2,3} L.A. Cornish,^{1,2} A.M. Venter^{2,3} and N. Sacks^{1,2}

¹ School of Chemical & Metallurgical Engineering, University of the Witwatersrand, Private Bag 3, WITS, 2050

² DST/NRF Centre of Excellence for Strong Materials, University of the Witwatersrand

³ Research & Development Division, NECSA Limited, Pretoria

Thermally sprayed coatings based on tungsten carbide are widely used in industry. Many authors have conducted research on the different types of deposition methods, the effect of powder morphology and spray parameters on microstructure evolution and coating properties¹⁻². However, not all aspects are fully understood. The principal application of these coatings is to resist severe wear associated with mechanisms such as abrasion, adhesion, fretting and erosion. The wear resistance of a coating depends not only on the spray system used, but also on the characteristics of the particular spray powder and substrate. This work is concerned with the effects of different substrates on the thermally sprayed WC-Co coatings.

Two substrates, 304L stainless steel and commercial aluminium, were coated with WC-Co using a High-Velocity Oxygen Fuel system (HVOF). The microstructures of the coatings were characterized by means of optical microscopy (Axion 25), scanning electron microscopy (SEM) (JOEL JSM-840), using backscattered electron imaging with EDX, and X-ray diffraction (XRD). The microhardnesses were determined by the Vickers indentation method.

EDX analysis of the 304L stainless steel sample microstructure shown in Fig. 1 gave identified components of W, Co, C and Al. The presence of aluminium at the interface is thought to originate from the grit blast preparation of the substrate before deposition of the coatings. The XRD results showed the presence of the crystalline WC phase with the (Co) preserved as an amorphous phase. Detection of the latter was slightly compromised as XRD is less sensitive for the detection of cobalt², and so smaller (Co) peaks were observed. The typical layered coating morphology from the superposed layers deposited parallel to the substrate interface was observed in both samples.

EDX analysis of the microstructure of the coating on the aluminium substrate, shown in Fig. 2, indicated the presence of W, Co, and C. The XRD analysis revealed the presence of W₂C in addition to the phases observed in the 304L stainless steel substrate.

Microhardness values measured across the width through cross-sections of the sample coatings and substrates are summarized in Table 1. The difference in the microhardness values between the coatings on the two substrates is due to the presence of porosity and the occurrence of W₂C, and may also be due to residual stresses resulting from the coating techniques, or due to minor diffusion of elements from the substrate to the coatings.

References

1. Shipway, P.H. *et al.* (2005) *Wear* **259**, 820.
2. Dalmas, D. *et al.* (2003) *Surface and Coatings Technology* **173**, 130.
3. Jenkins, R. *et al.* (1996), *Introduction to X-Ray Powder Diffractometry*. New York, J. Wiley.

Table 1. Average microhardness measurements taken across the cross-sectional slices.

Substrate	H _v Coating (GPa)	H _v Substrate (GPa)
304L Stainless steel	9.41 ± 0.01	2.71 ± 0.01
Aluminium	10.22 ± 0.02	0.90 ± 0.01

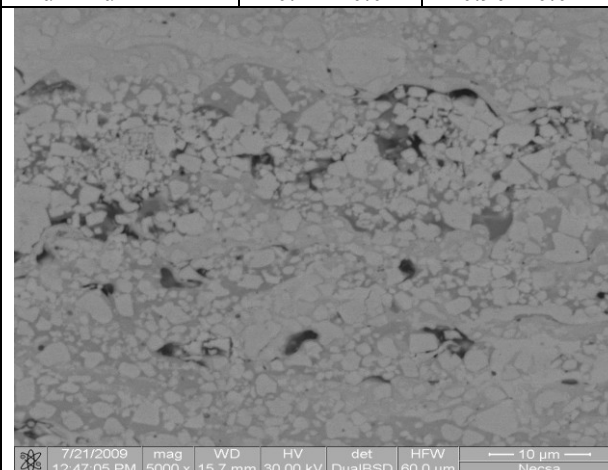


Figure 1. SEM-BSI of WC-Co coating on 304L stainless steel showing: (Co) (dark), WC (white) and medium stainless steel substrate.

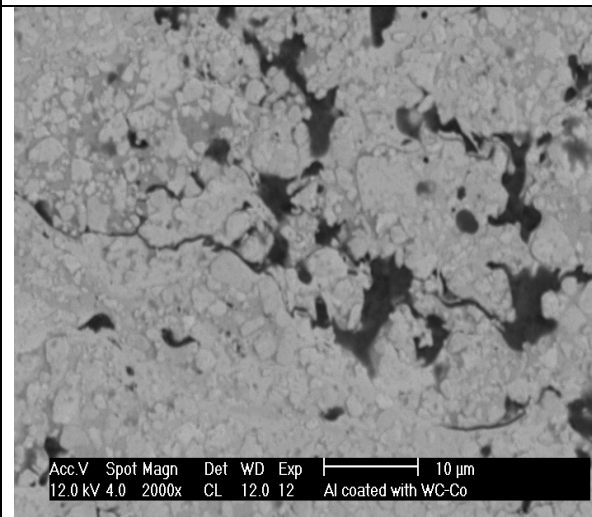


Figure 2. SEM-BSI of WC-Co coating on commercial aluminium showing: (Co) (dark), WC (medium light) and W₂C (light).

*Corresponding author: dijophilip2000@yahoo.com

INFLUENCE OF RESIDUAL STRESSES OF THE WC-Co THERMAL SPRAYED COATINGS ON METAL SUBSTRATE

O.P. Oladijo,^{1,2} L.A. Cornish,¹ A.M. Venter^{1,2} and N. Sacks¹

¹ School of Chemical & Metallurgical Engineering and DST/NRF Centre of Excellence in Strong Materials, University of the Witwatersrand, Private Bag 3, Wits 2050, Johannesburg; ² Research & Development Division, NECSA Limited, Pretoria

Tungsten carbide based cermet coatings with metallic cobalt binder has many applications because of its high surface hardness and excellent wear resistance¹. Residual stresses are inherent to many inhomogeneous materials or structural components, and are mostly produced during the fabrication due to cooling from an elevated temperature to the room temperature². The main objective of the present study is to measure the residual stress values in thermal sprayed WC-Co coatings, as well as the stress relaxation after cutting by wire electric discharge machining (EDM). Previous work had compared the hardness, phases and abrasion wear resistance found in the coatings^{3,4}.

Four substrates, size 75x25x9mm were used in this study were: brass, super-invar, 304L stainless steel and commercial grade aluminium. These were coated with WC-Co using a High Velocity Oxygen Fuel System (HVOF). After metallographic preparation, the microstructures of the coatings were characterized by scanning electron microscopy (SEM), using back-scattered electron imaging (BSE) and energy dispersive X-ray analysis (EDS). The residual stresses on the coatings were measured by means of X-ray diffraction using Co-K α radiation. The strains in the sample were measured using the {112} reflection of WC for peak $2\theta = 123.59^\circ$.

The coatings show a typical microstructure of a WC-Co alloy but varying porosities (Fig.1). EDX analysis confirmed the composition of the coatings to be W, C and Co. Figure 2 shows a graph of the measured values for residual stresses. It can be shown that the residual stress for the WC phase at the measured position were compressive however a noticeable difference between samples. Table 1 shows the results of the residual stresses after the large coated samples were cut into smaller sizes using wire EDM.

The compressive stress in the coated aluminium and 304L stainless steel increased despite change the sample measuring position might due to effect of cooling rate after thermal sprayed. The decreases in residual stress of coated super-invar with respect to measuring position is a result of the larger grain size despite the lower surface roughness. The coated brass showed a distinct difference in the results taken on the surface, which might be as a result of texturing effect observed on its surface during measurement. After cutting the samples to promote stress relaxation by wire-EDM (Table1), there was little stress relaxation in the coated aluminium, brass, and super-invar samples which are still useful during the service. However, more stress relaxation was observed in the coated 304L stainless steel, and changed to tensile stress.

A possible explanation for this behaviour is that melting is the primary material removal mechanism during EDM machining of the sample. Thus, upon solidification, considerable thermal residual stress was induced on the surface layer.

Studies of the four samples show that the residual stress is affected by porosity, grain size, and textured effect on the coatings.

References

1. Gruzdis, E. *et al.* (2009) Mat. Sci. **15**(1)35-39.
2. Schmauder, S. *et al.* (2003) Comput. Mat. Sci. **26**, 143.
3. Oladijo, O.P. *et al.* (2009) Proc. Microsc. Soc. South Afr. **39**, 51.
4. Oladijo, O.P. *et al.* (2010) Proc. Microsc. Soc. South Afr. **40**, 62.

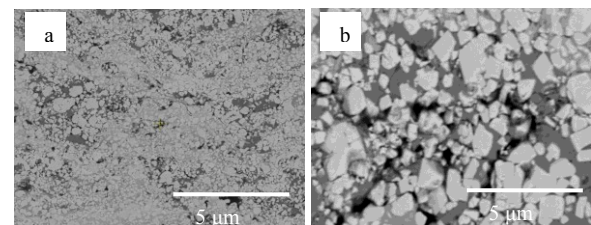


Fig. 1. SEM/BSE images of WC-Co coating in (a) 304L stainless steel substrate (b) Brass substrate.

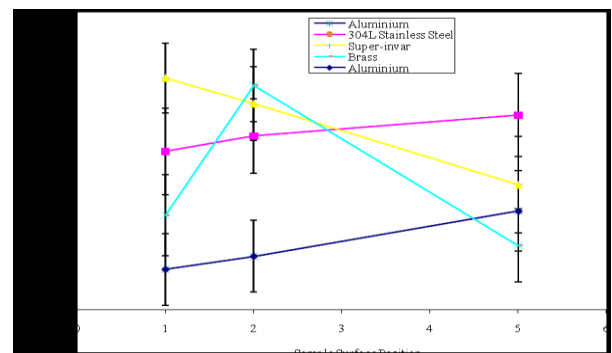


Fig. 2. Residual stresses taken at three differ. positions.

Table 1. Measured residual stresses for WC coatings

Coated substrate	Stress before cutting (MPa)	Stress after cutting (MPa)
Aluminium	-183.6 \pm 47.4	-153.8 \pm 42.9
304L stainless steel	-70.7 \pm 48.8	-151 \pm 38.0
Brass	-224 \pm 43.1	-79.2 \pm 35.4
Super-invar	-152.4 \pm 57.0	-139 \pm 37.9

*Corresponding author: dijophilip2000@yahoo.com

EFFECT OF HEAT TREATMENT ON THE MICROSTRUCTURE AND RESIDUAL STRESS IN THE WC-17Co COATED SYSTEM

O.P. Oladijo,^{1,2,3} L.A. Cornish,^{1,2} A.M. Venter^{2,3} and N. Sacks^{1,2}

¹ School of Chemical & Metallurgical Engineering, University of the Witwatersrand, Private Bag 3, WITS, 2050

² DST/NRF Centre of Excellence for Strong Materials, University of the Witwatersrand

³ Research & Development Division, NECSA Limited, Pretoria

Tungsten carbide based cermet coatings with metallic cobalt binders are widely used for cutting tools. They are known for their exceptional combination of toughness and hardness. However, severe cutting conditions produce high temperatures and the stresses produce plastic deformation of the cutting tool¹. Therefore, a better knowledge of the material behaviour at high temperature is therefore needed to improve the quality of the cutting tools. The main objective of the present study was to systematically investigate the residual stress in systems of thin WC-Co coatings on substrates that had different coefficients of thermal expansion (CTE) to the coating. This was conducted on the reference grit-blasted, as-sprayed WC-Co coatings and their annealed counterparts to ascertain whether heat-treatment was beneficial for stress relaxation/alteration procedure. Previous work had compared the microstructural characteristics and abrasion wear resistance found in the the as-sprayed coatings^{2,3}.

WC-Co coatings of about 200µm were deposited by TAFA JP500 High Velocity Oxygen Fuel System (HVOF) technique on brass substrates of size 25 x 25 x 6 mm². The grit-blasted and as-sprayed brass sample were heat-treated at 375°C for one hour in an argon environment. This annealing temperature was selected as 40% of the melting temperature of the substrate material. After standard metallographic preparation, the effect of annealing on the microstructures was characterized by scanning electron microscopy, using backscattered electron imaging with EDX, phase identification by X-ray diffraction (XRD) using Cu radiation, and Vicker's hardness for macrohardness. The residual stresses in the coatings were determined by means of the neutron stress diffractometer Kowari (ANSTO, Australia). Two approaches were used to measure residual stress in coating; Direct measurement (experimental) and indirect measurement (utilizing stress balance principle from the substrate stress profile).

The cross sectional microstructure of the coatings showed a typical microstructure of a WC-Co alloy but with varying porosities (Fig.1(a)). Typical characteristics were the lamellar structure, pores, rounded WC particles and distinct differences in the WC carbide grain size. After annealing (Fig.1(b)), the microstructure become more homogeneous. A noticeable reduction of pores, grain size and macrohardness was found. The EDX results indicated that both the as-sprayed and heat-treated coatings were composed of W, C, and Co. In addition, localised microcracking was found in the cross section of the annealed sample. These microcracks might have occurred as a result of both thermal expansion mismatch between the substrate and coating; from the thermal stresses generated during cooling and formation of the

coating. Comparison of the as-sprayed and annealed coated samples showed that no new phases were produced, but that the Co peaks became more pronounced, while all the WC peaks became sharper. This could be due to diffusion equilibrating the different cell sizes, and reduction in stress. The residual stresses in the WC phase coating (Table 1) determined under the different conditions were compressive, but quite different. There was good agreement between the two methods.

The stress in the as-sprayed brass substrate was moderately compressive. The homogenous microstructure of the coating influenced the residual stresses, including the distribution of microstructural defects, particularly pores and microcracks. The surface hardening, from grit-blasting might also influence the residual stress. After heat treatment, larger compressive values demonstrated the effect of temperature on the coefficient of thermal expansion of the substrate.

Studies of the brass samples to date showed more compressive stresses, as well as decreased grain size, hardness and porosity after heat-treatment. The residual stress was affected by the coating's microstructure and coefficient of thermal expansion of coating⁴.

References

1. Mari, D. *et al.* (2009) Int. J. Refr. Met. and Hard Mat. **27**, 282-287.
2. Oladijo, O.P. *et al.* (2009) Proc. Microsc. Soc. South Afr. **39**, 51.
3. Oladijo, O.P. *et al.* (2010) Proc. Microsc. Soc. South Afr. **40**, 62.
4. Oladijo, O.P. *et al.* (2012) Surf. Coat. Techn. **23**, 4011-4020.

Table 1. Residual stresses of WC coatings.

Substrate/Condition	Stress, MPa, experimental	Stress, MPa indirect
Brass / as-sprayed	-44 ± 107	-47 ± 48
Brass / annealed	-367 ± 86	-339 ± 27

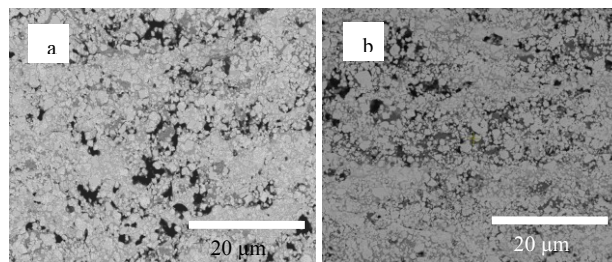


Fig. 1. SEM/BSE images of WC-Co coating on brass sample: (a) As-sprayed, (b) Annealed coating, showing WC grains (light), cobalt binder (grey), and black pores.

*Corresponding author: seyiphiphilip@gmail.com